Property Evolution in Ion-Irradiated FeCr Alloys for Fusion Reactor Applications



Kay Yunqi Song
Wadham College
University of Oxford

A thesis submitted for the degree of
Doctor of Philosophy
Michaelmas 2023

For my 老豆 and 妈咪

Acknowledgements

It took a village to raise this thesis.

I'd like to begin by thanking my supervisors, Felix and Dave, for their support over the years. Their wisdom, encouragement, and optimism has been invaluable. I am beyond grateful to both of them for the opportunity to undertake this adventure and their constant guidance along the way.

Thank you to my friends and colleagues in the Oxford Engineering Science and Materials departments, past and present, in and out of the lab. In particular David, Abdallah, Hongbing, Guanze, Rima, Ivan, Seb, Tom, Minyi, Phani, and Robin. Thank you to the workshop folks Andy, Simon, and Neil for turning my scrappy drawings into useful reality. I am also incredibly grateful for the tireless support of the beamline scientists at the APS, particularly Dina, Wenjun, and Jon.

Thank you to the General Sir John Monash Foundation for your support, both financially and through the incredible scholars' community. This journey would not have been possible otherwise.

My community in Oxford, you have shaped my time here in ways I could not have foreseen. My Wadham friends - Kate, Alex, Alice, Michael, Carina, and Will. My St Ebbe's family - Christy, Hazel, NP, Antje, Christopher, Glenn, and the Thesis community throughout the years. My frisbee pals - Laura, Grace, Grisel, Luka, Jonas, Carlota, and Mateo.

My friends back in Australia, from my Hornsby Girls to my ANU mates, I am so grateful for all your support from the other side of the world (and some right here in Oxford). Thank you to those who managed to even make a visit in person, as well as those poking me when I forgot to reply... again.

My family, especially my parents and grandparents for their endless support of my academic pursuits and curiosity since before my first day of school. I would not be here without your love and sacrifice.

And finally, how fitting is it that the motto of the University of Oxford is:

Dominus Illuminatio Mea – The Lord is my light

All praise and glory belong to Him forever and ever.

Abstract

Understanding irradiation-induced changes in the properties of structural steels is crucial for the operation of next-generation nuclear fusion reactors. In the absence of a fusion neutron source, irradiation with heavy ions enables the study of irradiation-induced microstructural and property evolution. The study of FeCr binary alloy as model steels provides fundamental understanding of irradiation damage mechanisms and validates predictions from simulations. To date, irradiation effects in FeCr alloys below 573 K have not been well-studied. However, they are key to understand for successful fusion reactor steel design and operation, which will span from cryogenic temperatures to over 800 K.

In this thesis, defect and material property evolution in FeCr binary alloys following room-temperature ion irradiation have been investigated. Irradiation-induced hardening and lattice strains were measured for doses as low as 0.00008 displacements-per-atom (dpa), well below the threshold for defect observation with electron microscopy. Lattice strain in FeCr increases with dose up to 0.8 dpa and then decreases with subsequent increase in dose, suggesting the formation of dynamic quasi-steady defect structures. Irradiation hardening increases with both dose and Cr content. In contrast, thermal diffusivity depends mainly on Cr content rather than irradiation dose.

The deformation behaviour of ion-irradiated FeCr binary alloys is further explored with nanoindentation techniques. The initiation of plasticity is primarily governed by pre-existing dislocation sources that are unaffected by ion irradiation and Cr content. Surprisingly, an irradiation-induced loss of strain hardening capacity is observed irrespective of Cr content. This results in 3D confinement of deformation fields in the irradiated materials.

Next, these techniques are applied to Eurofer-97, a prototypical FeCr-based reactor steel. Severe plastic deformation caused grain refinement along with marked increase in dislocation density. Irradiation caused hardening and reduction in thermal diffusivity for both as-received and deformed materials. However, deformation prior to irradiation did not have a significant effect in mitigating these changes.

By combining different characterisation techniques, a multi-faceted picture emerges of the irradiation-induced structural defects and resultant property changes in FeCr alloys. Interestingly, no technique on its own can capture all of this information, but a holistic approach is essential. These results have enabled key insights that are crucial for further optimisation of structural steels for advanced fission and fusion power reactors.

List of Abbreviations

AFM . . . . . Atomic force microscopy

APT . . . . . Atom probe tomography

BCC . . . . . Body-centred cubic

BCT . . . . . Body-centred tetragonal

DAXM . . . . Differential aperture X-ray microscopy

DBTT . . . . . Ductile-to-brittle transition temperature

dpa . . . . . Displacements-per-atom

EBSD . . . . . Electron backscatter diffraction

ECAP . . . . . Equal-channel angular pressing

EFDA . . . . . European Fusion Development Agreement

FCC . . . . . Face-centred cubic

HPT . . . . . High-pressure torsion

NRT . . . . . Norgett-Robinson-Torrens

RAFM . . . . Reduced-activation ferritic/martensitic

SAW . . . . . Surface acoustic wave

SEM . . . . . Scanning electron microscopy

SPD . . . . . Severe plastic deformation

SRIM . . . . . Stopping Range of Ions in Matter

TEM . . . . . Transmission electron microscopy

TGS . . . . . Transient grating spectroscopy

UFG . . . . . Ultra-fine grain

XRD . . . . . X-ray diffraction

Note: all chemical elements in this thesis will be referred to by their chemical symbols.

Contents

1 Introduction **1**

2 Scientific Background and Methods **4**

2.1 Structural Materials for Nuclear Fusion 4
2.2 The Collision Cascade 9
2.3 Quantifying Displacement Damage 11
2.4 Surrogates for Fusion Neutrons 12
2.5 Irradiation-Induced Defect Structure and Evolution in FeCr Alloys . . 17
2.6 Irradiation-Induced Property Changes in FeCr Alloys 24
2.7 Severe Plastic Deformation and Nanostructuring 37
2.8 Experimental Techniques 47
2.9 Summary of the Literature Review 64
2.10 Research Outline 65

3 Characterising Ion-Irradiated FeCr: Hardness, Thermal Diffusivity and Lattice Strain **68**

3.1 Abstract 69
3.2 Introduction 70
3.3 Methods and Materials 73
3.4 Results and Discussion 76
3.5 Conclusion 91

4 Dose and Compositional Dependence of Irradiation-Induced Property Change in FeCr **94**

4.1 Abstract 95
4.2 Introduction 96
4.3 Materials and Methods 100
4.4 Results 105
4.5 Discussion 113
4.6 Summary and Conclusion 122

5 Deformation Behaviour of Ion-Irradiated FeCr: A Nanoindentation Study **124**
5.1 Abstract . . . 125
5.2 Introduction . . . 126
5.3 Materials and Methods . . . 128
5.4 Results . . . 130
5.5 Summary and Conclusion . . . 148

6 Deformation Localisation in Ion-Irradiated FeCr **151**
6.1 Abstract . . . 152
6.2 Introduction . . . 153
6.3 Sample Preparation and Ion Implantation . . . 154
6.4 Nanoindentation and Atomic Force Microscopy . . . 155
6.5 X-ray Measurements of Lattice Rotation and Strain . . . 158
6.6 Discussion . . . 161
6.7 Conclusion . . . 162

7 Microstructural and Material Property Changes in Severely Deformed Eurofer-97 **163**
7.1 Abstract . . . 164
7.2 Introduction . . . 165
7.3 Materials and Methods . . . 167
7.4 Results . . . 173
7.5 Discussion . . . 190
7.6 Summary and Conclusion . . . 196

8 Conclusion **198**
8.1 Outlook . . . 202

Appendices

A Design of temperature-controlled sample holder **206**

B Chapter 3 Appendix **209**

C Chapter 4 Appendix **218**

D Chapter 5 Appendix **224**

E Chapter 6 Appendix **226**

F Chapter 7 Appendix **231**

References **240**

1 Introduction

Human activities, primarily through the emission of greenhouse gases, have caused an increase in global temperatures by 1.1 K in 2011 to 2020 compared to the pre-industrial era (between 1850 to 1900) [1]. One of the largest contributors to this is the burning of fossil fuels for the energy sector and the associated production of CO_2. If current rates of consumption continue, global warming is likely to reach 1.5 K between 2030 and 2052 [2], which would impart even greater disastrous consequences for the planet. Addressing the climate crisis demands the development and implementation of low- or zero-carbon alternative sources of energy.

Renewable energy, such as solar and wind, have been hailed as leading candidates to replace fossil fuel energy generation. However, despite technological improvements over the past decades, they are limited by low energy output density and high running costs [3]. Furthermore, due to the intermittent nature of most renewable energy sources, they cannot be fully relied on to meet base-load or sudden demand power needs without further costs due to energy storage requirements [4]. Renewable energy generation needs to be complemented by another source of 'dispatchable power'.

Nuclear fission technology has been growing in its scale of energy generation over the past 50 years and has prevented the emission of around 70 Gt of CO_2 globally [5]. It currently provides ∼10% of global energy generation, and many countries are taking steps to advance their nuclear power plants to complement the use of renewable energy in efforts to decarbonise the energy sector [5]. However, despite

improvements in reactor safety designs and ease of deployment, the production of long-lived radioactive waste from nuclear fission remains a key issue in their use [6].

Nuclear fusion is a promising candidate to provide an efficient, safe and low-carbon method of energy generation to meet the baseline energy needs of our society. There are currently a handful of research fusion devices in the world. However, the use of nuclear fusion for energy generation has not yet been realised due to technological challenges. To cause the fusion of two nuclei, their repulsive Coulomb forces need to be overcome. On Earth, the most achievable fusion reaction is that of a deuterium (D) and a tritium (T) nuclei to form helium (He) and a high energy neutron (n) [7]:

$$^2D + ^3T \rightarrow ^4He\ (3.56\ \text{MeV}) + n\ (14.1\ \text{MeV}). \tag{1.1}$$

This D-T fusion reaction requires temperatures of around 150 million degrees [8]. One type of proposed containment device is a tokamak, which is a toroidal chamber that uses magnetic fields to confine hot plasma [9]. In order to produce sufficient output power from a nuclear fusion reactor for commercial applications, the plasma density, confinement time, and temperature (the triple product) will all need to be increased [10]. All of this places much greater thermal and neutron loads on the materials of commercial fusion reactors compared to previous research reactors.

Meeting the materials requirements for building a device that can withstand extreme temperatures and irradiation conditions necessitates global scientific collaboration. ITER is one such collaborative science project currently underway to demonstrate the viability of nuclear fusion to generate net power [11]. It will also serve to inform the design of next-generation reactors including DEMO and beyond. Furthermore, there are also a number of private fusion companies working to develop tokamaks and other confinement devices to achieve commercially viable nuclear fusion energy.

The study of materials that will be used as structural components of the fusion reactor is crucial to the safety of its operation. In particular, understanding the response of the materials to in-service conditions will determine the range of operational limits and component lifetimes. Some of the key challenges facing nuclear structural steels from irradiation include hardening, embrittlement, and degradation

of fracture properties [12]. Many of these effects are also temperature-dependent [13], which is an additional challenge considering that structural components in a fusion reactor will be operating from cryogenic temperatures up to over 800 K. Knowledge of the irradiation-induced changes in materials, and how that is affected by factors such as material composition and processing parameters, is important for optimising the design of reactor components and materials. These factors are some of the key determinants on which the efficiency and viability of nuclear fusion power hinges [14].

This thesis explores the irradiation effects on the microstructure and properties of steels proposed for structural components in nuclear fusion reactors. Key literature and gaps in existing knowledge of irradiation damage in nuclear reactor structural steels will be reviewed in Chapter 2. The first four studies in this thesis (Chapters 3 to 6) focus on ion-irradiated FeCr binary alloys as model systems to understand irradiation damage in steels. By using a range of different techniques to characterise defect population and material properties, a full picture of the fundamental behaviour of irradiation damage emerges. The last study (Chapter 7) applies the techniques and insights from FeCr binary alloys to Eurofer-97, a prototypical fusion reactor structural steel. It focuses on the use of severe plastic deformation as a processing technique to improve the performance of the material against irradiation-induced changes. The results from this thesis provide a multi-faceted and comprehensive picture of irradiation-induced evolution in FeCr steels to guide the design and development of next-generation nuclear reactors.

2

Scientific Background and Methods

2.1 Structural Materials for Nuclear Fusion

One of the key materials issues for nuclear fusion reactors is the design of suitable structural materials to support reactor components such as the first wall and breeding blanket. For fusion devices beyond current capabilities, such as ITER then DEMO, the neutron fluence could be six to eight orders of magnitude, respectively, higher than that of current plasma devices such as JET [13]. Due to the use of superconducting magnets and the high operating conditions near the first wall, there will be a large range of operating temperatures (4–823 K) in next-generation fusion devices, presenting additional challenges to material requirements. Temperature effects are particularly important to understand as the irradiation response of materials is highly temperature-dependent [13, 15].

There are many considerations for selecting the most appropriate materials for fusion reactor structural components including intrinsic material properties, irradiation response, long-term activity, availability of raw materials and supply chain, maturity of production technology, and cost. Currently, the leading candidates for structural component applications are reduced activation ferritic/martensitic (RAFM) steels with 8–9%Cr [16, 17]. These are Fe-based steels with a body-centred cubic (BCC) and/or body-centred tetragonal (BCT) crystal structure. This class of steels was developed from conventional ferritic/martensitic 9Cr-1Mo and 8-12%Cr-

MoVNb steels, used in nuclear fission reactors [18–20]. Elements such as Mo and Nb, which are prone to neutron activation forming elements with long decay half-lives, are replaced with lower activation elements such as Ta and W [21]. RAFM steels are designed to take advantage of the presence of martensitic laths to yield high strength (300–600 MPa) [22]. Precipitates such as carbides and oxides can often be included to yield high-temperature strength [23]. RAFM steels also have good tensile ductility (>10%) under operational temperatures up to 773 K [12, 22, 24, 25].

Compared to traditional austenitic stainless steels, RAFM steels exhibit much less irradiation-induced swelling and dimensional changes (further discussed in Section 2.6.1) [13]. RAFM also have higher thermal conductivity and lower coefficient of thermal expansion, making them desirable as structural components [24, 26]. Ni, which is included in many conventional stainless steels, is excluded from RAFM to reduce the cost of manufacturing and more importantly reduce the transmutation rate and production of He and H gases [20, 27]. Finally, the existing manufacturing maturity required for the fabrication of RAFM makes it the most suitable candidate for next-generation reactors, such as DEMO and beyond [20, 22].

One of the key disadvantages of using RAFM steels is that they exhibit low-temperature (573 K to 623 K) irradiation-induced embrittlement, also leading to an increase in ductile-to-brittle transition temperature (DBTT) [28, 29]. In unirradiated RAFM steel, the DBTT is between 193 K and 203 K. The irradiation-induced DBTT increase has been found to depend on Cr concentration in the material and is minimum at ∼9%Cr (Figure 2.1). This is the primary motivation behind the extensive research and development of steels with 7–12%Cr content, including HT9 (United States) [30], F82H (Japan) [12, 31], Eurofer-97 (European Union) [12, 31], and their respective variants. However, the DBTT can still be as high as 450 K after irradiation expected within the lifetime of nuclear structural components even for RAFM steels with 9%Cr [32].

In summary, the main predicted operating temperature window for RAFM is between 623 K to 823 K [16, 20]. Above this range, the materials experience a significant decrease in tensile and creep strength. Below 573 K, the material is limited by low-temperature irradiation hardening, embrittlement and increase in

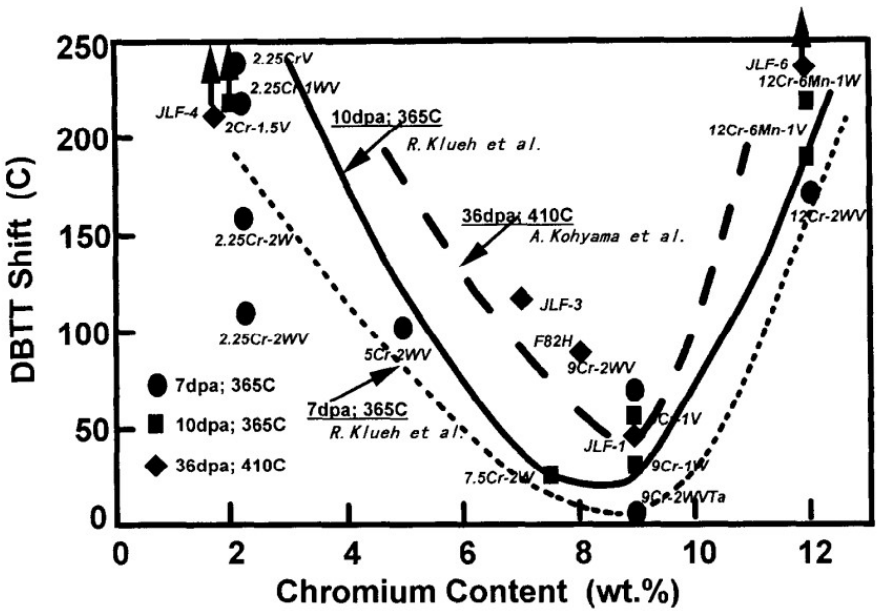


Figure 2.1: A review of the effect of Cr content on DBTT shift in RAFM steels following neutron irradiation [29]. The original data is from Klueh *et al.* [33] and Kohyama *et al.* [34]. The unit of damage 'dpa' will be further discussed in Section 2.3.

DBTT even for very low-dose irradiation [26]. However, irradiation effects for temperatures much lower than the main operational temperature window are still important to characterise as some steel components in the reactor will be operating well below 623 K down to cryogenic temperatures.

2.1.1 Eurofer-97

One of the most-studied RAFM steels is Eurofer-97, which was designed and has been manufactured in a limited number of batches in the European Union since 1997 [35, 36]. The detailed chemical composition of Eurofer-97 is shown in Table 2.1. A series of heat treatments is conducted to achieve the desirable material properties for RAFM steels described in the previous section. The exact heat treatment varies between batches but usually includes austenisation at 1253–1313 K for 27–30 minutes, followed by tempering at 1023–1033 K for 90–120 minutes [19]. A total of three heats have been used to produce samples of bars, plates, tubes, and wires. These samples have been distributed to researchers in various laboratories with an emphasis on reproducibility and traceability [22].

Elements	Radiologically desired (ppm)	Eurofer-97 specified (mass%)	Eurofer-97 achieved (mass%)
(a) Main alloying elements (mass%)			
C		0.09–0.12 [0.11]	0.105
Cr		8.5–9.5 [9.0]	9.08
W		1.0–1.2 [1.1]	1.07
Mn		0.20–0.60 [0.40]	0.56
V		0.15–0.25	0.235
Ta		0.10–0.14 [0.12]	0.125
N_2		0.015–0.045 [0.030]	0.039
P		<0.005	0.0025
S		<0.005	0.001
B		<0.001	0.0007
O_2		<0.01	0.0008
(b) Radiologically undesirable elements (ppm)			
Nb	<0.01	<50	50
Mo	<1	<50	50
Ni	<10	<100	130
Cu	<10	<100	50
Al	<1	<100	90
Ti	<200	<200	10
Si	<400	<500	240
Co	<10	<100	70

Table 2.1: Chemical composition of Eurofer-97 specified from [19, 35], target values are in square brackets. The achieved values reported are from batch 2, manufactured by Böhler Bleche [37], which is also the batch used for studies in this thesis (Chapter 7).

Many standard tests have been performed to measure the intrinsic material properties of Eurofer-97, including tensile, Charpy, and creep tests [38]. Long-term ageing was also investigated and it was found that hardness was not affected after annealing to 823 K for up to 5000 hours. The irradiation response of Eurofer-97 has also been investigated in many different studies, which found hardening and embrittlement at low temperatures (<600 K) [39–41] but little change to hardening and fatigue behaviour at higher temperatures (>723 K). More recently, the focus shifted to other post-processing treatments, such as thermo-mechanical treatments, to improve the irradiation resistance of Eurofer-97. For example, Rieth *et al.* [42] found that lowering the normalising temperature can improve the ductility and

irradiation-induced DBTT shift of Eurofer-97.

2.1.2 FeCr Binary Alloys

Many of the studies described thus far for RAFM steels and Eurofer-97 have made use of fission neutron irradiation or ion irradiation to simulate the fusion reactor environment. Their advantages and drawbacks will be discussed in more detail later in the chapter (Section 2.4). To supplement this, extensive modelling efforts have been made to understand the effect of irradiation on structural steels [43–45]. These include molecular dynamics (MD) to simulate displacement cascades [46–49], density functional theory (DFT) to predict defect structures and material properties from first principles quantum mechanics [50–52], and finite element modelling (FEM) for structural mechanics [53–55]. Modelling studies allow researchers to study irradiation scenarios that might otherwise be inaccessible to experimentalists, as well as investigate effects on different time- and length scales [56]. The process of developing useful and accurate models requires extensive experimental validation [57]. However, modelling a steel such as Eurofer-97, particularly with precise first-principles techniques, is challenging due to the microstructural complexities arising from different alloying elements. As a result, pure Fe or FeCr binary alloys are often considered to gain a representative understanding of irradiation effects in RAFM steels [58]. This makes the experimental study of FeCr binary alloys as a function of different irradiation and composition parameters important for providing validation for modelling studies [50].

Moreover, by developing a mechanistic understanding of the principles and effects of irradiation damage on model systems, a knowledge base can be established to guide necessary experiments on industrial steels and inform the development of future steels. Furthermore, the relative microstructural simplicity of FeCr binary alloys makes them ideal systems for developing characterisation methods that can be later implemented on more complex steels.

In light of the importance of studying FeCr binary alloys, the European Fusion Development Programme (EFDA, now EUROfusion), commissioned a series of high-purity alloys to be produced in 2007. Similar to Eurofer-97, these alloys have been

distributed to a range of laboratories for investigation, with the goal of being able to compare the results from the same starting material. A non-exhaustive list of other studies using these alloys include [59–65]. A subset of these alloys have been studied in this thesis. The composition of these alloys and the relevant chapters they are covered in are listed in Table 2.2.

Alloy	Cr (wt %)	C (wppm)	S (wppm)	O (wppm)	N (wppm)	Chapter(s) in this thesis
Fe	<0.0002	4	2	4	1	4, 5, 6
Fe3Cr	3.05	4	3	6	2	3, 4, 5
Fe5Cr	5.40	4	3	6	2	3, 4, 5
Fe8Cr	7.88	6	2	10	2	4
Fe10Cr	10.10	4	4	4	3	3, 4, 5, 6
Fe12Cr	11.63	6	2	4	<10	4

Table 2.2: The chemical compositions of the EFDA FeCr alloys used in this study as measured by the manufacturer using glow discharge mass spectrometry [66, 67].

To summarise, RAFM steels have been identified as one of the leading candidate material groups for nuclear fusion reactor structural components. The composition, in particular the Cr content, of the steel has a great impact on its operational limits, including temperature range. The study of Fe and FeCr binary model alloys will provide useful baseline knowledge of the irradiation damage effect in RAFM steels and validate important modelling studies.

2.2 The Collision Cascade

Ions and neutrons cause damage to materials by displacing atoms in the material lattice. The incoming particle collides with and transfers energy to an atom in the lattice. If the transferred energy is greater than the displacement threshold, E_d, of the lattice (on the order of tens of eV for most materials [68]), the atom becomes a primary knock-on atom (PKA) and is displaced from its lattice site. It then moves through the material lattice, transferring the energy to other atoms, creating a

displacement cascade consisting of point defects (vacancies and interstitials). This continues until the PKA eventually comes to rest as an interstitial, leaving a vacancy elsewhere in the lattice [46, 69]. The displaced atoms (secondary knock-ons) can also move through the lattice, displacing more atoms (higher-order knock-ons) until the energy has been dispersed and each atom has kinetic energy less than E_d. For Fe and FeCr alloys, E_d is approximately 40 eV but can depend on the crystal orientation relative to the PKA trajectory [70].

This initial process is referred to as the collisional, or ballistic, stage (lasting <1 ps) [69] and no stable defects are formed. This is followed by the thermal spike stage, lasting on the order of a few ps [46], where the kinetic energy of the displaced atoms is spread amongst its neighbours, producing a region of high temperature that behaves like molten metal [71]. The subsequent evolution of defects depends significantly on the material and irradiation conditions. This can affect the recombination of interstitials with vacancies, the formation of stable point defects or defect clusters, and the thermally-activated diffusion of defects [69]. An MD simulation of these processes is depicted in Figure 2.2 for a 10 keV recoil atom in Fe.

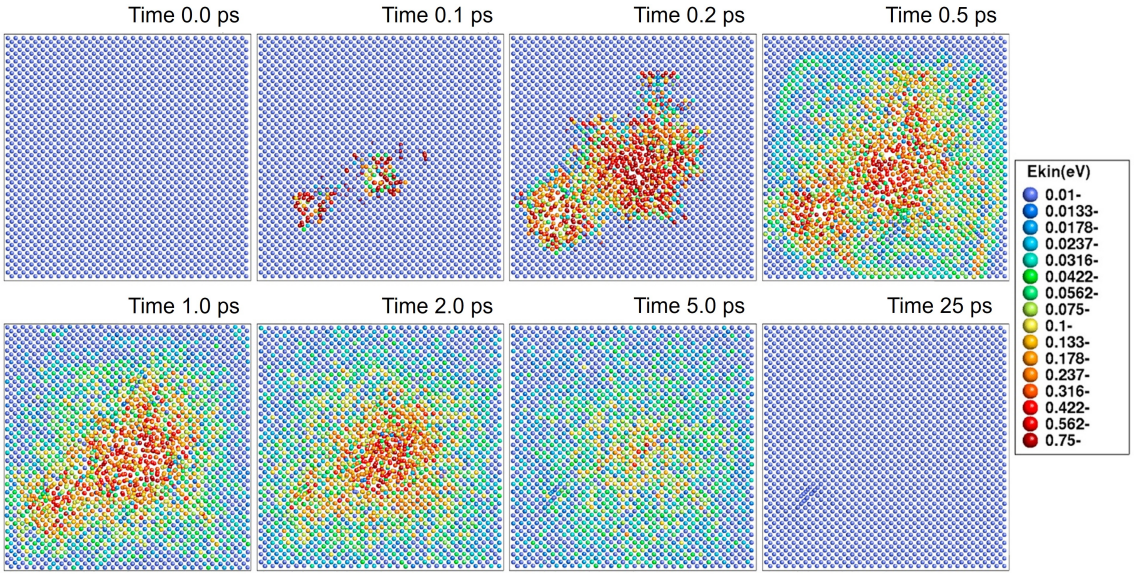


Figure 2.2: The kinetic energy of atoms in Fe following a collision cascade induced by a 10 keV recoil at 0 K [72]. Though many atoms are initially displaced, a majority of them return to 'perfect' crystal positions (not necessarily where they started) after the cascade cools down, with very few existing as interstitials.

Studies in FeCr have shown that the addition of Cr atoms does not impact the ballistic phase and cascade formation compared to the case of pure Fe [48, 73, 74]. This is likely due to the similarity in mass between Cr and Fe atoms. However, Cr affects the recombination stage by changing the mobility of defects in the material [75] (further discussed in Section 2.5.2).

2.3 Quantifying Displacement Damage

The Norgett-Robinson-Torrens (NRT) model is widely used to calculate the number of displaced atoms as a function of the displacement energy of the material [76, 77]. It considers the process described in the ballistic phase and also some recombination from ballistic collision approximation simulations [76, 78]. The NRT model gives the number of defects (N_d) produced as:

$$N_d(T_d) = \begin{cases} 0 & T_d < E_d \\ 1 & E_d < T_d < \frac{2E_d}{0.8} \\ \frac{0.8T_d}{2E_d} & \frac{2E_d}{0.8} < T_d < \infty \end{cases} \tag{2.1}$$

where T_d is the energy available to produce damage, which is the total particle energy minus the energy loss due to electronic excitations.

From the NRT model, the ratio of displaced atoms to the total number of atoms in a particular volume can be calculated and is referred to as 'displacements-per-atom' (dpa). In principle, this gives the concentration of defects in the material assuming no defects are lost to defect sinks or recombination. It is a useful measure for comparing displacement damage exposure between experiments with different irradiating particle species, fluence, and energy [72].

There are many cautions and drawbacks that one must keep in mind when using the concept of dpa. For instance, it does not take into account defect recombination due to thermal fluctuations, which becomes increasingly significant with temperature. The definition of the threshold energy, E_d, is also not straightforward as it can depend on the crystallographic orientation and the interatomic potential used in simulations [47]. Furthermore, it has been shown from MD simulations that defect production is not a linear function of damage energy. This is due to the athermal recombination

of defects immediately following the thermal spike phase, which happens regardless of the sample temperature [72]. The fraction of surviving defects decreases rapidly with increasing recoil atom energy. When damage energy exceeds ∼1 keV, the fraction of surviving defects is ∼0.3 for a range of materials [77, 79], including Fe [49]. An efficiency parameter ξ, the NRT efficiency, can be used to describe a ratio of the actual damage or defect concentration measured experimentally to the damage predicted by the NRT model (Equation 2.1) [72, 77].

One of the most common ways to estimate dpa for ion irradiation studies is with the Monte Carlo code SRIM (Stopping Range of Ions in Matter) [80]. As the SRIM code uses the NRT model, it suffers from the limitations outlined previously. Stoller *et al.* [70] have presented further discussions and guidelines on using SRIM for dpa calculations, including recommended simulation procedures and $E_d = 40$ eV for Fe. These procedures have been followed for the work undertaken in this thesis unless explicitly stated.

2.4 Surrogates for Fusion Neutrons

As commercial fusion reactors and sources of 14 MeV fusion neutrons do not yet exist, alternative methods have to be employed to mimic their effects. The most commonly-used methods include neutrons from spallation and fission sources, as well as ion irradiation using particle accelerators. Ion irradiation can include the use of protons or heavy ions, which generally refer to elements heavier than hydrogen and sometimes helium. Each method has distinct advantages and similarities to fusion neutrons, as well as limitations. It is important to understand these factors when interpreting and comparing results.

2.4.1 Energy Spectra

Two different energy spectra are important to consider for irradiation studies mimicking neutrons from D-T fusion (Figure 2.3). The first is the energy spectrum of the incident neutrons. Figure 2.3(a) shows a comparison of the neutron spectra from different existing neutron sources with those expected from DEMO and IFMIF

(a proposed dedicated fusion neutron source [81]). It can be seen that fission reactors (BOR60 and HFR) match the spectrum expected from DEMO to varying degrees. The key difference is the lack of the 14.1 MeV peak (where 80% of the D-T fusion energy is delivered). Spallation sources (ESS and XADS) also do not provide that peak but have a much higher energy range due to their method of neutron production using protons with ∼1 GeV energy. The different energy spectra, along with different total neutron fluxes, will impact the rate and amount of transmutation in the irradiated materials [82].

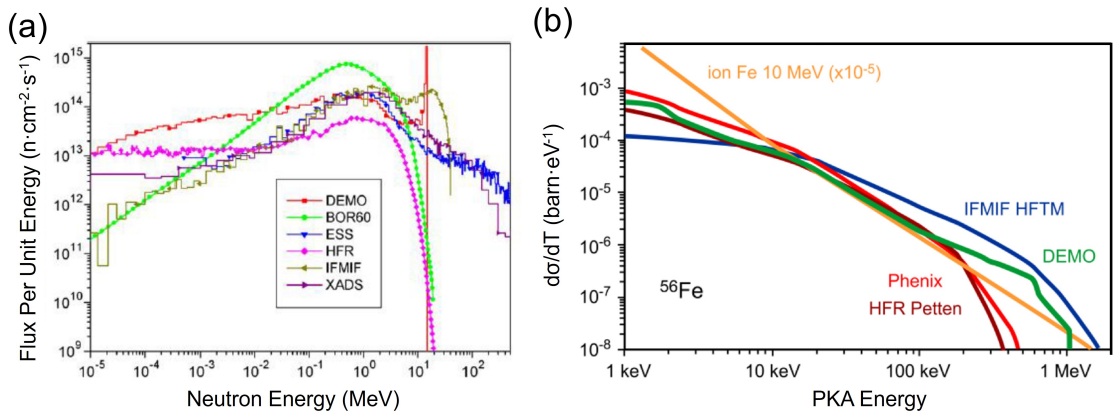


Figure 2.3: (a) Comparison of neutron spectra of DEMO, IFMIF, fission reactors (BOR60, HFR) and spallation sources (ESS, XADS). (b) Comparison of PKA energy spectra of neutron sources including Phenix, a fast fission reactor, and Fe ion irradiation. Both figures are reproduced from [83].

The other important energy consideration is that of the recoil spectrum, which is different for each irradiation source type [84]. Even for nominally the same particle energy, the average transferred energy per PKA, the defect production efficiency, and the cascade characteristics can vary greatly [85]. Figure 2.3(b) shows for Fe that while self-ion irradiation can reproduce some of the high-energy (MeV) PKAs expected from D-T fusion, it also produces a large population of low-energy PKAs due to their long-range Coulomb interactions. These low-energy PKAs have a higher defect survival fraction for a given dose [86]. Whereas neutrons from fission reactors (Phenix and HFR) are well-matched to the PKA spectra of DEMO at low energy ranges but do not produce any significant populations of the high energy PKAs.

2.4.2 Dose Rate Differences

A key advantage of using ion irradiation as a surrogate for neutrons is that high irradiation doses, which might take months or years to receive from a neutron source, can be achieved in shorter periods of time, on the order of hours. Heavy ion irradiation results in dose rates ∼3 orders of magnitude higher than expected for fusion first wall, and up to 7 orders of magnitude higher than that from fission neutron sources [83]. The difference in dose rate is a key factor to consider when comparing results between ion and neutron irradiation [87].

Differences in dose rate can affect the evolution of defects [88]. A lower dose rate leads to a lower concentration of point defects, which results in a more sink-dominate regime where defects are mainly lost to sinks such as grain boundaries and dislocations. A higher dose rate results in defect loss mainly from the recombination of vacancies and interstitials [69]. Interestingly, the effect of dose rate works in opposition to temperature, and some have theorised that shifting the irradiation temperature can compensate for the dose rate effects [89, 90]. However, changing the irradiation temperature could also affect other thermally activated mechanisms and thus not fully replicating irradiation damage at different dose rates.

2.4.3 Damage Microstructure

Hernández-Mayoral *et al.* [91] compared the microstructure of FeCr (2.5–12%Cr) irradiated by neutrons and self-ions at 573 K up to 0.6 dpa. They found that following ion irradiation, the spatial distribution of dislocation loops in FeCr was homogeneous, whereas neutron irradiation resulted mainly in loops decorating existing dislocations. This difference was largely attributed to the different dose rates between ion and neutron irradiation. A higher dose rate, in the case of ion irradiation, corresponds to a greater rate of production of damage cascades and point defects, which allows them to grow to a size observable by TEM close to the site of the initial damage cascade and defect nucleation. A lower dose rate, such as during neutron irradiation, allows point defects to migrate to dislocations and grain boundaries where they stop and subsequently grow larger.

A different study by Hardie *et al.* [92] for Fe6Cr irradiated up to 1.7 dpa at 561 K found slightly lower dislocation loop densities following ion irradiation compared to neutron irradiation. They also found that neutron irradiation caused Cr segregation to the dislocation loops, which did not occur following ion irradiation. Haley *et al.* [93] found larger dislocation loops in Fe9Cr irradiated with Fe ions, compared to neutron-irradiated material at conditions similar to that of Hardie *et al.* [92]. They also found that dislocation loops in ion-irradiated material were mainly vacancy loops, compared to all interstitial loops found in the neutron-irradiated material. Swenson *et al.* [94] performed a comparison of neutron and ion irradiation for a range of FeCr-based commercial steels (8-12%Cr) and found no statistically significant differences in the size and density of the dislocation loops when irradiated to ∼3 dpa at 773 K.

However, there are differences in Cr clustering between neutron- and ion-irradiated FeCr. Atom probe tomography studies identified Cr clusters in Fe18Cr irradiated at 573 K with neutrons at a dose rate of 3×10^{-7} dpa/s, but not in the same material irradiated with heavy ions at dose rates above 10^{-5} dpa/s [95]. The authors of that study attributed differences in clustering to a ballistic mixing mechanism, which ejects Cr cluster solutes into the Fe matrix. At low dose rates, this is balanced by a back diffusion of atoms to recover the equilibrium composition of the Cr clusters. However, in the high dose rate case, the diffusion rate is not fast enough to recover the dissolution of Cr clusters.

2.4.4 Irradiation Profiles

Due to the different electrical charge states of irradiating particles, they also have different penetrating abilities into materials. Neutrons can pass through most materials as they are electrically neutral and do not interact with the lattice atoms via long-range Coulomb forces, allowing the implantation of materials for macro-scale testing. In contrast, due to the charged nature of heavy ions, they can only penetrate a distance on the order of microns into a bulk material [84]. This necessitates micro- and nano-scale characterisation to study the damage in materials irradiated with heavy ions. These techniques will be further discussed in Section 2.8.

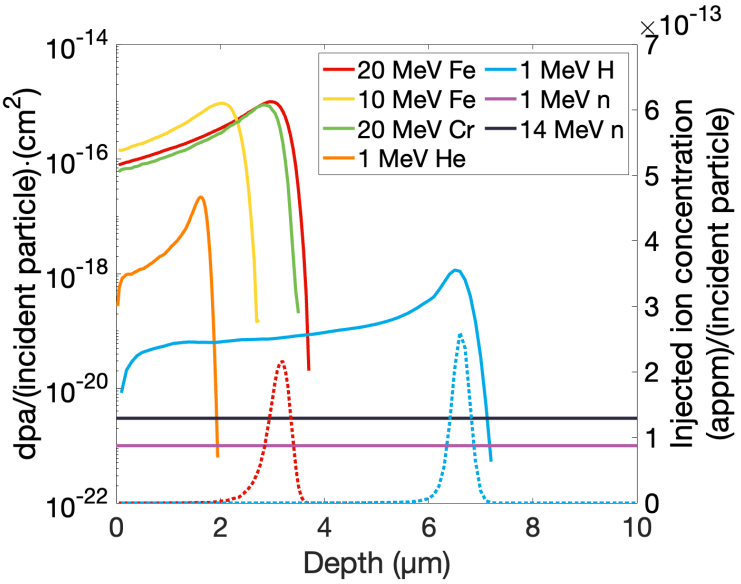


Figure 2.4: Comparison of the damage profiles (solid lines) from different ion species and energies in Fe, calculated from SRIM. Neutron data taken from [96]. Some injected ion profiles are included for comparison (dashed lines of the same colours).

The damage profile induced from heavy ion irradiation is also not uniform (Figure 2.4). It is generally characterised by a low dose region close to the surface and an end-of-range peak in dose. The spatial extent of ion penetration depends on the target material, and the implanting ion species and energy. Some studies use degrader foils or sequential irradiation with different energies to produce a more flattened damage profile [97, 98]. Neutrons, on the other hand, produce a flat damage profile.

Heavy ion irradiation introduces another unique artefact that is absent in neutron irradiations, which are the injected interstitial ions. When the injected ions come to rest at the end of their range (Figure 2.4), they remain in the material as extra interstitial atoms, which can change the balance of different types of defects in the material. The presence of injected interstitials has been shown to reduce the population of α' (Cr-rich) precipitates in ion-irradiated Fe15Cr compared to neutron irradiation [99]. Some studies have found that injected interstitials caused suppressed void growth in Fe [100] and Ni [101], mainly due to defect recombination.

2.4.5 Advantages of Using Heavy Ions

The use of heavy ion irradiation as a surrogate for neutrons does not cause transmutation in the target material, which ensures that chemical evolution does not occur.

However, to study the effects of gases from transmutation, heavy ions co-implanted with H or He is often required [62, 102–104]. Similarly, to study the effect of other transmutated elements, prior alloying is often performed [105–107].

Compared to irradiation from fission reactor neutrons, irradiation with heavy ions allows better control over a wider range of temperatures [83, 108]. This, along with the absence of transmutation during irradiation ensuring elemental consistency, and the ease of control of irradiation dose, helps to facilitate systematic studies that can be difficult to achieve with neutron irradiation (Section 2.5.3). Furthermore, heavy ion irradiation also allows in-situ studies for observing defect evolution in the same sample [62, 104, 109, 110], which are otherwise impossible to conduct.

From a practical perspective, the high dose rate and absence of transmutation during heavy ion irradiation mean that it requires less time and financial resources to conduct compared to neutron irradiation, as samples are also not radioactive following irradiation. Some important drawbacks, particularly concerning defect structure evolution, have already been outlined in this chapter. Other comparisons of heavy ion irradiation with neutron irradiation, particularly concerning material properties, will be outlined in the coming chapters where relevant.

2.5 Irradiation-Induced Defect Structure and Evolution in FeCr Alloys

Experimental observations of irradiation-induced defect structure and evolution have mainly relied on transmission electron microscopy (TEM) for direct imaging. Dislocation loops are one of the main types of defects imaged with TEM in irradiated FeCr [109, 111–113]. Their size, density and orientation depend strongly on the material composition, irradiation dose and temperature.

Loop formation in FeCr is triggered by the impact of a new cascade in a ‘sea’ of cascade debris, which is a region of dispersed nano-scale point-defect clusters induced by previous cascade events [109]. The loops then grow in size by the diffusion of point defects from the cascade periphery [114].

The different formation and binding energies of interstitials and vacancies in Fe and FeCr greatly impact the evolution and behaviour of different defects in the material. Point defect migration energies are respectively 0.34 eV and 0.67 eV for interstitials and vacancies in Fe [115, 116]. This means that the movement of interstitial defects dominates defect evolution. Molecular dynamics (MD) simulations have found that cascades from high energy (>10 keV) particles often result in interstitial clusters [46]. In some cases, these can subsequently transform into prismatic loops (pure edge loops) [44], which can be easily lost due to glide to the surface or recombination [117]. Single interstitials and interstitial loops of all orientations have also been found to diffuse much faster than their vacancy counterparts [44].

This also has an impact on the types of defects that are observed in TEM. Interstitial loops have been observed to easily grow from the diffusion and coalescence of interstitials, but are also easily lost to the material surface through gliding [111]. The lower mobility of vacancies leads to less growth of vacancy loops to sizes visible in TEM. These factors all contribute interstitial loops being more commonly observed than vacancy loops in irradiated Fe and FeCr [109, 118–124]. The formation of vacancy loops is possible and has been experimentally observed [109]. MD simulations by Soneda *et al.* [125] have also found that, even though rare, vacancy loops can directly form from cascade collapse, where the vacancy-rich region near a cascade forms a dislocation loop. However, it can also be difficult to experimentally distinguish between the interstitial and vacancy nature of small defect clusters.

The general lack of TEM observations of vacancy loops may also be explained by spherical voids being the more favourable configuration for vacancy clusters, of any size, than dislocation loops [117], and voids less than 2 nm are difficult to image in TEM [126]. Studies with positron annihilation spectroscopy revealed large numbers of small voids at damage levels as low as 10^{-3} dpa in neutron-irradiated Fe [127–129]. Void size and density increase with irradiation dose and temperature [130].

In BCC Fe and FeCr alloys, two types of dislocation loops are commonly observed, with Burgers vector $\mathbf{b} = a/2\langle 111\rangle$ and $\mathbf{b} = a\langle 100\rangle$, where a is the lattice parameter [121–123, 131, 132]. The $\langle 111\rangle$ loops are very mobile and can easily migrate compared

to the ⟨100⟩ loops [133]. The relative populations of each type of dislocation loop depend on temperature, which will be further discussed in Section 2.5.3.

There are many factors that impact the microstructure and evolution of defects in irradiated FeCr steels. The rest of this section will focus on three of the key factors relevant to this thesis: irradiation dose, Cr content of the steel, and irradiation temperature.

2.5.1 Effect of Dose

In a reactor environment, different components will experience different irradiation exposures up to hundreds of dpa. Knowledge of defect microstructure at a range of doses is important for the design of reactor components and prediction of safety limits. Experimental studies of dose effects are also crucial for comparison and validation of modelling studies. Furthermore, the damage microstructure of materials has been found to depend on pre-existing damage [134, 135], making the study of low-dose defect microstructure very important.

In many irradiated metals, the defects spontaneously collapse or cluster to form loops and stacking faults that are visible in TEM [136]. However, it has been proposed that for Fe and ferritic alloys, an overlap of cascades is required before the formation of TEM-visible dislocation loops [109, 137, 138]. The 'threshold dose' for cascade overlap in Fe and FeCr, and the formation of visible defects in TEM, is ∼0.01 dpa [109, 114]. However, MD and density functional theory (DFT) simulations have shown that very small interstitial clusters (<51 atoms) are most stable in the C15 laves phase, around 1–2 nm in size but they have not been experimentally observed thus far [139–141]. This may also explain the lack of defects imaged in TEM at very low doses. However, a more recent study by Schäublin *et al.* [59] imaged dislocation loops in Fe after irradiation with 500 keV self-ions to 0.0015 dpa, below the 'threshold dose'. From this, the authors suggested that the collapse of individual displacement cascades can in fact lead to the formation of dislocation loops at high energies. This is in agreement with previous observations from English *et al.* [124, 142]. They found that implanting Fe with 80 keV W^+ ions resulted in dislocation loops while

implanting with 80 keV Fe^+ self-ions did not. The authors attributed cascade collapse happening from a higher energy density from the W^+ ion implantation.

Yao *et al.* [109] observed that at low doses (∼0.3 dpa), the defects in FeCr are visible as small dislocation loops (1–5 nm in diameter) distributed homogeneously through the material (Figure 2.5(a)). Below 1 dpa, the sizes of the loops were not observed to increase with dose, which also suggests that loops are formed by cascade events rather than diffusion of defects in this damage regime. The density of defects, N, increased with dose, Φ, as $N = \Phi^n$ with n around 2 for Fe^+ irradiation of pure Fe at room temperature [109]. For Fe3Cr, Fe8Cr and Fe11Cr irradiated at room temperature, n was greater than 1 at low doses (<0.3 dpa), but then decreased with increasing dose, corresponding to loop coalescence and loop loss by cascade-loop overlap [109].

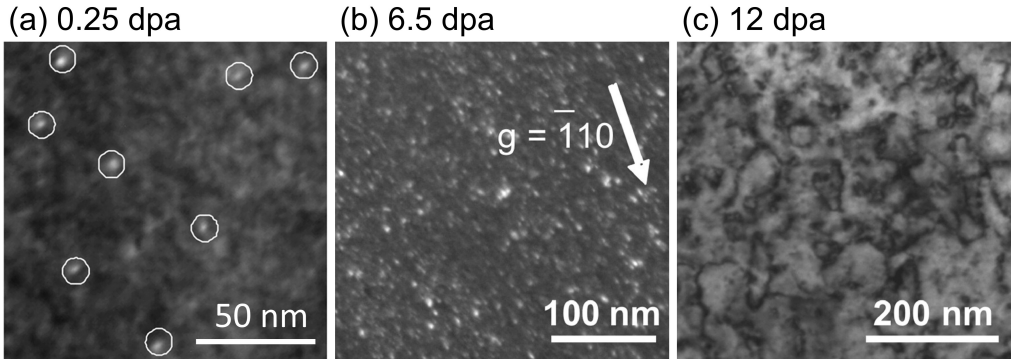


Figure 2.5: TEM micrographs of Fe8Cr irradiated at room temperature with 150 keV Fe^+ ions to (a) 0.25 dpa [109], (b) 6.5 dpa, and (c) 12 dpa [111]. (a) was taken under weak beam conditions, ($\mathbf{g}, \sim 3\mathbf{g}$) using reflection $\mathbf{g} = 110$. (b) was also taken under weak beam conditions, and (c) under kinematical bright-field conditions.

Increasing the dose causes defect cluster sizes to grow by diffusion and coalescence processes. For pure Fe, at high doses (∼10 dpa), the loop density starts to decrease due to the coalescence of loops, but in FeCr the densities continue to increase [111] (Figure 2.5(b)–(c)). There is also evidence of loss of mobile loops, those of ⟨111⟩ orientation, to the surface of the TEM samples. Thus, it is important to consider the effect of loop loss when extending TEM observations to the behaviour of defects in the bulk material.

Schäublin *et al.* [59] observed mainly ⟨111⟩ loops during the initial stages of cascade overlap before the ⟨100⟩ loop population dominated at higher doses (>0.5 dpa). This was attributed to the formation of ⟨100⟩ loops by the reaction of $a/2\,[111] + a/2\left[1\bar{1}\bar{1}\right] \rightarrow a\,[100]$ [59, 143–146].

In RAFM steels such as Eurofer-97, a ∼40% increase in dislocation loop size with dose was observed from 15 to 32 dpa following neutron irradiation [147]. This was also accompanied by a slight increase in dislocation loop density. On the other hand, an increase in dose caused a decrease in void size with an increase in void density.

Simulation work by Derlet and Dudarev [148] found that with the continuous insertion of Frenkel pairs in Fe, the number of vacancy defects will rise monotonically and their spatial distribution remains homogeneous. However, the number of isolated interstitial defects grew sharply at first (up to a damage level of 0.2 Frenkel pairs per atom), then gradually reduced as the interstitials cluster to form dislocation loops, mostly ⟨111⟩ loops. At even higher damage levels, extended dislocation networks were formed from the coalescence of smaller loops. Eventually the dislocation structures formed from interstitial atoms also formed extra lattice planes.

2.5.2 Effect of Cr Content

Understanding the effect of Cr content on defect microstructure and evolution is important for the development and optimisation of steels for next-generation fusion reactors.

Irradiated FeCr showed higher loop number density compared to pure Fe irradiated under the same conditions [111, 149–151], sometimes by up to a factor of 10 [109]. This has been attributed to Cr decreasing loop mobility due to long-range attractive forces between Cr and defect crowdions. This is also supported by the observations made by Yao *et al.* [109] that loops hopped less in FeCr during in-situ irradiation TEM measurements. Reduced mobility of loops, particularly the more mobile ⟨111⟩ loops causes less loop loss to the surface of the TEM samples for FeCr compared to Fe. This is evidenced by a higher percentage of ⟨111⟩ loops found in FeCr compared to Fe [109]. The study also suggested that the number of loops produced in FeCr is the same as in Fe, but in the latter case, more loops are lost to the surface. However, the dependence of loop density on Cr differs between studies, with one study [109] finding

no dependence between 5%Cr to 11%Cr and others [59, 152] observing decreasing defect density with increasing Cr content from 5%Cr to 14%Cr.

Loop sizes distribution is also affected by the inclusion of Cr, with a larger average loop size reported in Fe11Cr compared to pure Fe at ∼0.1 dpa, following both room-temperature and 573 K irradiation [109]. However, in a different study of irradiation to 0.3 dpa at 573 K and 673 K, it was found that the irradiation-induced loop sizes are greater in Fe compared to Fe5Cr [153]. At a higher dose (>1 dpa), the maximum loop size was larger in Fe than Fe8Cr, which was consistent with the lowered mobility of loops due to the presence of Cr [111].

The dependence of loop morphology on Cr has also been debated with slightly contradicting results depending on the irradiation conditions. In pure Fe, a higher percentage of ⟨100⟩ loops has been seen compared to ⟨111⟩ loops [109, 122, 149]. In FeCr both types appear in comparable numbers and more ⟨111⟩ loops are present with higher Cr content [109, 122, 130, 149, 150]. This is again attributed to the impedance of the motion of the mobile ⟨111⟩ loops in FeCr by the Cr atoms [149, 152]. This leads to less loop loss to the surface of FeCr samples and to dislocations in the bulk, resulting in a more homogeneous distribution of loops [109, 112, 149, 150]. Reduced ⟨111⟩ loop movement also leads to a lower chance of transformation into ⟨100⟩ loops [149]. However, at a damage level of 0.05 dpa, more ⟨100⟩ loops are found in FeCr, which could suggest the preferential formation of ⟨100⟩ loops over ⟨111⟩ loops in the presence of Cr at low doses [59]. A different study of FeCr irradiated to 1 dpa with self ions also found an increased percentage of ⟨100⟩ loops with Cr content [122]. This is contrary to many other studies mentioned before, which predominantly observed an increasing percentage of ⟨111⟩ loops with Cr content.

Molecular dynamics simulations have played a crucial role in shedding light on the behaviour of defects in FeCr. These simulations help us understand how the presence of Cr affects defect mobility and the formation of defect clusters. Simulation studies have also shown that the presence of Cr lowers the mobility of defects [154] and causes the formation of fewer large defect clusters with increasing Cr [133]. The onset of cluster formation also occurs at a higher dose in FeCr than in pure Fe [133].

2.5.3 Effect of Temperature

Irradiation temperature can strongly affect defect microstructure and evolution. It is important to understand its effects as the irradiation temperature, like dose, will vary for different FeCr structural steels in the reactor environment.

Yao *et al.* [109] found that following irradiation at 573 K, the average loop number density and size in Fe11Cr were lower compared to room-temperature irradiation. One explanation is that at 573 K, the vacancies are mobile and enhanced defect recombination may occur. This causes the background of cascade debris to build up more slowly and reduces the formation of observable defects. A different study of loop size as a function of irradiation temperature found no changes between 543 K to 673 K, but at 773 K the loops formed large (∼1000 nm) disc-shaped clusters [153].

Irradiation temperature also changes the morphology of the resultant dislocation loops. With increasing temperature, from room temperature up to 773 K, the fraction of ⟨100⟩ loops compared to ⟨111⟩ loops increased in irradiated TEM foils of Fe and FeCr [109, 112, 155]. At 573 K or below, mainly ⟨111⟩ loops with a small fraction of ⟨100⟩ loops were found. However, following irradiation at 773 K, only ⟨100⟩ loops were observed [112]. TEM lift-outs from ion-irradiated bulk specimens have also been examined and similar observations were made between 573 K and 773 K for pure Fe and Fe11Cr [156]. Higher temperatures increase the mobility of the dislocation loops causing further losses, particularly the higher mobility ⟨111⟩ loops, to the sample surface [157]. Additionally, theoretical work by Dudarev *et al.* [158] found that the reduction of the shear stiffness of BCC Fe at higher temperatures changed the stability of prismatic loops of different orientations, and in turn, favoured loops with ⟨100⟩ orientation.

Similar findings have been made in neutron-irradiated Eurofer-97, where predominantly ⟨100⟩ loops were found at irradiation temperatures of 623 K and above [159]. The average dislocation loop size also increased with irradiation temperature. Interestingly, neutron-irradiation at these higher temperatures ($\geq$ 623 K) also resulted in the formation of some He bubbles and voids, which were attributed to the B segregation in the material [160].

2.5.4 Summary

To summarise, the main type irradiation-induced defects in FeCr observed by TEM is dislocation loops with Burgers vector $\mathbf{b} = a/2\langle 111\rangle$ or $\mathbf{b} = a\langle 100\rangle$. They are mainly interstitial loops, which are more mobile than vacancy loops. They form from the diffusion and clustering of point defects following a collision cascade.

Dislocation loops are observable by TEM for an irradiation dose as low as 0.0015 dpa [59]. With increase dose, they grow in size and eventually decrease in density due to loop coalescence. At very high doses, they form extended dislocation networks [111, 148].

The presence of Cr acts largely to reduce the mobility of dislocation loops, particularly noticeable for the more mobile $\langle 111\rangle$ loops. Overall, the presence of Cr increases the loop number density and size in FeCr compared to Fe.

The effect of temperature on the irradiation defect population is largely due to its impact on interstitial-vacancy recombination. Lower irradiation temperatures lead to less recombination, causing increased loop number density and size. Higher irradiation temperature also favours the $\langle 100\rangle$ loop population in Fe and FeCr.

2.6 Irradiation-Induced Property Changes in FeCr Alloys

Following a review of the nature of irradiation-induced defects in FeCr in the previous section, this section will discuss the subsequent material property changes. The effect of irradiation dose, Cr content, irradiation temperature, and other relevant irradiation parameters on the material properties will be reviewed.

2.6.1 Void Swelling

As discussed previously in Section 2.5, vacancies introduced into materials following irradiation can cluster into voids. The growth of voids can be described by a rate theory approach, where growth occurs when the thermal emission of vacancies is balanced by the influx and accumulation of vacancies [161, 162]. At high irradiation doses, particularly in austenitic steels, the accumulation of voids can cause the

material to physically swell, inducing a volumetric change. This effect was first observed in 316 stainless steel in 1967 [163]. The irradiation-induced dimensional change is of grave concern for reactor structural components and as such, many studies have been conducted to gain a better understanding of the phenomenon [164–166]. Swelling is usually measured by TEM observations of cavities [61, 130, 153], or by measuring the density of the sample using the Archimedes' method [167].

Ferritic/martensitic steels swell significantly less than austenitic steels following irradiation. Garner *et al.* [165] attributed this to ferritic/martensitic steels having a much longer transient regime, as a function of dose, before the onset of swelling compared to austenitic steels. The onset of void swelling with irradiation dose occurs as low as 5.5 dpa in Fe and FeCr alloys following neutron irradiation at 673 K [150]. Void swelling is usually a phenomenon associated with high dose irradiation, and typically at a high temperature, as those are the conditions most favourable for voids and vacancy clusters to grow [130, 165, 167]. After the onset of void swelling, the swelling rate is usually constant, at around 0.2–1%/dpa [165, 168].

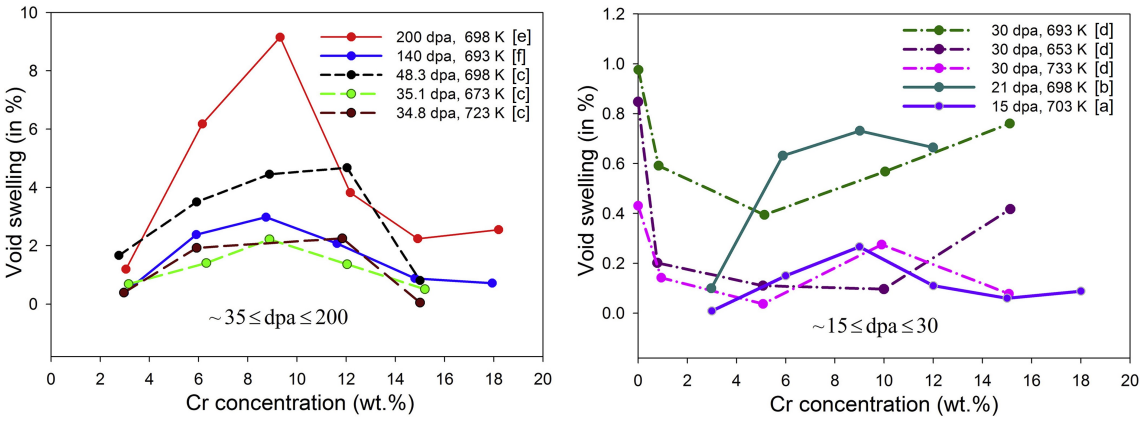


Figure 2.6: A comparison of void swelling data summarised in [61]. The data [a–f] is sourced from [130, 150, 165, 167, 169, 170], respectively.

Cr content has a large effect on the extent of swelling in FeCr alloys. Bhattacharya *et al.* [61] presented the summary of existing literature for neutron-irradiated FeCr, reproduced in Figure 2.6. Swelling does not depend monotonically on Cr content, but there tends to be a local maximum occurring around 9%Cr, particularly at high doses (>35 dpa). However, at lower doses (≤30 dpa), some studies have shown that there is a local minimum in void swelling between 4–10%Cr [167]. Discrepancies between

the studies might be attributed to the temperature variations during irradiation, influenced by the respective reactor histories [108]. Many ion irradiation experiments to study void swelling with better temperature control did not investigate a sufficient sample of Cr composition amounts to draw confident conclusions on the role of Cr in void swelling [62, 102, 171]. Bhattacharya *et al.* [61] did conduct ion irradiation (Fe and Fe+He) to 128 dpa and 13 appm He/dpa at 773 K for EFDA alloys across a range of Cr content. For pure Fe, both Fe and Fe+He irradiation caused strong void swelling up to 1%. The presence of Cr strongly suppressed this swelling, with no swelling found following Fe implantation. For Fe+He implantation, swelling was found to be non-monotonic with Cr content, peaking at 10%Cr. However, ion irradiation may also potentially affect cavity behaviour due to the injected interstitials [100, 172].

Irradiation temperature also affects swelling behaviour, with peak swelling temperature generally found between 723 K to 853 K [64, 65, 102, 171, 173]. The specific temperature at which swelling peaks also depends on the material composition and irradiating particles.

The presence of H and He as transmutation products, especially at fusion-relevant levels, is also important [102]. Gaseous impurities such as He and O can act as nucleation points for voids, whilst also stabilising them [174]. Tanaka *et al.* [102] found that for FeCr, simultaneous triple-beam irradiation with Fe^{3+}+H^{+}+He^{+} caused enhanced swelling of up to 5% with large void formation. In comparison, single and dual beam irradiation caused at most 0.4% swelling.

2.6.2 Lattice Strain

A relatively less-studied phenomenon that occurs predominately at low irradiation doses is that of lattice strain, or lattice swelling. It describes the change to the lattice plane spacing of a material due to the presence of defects. Though these local strains are small, on the order of 10^{-4}, they can give rise to local volumetric swelling, which in turn can result in macroscopic stresses, swelling and heterogeneous deformation of reactor materials [175]. These stresses can be on the order of hundreds of MPa [176, 177].

The origin of lattice strain is the finite elastic relaxation volume of defects, which causes local deformation of the material crystal lattice. The relative relaxation volume, Ω_{rel}, is a quantity that describes the extent of lattice contraction or expansion due to the presence of a defect [178]. Considering a defect in an elastically isotropic medium, under traction-free boundary conditions, the elastic relaxation volume can be written as:

$$\Omega_{rel} = \frac{1-2\nu}{2\mu(1+\nu)} Tr\left(P_{ij}\right) \tag{2.2}$$

where ν is the Poisson ratio, μ is the shear modulus and $Tr\left(P_{ij}\right)$ is the trace of the elastic dipole tensor [178].

In Fe, the relative relaxation volume of a single interstitial atom is between 1.6–1.8Ω_0 (atomic volume unit) depending on the defect configuration [179]. For a vacancy, it is -0.22Ω_0 [179]. The relaxation volume of a defect cluster, or dislocation loop, is different to the sum of the relaxation volume of the individual point defects [175]. In the macroscopic limit, the relaxation volume of a dislocation loop is the scalar product of its Burgers vector and area ($\mathbf{b} \cdot \mathbf{A}$), and for a void (a large cluster of vacancies) it is zero [175].

It's important to note that boundary conditions can change the effect that lattice swelling has on the material due to associated stresses and strains [175, 180]. For example, Hofmann *et al.* [176] derived the magnitude of swelling in the ion-implanted layer above an unimplanted substrate:

$$\epsilon_{zz} = \frac{1+\nu}{3(1-\nu)} \sum_A n^{(A)} \Omega_r^{(A)} \tag{2.3}$$

where ϵ_{zz} is the component of the elastic strain tensor perpendicular to the implanted layer surface, $n^{(A)}$ and $\Omega_r^{(A)}$ are respectively the number density and relative relaxation volume of each type of defect present (e.g. vacancies, interstitials, dislocation loops). Note that this derivation assumes zero in-plane strains ($\epsilon_{xx} = \epsilon_{yy} = 0$) due to the required geometric continuity between the implanted layer and the unimplanted substrate. The ion-implanted layer is only allowed to change dimensions along the out-of-plane direction, $\boldsymbol{z}$.

There is a general trend of an increase in positive elastic strain at the early stage of irradiation for a crystalline material [176, 177, 181–183]. In all the aforementioned cases, strain relaxation is observed with further irradiation past a threshold dose, on the order of 0.1 dpa or above. Mason *et al.* [183] compared experimental measurements of lattice strain induced by self-ion irradiation in W with atomistic simulations to determine the origin of the strain relaxation. They confirmed that at high irradiation doses, the formation of extended defect networks caused the crystal structure to return to a less damaged state thereby reducing lattice strain. This is consistent with predictions from earlier studies [181].

The implantation of He has also been found to have a large effect on irradiation-induced lattice strain, similar to void swelling as discussed in Section 2.6.1. Das *et al.* [177] found that for W, an increase in the implanted He concentration from 300 appm to 3000 appm caused a factor of 24 increase in lattice strain. This demonstrates that lattice strain behaviour changes depending on irradiation dose. They also found that alloying W with 1%Re did not affect defect retention.

There are very few studies of irradiation-induced strain in Fe and Fe-based materials. Papamihail *et al.* [184, 185] studied the irradiation of Fe thin films with self-ions and found a monotonic increase in lattice constant up to 341 dpa. In NiFe following Ni^+ irradiation up to 0.13 dpa, elastic strains on the order of 10^{-4} were measured and found to increase with dose [186]. To date, there have been no studies on the effect of alloying, particularly with Cr, on lattice strain in Fe.

Figure 2.7 shows the predicted strains from atomistic simulations performed by Derlet and Dudarev [148] for irradiated Fe. The authors used a creation relaxation algorithm (CRA), which involves randomly choosing an atom in the simulation cell and reinserting it in a different random location within the cell, before relaxing the structure by minimising the potential energy [148, 183]. The damage dose is measured with canonical dpa (cdpa), which is the ratio of reinserted atoms (Frenkel pairs) to the total number of atoms in the simulation cell. At doses greater than 0.05 cdpa, the lattice strain decoupled from the volumetric strain. The volumetric strain is a measure of macroscopic swelling, as discussed in Section 2.6.1 previously. This also suggests that the origins of macroscopic void swelling at low doses is due

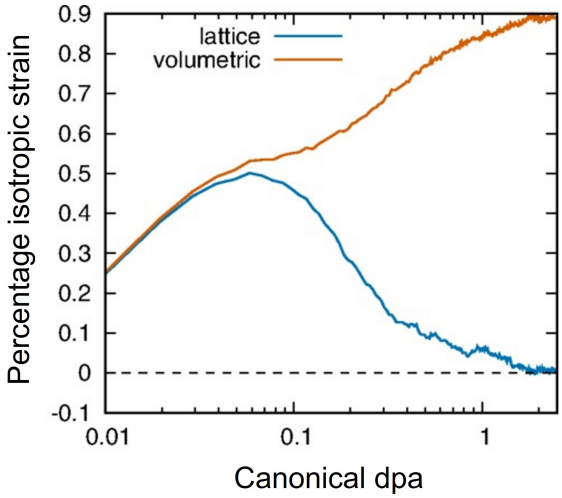


Figure 2.7: The predicted volumetric and lattice strain in Fe as a function of cdpa (a measure of dose in atomistic simulations with the CRA algorithm) [148].

to the relaxation volume and lattice strain of the point defects. At high doses, the interstitial point defects evolved into dislocation loops and eventually into an exposure-invariant steady state with extended dislocation structures [148]. This is similar to the findings for W from Mason *et al.*, as discussed previously. However, to date this has not been experimentally investigated for Fe and FeCr.

The investigation of lattice strain can also reveal important information about the defect population in the irradiated material. By using Equation 2.3, the defect density can be calculated from the measured lattice strain [187, 188]. The defect density as measured by X-ray diffraction through lattice strain can be up to 3 orders of magnitude higher than that observed with TEM [187]. This can be attributed to the low sensitivity of TEM to small defects below 1.5 nm [189]. This also suggests that to fully study irradiation-induced defect populations, TEM needs to be complemented by other characterisation techniques.

2.6.3 Mechanical Properties

The use of neutron irradiation allows the production of damaged material samples large enough for bulk mechanical testing. This allows the measurements of stress-strain relationships and other quantities such as yield stress, flow stress, and total and uniform elongation as a function of a range of parameters. Zinkle and Singh

[129] found that in Fe at a dose as low as 0.00012 dpa, an increase in yield stress from 138 MPa (unirradiated case) to 145 MPa was observed at a testing temperature of 343 K. Despite measuring a change in yield stress, no defects were observed by TEM. This further suggests that multiple methods of characterisation are required for a complete understanding of the defect population.

Yield stress of Fe increases with irradiation dose up to ∼1 dpa [129, 190, 191]. Byun and Farrell [190] found that the irradiation-induced yield stress increase, $\Delta\sigma_{YS}$, followed a power law in the form of $\Delta\sigma_{YS} \propto (dpa)^n$. However, n reduced from 0.26 to 0.11 after a dose of 0.05 dpa. The source of hardening was due to the introduction of defects as sessile clusters in the material, which acted as obstacles to glide dislocations [15]. The Orowan mechanism, or the dispersion barrier model, is often used to model irradiation hardening [192]:

$$\Delta\sigma_{YS} = M\alpha\mu b(Nd)^{1/2} \tag{2.4}$$

where M is the Taylor coefficient, α is the obstacle strength, μ is the shear modulus, b is the Burgers vector magnitude, and N and d are respectively the density and diameter of the obstacles.

Matijasevic and Almazouzi [193] found that yield strength increases with Cr in FeCr alloys, for both the unirradiated materials and those irradiated at 573 K with neutrons up to 1.5 dpa. The hardening rate was higher for FeCr than Fe, but no strong dependence on Cr content was observed. They also found that increasing the testing temperature caused a decrease in yield strength. The effect of irradiation temperature on mechanical properties is difficult to test for neutron-irradiated materials, as discussed in Section 2.4.5. Investigations into the effect of irradiation temperature on mechanical properties with ion-irradiated materials will be discussed in the following section.

Many neutron irradiation campaigns have also been performed on Eurofer-97 to determine the changes to mechanical properties. For irradiation up to 10 dpa, the irradiation hardening increased as the square root of dpa for irradiations performed at ∼573 K [25, 194]. This was also accompanied by a reduction in strain hardening and ductility following irradiation [25]. For irradiations performed at lower temperatures

(333 K to 353 K), the material hardening rate has been found to be greater and hardening saturates at 0.5 dpa [194].

Dislocation channels along slip planes have been observed following post-irradiation deformation at doses as low as 0.01 dpa [195]. Some examples are shown in Figure 2.8. The widely accepted mechanism is that glide dislocations move through irradiation-induced dislocation loops and destroy them [196, 197]. The exact mechanism of defect annihilation is complex and depends on the nature of the dislocations [198]. Studies to capture all these effects are ongoing [199, 200]. Dislocation-free channels are usually created following plastic deformation of irradiated materials and they act to locally confine subsequent deformation [201]. This is also referred to as 'strain localisation', which is the focus of Chapter 6. This leads to a decrease in uniform elongation and work hardening [40, 129, 202, 203], which is one of the biggest causes of concern for reactor structural materials.

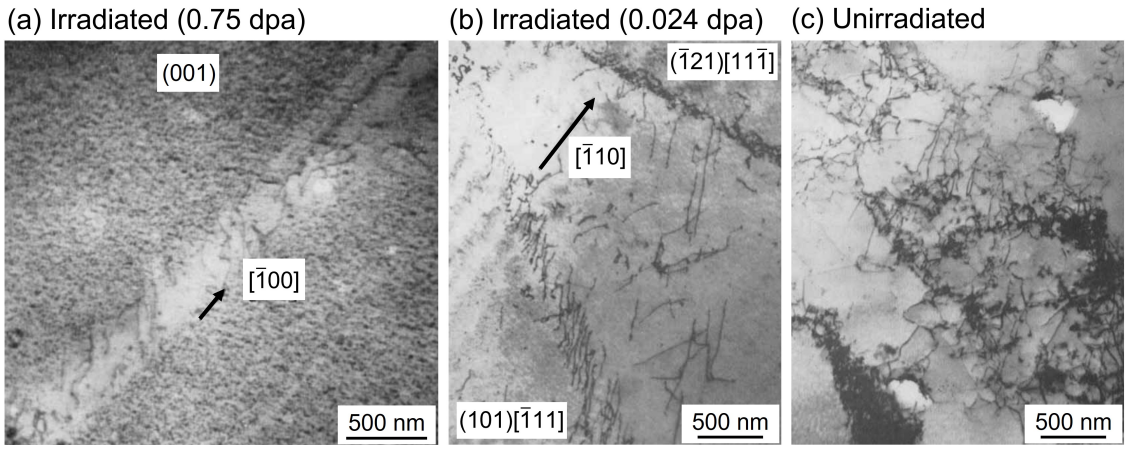


Figure 2.8: (a) Channel free of neutron-irradiation-induced defects in deformed Fe [204]. (b) Neutron-irradiated and (c) unirradiated Fe deformed to 5% strain [205]. In the irradiated material, screw dislocations are largely confined to specific slip systems. Neutron doses are converted to dpa according to ASTM E1035-18 [206].

Micromechanical Testing

As discussed in Section 2.4.4, the thickness of the damaged layer produced by heavy ion irradiation is only on the order of microns, which means micromechanical testing methods are needed to investigate the corresponding material property changes [98, 207, 208]. The technical details of the relevant micromechanical testing techniques,

and their comparison to bulk results, will be reviewed in Section 2.8.3 and is also the focus of Chapter 5. For now, an overview of the trends found in the literature for Fe and ferritic steels will be given.

The amount of Cr present has a large effect on the hardness of ion-irradiated FeCr. Even for unirradiated FeCr, the hardness increases with Cr content [98, 209]. Following irradiation up to 1 dpa at room temperature, the amount of irradiation hardening increases with Cr content (between 5 to 15%Cr) [98, 132]. Jin *et al.* [132] attributed the higher levels of hardening in Fe15Cr, compared to Fe5Cr, to the increased presence of ⟨100⟩ loops seen in their TEM measurements, which act as stronger obstacles for dislocation movement.

Hardie and Roberts [210] investigated the effect of irradiation dose on Fe and FeCr alloys irradiated with Fe ions at 593 K. They found that the saturation of hardness was reached by 2 dpa for materials with Cr content greater than 5%. The formation of dislocation channels and subsequent confinement of dislocation distribution were also directly observed in Fe12Cr [210, 211] (Figure 2.9). Halliday *et al.* [209] found that for FeCr following Fe ion irradiation at 573 K up to 5.3 dpa, hardness increased with dose for Cr content between 3–12%, except Fe5Cr .

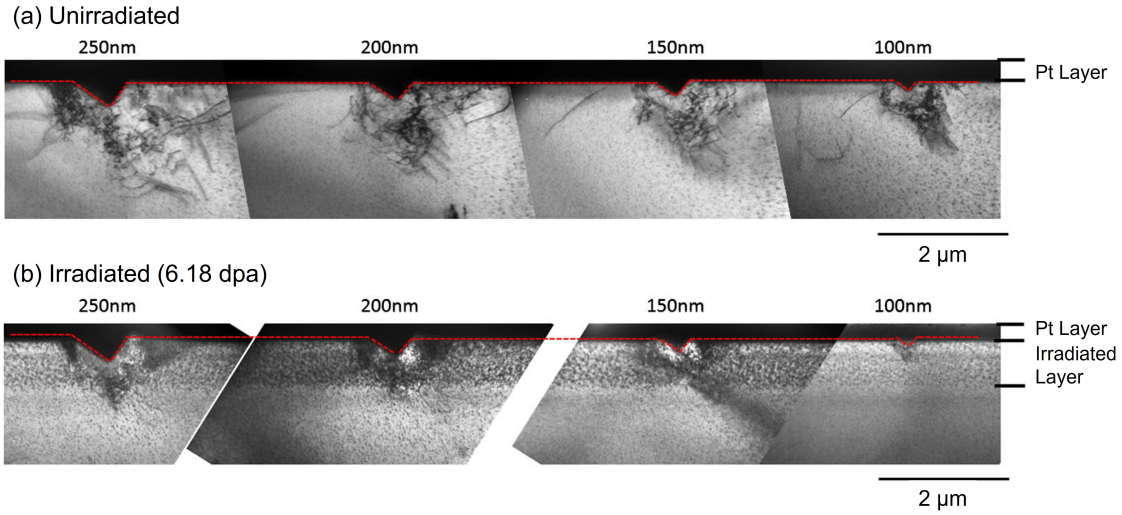


Figure 2.9: TEM cross-sectional images from cube corner indents of 50–250 nm deep in the (a) unirradiated and (b) ion-irradiated (6.18 dpa) regions of the same grain in Fe12Cr [211]. It is clear that following nanoindentation in the irradiated material, the spatial distribution of dislocations was largely confined to the irradiated layer.

Since irradiation temperature can be well-controlled during ion irradiation, its effect on subsequent mechanical properties can be probed. Heintze *et al.* [98] observed irradiation hardness trends that were dependent on both irradiation temperature and Cr content. For Fe2.5%Cr, no significant hardening was observed for irradiation at room temperature and 773 K. However, hardening was observed for irradiation at 573 K. For Fe9%Cr, hardening was observed at room temperature and 573 K but not 773 K. For Fe12.5%Cr, hardening to a similar extent was observed for all temperatures and was much higher than the hardening of the other two lower Cr content alloys.

Hardie *et al.* [60] investigated the effect of irradiation temperature and dose rate on the hardening of pure Fe and FeCr (5, 10 and 14%Cr). They found that at 573 K, all materials exhibited hardening after irradiation. At 673 K, only FeCr alloys showed hardening, and at 773 K, no hardening was measured for any of the samples. This can be attributed to the increased mobility of defects at higher temperatures causing defect loss due to recombination and extended sinks such as dislocations and grain boundaries. They found that at 573 K and 673 K, the hardening decreased with Cr content, which was different to the trend found for room-temperature irradiation [98, 132, 209]. This suggests that the changes to defect mobility at higher temperatures have a large effect on irradiation hardening.

Irradiation dose rate also has a large effect on the irradiation hardening. Hardie *et al.* [60] found that FeCr samples exposed at a low dose rate (3×10^{-5} dpa/s) experienced more hardening than samples exposed at a high dose rate (6×10^{-4} dpa/s). This was attributed to the precipitation of Cr at a low dose rate and potentially the development of defect structures that are not seen in TEM.

Ion-irradiation also facilitates the study of the effect of He and H co-implantation on the mechanical properties of Fe, FeCr, and RAFM steels. Heintze *et al.* [212] conducted a comprehensive study involving single, co- and sequential implantation of He and Fe ions, respectively to 100 appm and 5 dpa, into Fe9Cr alloys at 573 K. Single implantation of He did not cause any hardening change, while single implantation of Fe caused significant hardening (0.83 GPa for Fe9Cr and 1.03 GPa for Eurofer-97). Subsequent implantation of He to Fe-implanted material did not cause further hardening. Co-implantation of He and Fe caused the highest level of

hardening in all steels observed (1.06 GPa for Fe9Cr and 1.62 GPa for Eurofer-97). The authors argued this was due to displacement-damage-induced stabilisation of He-vacancy clusters, which then acted as obstacles for glide dislocations.

A comparison of neutron and heavy ion implantation in Fe6Cr was conducted by Hardie *et al.* [92] using nanoindentation and micro-cantilever tests. Following irradiation at 561 K to a nominal dose of 1.7 dpa, it was found that neutron irradiation resulted in 2–3 times more hardening than ion irradiation. It is important to note that there were some discrepancies between the actual doses received by each irradiation method due to inconsistencies in damage calculation. However, the authors noted that this would not be enough to explain the hardness differences. Instead, they attributed some of the hardness differences to a higher level of dislocation loops and a tendency to form Cr clusters in the neutron-irradiated material due to the lower dose rate. Interestingly, the neutron-irradiated material also exhibited work hardening, which was not observed in the unirradiated and ion-irradiated materials.

2.6.4 Thermal Properties

Understanding thermal transport and its changes due to material composition and irradiation is essential for structural materials to prevent undesirable stresses caused by thermal gradients and expansion. In metals, heat is primarily transported through the movement of electrons [213]. Irradiation degrades the thermal conductivity of materials by the introduction of point defects and defect clusters, which act as electron scattering sites [214]. For metals, such as copper and copper alloys, irradiation-induced defects contribute to a $\sim$1% degradation in thermal diffusivity, which remains relatively stable up to 5 dpa [215]. Beyond this damage level, the thermal conductivity is further degraded with increasing dose due to the formation of irradiation voids [216].

Ferry *et al.* [217] have measured changes thermal diffusivity in ion-irradiated Nb. A 70% drop in thermal diffusivity was found at 0.006 dpa, but there was a partial recovery of up to 50% of its initial value after further irradiation of 0.2 dpa and above. This suggests that there was initially a large population of point defects, which scattered electrons very efficiently, as confirmed by TEM. After further irradiation, the point defects clustered into mesoscale defect structures such as

dislocation loops, occupying a smaller volume fraction of the material, allowing the thermal diffusivity values to recover.

Moreover, Wylie *et al.* [218] made thermal diffusivity measurements in irradiated single crystal pure metals, including W, Cr, Fe, and V[1], irradiated up to 3 dpa. While Fe, Cr, and V experienced very little change in thermal diffusivity following irradiation, W experienced a substantial reduction at doses beyond 0.0001 dpa. The authors attributed this to the high defect retention in W, compared to the other metals in this study. It is interesting that thermal diffusivity in Fe is not strongly affected by irradiation, in contrast to mechanical properties that changed even at 0.00012 dpa [129], as discussed in Section 2.6.3. However, the differences in sample composition, initial microstructure, and irradiation conditions complicate this comparison.

In the case of neutron irradiation, transmutation can occur and introduce other elements into the material. These elements can play a more significant role in reducing thermal conductivity than irradiation defects, by also acting as electron scattering sites [214]. In copper, the effect of transmutation products in reducing thermal conductivity increases with dose [215]. In steels, the alloying elements have a similar effect in reducing thermal conductivity [220], though this can be further complicated by potential irradiation-induced clustering of the alloying elements [221]. In Fe-based alloys, the nature of the alloying elements also affects the changes to thermal conductivity. For example, the presence of Cr causes a greater reduction than Ni in similar quantities [220]. However, the combined effects of alloying and irradiation in iron-based alloys have been little explored. To date, the only study conducted involved neutron irradiation at 563 K on ASTM A533 grade B class 1 steel (1.5%Mn, 0.5%Mo, 0.7%Ni), which found a small (1.7%) increase in thermal conductivity after irradiation to 2.4×10^{23} n/m^2 [222].

2.6.5 Summary

Material properties have been investigated to different extents following irradiation damage in metals. The introduction of irradiation defects causes changes to the

[1]The melting points of these metals are: W (3695 K), Cr (2180 K), Fe (1811 K), and V (2183 K) [219].

material structure on the scale of atomic planes, causing lattice strain on the order of 10^{-4} or higher. Analysis of this strain behaviour, for example as a function of dose, can reveal insights into the defect population in the material and provide a complementary picture to TEM analysis. This lattice strain is the origins of void swelling at high doses and temperatures. This macroscopic swelling has a non-monotonic dependence on Cr content, but the exact nature of this relationship differs between studies.

Irradiation also causes many changes to the mechanical properties of Fe and FeCr alloys. There have been many studies conducted at temperatures above 573 K. Irradiation hardening, or increase in yield stress, is a common observation below 773 K. However, the exact trends of irradiation hardening as a function of dose or Cr content in FeCr following room-temperature irradiation have not been well-studied. Moreover, another key phenomenon following irradiation is the localisation of deformation due to the formation of defect-free channels. This leads to irradiation-induced embrittlement of nuclear structural steels, which is a key concern for their operation. However, the dependence of this deformation location on dose, Cr, and irradiation temperature in FeCr alloys is currently unclear.

Finally, the thermal diffusivity is another important property to consider given the large thermal gradients that will be present in a nuclear fusion reactor. Irradiation and alloying have been found to affect thermal diffusivity of metals, but this has not been systematically investigated for FeCr alloys.

The analysis of material properties is significant not only for directly predicting the behaviour of reactor components in-service, but also for the ability to reveal insights into defect population that may not be accessible by TEM imaging. For FeCr alloys, the effects of dose and Cr, particularly following irradiation at lower temperatures (<573 K) are currently unclear. However, in order to compare different material property trends, large systematic studies are required to ensure consistency in sample composition, processing, and irradiation history.

2.7 Severe Plastic Deformation and Nanostructuring

Structure and processing are important ways to modify material properties and performance alongside changes in composition. Over the past few decades, ultrafine-grained (UFG) materials, with sub-micron grains, have gained a lot of attention for their improved strength and other favourable properties [223]. This section will review the process of severe plastic deformation (SPD), its impact on material microstructure and properties, as well as how it might change the irradiation response of RAFM steels to potentially improve their performance.

There are broadly two approaches to producing UFG materials. The 'bottom-up' methods involve assembling nanostructured materials from nano-scale components such as nano-blocks and atoms. These techniques include inert gas condensation with subsequent consolidation, and a range of deposition methods [224, 225]. However, these methods suffer from some drawbacks, including the limited size of the final samples, as well as the porosity and impurities present in the final materials [226, 227]. In contrast, the 'top-down' techniques of fabricating UFG samples involve processing a bulk coarse-grained material to induce grain refinement [228]. These methods apply high shear stresses, sometimes simultaneously under high hydrostatic pressure (∼GPa) in order to prevent fracture, to achieve SPD and grain refinement without significant changes to the overall dimension of the material [229].

2.7.1 Severe Plastic Deformation Methods

There are many different methods to achieve SPD and in this section, the focus will be on two of the most commonly investigated and developed techniques: high-pressure torsion (HPT) and equal-channel angular pressing (ECAP). It's important to note that researchers often modify or combine these basic methods to alter the final material microstructure and properties [230].

High-Pressure Torsion

In HPT, a sample is held between two anvils, which subject the sample to compressive pressures on the order of GPa while simultaneously applying a torsional strain [227]. There are three main variations of HPT set-ups, depending on the shape of the anvils, which affect the pressures experienced by the sample during deformation [227] (Figure 2.10). The first is an unconstrained set-up, where the material is free to flow outward under applied pressure, and a minor back-pressure is applied from the friction between the sample and anvils. In the constrained set-up, the material is positioned in a cavity in the bottom anvil, and there is effective back-pressure from the inner walls of the anvil, stopping the outward flow of material. However, this set-up is difficult to achieve in practice and often a quasi-constrained set-up is used, where there is a cavity in both the top and bottom anvil. In this case, the outward flow of material is limited.

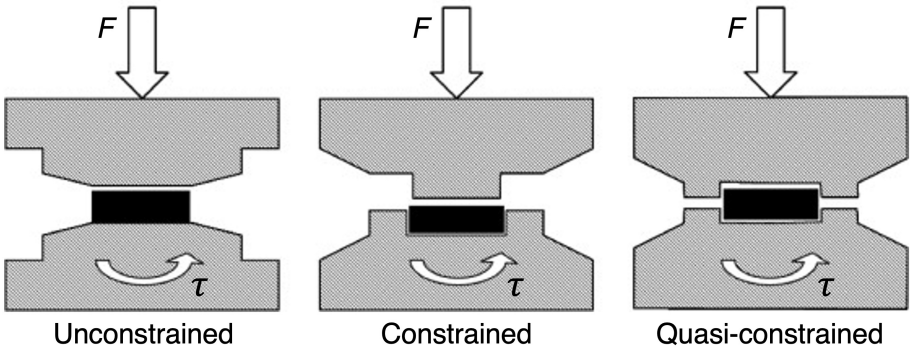


Figure 2.10: The three types of geometries for HPT set-up [227].

The process of HPT produces disc-shaped samples. The shear strain, γ, in an HPT sample with constant thickness, h, and no outward flow of material is given by [227]:

$$\gamma = \frac{2\pi N r}{h} \tag{2.5}$$

where N is the number of rotations completed and r is the distance from the centre of the disc. This allows the testing of different levels of strain in one sample and changing the total strain across a sample by varying the rotation angle [230]. However, it has been observed that above a certain level of strain, the material microstructures and properties reached a saturation state [227, 230].

Compared to other SPD methods, such as ECAP, HPT tends to produce smaller grain sizes [231, 232] and a higher fraction of high-angle grain boundaries [232, 233]. However, the size of an HPT-deformed specimen is limited to below ∼20 mm, with a thickness of ∼1 mm. Larger samples suffer from the problem of inhomogeneous microstructure [234]. However, some recent developments [235] including HPT extrusion [236] and incremental HPT [237] show promise for processing larger samples.

Equal-Channel Angular Pressing

ECAP involves pressing a billet, with a circular or square cross-section, through a die within two channels intersecting at an abrupt angle. Since the cross-section of the material remains unchanged, successive pressing can be used to increase the strain [229]. The amount of equivalent strain, ϵ, introduced to the material during ECAP is dependent on two parameters: the die angle Φ, where the two parts of the channel intersect, and the outer angle Ψ, which is the outer arc of curvature of the bent channel (see Figure 2.11). The relationship between these quantities is given by [238]:

$$\epsilon = \frac{N}{\sqrt{3}}\left(2\cot\left(\frac{\Phi+\Psi}{2}\right) + \Psi\csc\left(\frac{\Phi+\Psi}{2}\right)\right) \tag{2.6}$$

where N is the number of passes through the channel.

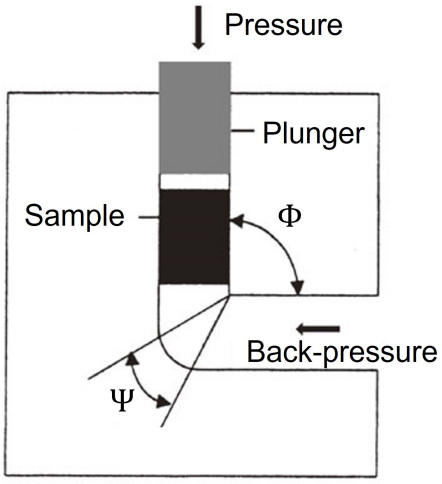


Figure 2.11: The schematic of ECAP and the definition of the die angle Φ and outer angle Ψ [239].

The process of ECAP can also be varied by changing the temperature at which deformation is conducted and the rotation of the billet along its longitudinal axis

in between passes (the processing route) [228]. In fact, it has been found that the latter factor has more of an effect on the final microstructure than the strain as different shearing patterns are developed [238, 240]. The main advantage of ECAP is the ability to produce industrial-scale samples while maintaining microstructural homogeneity with submicron grains [241]. However, it may not be suitable for certain intermetallic or brittle materials, limiting its applicability [228, 230].

2.7.2 Microstructural Changes

One of the key features of SPD-processed materials is the formation of UFG structures, with average grain sizes of less than 1 µm. A leading theory to explain the formation of UFG structures is the 'grain subdivision' mechanism [242, 243]. Briefly, in a polycrystalline material, the presence of neighbouring grains imposes constraints that cause the activation of different slip systems, not just the primary slip system with the highest resolved shear stress. This results in different local crystal rotations within the grain, leading to the formation of geometrically necessary boundaries (GNB). Large populations of dislocations introduced to the material during plastic deformation can accumulate in these GNB areas. The dislocations can also form incidental dislocation boundaries (IDB), which originally arise from the statistical trapping of glide dislocations. With increasing plastic deformation, both GNB and IDB increase in population and subdivide the original grain, leading to UFG structures.

The final distribution of grain size and shape can depend on the initial microstructure of the material, phase composition, method of SPD, and the processing conditions. Both ECAP and HPT have been used to produce equiaxed grains, around 100 nm, in a range of metals and alloys [244–247]. In some cases, the final grain shapes can be elongated, although not necessarily parallel to the major deformation direction [243, 248–251]. Grain size has been found to follow a logarithmic distribution [247, 252–254]. The refined grain sizes in alloys appear to be smaller than in pure metals [228, 255]. Edalati *et al.* [255] attributed this to the mismatch in atomic size and elastic modulus between the solute and matrix atoms in alloys. In some cases, total amorphisation of structures has even been observed, such as in TiNi alloys [256].

Aside from refined grains, the microstructure of materials processed by SPD can be complex, containing non-equilibrium (unstable) grain boundaries, lattice defects and changes to local phase composition. In a study of copper deformed via HPT, it was observed that low-angle subgrain boundaries transformed into high-angle grain boundaries with increased strain [257]. The grain boundaries also appeared to be non-equilibrium, with diffuse boundaries in TEM images. Instances of non-equilibrium grain boundaries were first described by Valiev *et al.* [226], shown here in Figure 2.12. Their occurrence is attributed to a high density of dislocations being trapped at the grain boundaries and also an elastically distorted layer being contained along the grain boundaries themselves [258–260].

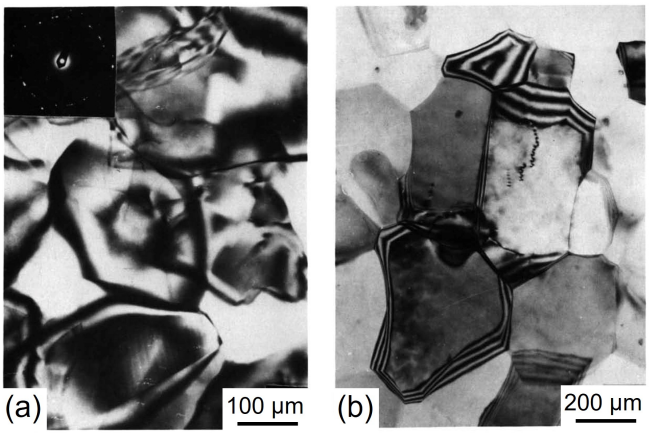


Figure 2.12: TEM images and diffraction pattern of the structure of Al-4%Cu-0.5%Zr alloy (a) after HPT deformation at room temperature to a shear strain of $\gamma = 12$, and (b) after post-deformation annealing at 433 K for 1 hour [226]. The non-equilibrium state of the grain boundaries is apparent before annealing from the 'diffusive' diffraction contrast in the image, which indicates higher energy and long-range stresses.

The dislocation density in SPD-processed materials can be very high, on the order of 10^{14}–10^{16} m^{-2} [254, 261, 262]. The final dislocation density depends greatly on the temperature during deformation relative to the melting point of the material. Materials with higher melting points tend to contain higher dislocation densities following SPD as there is a greater barrier to defect annihilation [263]. The stacking fault energy (SFE) of a material, more relevant for FCC structures, can also impact the resultant dislocation density [264]. Materials with lower SFE, e.g. Ag, exhibit a larger splitting distance between the partials from dissociated dislocations, which

will hinder their annihilation by cross slip and climb mechanisms [263, 265]. Material with low SFE and refined grains will have an increased probability of twin formation, which is commonly observed [266, 267].

Excess vacancies are commonly observed following SPD processing of metals and attributed to the non-conservative motions (e.g. climb) of dislocations during plastic deformation [267]. Their concentration following SPD can be on the order of 10^{-4}–10^{-3} at^{-1}, which is up to 17–18 orders of magnitude higher than their equilibrium concentration in metals at room temperature [265, 268–271]. These vacancies increase in concentration with applied strain and also tend to form clusters to reduce their total energy [267].

Material texture is affected significantly during SPD processing due to the rotation of grains along different slip systems. Shear-type textures are formed following ECAP, HPT, and many other forms of SPD processing [272–274]. Subsequently, this has a significant impact on material properties, which will be discussed in the following section.

Thermal annealing studies of SPD-processed structures have revealed that the extent of grain growth and dislocation annihilation depends on the annealing temperature and deformation regime. Interestingly, it has been observed that nanocrystalline structures (<100 nm) have been retained following annealing of SPD-processed Cu [275], Cu-Nb composites [276], and Ti [277].

At high strains, the saturation of grain refinement has been observed, where further straining does not change the average microstructural features such as grain size and dislocation density. In this state, a dynamic equilibrium exists between the generation of deformation-induced defects and their annihilation [230, 245]. This has been observed for many materials at strains on the order of 10 or above [249, 278]. The occurrence of a saturated 'steady-state' necessitates recovery processes to counteract the grain refinement induced by the applied strain [278]. Renk *et al.* [278, 279] have proposed that the mechanism for this comes from the migration of triple junction and/or grain boundaries during deformation, leading to a coarsening of grain structures. The microstructure in the saturation regime depends on the migration velocity of junctions and boundaries. This is affected

mainly by the homologous processing temperature and the impurities or alloying elements present in the material. At low temperatures, the migration of boundaries becomes mechanically driven rather than thermally driven [278, 279], resulting in much smaller saturated grain sizes [280, 281].

2.7.3 Material Property Changes

For crystalline materials at low homologous temperatures (less than half of the absolute melting temperature of the material), the Hall-Petch relationship can describe the yield stress, σ_{YS}, of the material as a function of grain size [282, 283]:

$$\sigma_{YS} = \sigma_0 + k_y d^{-1/2} \tag{2.7}$$

where σ_0 is the friction stress of mobile dislocations, k_y is the constant of yielding, which is related to the transmission of plastic flow across grain boundaries, and d is the grain size. Due to the presence of UFG structures in materials processed by SPD, it is expected that these materials will possess very high yield strength. It has been difficult to directly test the Hall-Petch relationship for a range of materials processed by SPD, particularly from HPT, as the sample sizes are often too small for tensile testing to determine yield stress. However, Furukawa *et al.* [284] proposed that by assuming a linear relationship between yield stress and hardness (Vickers or nanoindentation), the same dependence on $d^{-1/2}$ can be upheld. This has been observed for many materials including Cu [285], Ni [285, 286], CuZn alloys [266], Ti [287], and stainless steel [288].

Nevertheless, grain size is not the sole determinant of hardness or strength in materials processed by SPD. The homologous temperature of processing can affect the subsequent deformation behaviour due to the dynamic softening, from recovery or recrystallisation, that may occur during the process of deformation [289, 290]. For metals with low melting points, including In, Pb, Sn, and Zn, the hardness actually decreases with strain [289]. However, for most materials, including Al, Cu, and steels, the hardness increases following SPD [262, 264, 289, 291].

Small grains are also associated with low ductility, which at room temperature is primarily determined by strain hardening [292, 293]. In coarse-grained materials, strain hardening occurs during deformation by the accumulation of dislocations and defects within grains. Dislocations annihilation requires cross-slip as well as climb [294], which is governed by slow bulk diffusion [295]. However, in UFG materials, there are very few dislocation sources in grain interiors, and defects are instead mainly generated at grain boundaries. Dislocations also glide across grain boundaries and disappear without accumulating in great numbers inside grains, leading to low strain hardening and low mechanical stability, causing necking at low strains [296]. However, there have been studies on methods to increase the ductility of SPD-processed materials. These include thermo-mechanical treatments to obtain a bimodal distribution of grain size [297], and the introduction of nanoscale second-phase particles through ageing [298]. Some SPD-processed materials inherently exhibit high ductility. This has been observed in Cu and Ti following ECAP and HPT, separately, resulting in increased ductility with strain [247, 299]. The authors attributed this to a combination of grain boundary sliding and enhanced grain rotation in the UFG material.

SPD-processing can cause a reduction in the Young's modulus of materials (>10%) including in Cu [300–303] and Ti [304]. This has been attributed to the process of grain refinement causing an increased fraction of grain boundaries, which have different elastic moduli to that of the original 'ideal' crystal [304–306]. In UFG Cu, the velocity of the ultrasound waves (related to Young's modulus), was recovered following annealing up to 448 K to 523 K [300].

The thermal properties of materials processed by SPD, particularly metals, have been much less studied compared to mechanical properties. Recent studies on SPD Ti and 316L stainless steel have shown a reduction in thermal conductivity compared to the coarse-grained material [307]. In other materials such as thermoelectrics and semiconductors, SPD has been shown to reduce thermal conductivity by the introduction of large volumes of grain boundaries and defects, which greatly increase phonon scattering [308, 309]. In metals, including Cu and Al, electrical conductivity is also reduced following SPD, indicating increased electron scattering [310, 311].

Due to the deformed structures present, SPD-processed materials contain a significant amount of stored energy, and the microstructure can become unstable upon post-deformation heat treatment. Hung *et al.* [312] conducted annealing studies for UFG CoCrFeNi alloy and measured two major heat release stages occurring approximately at 625–725 K and 870–880 K. The heat release at the lower temperature corresponded to the annihilation of dislocations, while the second was attributed to the reduction of grain boundaries due to grain growth. Thermal stability in Cu has been found to decrease with increasing dislocation density and decreasing grain size [313]. Metals with low melting points and low SFE, such as Cu and Ag, have even exhibited the self-annealing of defects at room temperature, as measured by hardness evolution [265, 313, 314]. Popov *et al.* [315] also observed an increase in grain size and a corresponding decrease in hardness with annealing temperature for SPD Ni.

2.7.4 Irradiation Response

Over the past decade, nanostructuring has received increased attention as a potential method for increasing the radiation tolerance of materials [316]. The goal for a radiation-resistant material is for its structure and properties to remain stable, or unchanged, under irradiation. It has been proposed that increasing the density of grain boundaries in the material will provide more sinks for irradiation-induced defects such as vacancies and interstitials. Therefore, more defects will be removed from the bulk material and their overall effect on the material properties will be reduced [317]. Furthermore, MD simulations have shown that interstitials loaded into the grain boundary can subsequently cause interstitials to be emitted into the bulk, annihilating with the vacancies to further reduce the effect of irradiation [318].

One of the earliest studies of irradiation effects in UFG materials was in nanostructured Pd [319]. Following Kr ion irradiation, a correlation between grain size and defect density was found, with no defects observed for grains smaller than 30 nm. Similar results were found in Au irradiated at 300 K, where the UFG material showed much lower defect accumulation than the coarse-grained material [320]. Interestingly, the reverse behaviour was found following irradiation at 15

K. However, it's worth noting that in these studies, the UFG structures were not produced by SPD but by gas-deposition.

For 316 stainless steel processed by SPD, subsequent irradiation has caused less irradiation-induced grain boundary segregation, or even intragranular segregation, clustering or precipitation compared to the coarse-grained materials [321–323]. Furthermore, SPD-processed materials have also shown a reduced population of irradiation defects compared to the coarse-grained material [324–326].

El-Atwani *et al.* [327, 328] carried out numerous studies on nanocrystalline W for fusion since the early 2010's, with a particular focus on He irradiation. It has been found that nanocrystalline W exhibited a lower density of defect clusters and dislocations but higher density of He bubbles trapped at grain boundaries compared to coarse-grained W [328]. This highlights the importance of grain boundaries as sinks for He, which could potentially improve its irradiation resistance.

Some studies have shown that grain refinement suppressed irradiation-induced void swelling by over an order of magnitude [326, 329]. However, higher swelling near the surface region (top 1 µm) has also been found in the irradiated SPD materials compared to the as-annealed materials [330, 331].

Irradiation of SPD-processed materials has been observed to induce grain growth. Nita *et al.* [325] examined Cu with 5% Al_2O_3 strengthening particles processed by ECAP and then subsequently HPT. Following proton irradiation at room temperature to 0.9 dpa, the average grain size increased from 178 nm to 493 nm. However, in that same study, Ni processed by SPD and irradiated in the same manner exhibited no irradiation-induced grain size changes.

SPD-processing prior to irradiation has been shown to influence subsequent irradiation-induced property changes. In the case of 316 stainless steel, material processed by HPT before irradiation to 2.7 dpa exhibited less irradiation hardening compared to the coarse-grained material [332]. Similar results for irradiation up to 15 dpa have been found in other austenitic [333] and ferritic steels [334]. However, it's worth noting that the hardness of the irradiated UFG steel is still higher than that of the irradiated coarse-grained steel due to strain hardening from SPD. The reduction in ductility due to irradiation was also less for UFG materials [333,

334]. Fe-Cr-Ni austenitic steel nanostructured by ECAP and then subsequently neutron-irradiated was found to have higher impact toughness than the irradiated coarse-grained material [335].

SPD has the ability to modify the microstructure and properties of materials, such as grain size, dislocation density, and deformation behaviours. However, many of the trends studied so far vary greatly depending on the intrinsic material properties (e.g. crystal structure and SFE), processing routes and temperature, as well as post-deformation heat treatments. Furthermore, much remains to be studied regarding the properties and irradiation response of SPD-processed materials. This includes thermal transport, elastic modulus, material strains, and their corresponding changes due to irradiation. A better understanding of SPD for fusion-relevant materials could potentially improve the processing of materials for reactor structural components.

2.8 Experimental Techniques

This section outlines the key techniques used for the characterisation of irradiation damage and deformation-induced changes. The basic principles of each technique will be outlined, along with key advantages and capabilities relevant to the materials that will be examined in this thesis.

2.8.1 Electron Microscopy

Electron microscopy allows many different techniques to be carried out for the characterisation of material microstructure and irradiation damage. There are two categories of electron microscopy: transmission electron microscopy (TEM) and scanning electron microscopy (SEM).

TEM is commonly used for the study of dislocations and defects in metallic materials, including FeCr alloys. The basic components of a TEM consist of an electron source, along with focusing magnets and imaging devices arranged vertically in an evacuated column ($<10^{-7}$ Pa). A beam of electrons is generated, accelerated by the applied voltage down the column and focused by the magnetic field. As the electrons travel through the sample, they interact with the material and form

an image below the sample on the imaging device. TEM allows direct imaging of defects for the study of their size, morphology, and spatial distribution. The volume of sample required for TEM is very small (thickness on the order of tens of nanometres). This means TEM is suitable for the study of neutron- and ion-irradiated materials. However, the requirements for sample preparation are often key drawbacks to TEM. Focused ion beam (FIB) milling is commonly used for making TEM samples from bulk material that has already been irradiated. It is useful as the rest of the bulk material can still be retained for characterisation via other techniques. However, FIB-based techniques are typically very time-intensive, produce specimens only on the order of microns in area, and require careful preparation to avoid introducing additional damage to the material [336]. Another method of TEM sample preparation is jet electropolishing, which can produce larger areas of samples thin enough for TEM. The drawback is that the rest of the sample cannot be easily used with other characterisation techniques.

Many TEM studies of irradiation defects have already been described in Section 2.5. TEM is useful for the observation of irradiation loops and extended dislocation structures. Interestingly, simulation studies have shown that TEM has low sensitivity to defects smaller than $\sim$1.5 nm, and their sizes as observed by TEM can depend on imaging conditions [189]. Experimental studies of defect populations that use other techniques to measure defect density have shown a deviation from TEM-based results for populations of small defects (<1 nm) [129] and at low doses (<0.01 dpa) [337]. In-situ irradiation of pre-thinned TEM samples has provided useful information on the evolution of defects with dose [62, 109, 111]. However, due to surface effects, the comparison to the irradiation of bulk samples requires careful analysis [117].

In recent years, many SEM techniques have been developed to enable non-destructive characterisation of materials with high spatial resolution and to obtain unique information about the material and defect microstructure. One of the most commonly-used techniques is electron backscatter diffraction (EBSD) [338]. This relies on the incident electron beam interacting with a crystalline sample, with the diffracted electrons forming a pattern depending on the orientation of the crystal relative to the beam. For EBSD, the bulk sample is tilted at an angle,

usually 70°, relative to the incident electron beam. The diffraction patterns are then recorded from a fluorescent screen positioned perpendicular to the incident electron beam. By analysing, or indexing, the diffraction patterns, information can be obtained about the crystal structure and orientation. By scanning the incident electron beam over a large area, measurements of grain size, dislocation density, and texture can be obtained. This is particularly useful for studying the effects of grain refinement via SPD [227, 251].

Some techniques build on the fundamental principles of EBSD to extract more detailed information. For example, with high-resolution electron backscatter diffraction (HR-EBSD), the EBSD patterns from different points of a map are directly compared to a reference pattern. This allows measurements with strain sensitivity on the order of 10^{-4} [339–341]. This technique has been used to measure the strain fields around deformation structures in metals as well as geometrically necessary dislocation (GND) density [342–345]. The strain fields from individual dislocations and lattice strains from irradiation defects have been also probed using HR-EBSD [346]. The spatial resolution of (HR-)EBSD is on the order of tens to hundreds of nm in bulk material, as it depends on the backscattered electron interaction volume [347].

Another useful variant of EBSD is transmission Kikuchi diffraction (TKD), sometimes also known as transmission-EBSD. The principles are very similar, except the sample is thin, usually a TEM lamella, and, in the on-axis geometry, the diffraction patterns are measured with the detector positioned below the sample [348]. This method has the advantage of achieving higher spatial resolution (2–4 nm), which increases the capabilities of measuring grain refinement in SPD-processed materials [349]. High-resolution TKD (similar operating principles to HR-EBSD), has also been used to measure the strain fields from individual dislocations [350] and irradiation defects, [351].

2.8.2 X-ray Diffraction

X-ray diffraction (XRD) allows the measurement of phase composition, crystal structure, crystal size, lattice strain and texture of materials. It can probe much deeper into materials than electrons and can also sample large volumes for more statistical

information. XRD results are often complementary to electron microscopy methods, which can obtain high spatial resolution but only measure small sample volumes.

X-rays are ideal for probing the atomic arrangements of atoms in materials as their wavelengths are comparable to the interatomic spacing. When an incident beam of X-rays interacts with a crystalline material, the resultant beams are scattered in particular directions. The elastically scattered X-ray waves of wavelength λ will constructively interfere with each other in certain directions and destructively in others. The condition for constructive interference, known as Bragg's law, is described by [352, 353]:

$$2d\sin(\theta) = n\lambda \tag{2.8}$$

where d is the spacing between the atomic planes, θ is the angle between the incident (and reflected) beam and the crystal planes, and is referred to as the scattering angle. 2θ is also the angle between the incident and reflected beams. n is an integer. This is all illustrated in Figure 2.13.

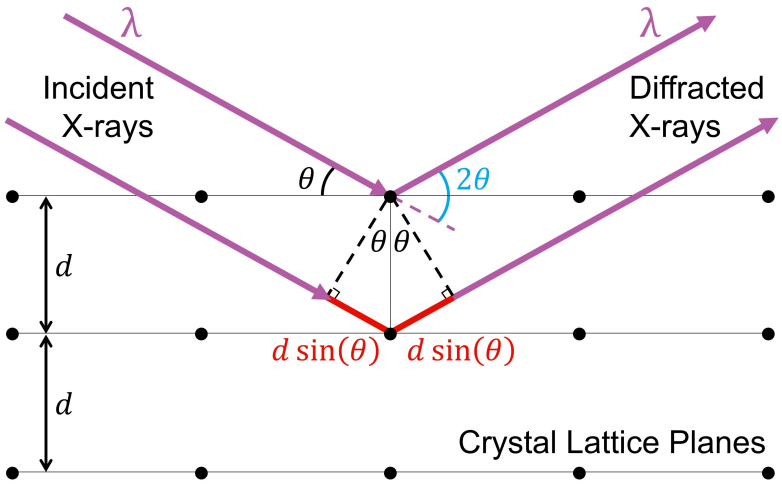


Figure 2.13: A schematic illustrating the principles of Bragg's law. If $2d\sin(\theta)$ is an integer multiple of the wavelength λ then the diffracted wavefronts will be in phase, resulting in constructive interference.

Each set of crystal plane directions has a particular d-spacing. For a fixed wavelength, there is then a set of fixed θ values for measuring the diffracted X-rays, called 'diffraction peaks'. For an infinite and perfect crystal structure, each diffraction peak from a perfectly monochromatic (single energy) X-ray beam will be a delta

function. In practice, the peaks will be broadened, i.e. have a finite distribution in θ-space. Factors that contribute to peak broadening include instrumental imperfections (e.g. a finite distribution of incident wavelengths), sample strain heterogeniety (a distribution of d-spacing), and small scattering domain size (the destructive interference will not perfectly cancel out). The last two factors will be discussed in more detail in the following section.

XRD can be conducted on single crystals or polycrystalline materials, using monochromatic or polychromatic beams, depending on the specific application, but they all rely on the principle of Bragg's law. There are also many different diffraction geometries available, including reflection, grazing-incidence and transmission. X-ray sources themselves can also vary from lab-based cathode-ray tubes to synchrotron sources, which provide orders of magnitude higher X-ray brilliance.

Powder Diffraction With Convolutional Multiple Whole Profile Fitting

X-ray powder diffraction uses a monochromatic X-ray beam on a polycrystalline sample. The technique relies on having a large population of crystallites that satisfy the Bragg condition for different crystal planes to produce the diffraction pattern or line profile, usually as a function of 2θ.

Analysis of the diffraction pattern, specifically the broadening of the diffraction peaks can reveal information about crystallite size and strain. There have been two different methods commonly used to analyse these quantities: the Williamson-Hall [354] and Warren-Averbach [355] method. They both make assumptions of isotropic crystallite shape and/or strain, and analyse each peak in the diffraction pattern individually. In practice, the nature of peak broadening is not solely a function of the scattering angle, as would be the case for isotropic strain broadening, but is usually dependent on the specific families of crystal planes. In metals, the main cause of strain broadening is attributed to dislocations and planar faults [356]. The type of dislocation, their Burgers vector, the slip systems of the material, and the elastic anisotropy of the crystal lattice all contribute to the anisotropy of the resultant strain from the dislocations. This means that strain varies with crystallographic orientation as well as scattering angle [357]. A description of the peak broadening

that takes into account the strain anisotropy of the dislocations has been developed [358, 359], and will be described later in this section.

The convolutional multiple whole profile (CMWP) fitting method, developed by Ungár *et al.* [357], enables the analysis of microstructural parameters, including crystallite size and dislocation density, by examining the whole diffraction profile. The method models the diffraction intensity profile (I_{tot}) as a convolution of contributions from the crystallite size (I_S), strain from dislocations (I_D), planar defects (I_{PD}), intergranular strains (I_{IGS}), and instrumental effects (I_{Inst}) [360]:

$$I_{tot} = I_S * I_D * I_{PD} * I_{IGS} * I_{Inst}. \tag{2.9}$$

Fourier transformation of the diffraction pattern is performed, and according to the convolution theorem, the contributions in Fourier space are simply multiplied together. The instrumental contribution can be determined by measuring a standard strain-free sample, such as Si, CeO_2 or LaB_6. The size profile is calculated by assuming a log-normal distribution [357]. The other profiles contributing to strains in the sample are calculated by considering strain fields associated with different types of lattice defects [261, 360]. For example, strain broadening from dislocations, I_D, depends on the mean square strain $\langle \epsilon^2 \rangle$ [361]. In Fourier space, with Fourier variable L, this can be expressed as:

$$\langle \epsilon^2 \rangle = \frac{\rho C b^2}{4\pi} f\left(\frac{L}{R_e}\right) \tag{2.10}$$

where ρ is the dislocation density and b is the Burgers vector magnitude. C is the dislocation contrast factor, which depends on the relative orientation of the diffraction vector, the Burgers vector and the line vector of dislocations, and the elastic constants of the material [359]. This factor accounts for the strain anisotropy of the dislocations. f is the Wilkens function [362], which describes the range of the defect strain field, and R_e is the effective cut-off radius of that field, on the order of nm.

These theoretical functions are multiplied in Fourier space, then an inverse Fourier transform is taken to obtain the calculated diffraction pattern. Fitting is performed by minimising the weighted sum of squared residuals (WSSR) by using the Levenberg-Marquardt (LM) nonlinear least-squares algorithm [363, 364].

The physical parameters optimised include those that describe the distribution of crystallite sizes, dislocation density and configuration, planar defect densities, and elastic intergranular strain. A Monte Carlo (MC) statistical algorithm is also applied to find the global minimum of WSSR. The CMWP program [261] uses the LM and MC algorithms in multiple succession. The errors of the fitted parameters are determined by the p% of the WSSR in the following manner [365]. First, n_0 iterations of LM+MC are performed to find the lowest WSSR ($\mathrm{WSSR_{best}}$). Then a number of MC steps are performed to obtain a n_p number of WSSR that satisfy the following condition:

$$\mathrm{WSSR_{best}} < \mathrm{WSSR} < (1 + p\%) \cdot \mathrm{WSSR_{best}}. \tag{2.11}$$

The physical parameters that correspond to the WSSR value found are stored in an array. The final error for each physical parameter is then the corresponding range of that parameter in the stored array. Ribárik *et al.* [261] have found that $p = 3.5$, $n_0 = 2000$, and $n_p = 100$ gave good fittings even for complicated patterns.

CMWP has been successfully used to analyse irradiation defect populations in Zr [366–368]. It is able to determine the density and size distribution of dislocation loops, obtaining results comparable to *ab initio* calculations [366]. Since its inception in the early 2000's, it has also been used in numerous studies to investigate the microstructure of SPD materials [369–371]. CMWP analysis to examine dislocation density have also been conducted on ferritic/martensitic steels from both XRD [270] and neutron diffraction [372, 373]. It provides information on grain size and dislocation density that are complementary to electron microscopy results due to the sensitivity of X-rays to small degrees of misorientation [254].

Differential Aperture X-ray Microscopy

One of the features of XRD is that the information is integrated over the finite volume through which the X-ray beam passes. For ion-irradiated materials, the use of XRD requires precise set-up to distinguish between the signal from the thin irradiated layer from that of the thicker unirradiated bulk beneath. Grazing-incidence geometry and the use of lower energy X-rays are helpful in this regard, but achieving three-dimensional spatial resolution has proven challenging.

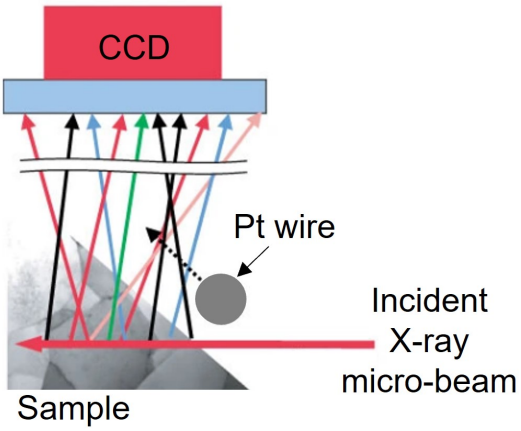


Figure 2.14: A schematic of the DAXM set-up showing the relative positions and orientations of the incoming X-ray micro-beam, the sample surface and the CCD detector. The Pt wire is stepped in parallel to the sample surface. The diagram is adapted from [374].

Differential aperture X-ray microscopy (DAXM) was developed in the early 2000's. It allows the determination of local crystal structure, orientation and strain tensors with sub-micron three-dimensional spatial resolution [374–376]. A schematic of the technique is shown in Figure 2.14. A focused monochromatic or polychromatic X-ray beam, less than 500 nm wide in each direction, is incident on the sample surface at 45°. The resultant diffraction pattern is collected on a CCD detector positioned such that the normal of the detector is at 90° to the incident beam. Beam penetration can be between tens and hundreds of microns into the material, depending on the material composition and X-ray energy. The detector will collect a diffraction pattern containing information over a volume of around 500 nm in diameter and along the whole length of the beam penetration [376]. To resolve the information from different depths in the material, a platinum wire, ∼100 µm diameter, is incrementally moved across the sample surface in submicron steps. For each pixel in the detector, by comparing the intensity as the wire moves along the sample, and triangulating using the position of the pixel, the incident beam, and wire edge, a profile of the pixel intensity as a function of sample depth can be calculated. Performing this calculation for the whole detector allows the diffraction pattern from submicron voxels along the beam penetration direction to be reconstructed [377].

Typically, the analysis of DAXM measurements, including depth-reconstruction of the diffraction patterns, indexation of the patterns, and calculation of strain and lattice rotation information, is performed in LaueGo. This is a custom program written by Dr. Jon Tischler at the Advanced Photon Source, Argonne National Laboratory, IL, USA. Further details of the program can be found in [378].

To extract information about lattice rotation and strains (in Chapters 3, 4, and 6), it is necessary to use X-ray Laue diffraction. This differs from powder diffraction, where Laue diffraction typically examines a single crystal, or grain, at a time and the sample is fixed relative to the incident X-ray beam. The resulting diffraction peaks are measured as diffraction spots on the 2D area detector. By examining the polychromatic Laue diffraction pattern, the deviatoric strain tensor of the sample can be determined. However, if the incident X-ray beam is scanned in energy, the diffraction peaks can be captured in full 3D reciprocal space. This allows the absolute spacing of the lattice planes to be determined, which can be combined with the deviatoric strain tensor to determine the full lattice strain tensor [379]. This can be combined with the ability of DAXM to scan in a 2D grid on the surface of the sample, and at each point perform depth resolution. In principle, DAXM can completely resolve diffraction peaks in 3D reciprocal space along with 3D real space resolution.

DAXM measurements have been performed on W implanted with self-ions [183] and He ions [176, 177]. The ability to depth-resolve allows the unambiguous measurement of lattice strain in the irradiated layer. Much of this work was discussed in detail in Section 2.6.2. Briefly, Hofmann *et al.* [380] found that a majority (>99%) of helium-generated Frenkel pairs in W recombined. Lattice strain as a non-linear function of He implantation dose was also measured [177]. The measurement of irradiation-induced lattice strains in self-ion implanted W has also been compared with *ab initio* studies [183].

The capability of using DAXM to examine a sample in 3D real space has been applied in unimplanted and He-implanted W to examine the 3D deformation field around a nanoindent [343, 381]. The strain field and lattice rotations under the indent in the implanted material are much smaller in magnitude compared to the unimplanted case [381]. The authors were able to compare their results with finite

element modelling to formulate an explanation where the hardening of W was initially caused by the presence of irradiation-induced defects. However, these defects were removed following interactions with glide dislocations, subsequently leading to an observed softening [343].

2.8.3 Nanoindentation

Nanoindentation is a widely used method to measure the hardness of materials with small sample volumes, including HPT-processed and ion-irradiated materials, as it can probe the thin irradiated layer situated on top of a much thicker unirradiated bulk. The technique consists of pressing a hard tip, commonly made of diamond, into the surface of the material to a certain maximum load or depth while measuring both the applied load and the resultant displacement. One of the most common ways to apply load is the constant strain rate test, where the ratio of the indenter velocity to the depth of penetration is held constant [382]. Figure 2.15(a) shows a schematic of the shape of a typical load-displacement curve.

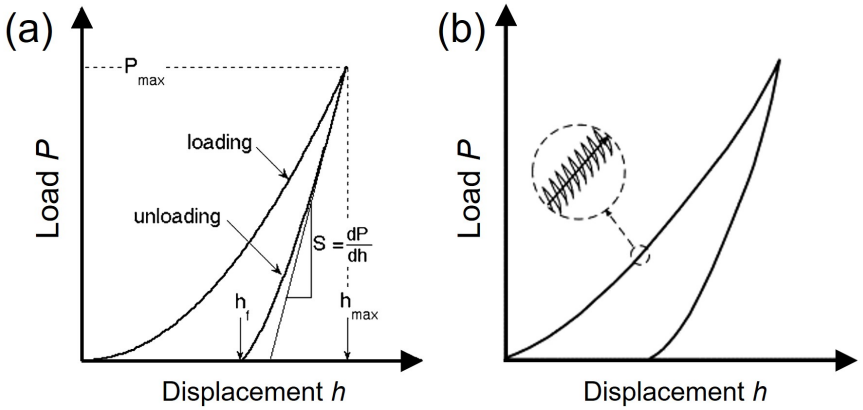


Figure 2.15: (a) A schematic of a typical load-displacement curve [383] and (b) that of a typical CSM loading cycle [384].

Hardness, H, is defined as:

$$H = \frac{P_{max}}{A} \tag{2.12}$$

where P_{max} is the maximum indentation load, and A is the projected contact area of the indent [385]. The measurement of the contact area will be discussed later.

From the unloading stiffness, S, which is the slope of the load-displacement curve upon unloading, the reduced modulus, E_r, can also be calculated:

$$S = \frac{\mathrm{d}P}{\mathrm{d}h} = \frac{2\beta}{\sqrt{\pi}} E_r \sqrt{A} \tag{2.13}$$

where β is a dimensionless parameter that depends on the shape of the indenter [386, 387]. For axisymmetric indenters $\beta = 1$ and for a triangular indenter $\beta = 1.034$ [388]. The unloading curve is usually fitted to the power-law relation [385]:

$$P = \alpha(h - h_f)^m \tag{2.14}$$

where α, m, and h_f are determined using least-squares fitting. Physically, h_f corresponds to the depth of the indent once unloading is completed.

The reduced modulus E_r accounts for the elastic deformation of the indenter during indentation:

$$E_r = \frac{1 - {\nu_s}^2}{E_s} + \frac{1 - {\nu_i}^2}{E_i} \tag{2.15}$$

where ν_s and ν_i are the Poisson's ratio for the sample and indenter, respectively, and E_s and E_i are the corresponding elastic moduli. For diamond, the most common indenter tip material, $\nu_i = 0.07$ and $E_i = 1140$ GPa [389].

As seen in Equations 2.12 and 2.13, the measurement of hardness and elastic modulus relies on the accurate determination of contact area. The Oliver-Pharr method, first described in 1992, uses a series of indents of different depths into a material of known stiffness [385]. The most common material is fused silica with $E = 72$ GPa and $\nu = 0.17$ [385]. This allows E_r to be determined using Equation 2.15, assuming it is independent of depth. The measured compliance, $C = 1/S$, is modelled as a sum of the sample compliance, C_s, and load frame (machine) compliance, C_f:

$$C = C_s + C_f. \tag{2.16}$$

Re-writing Equation 2.13 as compliance, and substituting into Equation 2.16:

$$C = C_f + \frac{\sqrt{\pi}}{2\beta E_r} \frac{1}{\sqrt{A}}. \tag{2.17}$$

If E_r is independent of depth, then a plot of C vs $1/\sqrt{A}$ will be linear, with an intercept at C_f. Rearranging Equation 2.17 yields:

$$A = \frac{\pi}{4}\frac{1}{{E_r}^2}\frac{1}{C - C_f}. \tag{2.18}$$

For a Berkovich tip, a three-sided pyramid shape with a half-apex angle of 65.3°, the area function can be written as:

$$A(h_c) = 24.5{h_c}^2 + C_1{h_c}^1 + C_2{h_c}^{1/2} + C_3{h_c}^{1/4} + ... + C_8{h_c}^{1/128} \tag{2.19}$$

where the leading term ($24.5{h_c}^2$) describes a perfectly sharp Berkovich indenter. C_n are fitted constants, which describe the deviation of the real tip from the perfect shape due to blunting. The area function is given as a function of h_c, the contact depth, describing the vertical distance along which contact is made with the sample.

Building on the basic nanoindentation procedure, the technique of continuous stiffness measurement (CSM) was developed [385, 390]. During loading, a small dynamic oscillation is imposed on the force signal and the corresponding oscillation of the displacement signal is recorded, see Figure 2.15(b). One of the key advantages of this technique is that it can provide measurements of hardness and elastic modulus as a function of depth without the need for multiple indentations and unloading steps [384].

There are some particular challenges when measuring the hardness of ion-irradiated materials using nanoindentation: The first is the non-uniform depth profile of the damage levels induced by irradiation (as discussed in Section 2.4.4). When the indenter tip penetrates the material surface, a plastic zone is generated around the indented volume where dislocations have formed and deformation has occurred [391, 392]. For metals, this plastic zone can extend 5 to 10 times the indented depth [53, 393, 394] and the microstructure in the entire volume of the plastic zone will have an effect on the hardness value measured. This means that nanoindentation is not able to associate a hardness measurement to a single damage level, but rather it is an average of the hardness from the layer of material, with a range of damage levels, through which the plastic zone extends. Kiener *et al.* [395] have demonstrated that cross-sectional indentation, a series of indents made perpendicular to the direction of irradiation, could potentially be more selective about the region of damage probed.

Pile-up, a phenomenon where the material surface near the periphery of the indent increases in height, commonly occurs in irradiated materials [208, 211, 396]. This can affect the actual contact area between the indenter and the sample, which subsequently impacts the hardness and modulus measurements. Some studies have attempted to correct for this by measuring the indent residual area with atomic force microscopy (AFM) [397, 398], or to independently measure the elastic modulus to back-calculate the contact area [399].

The indentation size effect, often observed as increased hardness for shallow indents, is also commonly observed in nanoindentation. This has been justified by Nix and Gao [392] as the initial generation of geometrically necessary dislocations (GND), which arise to accommodate the displacement of material by the indenter. The generation of these extra dislocations increases the measured hardness of the material [400]. The GND density is inversely proportional to the depth and the effect is larger for shallow indents [401], so it can affect nanoindentation analysis of ion-irradiated materials. Due to the different length scales and stress states associated with nanoindentation and bulk tensile testing, the factors affecting deformation are different, leading to different measurements of hardness. An extended discussion of this is provided in Section 5.4.2.

Applications of Nanoindentation

Nanoindentation allows the study of plasticity on the nanoscale, including the initiation of plasticity through the nucleation of dislocations or the activation of pre-existing dislocation sources. The analysis of pop-ins, which are sudden excursions in displacement during nanoindentation, provides insight into the transition between elastic to plastic deformation in materials, to better understand their deformation behaviour [54, 402, 403]. The indentation load at the point of pop-in can depend on the material composition, impurity content, and dislocation density [403].

Various indenter tip shapes are used for different applications. The Berkovich tip is most commonly used to measure hardness. It is favoured for its self-similar geometry, simplifying analysis, and the ease of fabrication of a sharp tip with only 3 sides. The use of a sharp tip also allows plastic deformation in materials to be

studied with smaller indentation loads. Another commonly used tip shape is a spherical tip, with different effective radii from 1 µm to >100 µm. A key capability of using spherical tips for nanoindentation is that a smoother stress field can be generated with a larger elastic segment compared to sharp indenters. This allows the measurement of stress-strain relationships on the nanoscale [404]. The mathematical details of this procedure are further outlined in Section 5.4.2.

Section 2.6.3 has already outlined many micromechanical studies of ion-irradiated FeCr, with most studies conducted using nanoindentation, with Berkovich tips, to measure hardness. Spherical nanoindentation has been performed on many ion-irradiated materials, including FeCr alloys [211, 405, 406]. Stress-strain relationships from the thin ion-irradiated layer can be extracted, allowing observations of strain softening due to the annihilation of irradiation-induced defects by glide dislocations.

Nanoindentation is also very helpful for measuring hardness evolution for SPD-processed materials, especially materials processed via HPT due to their small sample size [407]. The studies of hardness as a function of grain size using micro- and nanoindentation have been covered in Section 2.7.3. Additionally, a investigation of pop-in behaviour in HPT materials to measure the critical shear stress required for plasticity initiation has been conducted in UFG ZK60 Mg alloy [408]. It was found that the process of HPT did not change the inherent mechanisms of yielding by heterogeneous dislocation nucleation, which was from pre-existing dislocation sources in the material, and subsequent plastic flow via grain boundary sliding.

2.8.4 Transient Grating Spectroscopy

One of the challenges with measuring thermal transport properties on ion-irradiated materials is isolating the signal from the thin damaged layer positioned on top of a much thicker bulk. Transient grating spectroscopy (TGS) provides a rapid, non-destructive method of measuring thermal diffusivity in the top few microns of a sample. It has been used for characterising properties of thin films [409, 410] but is also suitable for studying the thin damaged layer of ion-irradiated materials.

A schematic of TGS is shown in Figure 2.16(a). Two short laser pulses (excitation beams) of wavelength $\lambda \sim 500$ nm, typically <500 ps and a few µJ in energy, are

overlapped on the surface of the material with a well-defined angle θ [411]. They form an interference pattern on the surface with a specific wavelength Λ, given by [412]:

$$\Lambda = \frac{\lambda}{2\sin(\theta/2)} \tag{2.20}$$

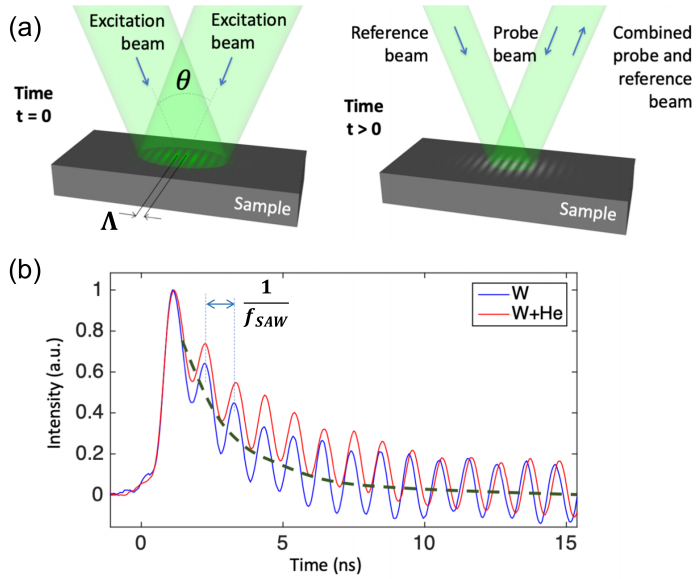


Figure 2.16: (a) The schematic of a TGS set-up with the excitation beams at $t = 0$ forming a transient grating on the surface of the material, then at $t > 0$, the decay of the grating is measured by the probe and reference beams. (b) The measured signal as a function of time on pristine and He-implanted W, with the dashed line showing the changing signal intensity due to the transient grating decay [411].

The energy of the excitation beams is absorbed by the material at regions of constructive interference and subsequently leads to local thermal expansion. This causes a variation in surface height, forming a spatial displacement grating of wavelength Λ, which is referred to as the 'transient grating'. Heat diffuses from maxima to minima, as well as into the material bulk, leading to the decay of the transient grating [337, 412, 413]. This decay response is measured by diffracting a probe beam, combined with a reflected reference beam for heterodyne amplification and detection [337, 412, 414].

The sudden thermal expansion of the surface also launches two counter-propagating surface acoustic waves (SAW) with wavelength Λ across the surface. SAW velocity, v_{SAW}, can be measured and give information on the elastic properties of the material [415].

Examples of a TGS signal, measured from pristine and He-implanted W, are shown in Figure 2.16(b) and two key features can be seen. The first is the reduction of the signal intensity over time due to the decay of the temperature grating as heat diffuses into the material bulk (dashed line). The second feature is the set of oscillations of a fixed frequency due to the counter-propagating SAW waves. The full fit of the signal intensity, I, is given by [416]:

$$I = A\left[\text{erf}\left(q\sqrt{\alpha t}\right) - \frac{\beta}{\sqrt{t}}\exp(-q^2\alpha t)\right] + B\sin(2\pi f_{SAW}t + \theta)\exp(-t/\tau) + C \quad (2.21)$$

A, B, and C are parameters determined during fitting. $q = 2\pi/\Lambda$ and t is time. The part of the response affected by thermal diffusivity, α, is described by the first set of terms in Equation 2.21. It comprises of the spatial displacement profile due to the temperature grating (the error function term) and the temperature dependent reflectivity of the material (the exponential term). β describes the ratio of the displacement and reflectivity contributions. For Fe, the change in reflectivity due to temperature is negligible [417] and hence β is small and the associated term is neglected in the analysis. The second set of terms describe the SAW oscillations. f_{SAW}, θ, and τ are respectively the frequency, initial phase offset, and the time constant for the decay of the SAW oscillations. C is the background in the signal.

For an elastically isotropic material, the elastic modulus E can be calculated by fitting the SAW velocity, v_{SAW}, to an approximate solution to the Rayleigh wave equation [418]:

$$v_{SAW} = f_{SAW}\Lambda = \left(0.874 + 0.196\nu - 0.043\nu^2 - 0.055\nu^3\right)\sqrt{\frac{E}{2(1+\nu)\rho}} \quad (2.22)$$

where f_{SAW} is the SAW frequency fitted from Equation 2.21, ν is Poisson's ratio (valid for ν between -1 and 0.5), and ρ is the density of the material. In the case of elastic anisotropy, if the relative orientation of the SAW propagation and crystal lattice is known, the determination of elastic constants is more complicated but still possible [419].

Käding *et al.* [413] found that the measurement of the thermal properties using TGS is sensitive to a depth of Λ/π, while elastic property signal is dominated by the top layer of thickness $\Lambda/2$. This makes TGS an ideal technique to measure

thermal transport and elastic properties of ion-irradiated materials where the probed depth can be tuned to isolate the signal from the thin irradiated layer situated on top of the unirradiated bulk material.

Using TGS, Reza *et al.* [337] measured degradation of up to 55% in thermal diffusivity of W irradiated with self-ions at room temperature. A saturation effect was found for damage levels above 0.1 dpa. Notably, the defect density calculated from thermal diffusivity, using a simple kinetic theory model, was much higher than measured by TEM. This suggests that a significant contribution to thermal diffusivity degradation is from defect clusters smaller than 1.5 nm, below the sensitivity limit of TEM measurements but accounted for using MD simulations. These results are consistent with a separate study of thermal conductivity in W, implanted with self-ions, measured with the '3ω' method of applying a periodic heat flux and measuring the surface temperature with a sensitive thermometer [420]. In that study, a decrease of 70% in thermal diffusivity was detected after irradiations of up to 0.2 dpa at room temperature. Hofmann *et al.* [411] also measured the thermal diffusivity of He-implanted W at room temperature. The thermal diffusivity of the damaged W decreased by as much as 30% even with a small amount of implanted He ($\sim$0.03 at%). A subsequent 10-fold increase in implanted helium only caused an additional 20% drop in thermal diffusivity, suggesting a saturation effect.

TGS has been used to measure thermal diffusivity changes following irradiation in pure metallic elements, including Nb [217], W, Cr, Fe, and V [218], as discussed in Section 2.6.4. The use of TGS on FeCr alloys has recently been conducted by Wylie *et al.* [421] on laser-welded Eurofer-97. The authors found that welding caused a reduction in thermal diffusivity compared to the as-received material. However, the difference in thermal diffusivity between the two materials disappeared with annealing up to 873 K due to freshly formed martensite in the welded material.

To date, no study has been performed on the thermal properties of self-ion FeCr binary alloys. TGS not only provides thermal diffusivity and elastic property information but also reveals important insights into the defect population induced by irradiation.

2.9 Summary of the Literature Review

In this chapter, the use of RAFM steels in next-generation nuclear reactors and the need to study their response to neutron irradiation whilst in operation have been discussed. Eurofer-97 is a prototypical RAFM steel that is important to characterise to optimise future reactor performance. At the same time, the study of FeCr binary model alloys is important both to validate modelling studies and gain a mechanistic understanding of the irradiation response of more complex steels.

An irradiating particle (e.g. neutrons, heavy ions, protons) produces a collision cascade, displacing atoms and leads to the formation of defects. The damage to the material can be quantified using the dpa unit, which allows irradiation damage from different particles and energies to be compared. Though in nuclear reactors, the irradiating particles are neutrons, the irradiation damage can be mimicked by heavy ion irradiation. This allows better control over irradiation parameters such as dose and temperature, but has the drawback of only producing a thin damaged layer.

Irradiation damage has been extensively characterised by TEM in FeCr alloys. The increase of irradiation dose initially causes the formation of point defects and small dislocation loops, which grow in size and turn into extended dislocation networks at dose levels of several dpa. The presence of Cr reduces defect mobility, which affects defect size and density. Higher irradiation temperatures enhance defect recombination and alter the morphology of the dislocation loops.

Irradiation parameters and material composition not only affect defect microstructure, but also the material properties. It has been found for irradiated W that lattice strain [183] and thermal diffusivity [337] are strongly affected by irradiation dose, showing saturation behaviour at ∼0.1 dpa. **However, for Fe and FeCr alloys, the irradiation effects on lattice strain and thermal diffusivity are not well-understood.**

Mechanical properties have been extensively characterised for FeCr alloys irradiated at temperatures above 573 K. Irradiation-induced hardening decreases with irradiation temperature, and saturates with dose above ∼2 dpa. The dependence of irradiation hardening on Cr content changes with irradiation temperature. **However,**

changes to material properties at low temperatures are poorly understood, yet are important to fusion reactor applications as structural steels will be operating from cryogenic to high temperatures (∼800 K).

Improving irradiation resistance is crucial for next-generation reactor materials. SPD-processing, including HPT and ECAP, and associated grain refinement have been proposed as potential pathways to achieve this by increasing grain boundary areas acting as sinks for irradiation-induced defects. **However, the effect of SPD on RAFM steels, including material microstructure, properties, and irradiation resistance have not been extensively studied.**

To investigate the effects of ion irradiation on materials, specialised techniques need to be used to characterise the small volume of damaged materials. There are many well-developed methods such as electron microscopy and nanoindentation. Recent developments, including HR-EBSD, TKD and spherical nanoindentation, have allowed more extensive insights into the dislocation distribution and micromechanical properties of materials. TGS and DAXM techniques have shown great potential for the characterisation of irradiation damage, in materials such as W, and are expected to be well-suited for the study of ion-irradiated FeCr alloys.

2.10 Research Outline

From surveying the existing literature, several important gaps have been revealed regarding our understanding of irradiation damage on FeCr steels.

Irradiation, both with neutrons and heavy ions, have been extensively characterised by TEM imaging, which has limited sensitivity to small defects ($\leq$1.5 nm). Studies of thermo-mechanical properties in irradiated Fe and W [129, 337] have measured changes that cannot be fully explained by TEM defect observations. Such studies of 'invisible defects' have not been investigated for FeCr alloys, but are crucial to fully characterising the defect population in these materials. Furthermore, thermal diffusivity and lattice strain have not been previously studied in irradiated FeCr materials, and their dependence on irradiation parameters and Cr content is not well-understood.

Defect and material property evolution studies have not been extensively performed on samples irradiated at below 573 K. This is critical to address as there many gaps in the irradiation damage knowledge base that are important to fill to fully understand the effects of irradiation and also for comparisons to modelling studies. For fusion reactors, irradiation effects at lower temperatures, are important to understand as reactor structural components will be operating down to cryogenic temperatures. In particular, irradiation effects at room temperature are readily accessible for study because the irradiation and subsequent characterisation can all be carried out at the same temperature. This allows a more accurate picture of irradiation damage during reactor operation to be gained.

Another limitation in the existing literature is that many studies on defect microstructure and material property changes often focus on one aspect of characterisation (either microstructure or material property), and/or only use one characterisation technique. Whilst this gives a lot of detail on certain aspects of irradiation effects, it is difficult to identify synergistic effects, e.g. of material composition and dose. It is also challenging to draw the relationship between defect microstructure and different material properties. This experimental link is crucial for a more complete understanding of the evolution of irradiation-induced changes in material microstructure and properties. It is also important for validating modelling studies to optimise reactor component design. To gain insights into this from current literature, it would be necessary to draw across multiple studies but this is often made difficult by the different experimental conditions employed in different studies.

This thesis aims to address these gaps in the literature under the following research questions:

1. What are the effects of room-temperature ion irradiation on Fe and FeCr alloys, especially defect populations and their impact on material properties?

2. How can micromechanical studies of ion-irradiated FeCr be used to understand the mechanisms of deformation in irradiated materials, and thus gain useful insights for reactor structural steels?

3. How can the knowledge from Fe and FeCr binary alloys be applied to improve the properties for reactor structural steels?

This thesis is comprised of 5 studies to address these questions. Question 1 is addressed in **Chapters 3 and 4**, which is focused on the effects of irradiation dose and Cr content on the hardness, thermal diffusivity and lattice strain in FeCr. A wide range of irradiation dose (from 0.00008 dpa to 6 dpa) were examined to fully characterise defect evolution at different dose regimes, from the onset of irradiation-induced changes through to approaching saturation. By comparing how irradiation affects different material properties, a multi-faceted picture of irradiation-induced damage and defect population can be formulated.

Question 2 is addressed in **Chapters 5 and 6**, which examine the irradiation-induced changes in deformation behaviour and associated microstructure in Fe and FeCr. Nanoindentation, as a rapid technique suitable for ion-irradiated materials, was used to study the characteristics of dislocation nucleation, activation, and propagation as a function of irradiation dose and Cr content (**Chapter 5**). Furthermore, non-destructive characterisation of the deformation microstructure surrounding nanoindents was applied to study the effect of irradiation-induced deformation localisation in Fe and FeCr (**Chapter 6**).

The insights from studying FeCr binary model alloys are then applied to Eurofer-97 to address Question 3. **Chapter 7** provides an extensive study on the effect of SPD-processed Eurofer-97, and the subsequent impacts on its thermal stability and irradiation response. Again, by using a range of characterisation techniques to examine the material microstructure and properties, a comprehensive understanding of irradiation damage can be obtained. This allows the assessment of the suitability of SPD as a method to improve the use of Eurofer-97 as a RAFM steel for nuclear fusion reactors.

Large systematic studies were conducted to study the effect of dose, composition, and deformation on FeCr steels. By using a range of characterisation techniques, the results from this thesis will allow a more comprehensive understanding of room-temperature irradiation damage in FeCr alloys.

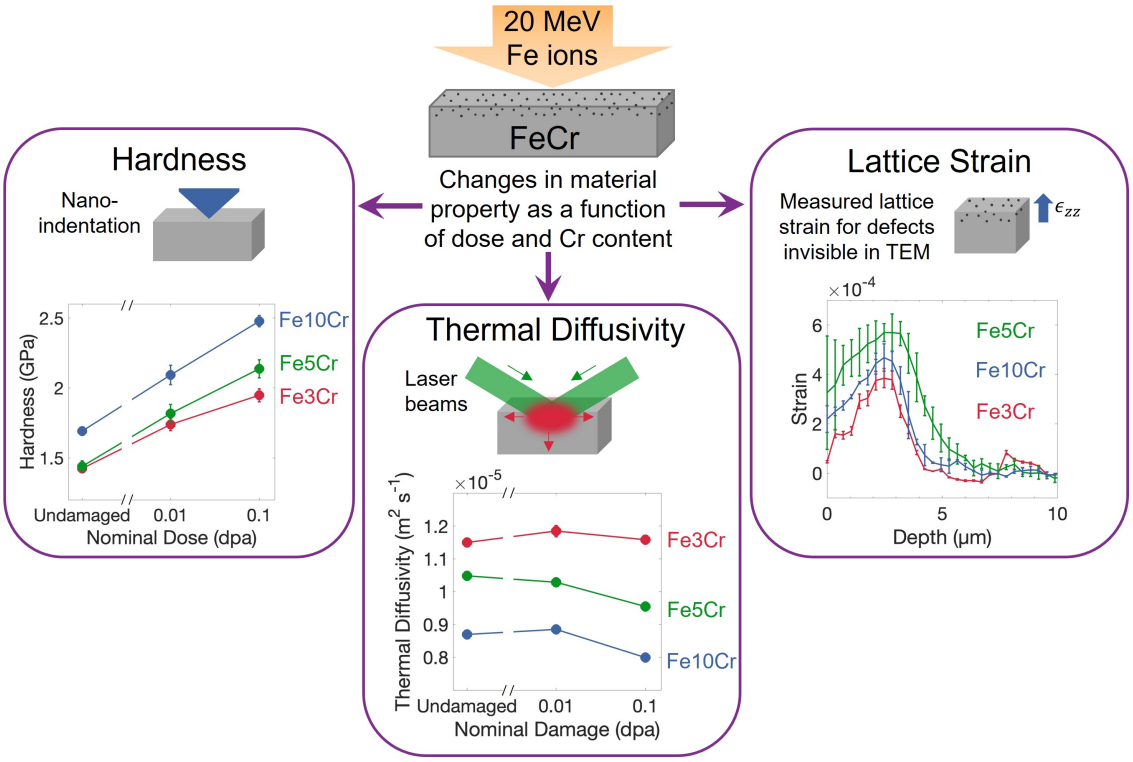
3

Characterising Ion-Irradiated FeCr: Hardness, Thermal Diffusivity and Lattice Strain

This chapter reports the first systematic study of the material property evolution of room-temperature ion-irradiated FeCr as a function of irradiation dose and Cr content. For the first time in FeCr, the thermal diffusivity has been measured with TGS and lattice strain of the material has been measured, which allows irradiation-induced defect density calculation. The comparison of hardness, thermal diffusivity, and lattice strain trends, allows insight into the effect on material properties from defect population that cannot be fully characterised by TEM.

The contents of this chapter have been published as: K. Song, S. Das, A. Reza, N. W. Philips, R. Xu, H. Yu, K. Mizohata, D. E. J. Armstrong, F. Hofmann, "Characterising Ion-Irradiated FeCr: Hardness, Thermal Diffusivity and Lattice Strain", *Acta Materialia*, vol. 201, pp. 535–546, 2020 [422]. S. Das assisted with nanoindentation data collection. A. Reza performed all TGS data collection and analysis. N. W. Philips and R. Xu assisted with DAXM data collection. H. Yu polished the samples. K. Mizohata performed the ion irradiation. The remainder of the work was carried out by the author with the supervision of D. E. J. Armstrong and F. Hofmann.

3.1 Abstract



Graphical Abstract

Ion-irradiated FeCr alloys are useful for understanding and predicting neutron-damage in the structural steels of future nuclear reactors. Previous studies have largely focused on the structure of irradiation-induced defects, probed by transmission electron microscopy (TEM), as well as changes in mechanical properties. Across these studies, a wide range of irradiation conditions have been employed on samples with different processing histories, which complicates the analysis of the relationship between defect structures and material properties. Furthermore, key properties, such as irradiation-induced changes in thermal transport and lattice strain, have been little explored.

Here we present a systematic study of Fe3Cr, Fe5Cr and Fe10Cr binary alloys implanted with 20 MeV Fe^{3+} ions to nominal doses of 0.008 dpa and 0.08 dpa at room temperature. Nanoindentation, transient grating spectroscopy (TGS) and X-ray micro-beam Laue diffraction were used to study the changes in hardness, thermal diffusivity and strain in the material as a function of dose and Cr content.

Our results suggest that Cr leads to an increased retention of irradiation-induced defects, causing substantial changes in hardness and lattice strain. However, thermal diffusivity varies little with increasing dose and instead degrades significantly with increasing Cr content in the material. We find significant lattice strains even in samples exposed to a nominal displacement damage of 0.008 dpa. The defect density predicted from the lattice strain measurements is significantly higher than that observed in previous TEM studies, suggesting that TEM may not fully capture the full irradiation-induced defect population.

3.2 Introduction

In next-generation fusion and fission reactors, reduced activation ferritic/martensitic (RAFM) steels are likely to be used as the main structural material [16]. They are chosen for their high thermal conductivity and resistance to swelling compared to austenitic steels [12]. In service, the steel components will be exposed to temperatures up to 823 K and intense irradiation by 14 MeV fusion neutrons [18]. For the optimisation of steel composition and operational safety, it is important to understand the defects formed, the microstructural changes due to irradiation, and the associated changes in thermomechanical properties.

To gain fundamental insight into the damage and defect population in steels due to irradiation, the study of iron-chromium (FeCr) binary alloys is useful, as it eliminates microstructural complications from other alloying elements. Ion implantation has become a widely used method to mimic neutron damage without the time and activation disadvantages of using neutrons in fission reactors [423–425]. Several past studies [112, 113, 122, 210] have shown the effective use of such ion-irradiated binary alloys with a range of Cr content to simulate the neutron irradiation conditions at various stages of component lifetime on differently composed steels.

There have been a number of transmission electron microscopy (TEM) investigations conducted on ion-irradiated FeCr alloys to directly image irradiation-induced defects. Ion implantation causes defects mainly in the form of dislocation loops, of both vacancy and interstitial types [109, 111, 112]. Many studies have found

that a 'threshold dose' of around 0.01 dpa is required before visible defects appear [109, 137, 138]. This has been attributed to the need for an overlap of damage cascades before they form visible defect loops [112, 124]. However, a more recent study has found visible damage in TEM from dose as low as 0.0015 dpa [59]. Higher dose results in the coalescence of loops as well as loop aggregation to form more complex microstructures such as loop strings [111]. Cr has been observed to reduce loop mobility, leading to a higher number density of observable defects with smaller sizes compared to the case of pure Fe [111, 113]. Irradiation temperature has also been observed to affect defect accumulation, with irradiation at 773 K resulting in larger loops of only $\mathbf{b} = \frac{1}{2}\langle 100\rangle$ whereas 573 K irradiation, at the same dose, produced smaller loops mostly with $\mathbf{b} = \frac{1}{2}\langle 111\rangle$ [112].

The effects of irradiation-induced defects on the mechanical properties of FeCr alloys have been studied with nanoindentation. Irradiation hardening has been observed in FeCr, and the amount of hardening increases with Cr content following irradiation to 1 dpa at room temperature [98]. It has also been reported that the hardening effect saturates at dose above 2 dpa for Cr content greater than 5% [210]. Another study found that hardness saturates at 1 dpa and above for Cr content >9% [98]. However, both of these studies were conducted with an irradiation temperature of 573 K. It has also been found that hardening actually decreases with increasing dose rate, between 3×10^{-5} to 6×10^{-4} dpa/s, for FeCr alloys, which has been attributed to the clustering of Cr into precipitates [60]. However, many of the existing TEM and nanoindentation studies on ion-irradiated FeCr were conducted on samples with different composition and processing history, as well as under different nominal irradiation conditions (total dose, dose rate and implantation temperature). As such, it is currently unclear how well these results can be compared and correlated with each other.

There are other important material properties that have not been extensively studied for ion-implanted FeCr. For example, it is crucial to study the effect of irradiation on the thermal diffusivity of FeCr as this will give a more accurate prediction of the temperatures expected for different reactor structural components and the amount of cooling required for safe operation. Little is currently known

about the effects of irradiation on the thermal properties of Fe-based alloys, with one study finding negligible changes to the thermal conductivity of ASTM A533 grade B class 1 steel (ferritic) after neutron irradiation with 2.4×10^{23} n/m^2 (∼0.036 dpa) [222]. However, in W, another BCC metal commonly studied for fusion applications, self-ion irradiation to dose levels as low as 0.1 dpa has resulted in a 55% degradation in thermal diffusivity [337]. The degradation in thermal properties results from irradiation defects in the material lattice acting as electron scattering sites [213]. An interesting observation is that the defects observed with TEM do not account for all the measured changes to thermal diffusivity in W, suggesting that small defects that TEM is not sufficiently sensitive to probe, have a significant effect on thermal and material properties following irradiation [189].

Irradiation-induced lattice swelling, and the associated stresses and strains, must also be considered for the design of structural reactor components [26, 164]. Previous experiments conducted on He-implanted W found large irradiation-induced strains and suggested higher defect retention per injected ion at lower doses [177]. This shows that not only is lattice strain important to consider for reactor materials, but also that the effect of dose and damage history can significantly alter the damage response of a material. There has been many studies conducted on neutron and ion irradiation induced void swelling in steels and FeCr [61, 130, 169, 170, 173]. They have examined macroscopic swelling, often resulting in volumetric changes to the material, caused by the formation of voids and cavities, >10 nm in diameter, after irradiation dose of tens to hundreds of dpa. However, this is different from the study of lattice swelling, which examines the microscopic strain induced by atomic defects [175, 176], and to date, little is known about the lattice swelling and strains in ion-irradiated FeCr.

Here we address these open questions with a systematic study of FeCr with different Cr concentrations (3, 5 and 10 wt% Cr) subjected to different irradiation dose levels, from 0.008 dpa to 0.08 dpa, at room temperature. Experimental characterisation of hardness, thermal diffusivity and lattice strain are conducted and the resultant trends discussed in terms of the underlying damage microstructure.

3.3 Methods and Materials

3.3.1 Materials and Preparation

High purity polycrystalline samples of FeCr containing 3, 5 and 10 wt% Cr respectively were produced under the European Fusion Development Agreement (EFDA) programme (contract no. EFDA-06-1901) [66, 67]. The alloys were prepared by induction melting under a pure argon atmosphere, then forging at 1423 K. This was followed by a cold reduction of 70% and heat treatment for 1 hour at 1023 K for Fe3Cr and Fe5Cr, and at 1073 K for Fe10Cr. The materials were then air cooled and delivered in the recrystallised state. The impurity content of the alloys is included in Appendix B.1. The alloy bars were sectioned with a diamond saw into samples approximately 5×5×0.7 mm^3 in size.

The sample surfaces were mechanically ground with SiC paper, diamond suspension, then colloidal silica (0.04 µm). The final polishing step was electropolishing with 5% perchloric acid in ethanol at 233 K, using a voltage of 28 V and current of 0.3 A. The polishing time was on the order of 3–4 minutes, depending on the composition, until the surface deformation accumulated from the previous polishing steps had been removed. This was determined by visual assessment under optical microscopy. An unimplanted reference sample was retained for each Cr content, and ion implantation was performed for the remaining samples.

3.3.2 Ion Implantation

The samples were implanted with 20 MeV Fe^{3+} ions at room temperature using a 5 MV tandem accelerator at the Helsinki Accelerator Laboratory. The beam size was approximately 5 mm and was rastered over a sample area of 10 × 10 mm^2 to achieve uniform implantation across the surface. The implantation chamber was held under vacuum at 8×10^{-7} mbar.

Figure 3.1 shows the damage dose profile calculated using the Stopping and Range of Ions in Matter (SRIM) code [80] using the Quick K-P calculation model with Fe ions and pure Fe as the target, with a displacement energy of 40 eV [426]. Cr has a similar displacement energy and density to Fe. Molecular dynamics simulations have

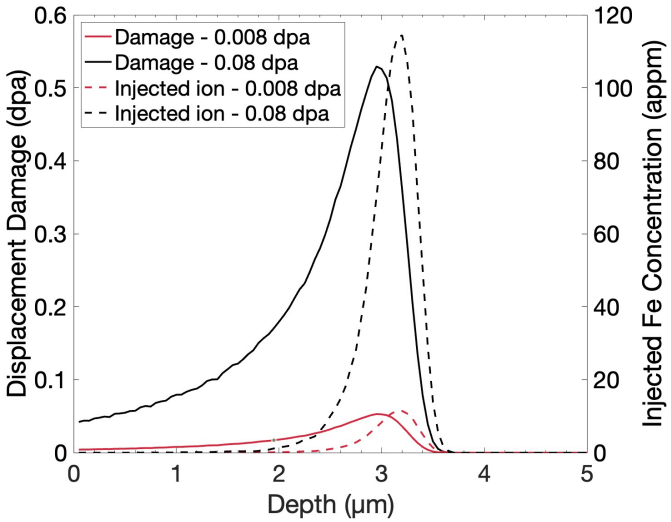


Figure 3.1: Damage profiles (solid lines) predicted by SRIM for the two nominal dose levels of 0.008 dpa (red) and 0.08 dpa (black), which is the average dose in the first 2 µm below the surface. Also shown are the calculated injected Fe-ion concentrations (dashed lines) from the implantation.

shown that there are no significant differences between the threshold displacement energies in FeCr and pure Fe [427]. Therefore the same damage profile is assumed for all samples of the same irradiation condition.

Two different fluences, 5.3×10^{13} cm^{-2} and 5.3×10^{14} cm^{-2} were used to achieve an average dose level of 0.008 dpa and 0.08 dpa, respectively, in the first 2 µm below the surface. This depth was chosen to calculate the nominal dose as it is before the sharp increase in damage level at the end of the implantation range (Figure 3.1). These will be referred to as the 'nominal dose level' from here onwards. The samples of different Cr composition were implanted at the same time for each nominal dose level at a dose rate of 1.6×10^{-5} dpa·s^{-1}. We took advantage of the graduated damage profile when using depth-resolved techniques (discussed later in section 3.4.3), allowing for a range of dose levels between 0 to ∼0.6 dpa to be probed. The damage dose level for a specific depth will be referred to as the 'dose-at-depth'.

3.3.3 Nanoindentation

Nanoindentation was performed using an MTS Nano Indenter XP with a Berkovich tip calibrated on fused silica with a known elastic modulus of 72 GPa. Continuous stiffness measurements (CSM) were made to a depth of 1 µm below the surface. Indents were

made at a strain rate of 0.05 s^{-1}, a CSM frequency of 45 Hz, and harmonic amplitude of 2 nm. At least 7 indents were performed on each sample, on grains within 10° of {001} out-of-plane orientation, identified with EBSD before nanoindentation. Indents were spaced at least 50 µm from each other and grain boundaries.

3.3.4 Transient Grating Spectroscopy

Transient Grating Spectroscopy (TGS) is able to provide rapid and non-destructive measurements of thermal diffusivity in thin surface layers. The technique is described in detail in [337, 380, 413, 414]. Two short laser pulses (pump beams of 0.5 ns at 532 nm) are directed at the surface of the sample at a fixed angle forming an interference pattern with a spatial period, Λ, on the sample surface. At the positions of constructive interference, the energy of the lasers is absorbed by the sample and causes local thermal expansion, which creates a spatial displacement grating on the surface. As the heat diffuses from maxima to minima, and into the material bulk, the transient thermal grating decays. This response can be measured by diffracting a second laser beam (probe beam, continuous at 559.5 nm) off the 'transient' grating on the sample surface. The decay of the diffracted signal intensity can be interpreted in terms of the thermal diffusivity of the material. The thickness of the probed layer is approximately Λ/π [413].

In this study, a grating wavelength of $\Lambda = 5.707 \pm 0.001$ µm was used to obtain a probed depth of approximately 2 µm, in order to study the irradiated layer. The average pump beam power was 1.5 mW operating at 1 kHz, and the probe beam power was 22 mW, at 1 kHz with a 25% duty cycle. The reflectivity of pure Fe for this wavelength is ∼50% [428, 429]. This corresponds to an approximate absorbed energy of 0.75 mW and 11 mW from the pump and the probe beams respectively. The pump beam and probe sizes were respectively 140 µm and 90 µm ($1/e^2$ width). 25 spot measurements were made on each sample across an area of 1 mm^2. At each location, 20000 laser pulses, and the corresponding signal traces, were recorded. The measurements were performed at room temperature under vacuum ($\sim 1 \times 10^{-3}$ mbar).

3.3.5 Micro-beam X-ray Laue Diffraction

Lattice swelling in the implanted layer of the FeCr samples was measured using micro-beam Laue diffraction at the 34-ID-E beamline, Advanced Photon Source, Argonne National Laboratory, USA. Using the Differential Aperture X-ray Microscopy (DAXM) technique, described in [177, 374, 430], depth-resolved lattice strain measurements were made. A thin platinum wire was scanned across the sample surface during the measurements. The diffraction patterns from subsequent positions of the wire were compared, with the wire edge positions acting as the 'differential aperture', allowing for the resolution of signals from different depths. Measurements were made to allow reconstruction of signals from as deep as 15 µm below the surface along the beam's penetration direction (45° to the sample surface). The size of the beam on the sample surface was approximately 400 × 200 nm^2 and the depth resolution was estimated to be ∼1 µm.

On each sample, grains within 10° of {001} out-of-plane orientation, previously identified with EBSD, were measured by diffraction of a monochromatic X-ray beam. At least 2 points were measured on each sample, except for Fe3Cr 0.08 dpa where only 1 point was measured as the strong material texture restricted the number of grains with the desired orientation. A $\{00n\}$ reflection with energy between 12–18 keV was selected and scanned across an average photon energy range of ∼40 eV with a step size of 1 eV. Only the out-of-plane strain was measured as previous experiments on W found that the in-plane strains from ion implantation are close to zero [176, 177]. Analysis of the diffraction patterns was performed with the LaueGo [378] to extract lattice strain as a function of depth in the sample.

3.4 Results and Discussion

3.4.1 Irradiation Hardening

From nanoindentation in CSM mode, hardness as a function of indentation depth was obtained for all the samples (Figure 3.2). The data shown is an average of all the measurements taken on each sample and the error bars represent ± one standard deviation from each set of measurements. The indentation size effect [392], resulting

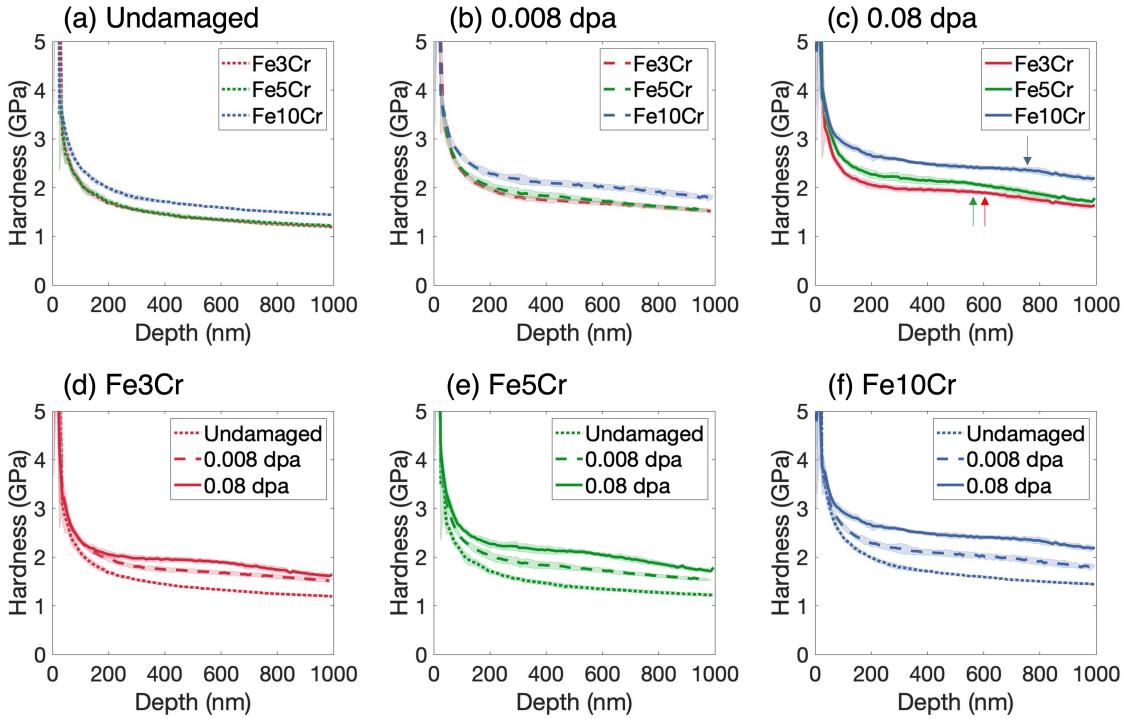


Figure 3.2: Hardness of the samples as a function of indented depth from CSM nanoindentation measurements. (a)–(c) show data grouped by dose level. The arrows in (c) indicate the depths at which the hardness curve of the corresponding Cr content (same colour) changes slope. (d)–(f) show data grouped by Cr content. The data shown consist of averaged hardness from all indents taken on each sample, with the error bars representing ± one standard deviation. Note that the damage layer as predicted by SRIM calculations extends to a depth of 3.5 µm.

in high hardness values measured in the first 200 nm below the surface, is very clear in all the measurements. Data from the unimplanted samples is shown in Figure 3.2(a). The hardness changes smoothly as a function of depth as expected for a homogenous bulk material. Fe10Cr shows the highest hardness, and the difference in hardness between the samples of different Cr content is similar at all depths.

Figure 3.2(b) shows that even at a low nominal dose level of 0.008 dpa, there is more spread in the hardness data for all Cr compositions compared to the undamaged reference samples. Figure 3.2(c) compares the effect of Cr at 0.08 dpa and it can be seen that Fe5Cr has hardened substantially more than Fe3Cr, up to 0.3 GPa more at a depth of 300 nm, considering the hardness values of the corresponding unirradiated samples are the same.

A change in the slope of the hardness plots as a function of indentation depth

is observed after 0.08 dpa of nominal dose for all Cr compositions. This feature is visible in Fe10Cr at around 750 nm, and Fe5Cr and Fe3Cr at 550 nm and 570 nm respectively (see arrows in Figure 3.2(c)). The depth at which the slope of the curve changes (h_c) is thought to correspond to the indentation depth at which the plastic zone extends into the unimplanted bulk material, which is softer [431]. The greater h_c is, the shallower the plastic zone ahead of the indenter tip is. The Johnson model of plastic zone size gives [391]:

$$\frac{c}{a_s} = \left(\frac{2E}{3\sigma_{ys}}\right)^{1/3} \tag{3.1}$$

where c is the radius of the plastic zone, a_s is the radius of the indenter imprint, E is the elastic modulus and σ_{ys} is the yield stress. This model was originally developed for a spherical indenter but it has been demonstrated to be valid for a Berkovich indenter if we substitute the ratio $\frac{c}{a_s}$ with $\frac{z_p}{h}$ where z_p is the depth of the plastic zone directly beneath the indenter at an indentation depth h [432].

For FeCr, the elastic modulus does not change significantly with Cr content for Cr <20% [433, 434] and this is also seen in our measurements in Appendix B.2. It has also been found that the yield stress of FeCr is proportional to indentation hardness [98]. The hardness measurements in Figure 3.2(a) indicate that yield stress increases with Cr content. Therefore the ratio $\frac{z_p}{h}$ is expected to decrease with Cr content, which agrees with the current observations. Furthermore, upon substituting the experimental values into Equation 3.1, both sides of the equation agree to within a factor of 3 (raw data included in Appendix B.3). This gives further confidence in the use of the Johnson model to explain our experimental observations.

Figure 3.2(d), shows quite clearly for Fe3Cr that, due to the change in the hardness slope at shallow depths (around 550 nm), the hardness values for 0.08 dpa of nominal dose are already approaching the 0.008 dpa values at 1000 nm. The Fe5Cr samples (Figure 3.2(e)) and Fe10Cr samples (Figure 3.2(f)) both show greater difference in hardness at all depths between different levels of dose than Fe3Cr. The difference in hardness at the greatest indentation depth of 1 µm increases with Cr content.

Figure 3.3 shows the change in hardness (ΔH), calculated as the difference between the irradiated samples and their corresponding undamaged counterpart of

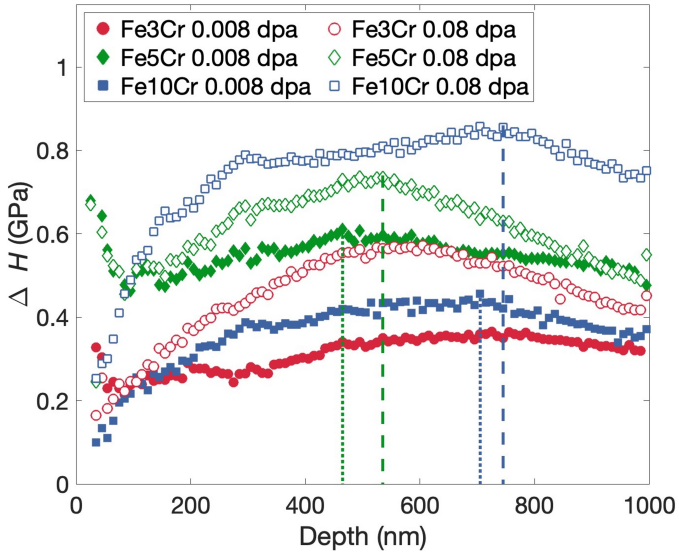


Figure 3.3: The absolute change in hardness (ΔH) compared to the undamaged samples of each composition. The dotted lines indicate the depth at which ΔH is maximum (h_c) for samples with a nominal dose of 0.008 dpa (filled markers) and the dashed lines indicate h_c for samples with a nominal dose of 0.08 dpa (unfilled markers).

the same composition, as a function of indentation depth. For Fe5Cr and Fe10Cr, there is a clear peak in ΔH at h_c for samples of both dose levels. For both Fe5Cr and Fe10Cr, h_c is greater at a nominal dose of 0.08 dpa than 0.008 dpa. Considering the 0.08 dpa samples are harder than 0.008 dpa, this suggests lower yield stress in 0.008 dpa samples [98]. Using the Johnson model [391], lower yield stress would correspond to larger plastic zone in the indented material, which qualitatively agrees with the findings of lower h_c in the 0.008 dpa samples compared to 0.08 dpa. The ΔH vs. indentation depth curves of Fe3Cr damaged to 0.008 dpa may exhibit a slightly larger h_c value than the 0.08 dpa sample, however, this is harder to discern compared to the case of Fe5Cr and Fe10Cr. As such, it has not been considered for analysis with the Johnson model.

The representative hardness values were then analysed in two ways (Figure 3.4(a) and (b) respectively). The first by taking the average hardness from CSM between indentation depths of 300–600 nm for all samples. This depth region was selected as it is deeper than the region dominated by the indentation size effect (ISE) but below h_c, representing the hardness in the irradiated layer.

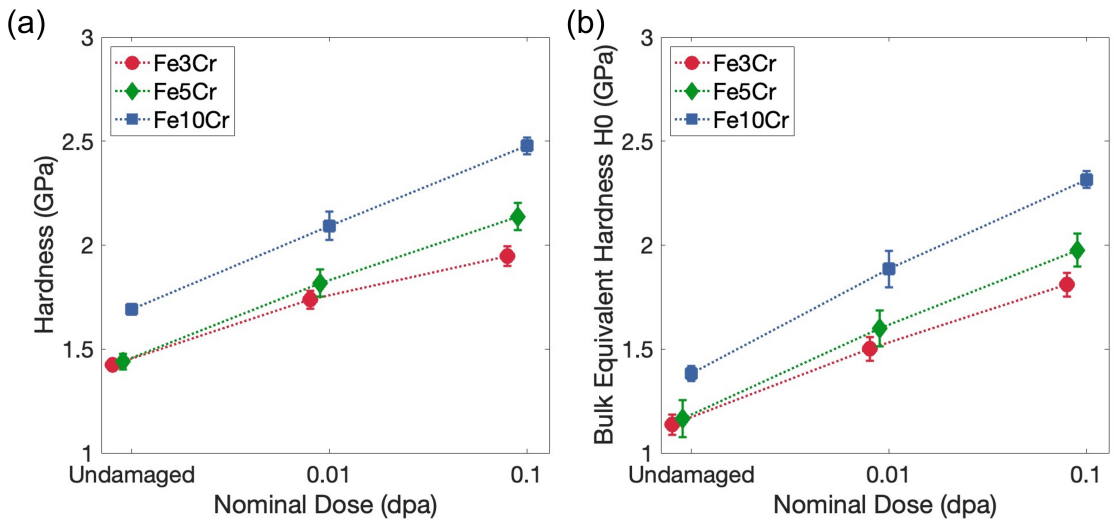


Figure 3.4: (a) Average hardness values for each sample averaged between indentation depths of 300 to 600 nm for Fe3Cr (red), Fe5Cr (green) and Fe10Cr (blue) at each dose level. (b) Bulk equivalent hardness H_0 extracted for all samples. Error bars represent ± one standard deviation from the measurements taken on each sample. Markers have been offset horizontally for clarity.

The second method considers the Nix-Gao model, which accounts for the contribution of geometrically necessary dislocations to correct for ISE [392]. The depth-dependence of hardness is described by:

$$\frac{H}{H_0} = \sqrt{1 + \frac{h^*}{h}} \tag{3.2}$$

where H is the measured hardness at indentation depth h, H_0 is the bulk equivalent hardness at infinite depth, and h^* is a characteristic ISE length scale that depends on the indenter shape and material hardness. This method has been previously applied to ion-irradiated ferritic alloys by limiting the indentation depth range over which the analysis is carried out to avoid contributions from the plastic zone extended into the unirradiated bulk [435]. For this study, the range of indentation depth for analysis is 100–600 nm. This minimises the effect of tip blunting and surface roughness at shallow indentation depths and avoids the bulk unirradiated material contribution. We note that for the unirradiated sample, the indentation depth range for analysis is 100–2000 nm, making use of the full depth range.

Figure 3.4(a) and (b) respectively show the average hardness value between 300–600 nm and the bulk equivalent hardness H_0 from using Nix-Gao analysis. In

both cases the error bars represent ± one standard deviation. The trends as a function of Cr content and dose appear to be the same between the two different analysis methods. The main difference is that the bulk equivalent hardness H_0 is lower than the constant-depth hardness for all samples. This demonstrates that there is still contribution to hardening due to ISE even when averaging between 300–600 nm indentation depth data.

All samples exhibit irradiation hardening following implantation and the hardness value at each dose level increases with Cr content. This is consistent with findings for room temperature irradiation to 1 dpa for Fe2.5Cr, Fe9Cr and Fe12Cr [98].

It can be seen that the amount of hardening relative to the undamaged samples of the same composition is higher for Fe5Cr and Fe10Cr than for Fe3Cr at 0.08 dpa of nominal dose. The relative hardness increase for Fe3Cr, Fe5Cr and Fe10Cr is respectively 36%, 48% and 46%. This suggests a greater retention of defects at higher Cr content. This is also consistent with TEM findings of reduced defect mobility and increased number density of defects with increasing Cr content [111, 113].

We also note that the amount of hardening between 0.008 dpa and 0.08 dpa of nominal dose is greater for Fe5Cr and Fe10Cr than Fe3Cr. Hardie *et al.* [210] found that hardening increases slightly with Cr content at low dose (∼2 dpa), but at a higher dose (∼6 dpa) samples with Cr content <7% exhibited much more irradiation hardening. However, that study was performed with an irradiation temperature of 573 K and at a higher dose level than those in the present study. As such, it would be of interest in follow up studies to conduct room-temperature irradiation to a higher dose level in order to compare differences in hardening for different Cr content.

3.4.2 Thermal Diffusivity

Figure 3.5(a) shows the thermal diffusivity, averaged over 25 measurement points, for the undamaged samples of different Cr content measured with TGS. The error bars represent ± one standard deviation computed from the measurement points. For Fe5Cr, the measured value agrees very well with the literature [438]. For Fe3Cr, the agreement is good (within 10%), a discrepancy that may be accounted for by some surface oxidation on our material [437] as low Cr content may be insufficient to

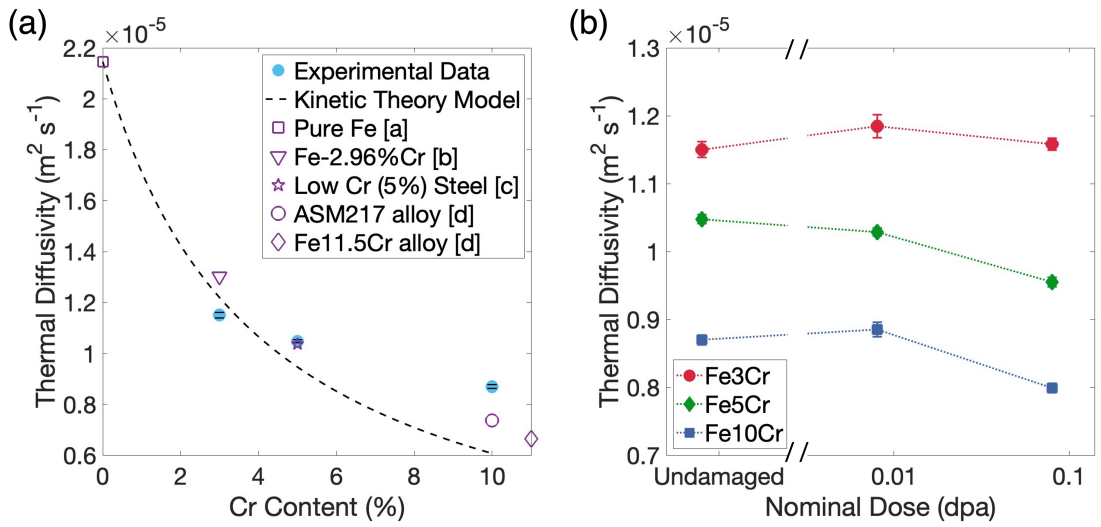


Figure 3.5: (a) The average thermal diffusivity values for undamaged samples (light blue circles). The predictions of thermal diffusivity based on the kinetic theory model (black dashed line) and the experimental data from other studies on Fe and FeCr (purple markers) are also shown. References [a–d] are respectively [436–439]. (b) Average thermal diffusivity values for each sample with error bars representing ± one standard deviation from the 25 measurement points on each sample.

prevent oxidation [440]. For the thermal diffusivity of undamaged Fe10Cr, there is limited information in existing literature and comparisons were made with ASM217 alloy (8–10% Cr, 0.2% C and 1% Si)[439] and a Fe11.5Cr alloy (0.4% C and 0.3% Mn)[441], giving 15% and 25% agreement, respectively. TGS values of thermal diffusivity have been validated for a number of other material systems [337, 380, 442, 443], which combined with the agreement with literature values for FeCr, gives confidence in our measurements.

A trend of decreasing thermal diffusivity with increasing Cr content is observed. This can be rationalised by considering Cr acting as 'impurities' that scatter electrons, decreasing the electron scattering time τ_e [444]. We can further analyse this by considering a kinetic theory model [380] that focuses on the contribution of electrons as the main heat carrier. Matthiessen's rule states that the total electron scattering rate $\sigma = \frac{1}{\tau_e}$ is the sum of the scattering rates from impurities (in this case Cr), phonons and other electrons, as long as the electron mean free path is larger than the separation between atoms [445, 446]. Focusing on the contributions of Cr altering

the scattering of electrons from the pure Fe case, the thermal diffusivity, α, is [380]:

$$\alpha = \frac{C_e {\nu_f}^2}{3\rho c_p} \left(\frac{c_{Cr}}{\tau_{e,Cr}} + \frac{1 - c_{Cr}}{\tau_{e,Fe}} \right)^{-1} \tag{3.3}$$

where C_e is the electronic heat capacity, ν_f is the Fermi velocity, ρ is the density and c_p is the specific heat capacity. c_{Cr} is the atomic fraction of Cr, $\tau_{e,Fe}$ is the electron scattering time of pure Fe and $\tau_{e,Cr}$ is the scattering time of Cr 'impurities', which is fitted from experimental data. $\tau_{e,Fe}$ is calculated from the thermal conductivity of pure Fe κ_{Fe} [436], given by [447]:

$$\kappa_{Fe} = \frac{1}{3} C_e {\nu_f}^2 \tau_{e,Fe} \tag{3.4}$$

The values of C_e, ν_f, ρ, c_p and κ_{Fe} used for the fit are shown in Appendix B.4. The contribution of Cr to electron scattering can be fitted from our experimental data as $\tau_{e,Cr} = 0.35$ fs compared to $\tau_{e,Fe} = 92$ fs. This kinetic theory model gives a good fit to the experimental data at low Cr content, shown in Figure 3.5(a). This is reasonable as the model assumes a dilute alloy.

Figure 3.5(b) shows the thermal diffusivity of all the samples, of different Cr content and dose levels. For Fe3Cr, there is no significant change in the thermal diffusivity following ion implantation. However, for Fe5Cr and Fe10Cr, there is a significant decrease in thermal diffusivity (∼8%) after a nominal dose level of 0.08 dpa. This suggests a higher retention of defects in Fe5Cr and Fe10Cr, which qualitatively agrees with previous TEM observations of Cr reducing defect mobility [111] and enhancing defect retention [113].

At a nominal dose of 0.008 dpa, both the Fe3Cr and Fe10Cr samples show a slight increase in thermal diffusivity compared to the respective undamaged samples of the same composition, though still within the error bars. This increase is surprising and the mechanism behind this is unclear. The only possible explanation is the clustering of Cr with dose but atom probe tomography measurements have shown that this only occurs at higher dose levels and irradiation temperature (∼0.6 dpa at 573 K) [210, 448]. It is worth noting that the error bars represent the standard deviation of the 25 spot measurements taken on each sample. Therefore, they are

indicative of the variation in measurements on each sample rather than the absolute accuracy of the measurements themselves.

TGS measurements on self-ion implanted W have shown a 55% decrease in thermal diffusivity following irradiation, and the effect saturates at 0.1 dpa of dose [337]. It would be of interest to investigate this for FeCr by conducting TGS measurements on samples damaged to higher dpa. Given that the decrease in thermal diffusivity at 0.08 dpa of nominal dose is quite small, this is potentially good news for future reactors as the changes in thermal diffusivity due to defects may be too small, compared to the effect from Cr content, to have an impact on predicted design purposes. However, the effect of alloying impurities on thermal diffusivity would need to be carefully considered in material design.

3.4.3 Lattice Swelling

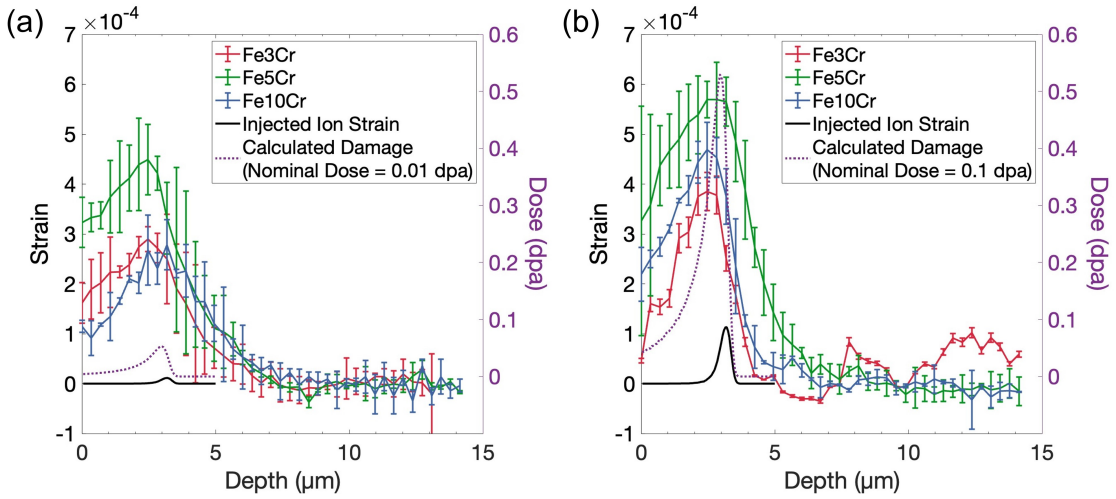


Figure 3.6: Measurement of average strain as a function of depth perpendicular to the surface of each sample for each composition (Fe3Cr - red, Fe5Cr - green, and Fe10Cr - blue) at (a) 0.008 dpa of nominal dose and (b) 0.08 dpa of nominal dose. The error bars are explained in the main text. Also shown in both plots are the predicted strains from injected ions (black line) if they all exist as ⟨111⟩ interstitials in the lattice [176, 179] and the damage profile (dotted purple line), both obtained from SRIM calculations.

Figure 3.6 shows the out-of-plane strains measured in the samples as a function of depth. The error bars represent ± one standard deviation across measurements on each sample. Only one measurement was taken for the Fe3Cr 0.08 dpa sample due to the lack of available grains with {001} out-of-plane orientation, and hence

the errors shown are the inherent measurement errors. The strains are greatest around 2.5–3 µm depth, which is the region with the highest dose and injected ion concentration (as predicted by SRIM). The amount of strain rapidly decreases to zero at depths greater than 5 µm, suggesting that there is little diffusion of defects from the implanted layer into the bulk. It can also be seen that the strain contribution calculated from the injected ions of the implantation, assuming they all exist as ⟨111⟩ interstitial defects in the lattice [176, 179], is small compared to the measured strain.

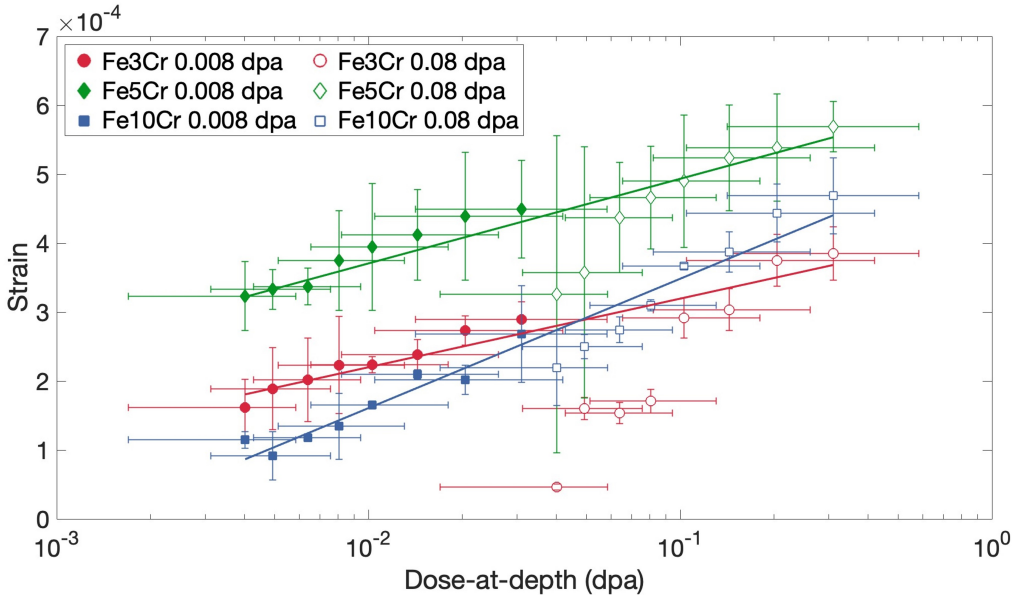


Figure 3.7: The average measured strain as a function of dose at depth with the vertical error bars as ± one standard deviation of all the measurements on each sample. The dose-at-depth values have been converted from the depth of the measurements using the damage profile calculated using SRIM. The horizontal error bars are calculated from the depth uncertainty in the depth resolution being ± 0.5 µm.

At each measured depth below the sample surface, the SRIM calculations shown in Figure 3.1 provide us with a corresponding dpa value (the dose-at-depth). Using these depth-dependent dpa values, the strain (shown in Figure 3.6) can be plotted as a function of the dose-at depth. The resulting plot is shown in Figure 3.7 for all dose-at-depth levels considered. Fe5Cr exhibits the highest strain compared to Fe3Cr and Fe10Cr which show similar strain values. The mechanism behind this is unclear. It has been observed in several studies of FeCr irradiated with neutrons and self-ions, that for Cr content <20%, the greatest amount of macroscopic irradiation void swelling have been found in Fe9Cr [61, 130, 170] and Fe6Cr [169, 173]. We have

found lattice swelling to be greatest at Fe5Cr in this study, which is close to the findings in literature for macroscopic swelling. However, the effect of Cr on lattice strain and swelling still requires further investigation.

The increase in strain with dose shows a consistent trend for all compositions, despite the measurements of dose-at-depth from 0.004–0.03 dpa and 0.04–0.3 dpa being taken on separate samples for each composition. The trends observed are qualitatively similar to the elastic strains measured in ion-irradiated UO_2, cubic-ZrO_2, MgO and ZrC [181], where the strains at low dose levels (<0.5 dpa) could be fitted to the approximated form:

$$\text{strain} = m * \ln(\text{dpa}) + c \tag{3.5}$$

where m corresponds to the rate of strain increase with dose. The constant c offsets the fitting strain values trending towards negative infinity at low dpa in this approximated logarithm form. The values of the fit are shown in Table 3.1. The rate of strain increase, m, is higher for larger Cr content suggesting higher defect retention with increasing Cr content, which agrees with TEM findings [111–113].

Cr (wt %)	$\boldsymbol{m}$ **($\times 10^{-5}$)**	$\boldsymbol{c}$ **($\times 10^{-4}$)**
3	5.2 ± 0.6	4.2 ± 0.3
5	6.7 ± 1.2	6.1 ± 0.5
10	8.6 ± 1.0	5.2 ± 0.3

Table 3.1: Parameters fitted from experimental data to Equation 3.5.

From simulations of BCC Fe at $T = 0$ K [148], it has been observed at low dose levels (∼0.01 dpa) that Frenkel pairs form, but there is little clustering, leading to a rapid increase in total defect number density. With increasing dose (up to 0.5 dpa), the interstitials begin to cluster into loops and the growth in the number density of defects slows down. Then at even higher levels of dose (>2.5 dpa), extended dislocation networks are formed, reducing the number of isolated interstitials. It is likely that our experimental observations span the first two stages of defect evolution.

We observe a rapid increase in strain at lower dose ∼0.01 dpa then a slower strain increase around 0.1 dpa, approximated by the logarithmic increase in strain with dose. It is also likely that we are observing defect clustering, and hence slower strain increase, at a lower dose level than in simulations, as small dislocation loops are mobile at room temperature.

All the strains measured from the samples in this study are positive, corresponding to lattice expansion, suggesting that some interstitial defects have been retained after irradiation. We can use the measured lattice strain to estimate the equivalent Frenkel pair density in the materials. By considering the relative relaxation volumes (Ω_r) of defects in pure Fe [179], the measured strain can be used to calculate the defect density in the material, by using the following expression [176]:

$$\epsilon_{zz} = \frac{1}{3}\frac{(1+\nu)}{(1-\nu)}\sum_A n^{(A)}\Omega_r^{(A)} \tag{3.6}$$

where ϵ_{zz} is the measured out-of-plane strain, $\nu = 0.3$ is the Poisson ratio (for pure Fe [449]), $n^{(A)}$ and $\Omega_r^{(A)}$ are respectively the number density and relative relaxation volume for each type of defect (A).

In FeCr, both $\langle 111\rangle$ and $\langle 100\rangle$ dislocation loops are observed and their relative proportions depend on the Cr content [59, 109]. The relative relaxation volume of a single self-interstitial defect (1 atom) in a $\langle 111\rangle$ configuration is $\Omega_r^{\langle 111\rangle} = 1.65$ and that of a $\langle 100\rangle$ interstitial defect is $\Omega_r^{\langle 100\rangle} = 1.86$ [179]. These values correspond to isolated defects, not defects in clusters. We assumed that there is no clustering of interstitials, which is reasonable as we are examining low levels of dose, where large dislocation networks have not yet been formed [148]. If we were to account for the decrease in relaxation volume, per point defect, due to the clustering of interstitials [450], our estimated equivalent point defect density would increase.

We will consider both the case of all interstitials being of $\langle 111\rangle$ nature, and the case of all $\langle 100\rangle$ interstitials. This will give the range of interstitial densities in the present FeCr samples. Furthermore, we need to consider the lattice strain due to the presence of vacancy defects, which have a relative relaxation volume of Ω_r^v = -0.22 [179]. At room temperature, vacancies are almost immobile and do not cluster [44]. The relaxation volume of a Frenkel pair can be taken as the sum of an interstitial

and a vacancy [450]. We also assume that no interstitials have been lost from the sample and that the number of interstitial atoms to be the same as the number of vacancies ($n^i = n^v$), which is the number of equivalent Frenkel pairs.

From the measured strains at 0.3 dpa of dose-at-depth, the volumetric number density of equivalent Frenkel pairs is $(3.2 - 5.4) \times 10^{25}$ m^{-3}. The lowest density is observed in Fe3Cr, assuming all interstitial defects are of $\langle 100 \rangle$ in nature, and the highest is in Fe5Cr, assuming all interstitial defects are of $\langle 111 \rangle$ in nature. For 0.03 dpa of dose-at-depth, the corresponding volumetric number density of equivalent Frenkel pairs is between $(2.3 - 4.3) \times 10^{25}$ m^{-3}. Note that these estimates provide a lower bound on the number of equivalent Frenkel pairs present in the irradiated material. We did not account for the reduction in relaxation volume per point defect (Ω_r) if interstitials existed in clusters. In the case of defect clustering, to produce the same strain from dislocation networks as isolated defects, a higher equivalent Frenkel pair number density would be required. Similarly, in assuming no loss of interstitials, which provide the positive contributions to the lattice strain, we have estimated the minimum number of equivalent Frenkel pairs required to produce the measured strain. Further details of this calculation, and of the TEM comparisons to follow, can be found in Appendix B.6.

Previous TEM studies of FeCr found an areal defect density of around 1×10^{15} m^{-2} at 0.3 dpa [109]. The average diameter of the loops observed was 2 nm from measurements made in weak-beam dark field conditions with $\mathbf{g} = \{110\}$. The thickness of the damaged layer was 19 nm, from irradiation with 100 keV Fe^+ ions, as determined by SRIM calculations [109]. We assume that all imaged loops are of interstitial nature. This can be justified as vacancies have low mobility and do not cluster significantly at room temperature. In making this assumption, the following estimates provide an upper bound on the equivalent Frenkel pair density observed in TEM.

Consider for BCC Fe, the lattice parameter is $a_0 = 0.287$ nm, the (111) and (100) planar densities are respectively $\sim$7 atoms·nm^{-2} and $\sim$12 atoms·nm^{-2}. Again, we consider the two extreme cases of all $\langle 111 \rangle$ loops and all $\langle 100 \rangle$ loops to obtain a range of the possible interstitial densities. We also account for the loops that are

invisible when $\mathbf{g} \cdot \mathbf{b} = 0$, which includes $\frac{1}{2}$ of the $\langle 111 \rangle$ loops and $\frac{1}{3}$ of the $\langle 100 \rangle$ loops. This gives the volumetric number density of interstitial atoms, and hence equivalent Frenkel pairs, to be between $(2.3 - 3.0) \times 10^{24}$ m^{-3}. This value is an order of magnitude lower than the densities obtained from our lattice strain measurements.

At lower doses, we can compare with TEM measurements from a study with dose level of 0.05 dpa on FeCr which found defect densities of up to 1×10^{23} m^{-3} [59]. The authors of that study have already corrected for the cases of $\mathbf{g} \cdot \mathbf{b} = 0$. In the irradiated Fe5Cr and Fe10Cr (which are the same materials as this study), the reported average defect size is 1.1 nm. Using similar calculations as above, this gives the number density of interstitial atoms, and hence equivalent Frenkel pairs, to be $(6.7 - 11.4) \times 10^{23}$ m^{-3}. This point defect density obtained from TEM measurements is over an order of magnitude lower than the values estimated from our lattice strain measurements.

The discrepancy in defect densities between TEM and lattice strain measurements may be partially accounted for by the loss of defect loops to the surface of TEM samples. Another factor to consider is contributions from defects below the sensitivity limit of TEM [188]. One point that supports this is that in TEM measurements, the density of defects increases as $(\text{dpa})^n$ with $1 \leq n \leq 2$ [109], whereas the defect density calculated from strain measurements is proportional to the natural logarithm of dose. This suggests that TEM measurements could be underestimating the defect density particularly at lower dose levels where the defects are smaller. *Ab initio* calculations have shown that for small clusters of fewer than 51 self-interstitial atoms in Fe, C15-Laves phase clusters [451] are the most stable configuration but their size ($\sim$1.5 nm diameter) is not accessible to TEM [139]. The presence of these clusters would still impart measurable strain to the material [140] contributing to the discrepancy between the measured strain from this work and the defect density measured in TEM. The measurement of lattice strain from dose levels below 0.01 dpa shows that the 'threshold dose' derived from TEM studies [109, 137, 138] likely results from the lack of visibility of small defects in TEM rather than an inherent 'threshold' for damage formation. This is also supported by more recent research [59] which revealed that the dislocation loops are visible in TEM at 0.0015 dpa for Fe5Cr, Fe10Cr (both are

the same material as used in this study), Fe14Cr and pure Fe. Correlation between lattice strain and defect contrast in TEM offer a promising way forward for fully describing the irradiation-induced defect population at low dose levels.

3.4.4 Comparing Trends

The measurements of hardness, thermal diffusivity and lattice strain in this study were conducted on the same set of samples. However, different material properties resulting from the same damage microstructure exhibit different sensitivity to Cr content and irradiation dose. All three material properties show that the amount of Cr in the material has a significant effect on the response of the material to irradiation. Fe5Cr and Fe10Cr samples exhibit more change in hardening, thermal diffusivity and rate of lattice strain increase after irradiation than their Fe3Cr counterpart. This is attributed to the role of Cr in reducing defect mobility and thus enhancing total defect retention in the material, which has previously been observed in TEM measurements [109, 113].

The absolute values of hardness and thermal diffusivity at each dose level vary monotonically with Cr content, however, the absolute value of lattice strain is the greatest for Fe5Cr regardless of dose level. This non-monotonic variation in the lattice strain with Cr content could be due to the influence of Cr on the retention of each type of defect (interstitial vs. vacancy). Lattice strain is the result of the net contributions of position relaxation volume from interstitial defects and negative relaxation volume from vacancies. As such, it is sensitive to the population of different defect types, as well as extended defect structures [183], rather than the total defect population [148].

Irradiation hardening and lattice strain are both very sensitive to the presence of irradiation damage in the material. The effect of irradiation dose as low as 0.008 dpa can clearly be quantified in both these properties. The changes are very significant after 0.08 dpa of nominal dose, with Fe5Cr and Fe10Cr exhibiting over 46% increase in hardness and lattice strain of up to 5×10^{-4}. This shows that the presence of the irradiation-induced defects plays a large role in the changes of these properties. Since defect retention is increased by the presence of Cr atoms, which

in itself also affects hardness and lattice strain, these material properties are hence sensitive to both Cr content and dose levels.

In contrast, the decrease in thermal diffusivity of FeCr can only be measured after 0.08 dpa of dose, and even then, the changes are quite small (∼8% for Fe5Cr and Fe10Cr). The change to thermal diffusivity is dominated by the Cr content in the material, as the Cr atoms, as well as the defects, act as electron scattering sites. The lowest order scattering rate, in the dilute limit, of a Frenkel pair in Fe is 19 fs^{-1} (calculations included in Appendix B.5), which is much higher than that of a Cr atom at 2.9 fs^{-1}. However, since Cr atoms are also present in much higher concentration than the defects, this likely explains the greater role of Cr content than dose level on thermal diffusivity degradation.

Due to the different dependence of each material property on Cr content and irradiation dose, changes in different properties may not be necessarily directly correlated with each other. For hardness, hardening due to irradiation defects, dependent on dose level, appear to have a greater effect than solid solution hardening from Cr content. The hardening due to the presence of an irradiation defect is higher compared to the presence of a Cr atom. Whereas for thermal diffusivity, the changes are more governed by the level of Cr content compared to irradiation up to 0.08 dpa. It is likely that in the dilute limit of low irradiation level and Cr content, changes to thermal diffusivity are more dependent on the concentration of electron scatterers. In this case, there is a greater concentration of Cr atoms compared to irradiation defects, and hence thermal diffusivity is more affected by Cr concentration. Although Cr content and irradiation dose, individually and synergistically, cause changes to material properties, the specific trends for each property are expected to have different dependence on each parameter.

3.5 Conclusion

We have studied Fe3Cr, Fe5Cr and Fe10Cr implanted with 20 MeV Fe^{3+} ions to nominal dose levels of 0.008 dpa and 0.08 dpa at room temperature. The hardness, thermal conductivity and lattice strain were probed with nanoindentation, transient

grating spectroscopy and X-ray micro-beam Laue diffraction respectively. From these findings, we conclude the following:

- All irradiated samples exhibit hardening with measurable changes observed at nominal dose level as low as 0.008 dpa.
- Fe5Cr and Fe10Cr samples show greater irradiation hardening at each nominal dose level than Fe3Cr. This is attributed to higher defect retention induced by increasing Cr content. The shape of the hardness vs. indentation depth curves qualitatively agrees with an existing plastic zone model.
- Thermal diffusivity of the materials could be successfully measured by TGS. The values from unirradiated Fe3Cr and Fe5Cr agree with a kinetic theory model that attributes the degradation in thermal diffusivity to Cr atoms acting as electron scattering sites.
- The thermal diffusivity of Fe5Cr and Fe10Cr show an 8% reduction after 0.08 dpa of nominal dose, while Fe3Cr samples exhibit negligible change after irradiation. After irradiation to 0.008 dpa, Fe3Cr and Fe10Cr show small increases in thermal diffusivity. The reduction of thermal diffusivity after 0.08 dpa is probably due to Cr atoms causing a greater retention of irradiation-induced defects, which also act as electron scattering sites. Overall the changes in thermal diffusivity as a function of irradiation damage dose are small.
- Measurable strain is observed for dose-at-depth levels below 0.008 dpa, and lattice strain of over 5×10^{-4} is measured in FeCr at a dose level of 0.3 dpa in dose-at-depth. Although lattice strain show different dependence on Cr content between irradiation to 0.008 and 0.08 dpa, the rate of increase in lattice strain is higher for greater Cr content. This is again attributed to greater defect retention due to Cr atoms.
- The lower bound of defect density in the irradiated FeCr, calculated from the measured strain, is higher than that previously observed in TEM studies of corresponding dose levels. This indicates that both lattice strain and TEM

measurements are crucial to fully characterise the irradiation-induced defect population at low doses.

Data Availability

All data, raw and processed, as well as the processing and plotting scripts used in this study are available online at: https://doi.org/10.5287/bodleian:xvNyeYP0z

4

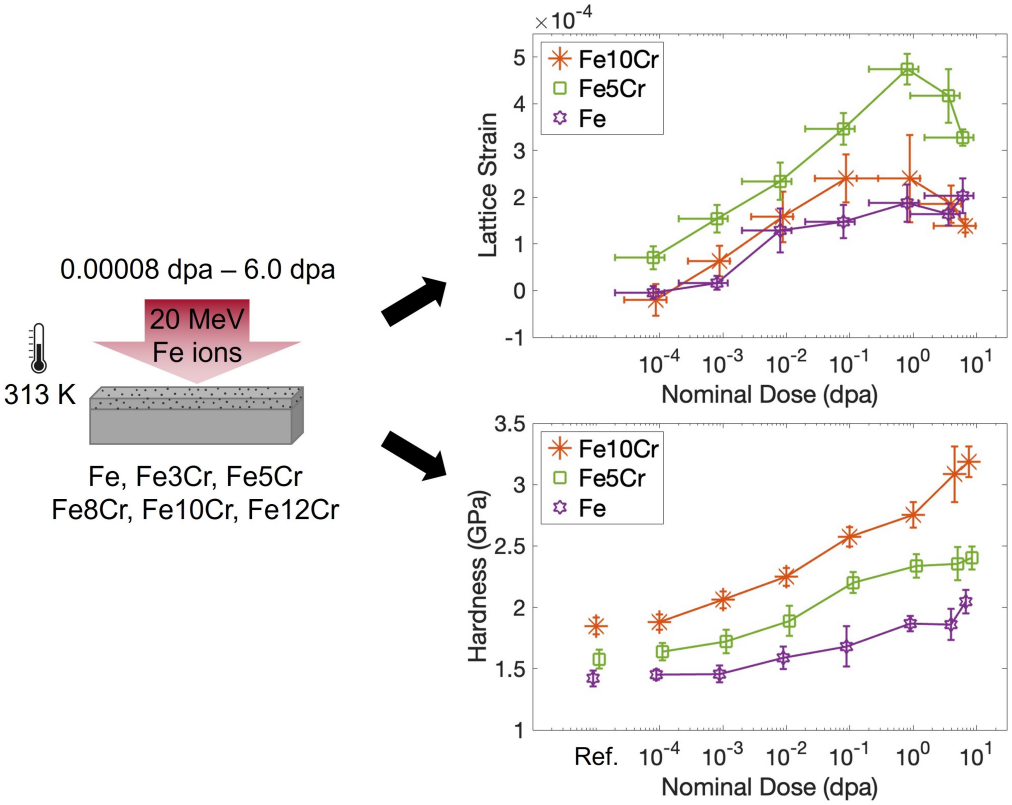
Dose and Compositional Dependence of Irradiation-Induced Property Change in FeCr

This chapter presents a study that extends the investigation detail in Chapter 3, covering a greater range of dose levels and Cr content. A key question following the previous results is how lattice strain evolves at low and high irradiation doses. In particular, atomistic simulations predicted that lattice strain in Fe initially increases with dose, then decreases and finally settles at zero for high doses (>1 dpa) [148]. Until this study, this phenomenon has not been studied experimentally in FeCr and the effect of Cr content is also not well-understood. Furthermore, the trends for irradiation hardening are not well-studied for room-temperature ion-irradiated FeCr with different Cr content and irradiation dose. This study aims to address those questions, and also adopt the approach of Chapter 3 of comparing different trends to obtain insight into defect population and evolution.

The contents of this chapter have been published as: K. Song, D. Sheyfer, K. Mizohata, M. Zhang, W. Liu, D. Gürsoy, D. Yang, I. Tolkachev, H. Yu, D. E. J. Armstrong, F. Hofmann, "Dose and compositional dependence of irradiation-induced property change in FeCr", *Journal of Nuclear Materials*, vol. 594, 154998, 2024 [452]. D. Sheyfer, W. Liu, D. Yang, and I. Tolkachev assisted with the collection of DAXM data. D. Gürsoy analysed the DAXM data for the two samples collected with the

coded aperture technique. K. Mizohata provided assistance with ion irradiation and helped with the design of the temperature-controlled sample holder (further detailed in Appendix A). M. Zhang collected the APT data. H. Yu assisted with sample polishing. The remainder of the work was carried out by the author with the supervision of D. E. J. Armstrong and F. Hofmann.

4.1 Abstract



Graphical Abstract

Ferritic/martensitic steels will be used as structural components in next generation nuclear reactors. Their successful operation relies on an understanding of irradiation-induced defect behaviour in the material. In this study, Fe and FeCr alloys (3-12%Cr) were irradiated with 20 MeV Fe ions at 313 K to doses ranging between 0.00008 dpa to 6.0 dpa. This dose range covers six orders of magnitude, spanning low, transition and high dose regimes. Lattice strain and hardening in the irradiated materials were characterised with micro-beam Laue X-ray diffraction and nanoindentation, respectively.

Irradiation hardening was observed even at very low doses (0.00008 dpa) and showed a monotonic increase with dose up to 6.0 dpa. Lattice strain measurements of samples at 0.0008 dpa allow the calculation of equivalent Frenkel pair densities and corrections to the Norgett-Robinson-Torrens (NRT) model for Fe and FeCr alloys at low dose. NRT efficiency for FeCr is 0.2, which agrees with literature values for high irradiation energy. Lattice strain increases up to 0.8 dpa and then decreases when the damage dose is further increased. The strains measured in this study are lower and peak at a larger dose than predicted by atomistic simulations. This difference can be explained by taking temperature and impurities into account.

4.2 Introduction

Reduced-activation ferritic/martensitic (RAFM) steels are leading candidate materials for structural components of fusion reactors, particularly for blanket/first-wall components [166]. They possess superior resistance to radiation-induced swelling and better thermal properties than austenitic stainless steels [16].

To better understand the effect of irradiation on the microstructure and material properties of RAFM steels, iron-chromium (FeCr) binary alloys have often been studied as a model system [28, 61, 73, 165, 167, 210]. The FeCr system can provide a mechanistic understanding of irradiation damage in ferritic/martensitic steels while removing many microstructural complexities. Consequently, it becomes more feasible to compare experimental and simulation data [50].

A significant challenge in fully understanding the effects of nuclear fusion operations on structural steels is the lack of an existing fusion power plant facility. While certain aspects of irradiation can be replicated with fission neutrons [17, 45, 453] and ion irradiation [88, 424, 454], it is costly and time-intensive to reproduce the full range of conditions expected for structural materials in a nuclear fusion power plant. This necessitates the development of reliable simulation models ranging from first principles atomistic simulations to simulations that capture evolution and degradation at the component scale [50, 56, 133, 455].

Comparison to experimental data is crucial for the validation and optimisation of these models. However, several key gaps exist in the literature on FeCr regarding experimental studies:

1. Low-temperature (<573 K) irradiation effects: The majority of experiments have been performed in the 623-773 K temperature window expected in-service for most of the structural components [20]. Hardening following ion-irradiation has been observed at these temperatures, reaching saturation around 1–2 dpa, particularly for Cr content greater than 5% [98, 210]. It is interesting to note that most of the data in the literature regarding hardening following neutron irradiation indicate hardness saturation beyond 5–10 dpa [20]. This could be a result of different dose rates and primary knock-on atom energy spectra between neutron- and ion-irradiation [92]. Extensive transmission electron microscopy (TEM) observations have revealed the presence of $a\langle 100\rangle$ and $\frac{a}{2}\langle 111\rangle$ dislocation loops, with the former more dominant at temperatures closer to 773 K and the latter prevailing at 573 K or below [112]. At high temperatures, the stability of dislocation loops is reduced [456] and dislocation microstructures also undergo coarsening, both of which affect their distribution and density [457].

   However, the effects of irradiation at low temperatures have not been extensively studied. Low temperatures are also of operational significance as reactor cooling components are expected to operate below 573 K [458]. Experimental data is required from irradiation in this temperature range, particularly at room temperature, in order to study and model the athermal effects of defect population and behaviour at lower temperatures.

2. An extensive range of irradiation levels: Reactor components in operation are expected to sustain irradiation exposure up to ∼100 dpa [169, 453]. Volumetric swelling, caused by the formation of voids at high doses (>1 dpa) and elevated temperatures (>673 K), has been extensively investigated for Fe and FeCr-based alloys [65, 173]. At low doses (< 0.1 dpa), volumetric swelling has been demonstrated to originate from the lattice strain of point defects [148]. The issue for reactor components is that even at low dose, lattice swelling can cause

large stresses on the order of hundreds of MPa [175, 176] and their non-uniform distribution due to irradiation will lead to macroscopic deformation. In FeCr, lattice strains are strongly dose- and composition-dependent [422], but the parameter space explored thus far is limited.

Studying material property changes at low doses ($\ll$1 dpa) is important for several reasons. Firstly, many irradiation-induced changes reach saturation at a certain dose [105, 183, 210]. Determining the dose threshold for saturation is important. Secondly, certain modelling techniques, such as *ab initio* and molecular dynamics [56], face limitations when trying to simulate a large range of exposures due to constraints in computational resources. Therefore, the availability of experimental results obtained at a range of, including very low, doses for comparison is needed. Thirdly, the distribution of defects and material property changes in a real-life reactor component will not be homogeneous. Predicting how these distribution gradients will affect material performance requires knowledge of material property changes across a wide range of dose levels. Finally, the damage microstructure of materials has been found to depend on pre-existing damage [134, 135]. As such, knowledge of the damage accumulation history and effects at lower doses is crucial.

3. The synergistic effect of dose and composition: Though there are many studies of irradiation-induced effects in FeCr that explore a range of sample conditions [20, 61, 166, 459], the parameter space covered in each individual study (e.g. dose level, compositional variation, temperature, irradiating ion species) is generally limited [61, 63]. For example, the nanoindentation work of Heintz *et al.* [98] only covers 2 doses (1 and 10 dpa) for Cr content ranging from 2.5% to 12.5% following ion irradiation at room temperature. For room-temperature irradiation, only a dose of 1 dpa was investigated. There is of course a trade-off between examining specific phenomena in detail versus covering a broader parameter space. However, identifying synergistic effects, as well as broader parameter space effects, from comparing different studies is difficult due to

variations in sample history and irradiation conditions. Hence, large systematic studies are needed.

To address these aforementioned gaps in literature, it is important to also consider which irradiation effects to focus on. TEM is one of the most common methods of studying irradiation-induced defect structures and populations [109, 112, 113]. TEM has provided many key insights on defect density, size distribution, and defect type. However, the lack of sensitivity of TEM to small defects (<1 nm) [189] makes it incomplete for the study of the full defect population, particularly at low doses where a majority of defects are below the detection threshold [110]. Positron annihilation spectroscopy revealed a 2 order of magnitude discrepancy in defect cluster density compared to TEM measurements at doses as low as 10^{-3} dpa [129]. Measurements of material properties such as thermal diffusivity [337] and lattice strain [422] have also revealed key insights into defect populations, while also showing significant discrepancies in defect density estimates compared to TEM studies at the same dose. The study of irradiation-induced changes in the mechanical properties of steels has also been useful to understand the effect of the damage microstructure [54, 207]. Therefore, lattice strain and hardness characterisation have been chosen for this study to obtain a broader understanding of defect populations in FeCr. Furthermore, key mechanistic insight can also be revealed by comparing and contrasting the evolution of different material properties.

In this study, we present the characterisation of lattice strain and hardness changes induced by Fe-ion irradiation of Fe and FeCr alloys. We examine a range of doses from 0.00008 dpa to 6 dpa, spanning six orders of magnitude, for six compositions of FeCr binary alloys ($0 \leq$ Cr% ≤ 12). We discuss key insights of defect production and retention rate, comparing with the commonly-used Norgett-Robinson-Torrens (NRT) model and microscopy results from the literature. The effect of dose and Cr concentration on defect mobility and clustering is explored by comparing experimental trends of hardness and lattice strain, as well as with simulations.

4.3 Materials and Methods

4.3.1 Sample Preparation and Ion Implantation

The high-purity FeCr alloy materials used in this investigation were manufactured under the European Fusion Development Agreement (EFDA) programme (contract no. EFDA-06-1901). The chemical compositions and mean grain sizes of the as-delivered alloys are listed in Table 4.1.

Alloy	Cr (wt %)	C (wppm)	S (wppm)	O (wppm)	N (wppm)	Mean grain size (µm)
Fe	<0.0002	4	2	4	1	187 ± 150
Fe3Cr	3.05	4	3	6	2	160 ± 114
Fe5Cr	5.40	4	3	6	2	112 ± 60
Fe8Cr	7.88	6	2	10	2	86 ± 63
Fe10Cr	10.10	4	4	4	3	98 ± 55
Fe12Cr	11.63	6	2	4	<10	281 ± 250

Table 4.1: The chemical compositions of the FeCr alloys used in this study as measured by the manufacturer using glow discharge mass spectrometry [66, 67]. The mean grain size was determined from EBSD measurements, with ± 1 standard deviation shown here (see Appendix C.1).

The alloys were produced by induction melting under an argon atmosphere, followed by hot-forging at 1273 K for Fe and 1423 K for all other compositions. The bars were subsequently cold-forged with a reduction ratio of 70%. Heat treatment of 1 hour was conducted at 973 K for Fe, 1023 K for Fe3Cr, Fe5Cr, and Fe8Cr, 1073 K for Fe10Cr, and 1123 K for Fe12Cr. The recrystallised materials were then air-cooled [66, 67]. Surprisingly, for Fe8Cr, our electron backscatter diffraction (EBSD) characterisation of the materials revealed significant signs of cold work (intragranular misorientation) in the microstructure of the materials, unlike the other compositions (Appendix C.1). In addition, the measured average grain size of 86 ± 63 µm differs noticeably from the manufacturer-quoted value of 320 µm [67]. As

such, we suspect that the Fe8Cr raw material may not have been fully heat treated to the conditions reported by the manufacturer.

The as-delivered samples were sectioned with a fast diamond saw into pieces of approximately 5 × 5 × 0.7 mm^3 in size. The polishing process consisted of mechanical grinding with SiC paper, followed by polishing with diamond suspension and colloidal silica. Finally, the samples were electropolished with 5% perchloric acid in ethanol, with 15% ethylene glycol monobutyl ether, at 293 K for 2–3 minutes using a Struers LectroPol-5. The voltage applied during electropolishing was 45 V for Fe and Fe3Cr, 35 V for Fe5Cr and Fe8Cr, and 30 V for Fe10Cr and Fe12Cr.

An energy of 20 MeV was chosen for Fe-ion irradiation, as this produced a damage layer of 3.5 µm thickness, allowing characterisation with X-ray diffraction and nanoindentation. Depth profiles of the damage and injected ion distribution (Figure 4.1) were calculated with SRIM using the Quick K-P model [80] with 20 MeV Fe ions on a Fe target with 40 eV displacement energy [460] at normal incidence. The dpa profile was calculated using the vacancy.txt method described in [70, 461]. In this study, the nominal dose of an irradiation profile refers to the average damage dose in the first 2 µm of the sample, where the damage profile is relatively flat and the injected ion concentration is still low.

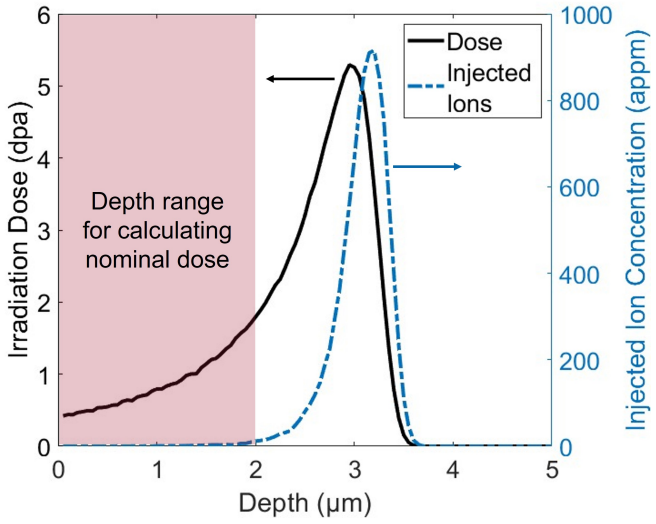


Figure 4.1: The calculated dose and injected ion profile from SRIM for 20 MeV Fe-ion irradiation on Fe target. The profile shown corresponds to a nominal dose of 0.8 dpa (average of the first 2 µm of the dose profile). It is assumed the total profile of the dose and injected ions scale linearly with irradiation ion fluence.

Ion implantation was performed at room temperature with Fe^{4+} ions using the tandem accelerator at the Helsinki Accelerator Laboratory. The vacuum level inside the irradiation chamber was maintained at 8×10^{-7} mbar. The irradiation conditions are listed in Table 4.2. For each sample composition, up to 7 different nominal dose levels were produced (0.00008 dpa, 0.0008 dpa, 0.008 dpa, 0.08 dpa, 0.8 dpa, 3.6 dpa, and 6.0 dpa). An unirradiated reference sample was also retained for each composition. To enhance readability, we will use scientific notation labelling for the lowest 4 doses in this study. 0.8 is used as the coefficient (e.g. 0.00008 dpa is written as 0.8E-4 dpa) to align the exponents in the notation with the exponents of the figures presented throughout the study.

A custom-built holder was designed for the irradiation process that allowed active temperature control using a combination of liquid nitrogen cooling and a cartridge heater. The samples were mounted on an aluminium block, and a thermocouple was positioned within 10 mm of the samples to monitor the temperature. For the irradiations in this investigation, the temperature was held constant at 313 K. Due to the spatial constraints of the sample holder, the samples had to be irradiated in two separate groups (Fe/Fe3Cr/Fe5Cr and Fe8Cr/Fe10Cr/Fe12Cr). The exception was for the 6.0 dpa irradiation where only Fe, Fe5Cr, Fe10Cr, and Fe12Cr were irradiated simultaneously due to time constraints.

4.3.2 Micro-beam X-ray Laue Diffraction

Lattice strain, i.e. change in the atomic plane-spacing of the crystal, caused by the irradiation was measured using micro-beam X-ray Laue diffraction at the 34-ID-E beamline, Advanced Photon Source (Argonne National Laboratory, IL, USA). Depth-resolution in the sample measurements was obtained using Differential Aperture X-ray Microscopy (DAXM), which has been described in detail elsewhere [177, 374, 375]. Briefly, the sample is mounted in 45° reflective geometry. An area detector (Perkin-Elmer, #XRD 1621, pixel size 200 × 200 µm^2) positioned above the sample records the Laue diffraction patterns. The key component of this technique is a platinum wire (∼100 µm in diameter, mounted on a silicon monocrystal) that is oriented perpendicular to the beam direction, and scanned parallel to the surface

Dose name	Nominal dose (dpa)	Total fluence (ions/cm^2)	Nominal dose rate (dpa/s)	Flux (ions/cm^2/s)	Irradiation time (hh:mm:ss)
0.8E-4	0.00008	5.30×10^{11}	3.54×10^{-6}	2.34×10^{10}	00:00:17
0.8E-3	0.0008	5.30×10^{12}	3.54×10^{-6}	2.34×10^{10}	00:03:12
0.8E-2	0.008	5.30×10^{13}	4.65×10^{-5}	3.08×10^{11}	00:02:51
0.8E-1	0.08	5.30×10^{14}	5.31×10^{-5}	3.52×10^{11}	00:25:06
0.8	0.8	5.30×10^{15}	2.78×10^{-5}	1.8×10^{11}	08:09:27
3.6	3.6	2.39×10^{16}	4.61×10^{-5}	3.05×10^{11}	21:42:00
6.0	6.0	3.98×10^{16}	4.50×10^{-5}	2.98×10^{11}	37:00:16

Table 4.2: Irradiation conditions for this study. The nominal dose is calculated from the average of the dose profile in the top 2 µm below the surface, as shown in Figure 4.1. The convention described for the dose name will be used for the rest of this paper.

of the sample through the diffracted beams. By comparing the intensity of each detector pixel as the wire is moved along consecutive positions, and triangulating using the position of the incident beam and the wire edge, a profile of intensity as a function of sample depth can be obtained for the whole detector. This enables the reconstruction of diffraction patterns as a function of depth into the sample along the beam path (i.e. at 45° to the sample surface). By also scanning the incident X-ray beam energy, a Bragg peak can be fully measured in 3D reciprocal space and as a function of depth into the sample. Note that for the subsequent analysis presented in this study, all profiles have been converted into a function of depth perpendicular to the sample surface.

The X-ray beam size at the sample surface was 190 × 360 nm^2, and the estimated depth resolution was ∼1 µm. For each sample, a minimum of 3 points were measured on grains within 10° of ⟨001⟩ out-of-plane orientation, identified in advance with EBSD. The energy of the monochromatic beam was chosen to match that of a $\{00n\}$ reflection in the range of 11 to 16 keV. This ensured that the dominant source of the diffraction signal is from the top 5 µm of the sample where the irradiated layer lies. For each measurement, an energy range of ∼40 eV was scanned to fully

capture the diffraction peak in 3D reciprocal space. An energy step size of 1 eV was used for all samples except for the lowest dose irradiation, where a 0.5 eV step size was used. It should be noted that measuring only the reflection closest to the normal orientation of the grain gives the out-of-plane strain, not the full strain tensor. Previous DAXM measurements on ion-irradiated W showed that the in-plane strains are small compared to the out-of-plane strain [176, 177]. This is due to the constraint imposed by the unimplanted material beneath the irradiated layer.

Two of the data points were further studied in a similar method, but depth-resolution of the diffraction signal was achieved using a coded aperture instead of a platinum wire. Specifically these measurements were performed for Fe8Cr 0.8E-4 dpa and Fe8Cr 3.6 dpa samples. Further details of the coded aperture technique can be found elsewhere [462, 463].

4.3.3 Nanoindentation

The hardness of the implanted layer was measured by nanoindentation using an MTS Nano Indenter XP with a diamond Berkovich tip (Synton-MDP). The tip area calibration was performed on fused silica (elastic modulus of 72 GPa). Indents of 2 µm deep were performed using continuous stiffness measurement (CSM) mode [385], with a strain rate of 0.05 s^{-1}, a CSM frequency of 45 Hz, and a harmonic amplitude of 2 nm. At least 35 indents, spaced at a minimum distance of 50 µm apart, were carried out across a minimum of 10 grains on each sample.

The representative hardness values were analysed in two ways. The first by taking the average hardness from CSM between indentation depths of 300–600 nm for all samples. This depth range was chosen to largely avoid indentation size effects (ISE) at shallower depths and contribution from the softer unirradiated bulk at greater depths.

The second method considers the Nix-Gao model, which accounts for the contribution of geometrically necessary dislocations to correct for ISE [392]. The depth-dependence of hardness is described by:

$$\frac{H}{H_0} = \sqrt{1 + \frac{h^*}{h}} \tag{4.1}$$

where H is the measured hardness at indentation depth h, H_0 is the bulk equivalent hardness at infinite depth, and h^* is a characteristic ISE length scale that depends on the indenter shape and material hardness. This method has been previously applied to ion-irradiated ferritic alloys by limiting the indentation depth range over which the analysis is carried out to avoid contributions from the plastic zone extended into the unirradiated bulk [435, 464–466]. For this study, the range of indentation depth for analysis is 100–600 nm. This minimises the effect of tip blunting and surface roughness at shallow indentation depths, and avoids the bulk unirradiated material contribution. We note that for the unirradiated sample, the indentation depth range for analysis is 100–2000 nm, making use of the full depth range.

4.4 Results

4.4.1 Irradiation-Induced Lattice Strain

Extracting Strain From Diffraction Data

Figure 4.2(a) and (d) show the measured integrated intensity for the (004) peak at 0.8 dpa in the Fe and Fe10Cr samples, respectively. The intensity is plotted as a function of the scattering vector magnitude $Q = |\boldsymbol{Q}|$ and of the reconstructed depth into the surface. The depth-reconstruction and integration procedure was performed with LaueGo [378]. The distribution of Q changes as a function of depth (Figure 4.2(b) and (e)), with the distribution in the first 6 µm shifting towards lower Q values compared to those measured from 7 µm and deeper. From Figure 4.1, the predicted range of displacement damage and injected ions only extend to 3.5 µm below the surface. Therefore, the distribution of Q at depths much greater than this can be attributed to the undamaged material in each sample, conveniently serving as a built-in strain-free reference.

For each depth, a single Gaussian function was fitted to the intensity distribution in Q, and the centre of the distribution (Q_c) was extracted. An intensity-weighted average of Q_c from depths 7 to 12 µm was used as the strain-free reference Q_0 of each sample. The lattice strain ϵ at each depth was calculated using the expression:

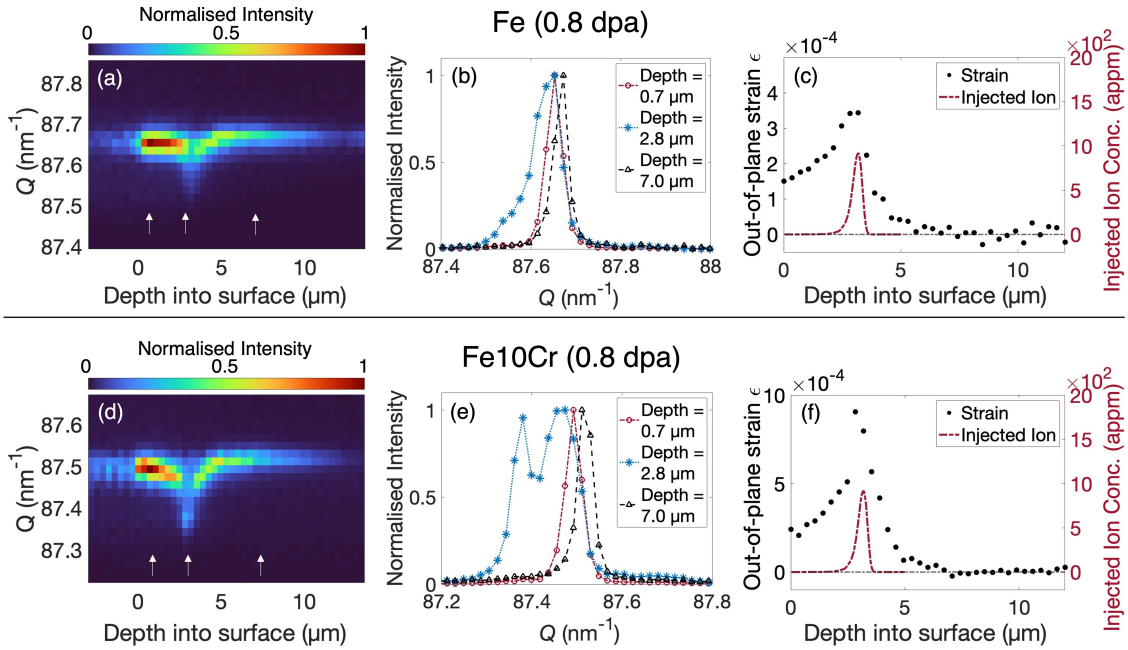


Figure 4.2: The integrated intensity plotted as a function of the magnitude of the scattering vector, Q, and depth perpendicular to the surface of the sample for (a) Fe at 0.8 dpa and (d) Fe10Cr at 0.8 dpa. (b)&(e) Intensity vs. Q for different depths into the sample (indicated by white arrows in (a) and (d)). The measured diffraction intensities shown here have been normalised to the point of highest intensity in each respective dataset. (c)&(f) The corresponding lattice strain in the sample as a function of depth into the surface. The dashed line showing zero strain is included for comparison, along with the profile of the injected ion depth distribution as calculated from SRIM.

$$\epsilon = \frac{Q_0 - Q_c}{Q_c}. \tag{4.2}$$

Performing this analysis for all depths yields the results shown in Figure 4.2(c) and (f), respectively, for Fe and Fe10Cr implanted to 0.8 dpa. These plots show that irradiation causes lattice strain changes down to 6 μm below the surface, which is significantly deeper than the damage layer thickness predicted by SRIM (Figure 4.1). The strain profile increases with depth, reaching a peak at 3–3.5 μm before decreasing to zero at a depths greater than 6 μm.

Interestingly, at depths corresponding to the peak injected ion concentration, the intensity vs. Q profile is not a single Gaussian distribution (depth between 2.8–3.2 μm in Figure 4.2(b) and (e)). An additional peak appears at lower Q, corresponding to lattice expansion. This is presumably a result of injected ions existing as interstitials in the material, which have a positive relaxation volume, leading to lattice swelling

[179]. The appearance of an additional Q peak is only observed for damage levels of 0.8 dpa or higher. Very clear splitting is observed for all FeCr alloys, while Fe samples only show a slight asymmetric peak broadening.

This study focuses on the lattice strain associated with the collision damage cascade formed during irradiation. As such, the subsequent analysis will focus on the measurements in the depth range of 0 to 2 µm, where the effect of the injected ions is negligible.

Strain as a Function of Dose

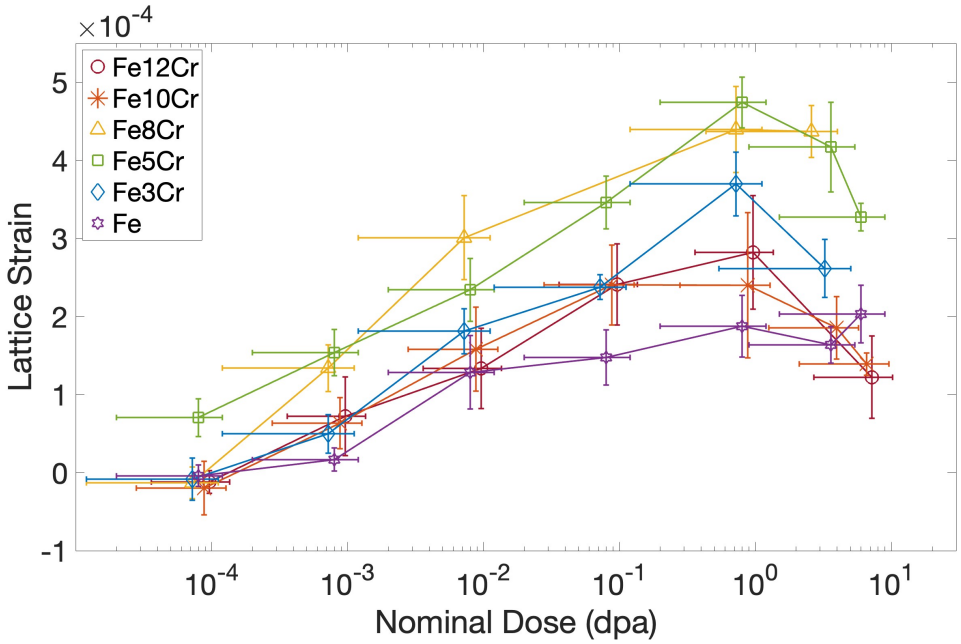


Figure 4.3: The average out-of-plane lattice strain in the top 2 µm of each sample plotted as a function of irradiation dose for all compositions. The vertical error bars represent the standard deviation in lattice strain across the 2 µm layer. The horizontal error bars represent the range of dose levels within the first 2 µm of the samples. Markers have been offset horizontally for clarity.

The lattice strain caused by the displacement damage, as opposed to the injected ions, was examined by analysing the average strains in the top 2 µm of the samples (Figure 4.3). The reported uncertainties in lattice strains are the standard deviation values across the top 2 µm of all measurements for each sample. The plotted error bars for dose represent the dose range in the top 2 µm of the irradiated samples. For all sample compositions, except Fe5Cr, no lattice strain is detected at 0.8E-4 dpa.

Lattice strain increases monotonically with dose from 0.8E-4 dpa to 0.8 dpa for all sample compositions. In the case of pure Fe, the strain does not change significantly as a function of dose beyond 0.8 dpa. However, for all FeCr alloys, there is a reduction in strain for doses greater than 0.8 dpa.

Positive lattice strain indicates lattice expansion associated with crystal defects that have a positive relaxation volume (Ω, in units of atomic volume). In BCC Fe, self-interstitials have a positive relaxation volume ($\Omega_{int} \sim 1.6 - 1.8$), while vacancies have a negative relaxation volume (Ω_{vac} = -0.220) [179]. Therefore, the net effect of a Frenkel pair is a positive relaxation volume. A reduction in lattice strain thus suggests that there is a removal of interstitial defects from the system with increasing irradiation dose, or a greater retention of vacancies than interstitials.

Strain as a Function of Cr

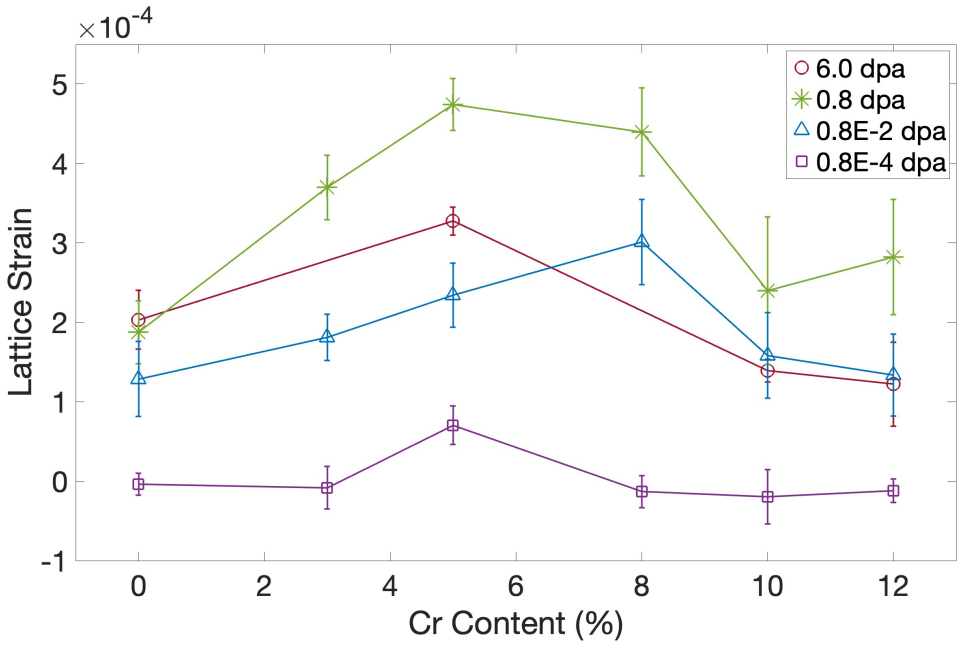


Figure 4.4: The average out-of-plane lattice strain in the top 2 µm of each sample as a function of Cr content for 0.8E-4 dpa, 0.8E-2 dpa, 0.8 dpa and 6.0 dpa. The vertical error bars represent the standard deviation in lattice strain in the 2 µm layer for all measurements taken for each particular composition and dose.

For all irradiation dose levels, a non-monotonic relationship between lattice strain and Cr content is observed (Figure 4.4). Pure Fe samples exhibit the lowest lattice strain level compared to FeCr samples at any given dose, except 6.0 dpa. Lattice

strain appears to be greatest for Fe5Cr and Fe8Cr at all measured doses. Fe10Cr and Fe12Cr generally show a similar amount of lattice strain at a given dose level.

Onset of Strain With Dose

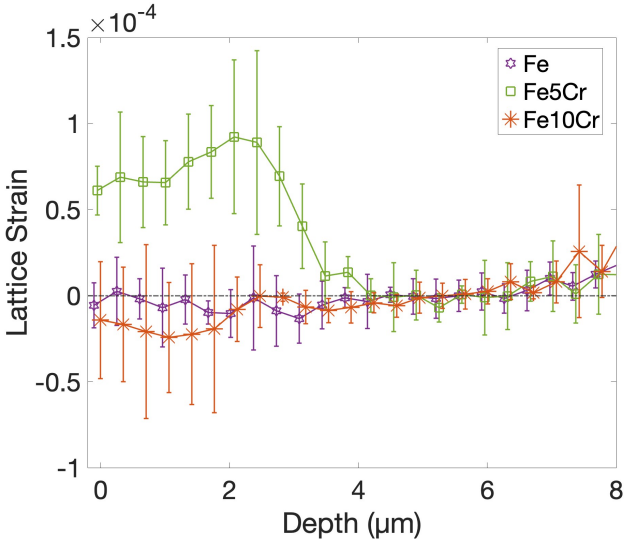


Figure 4.5: A comparison of the strain profile as a function of depth for Fe (purple), Fe5Cr (green), and Fe10Cr (orange) samples irradiated to 0.00008 dpa. The error bars represent ± 1 standard deviation from the measurements taken on each sample. Markers have been offset horizontally for clarity. A dashed line at zero strain is shown for reference.

At the lowest dose investigated for this study (0.8E-4 dpa), all samples except Fe5Cr show no statistically significant strain within any depth of the implanted layer (some representative examples are shown in Figure 4.5). There are some measurement points for Fe and Fe10Cr which appear to show negative strain. However, considering the size of the error bars, which represent ± 1 standard deviation from values across all measurements on each particular sample, these negative values are likely due to experimental uncertainty rather than an implantation effect.

Even though there are some fluctuations in the measurements and fitting of intensity vs. Q at these low dose levels, the Fe5Cr sample clearly exhibits positive strain in the first 4 μm (Figure 4.5). The strain profile peaks between depths of 2.5 μm to 3 μm, similar to profiles of samples implanted to higher doses (Figure 4.2(c) and (f)). This peak is likely due to the presence of injected Fe ions. From the measured strain level, a lower-bound estimate of the equivalent Frenkel pair density can be calculated (Appendix C.2). For the Fe5Cr sample at 0.8E-4 dpa, this value is

5.9×10^{24} m^{-3} within the first 2 µm below the surface. This corresponds to a defect retention efficiency of 87%, which is much higher than the expected 20–30% (further discussed in the subsequent section). This high defect retention is likely due to a combination of low irradiation temperature reducing recombination rates and the high interstitial defect retention of Fe5Cr. The detailed discussions of the possible mechanism for the latter factor are provided in Section 4.5.2.

Comparison to the NRT Model

The defect concentration predicted by the NRT model [76], which is used to calculate the dose in dpa, is a major overestimation, particularly at primary knock-on atom (PKA) energies much higher than the displacement energy of the material [72]. This is the case for the present study where the irradiation was performed with 20 MeV ions, while the displacement energy of Fe is only 40 eV. The 'NRT efficiency' is the ratio of the actual concentration of defects in the material, usually measured by electrical resistivity or calculated by molecular dynamics, to the NRT model predictions. From studies in the literature [72], the NRT efficiency of metals saturates at 0.2–0.3 at high PKA energy (>1 keV).

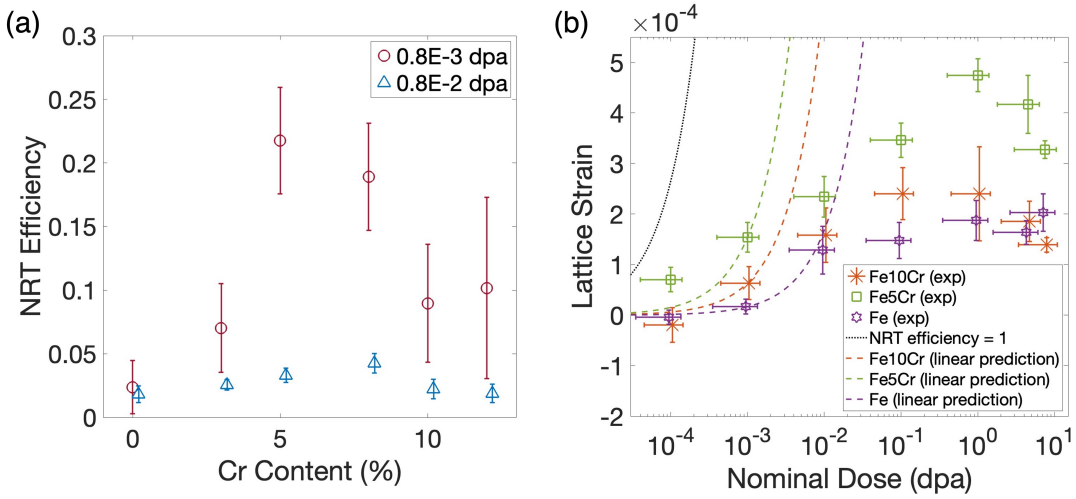


Figure 4.6: (a) The NRT efficiency as a function of Cr content for samples irradiated to 0.8E-3 dpa (red circles) and 0.8E-2 dpa (blue squares). (b) The measured lattice strain for Fe (purple), Fe5Cr (green) and Fe10Cr (orange) as a function of dose, compared to the predicted strain for a linear accumulation of isolated defects based on the NRT efficiency calculated at 0.8E-3 dpa (dashed lines of corresponding colours). The black dotted line shows the predicted strain profile in the case of 100% defect production and retention (i.e. NRT efficiency = 1).

By converting the measured lattice strain into a corresponding Frenkel pair density (Appendix C.2), the NRT efficiency in Fe and FeCr at 313 K can be calculated (Figure 4.6(a)). The lattice strain values at 0.8E-3 dpa and 0.8E-2 dpa were chosen for this calculation as all samples exhibit non-zero lattice strain at these doses. Uncertainties in the lattice strain measurements (from Figure 4.3) have been propagated forward when calculating defect densities and NRT efficiencies. Low irradiation doses were chosen because the NRT-dpa definition and the NRT efficiency are only applicable for non-overlapping cascades [467]. Furthermore at low dose, the effect of defect clustering can be minimised, which allows a more accurate conversion of strain to defect density. This is important as one of the key assumptions made in the defect density calculation is that all defects present in the samples are isolated Frenkel pairs (Appendix C.2).

The NRT efficiency is highest for Fe5Cr and Fe8Cr at both doses examined (Figure 4.6(a)), and the values fall within the expected range of 0.2–0.3 reported in the literature [72]. It is the lowest for pure Fe at ∼0.02.

There is a reduction in NRT efficiency for all FeCr samples from 0.8E-3 dpa to 0.8E-2 dpa. This suggests either a decrease in defect retention, or the occurrence of significant defect clustering or cascade overlap. Interestingly, this is not the case for pure Fe, which has the same NRT efficiency at both doses within measurement error.

By comparing to the theoretical strain from 100% defect production and retention (i.e. NRT efficiency = 1), it can be seen that our samples are in the regime where defect retention is much lower than predicted by the NRT model (Figure 4.6(b)). For all FeCr samples, defect accumulation deviates from linear behaviour from 0.8E-3 dpa onwards. For Fe, this deviation happens beyond 0.8E-2 dpa. This suggests the 'low dose' regime, before the onset of cascade overlap, ends between 0.001 to 0.01 dpa. This transition dose also depends on NRT efficiency, with a lower dose threshold for higher NRT efficiency material (such as Fe5Cr and Fe8Cr).

4.4.2 Hardness

Some solid solution hardening with the increase of Cr concentration is evident. From the constant-depth analysis (Figure 4.7(a)), hardness appears to increase linearly with Cr content. However, from the Nix-Gao model (Figure 4.7(b)), the

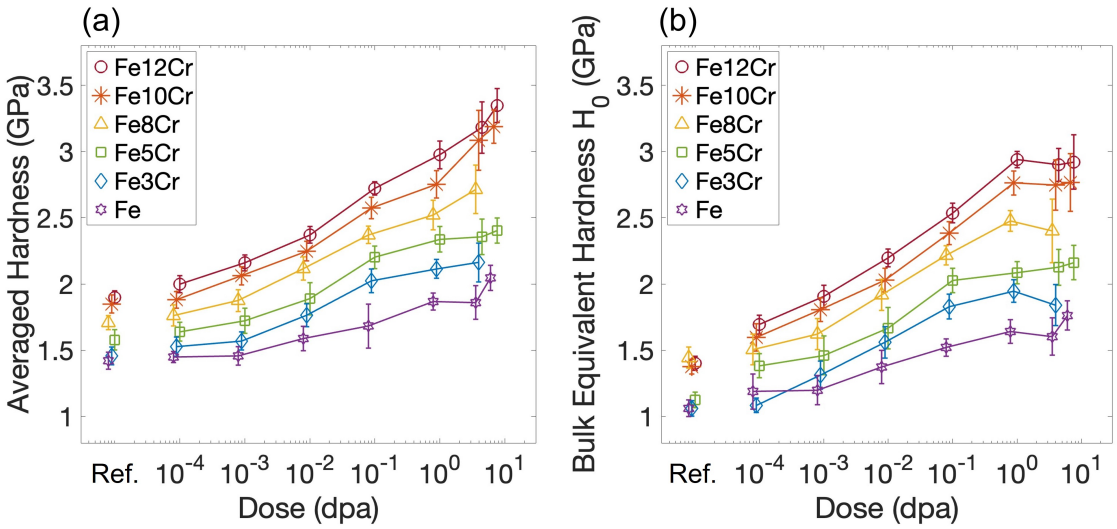


Figure 4.7: Hardness of samples analysed by (a) averaging between 300–600 nm (constant-depth analysis) and (b) using the Nix-Gao model, extracting the bulk equivalent hardness H_0. The unimplanted samples are included on the left side of each plot as a reference. The error bars represent ±1 standard deviation of all measurements performed on each sample. Markers have been offset horizontally for clarity.

bulk equivalent hardness shows that there appears to be negligible hardness change with the addition of up to 5% Cr, which agrees with previous findings from the same bulk materials [422]. There also appears to be no change in hardness from 8% to 12% Cr. Overall, the bulk equivalent hardness H_0 is lower than the constant-depth hardness, demonstrating that there is still contribution to hardening due to ISE even when averaging between 300–600 nm indentation depth data. Data of the fitted ISE length scale (h^*) is included in Appendix C.3.

The irradiation hardening increases as a function of dose up to 0.8 dpa. The difference in hardness between samples of different Cr content at each dose increases with dose. This corresponds to a greater irradiation hardening rate for samples of higher Cr content.

Beyond 0.8 dpa, the hardness curves appear to flatten out slightly for Fe, Fe3Cr, and Fe5Cr, suggesting the onset of saturation in irradiation hardening. However, for Fe8Cr, Fe10Cr, and Fe12Cr, the dose-dependence of hardening differs between the two analysis methods. The constant-depth analysis suggests an increase of hardness as a function of dose, whereas the Nix-Gao method suggests hardness saturation, similar to the samples of other compositions in this study.

4.5 Discussion

4.5.1 Trends With Dose

Low Dose Effects (< 0.008 dpa)

The lattice strain for Fe5Cr observed at 0.8E-4 dpa (the lowest dose in this study) corresponds to a lower bound equivalent Frenkel pair density of 5.9×10^{24} m^{-3}. The dose threshold for defect observation with TEM in irradiated FeCr (manufactured under the same project as the samples in this study) has been reported as 1.5E-3 dpa [59]. This threshold is 20 times higher than the dose at which we observe the onset of defect-induced lattice strain. The authors of the TEM study estimated the defect density at 1.5E-3 dpa to be 6.5×10^{20} m^{-3}. From the lattice strain measurements at a similar dose in this study (0.8E-3 dpa, Figure 4.3), the estimated defect density is between $(6.0 - 17.1) \times 10^{24}$ m^{-3} for Fe and FeCr alloys. The significant difference in defect density estimates from X-ray lattice strain measurements compared to TEM measurements may be attributed to the limited sensitivity of TEM to very small defect features (<2 nm) [189]. At low doses, these small defects are expected to dominate the defect population [110, 112].

Similar findings from a different study of Fe irradiated with neutrons at 325−345 K revealed that the defect cluster density estimated by TEM is over two orders of magnitude lower than that determined by positron annihilation spectroscopy [129]. From that study, a nanocavity density of 2×10^{23} m^{-3} at 1E-4 dpa was measured, with most nanocavities less than 1 nm in diameter (below TEM resolution limit). Even though this nanocavity density value is different from the equivalent Frenkel pair density found at 0.8E-4 dpa in this study, the difference can be reconciled by considering that an 1 nm nanocavity could contain an equivalent of up to 10 vacancy point defects [127].

Irradiation hardening is observed for all Fe and FeCr samples at 0.8E-4 dpa. The amount of hardening increases with Cr content, from 2% hardening for pure Fe to 5% hardening for Fe12Cr. Zinkle *et al.* [129] observed a 10% increase in yield stress (related to changes in indentation hardness) for pure Fe following neutron irradiation at 323–343K to 1.2E-4 dpa, comparable to the lowest dose explored

in this study. However, the TEM characterisation on the same sample did not identify any visible defects [129].

Hammad *et al.* [468] found that following a neutron dose of ∼0.7E-3 dpa in Fe, Fe4Cr and Fe9Cr at the same temperature as the current study (313 K), there was an increase in yield stress of 35–40%. In comparison, at 0.8E-3 dpa, an increase of 3-13% (increasing with Cr content) in nanoindentation hardness is measured in our study. However, a direct comparison of nanoindentation hardness and yield stress from bulk tensile testing is not straightforward due to the difference in length scale and mechanisms [391, 469]. Nanoindentation hardness depends on both the availability of sources for the nucleation of dislocations, and their subsequent propagation. On the other hand, macroscopic yield stress from bulk tensile testing depends mainly on the mobility of pre-existing dislocations. Another reason for the discrepancy between our study and that of Hammad *et al.* [468] could be due to the different levels of impurities present. The carbon content for our samples is less than 10 appm, according to the manufacturer [66, 67]. This value is 10 times lower than that reported in [468]. Lower impurity levels could greatly reduce defect retention, leading to less irradiation hardening in our samples.

The calculation of NRT efficiency at 0.8E-3 dpa for Fe5Cr (0.22) and Fe8Cr (0.19) is in good agreement with literature values (0.2–0.3) [49, 72]. An important consideration in this comparison concerns the clustering of defects. In this study, the calculation of defect density relies on the assumption that defects remain as isolated Frenkel pairs. When clustering occurs, the relaxation volume per defect decreases, requiring more Frenkel pairs to be present to produce the same amount of strain as a corresponding population of isolated point defects. Hence the estimates of defect density and NRT efficiency can be interpreted as a lower-bound estimate. Furthermore, measurements of NRT efficiency in most other studies [72] were performed at 4 K, which reduces the rate of defect recombination. Higher temperatures, such as in our study, therefore result in a further decrease of NRT efficiency [470]. The low levels of impurities present in our materials may further limit defect retention [471], which could contribute to a lower experimentally measured value of NRT efficiency compared to the other studies.

In the low dose regime (0.8E-4 dpa to 0.8E-3 dpa), an increase in irradiation dose leads to a monotonic increase in both lattice strain and hardness. Defects likely evolve from isolated Frenkel pairs to some clustering, resulting in a reduction in NRT efficiency with increasing dose. Eventually, the threshold dose is reached for direct observation of defects in TEM (∼1E-3 dpa [59]).

Intermediate Dose Effects (0.008 dpa ≤ dose < 0.8 dpa)

The hardness and lattice strain measurements of this present study are in good agreement with previous measurements conducted on Fe3Cr, Fe5Cr and Fe10Cr (same raw materials) in similar conditions to doses of 0.8E-2 and 0.8E-1 dpa [422]. The lattice strain measurements of this study agree with previous measurements (averaged within the top 2 µm of the sample) to within 30%. Discrepancies can be attributed to measurement uncertainties for small strains and slight variations between individual grains. The hardness measurements of this study agree with those from [422] to within 9%. The difference in hardness values can be attributed to the grain orientation specificity [472] of the previous study, which only considered grains with ⟨100⟩ out-of-plane orientation. In both cases, the evolution of hardness is similar with a monotonic increase with both dose and Cr content.

In the intermediate dose regime, the rate of lattice strain increase decreases with increasing dose. This indicates a deviation from a linear accumulation of isolated Frenkel pairs ($\Omega \sim 1.4 - 1.6$). This could result from the clustering of defects or a change in the ratio of interstitial to vacancy defects. Several factors likely contribute to this.

The first is the effect of cascade overlap, which becomes important at doses greater than ∼1E-2 dpa, leading to the formation of dislocation loops [109]. This causes a reduction in the relaxation volume, and thus lattice swelling contribution, per defect. Another factor is the reduction in the survival rate of subsequently introduced defects due to pre-existing defects in the crystal [134, 135]. This leads to an overall lower rate of defect population growth.

The effect of finite temperature is also important. Stages of defect recovery as a function of temperature have been identified from resistivity studies in Fe [473].

At 313 K, the active mechanisms include Frenkel pair recombination, as well as di-interstitial and vacancy migration. Since interstitials have much greater mobility than vacancy defects, they are more likely to cluster and reduce their contribution to overall lattice strain per defect. Furthermore, the increase in concentration of defects will also lead to a greater rate of recombination [473]. The net effect is the reduction in the rate of lattice strain increase, which is observed for all samples.

High Dose Effects ($\geq$ 0.8 dpa)

The reduction of lattice strain with increasing irradiation dose above 0.8 dpa in FeCr suggests a net removal of interstitial defects. This has been observed previously in self-ion irradiated W by Mason *et al.* [183]. In W, lattice strain increased monotonically up to 0.032 dpa, before dropping to zero at 0.056 dpa and ultimately becoming negative at doses beyond 1 dpa. This experimental result was compared to simulation results from Frenkel pair creation and insertion using the creation-relaxation algorithm (CRA). The CRA involves randomly displacing an atom to a new position within the simulation cell and then minimising the global potential energy in the cell [148]. Agreement was obtained between experiments and simulation results regarding the dose at which the strain peaked and then changed signs. But the simulation results predicted a strain level that was 10 times greater in magnitude than experimental observations.

For Fe, Derlet and Dudarev [148] have previously simulated strain induced by irradiation using CRA up to 2.5 cdpa (canonical dpa). Note that the definition of cdpa in CRA simulations is the ratio of the number of Frenkel pairs inserted to the total number of atoms in the simulation. This is an analogous measure of defect production to dpa. From CRA in Fe, an increase of strain was observed up to 0.07 cdpa, peaking at a strain of 5×10^{-3} before decreasing to zero strain beyond 2 cdpa. Compared to the experimental results of this study, the magnitude of strain predicted is 10 times greater than those experimentally observed in our study. The theoretical prediction of the dose threshold for maximum lattice strain is also a factor of 10 lower than we observe experimentally. These observations are similar to the results found for W when comparing between simulation and experimental results [183].

The phenomenon of a positive peak in strain followed by a trend towards zero strain (and in the case of W, ultimately negative strain) at high doses is attributed to the formation of large-scale defect microstructures from an accumulation of interstitial defects [183]. As the density of interstitial defects increases with dose, the defects begin to coalesce. The growth of these extended defect structures eventually causes an evolution back towards a less defective crystal structure, which removes positive lattice strain [148]. As vacancies are much less mobile, they largely remain as isolated defects, contributing negative lattice strain, which becomes dominant at high dose.

However, unlike W, the lattice strains in Fe and FeCr alloys do not become negative, either in simulations [148] or experimentally in this study. The reason for this could be the ratio of mobilities for interstitial and vacancy defects. In BCC Fe, the migration energy of a single vacancy is 0.65 eV [474] and for a self-interstitial loop, it can be as low as 0.1 eV [475]. Considering an Arrhenius rate behaviour for thermally-induced defect movement in crystals, there is a factor of ∼1.7 difference between interstitial and vacancy mobility. This is much lower than the corresponding ratio for W (>5) [476, 477]. This means for Fe, a higher rate of Frenkel pair recombination is expected. Furthermore, the rates of migration and annihilation of defects to sinks (e.g. dislocations and grain boundaries), and defect clustering would be more comparable between interstitial-type and vacancy-type defects. Therefore, even after the formation of extended dislocation networks at high doses, the imbalance of interstitial-type and vacancy-type defects is not sufficient to cause the net lattice strain in Fe to become negative. However for W, the low mobility of vacancies causes them to remain 'frozen' in the lattice, such that they ultimately cause a negative net strain at high doses after the interstitial defects aggregate to form new crystal lattice planes [183].

The formation of large extended defect microstructures in Fe following room-temperature high-dose (>6.5 dpa) irradiation has been previously observed by TEM [111]. This dose is different to the dose threshold of strain reduction that resulted from defect coalescence in the present study. However, it's worth noting that TEM irradiation also suffers from defect loss to the surface of the foil, which would delay the onset of defect coalescence [104].

The lattice strain predicted by CRA simulations of Fe [148] peaks at a dose 10 times smaller than the experimental observations in FeCr. This could be attributed to the greater mobility of defects in Fe and FeCr at 313 K which would lead to increased recombination and sink-annihilation of Frenkel pairs, thus delaying defect evolution and formation of extended structures. This temperature effect could also be the reason for the factor of 10 difference in the magnitude of strain between simulations and experiments. Since CRA simulations are athermal, with purely stress-driven relaxation of the lattice, there will be much higher levels of defect retention due to lower recombination rates. This is evident when comparing defect content and NRT efficiency between this experiments and CRA simulation. From CRA simulations, the ratio between defect content and cdpa value (analogous to NRT efficiency) for cdpa <0.01 is close to 1, corresponding to essentially zero recombination. Whereas from experiments, the NRT efficiency beyond 0.008 dpa is less than 0.1 for all compositions in this study (Figure 4.6), in part due to temperature-enhanced recombination.

It is worth noting that the presence of impurities in the experimental samples, even at low concentrations, compared to a perfect starting crystal in CRA simulations would cause enhanced retention of defects [478–480]. This effect would act in opposition to that caused by finite temperatures, as discussed previously. Interestingly, in our case, it appears that the temperature effect is dominant, resulting in a net delay in lattice strain evolution as a function of dose. This is consistent with the low impurity levels of the as-received materials in this study (Table 4.1).

The evolution of nanoindentation hardness is markedly different to the behaviour of lattice strain in this dose range above 0.8 dpa. We do not observe any changes in the sign of hardness change. Surprisingly, there does not appear to be any prior studies on hardness changes in FeCr as a function of dose following room-temperature irradiation with self-ions. A study at room temperature following irradiation with Ar ions for RAFM T91 steel suggests hardness saturation at 4 dpa [481]. A study of CLAM steel irradiated with Xe ions at room temperature up to 5 dpa showed no hardness saturation [482]. However, direct comparison with the results of the present study is not straightforward due to the use of noble gases as irradiating particles in these previous works.

Self-ion studies [98, 210] have only been performed for irradiation at 573 K and showed hardness saturation for pure Fe and FeCr alloys with Cr content greater than 5% above 1–2 dpa. For low Cr content, no saturation was observed even up to 10 dpa. The trends from these studies conducted at higher irradiation temperatures differ from our results. Following room-temperature irradiation, Fe, Fe3Cr and Fe5Cr approach hardness saturation at doses $\geq$0.8 dpa, but conclusive trends cannot yet be determined for Fe8Cr, Fe10Cr, and Fe12Cr. One reason for the discrepancy could be due to some carbon contamination from the irradiation process. Atom probe tomography data of Fe10Cr at 0.8 dpa is included in Appendix C.4. We estimate the carbon enrichment to be $\sim$100 appm after 0.8 dpa, compared to 18 appm reported by the manufacturer for the as-made samples. The additional carbon introduced, which scales with irradiation dose, could contribute in part to the hardening seen at high doses [483], particularly when analysed with the constant-depth method.

Another reason for the observed difference in hardening trends with other studies at higher irradiation temperatures could be enhanced defect mobility, which leads to more defect recombination. TEM studies have shown the movement of dislocation loops at 573 K around 0.6 dpa [111]. Even at lower doses, the same authors observed a much greater fraction of mobile loops at 573 K compared to at room temperature [109]. As such, one might expect the asymptotic or saturation state of defects in irradiated Fe and FeCr to occur at a lower dose for irradiation at higher temperatures.

In contrast to lattice strain trends in the high dose regime, the non-negative change of hardness as a function of irradiation dose indicates that the presence of all irradiation defects, both isolated and within aggregated structures such as dislocation loops and networks, contributes to the hardening of Fe and FeCr.

4.5.2 Trends With Cr Content

The trends for lattice strain and hardness as a function of Cr content differ greatly. While an increase in Cr content at each dose is associated with a greater increase in hardness, lattice strains peak between Fe5Cr and Fe8Cr at each dose, with lower strains for higher and lower Cr content. As previously discussed, hardness is an indicator of the overall defect population, with interstitials and vacancies additively

contributing. Lattice strain is dependent on the imbalance between interstitial-type and vacancy-type defects as their respective contributions (relaxation volume) have opposite signs. By examining both trends, we can gain an insight into how the defect populations are affected by Cr content.

There is a monotonic increase in hardness and hardening rate of Fe and FeCr with Cr content. This suggests that defect retention increases with Cr content, which causes an increase in defect number density and/or size [459]. Heintz *et al.* [98] measured hardness after room-temperature irradiation to 1 dpa and similarly found that hardening increased with Cr content. Interestingly, no hardening was observed for Fe2.5Cr in that study, which is different to our results.

In contrast to hardness trends, we found that the lattice strain trend is non-monotonic with maximum lattice strain at Cr content between 5–8%. This suggests that the defect populations and types depend on Cr content. Larger positive lattice strain can arise from a larger population and/or less clustering of interstitial-type defects, as well as a smaller population and/or more clustering of vacancy-type defects. Since interstitials are more mobile than vacancies in Fe [474], their population and mobility may have a greater effect on lattice strain at room temperature.

It is interesting to note that FeCr has many non-monotonic trends in the range of Cr content less than 20%. One such trend is that the change in ductile-to-brittle-transition temperature reaches a local minimum at 9%Cr [28]. For irradiation-induced void swelling, it also varies non-monotonically with Cr content [61, 65, 130, 165, 167]. The diffusivity of interstitial defects in FeCr is also a non-monotonic function of Cr content, as identified by molecular dynamics and Monte Carlo studies [484]. At low Cr concentrations, an increase in Cr content will increase the binding of self-interstitial clusters to the Cr atoms, reducing their mobility [456]. With further increase of Cr content past a critical minimum point, each interstitial atom could be interacting with more than one Cr atom simultaneously, effectively 'pulling' the defect in opposite directions. This then results in an increase of interstitial diffusivity with Cr content. The point of minimum interstitial diffusivity occurs around 10%Cr [485]. This mechanism has also been used to explain the local minimum of void swelling at 5–10%Cr observed in some neutron irradiation studies (653 K, 30 dpa) [167, 485]. It is

proposed that the origin of void swelling lie in the absorption of fast-moving interstitial defects at sinks, such as grain boundaries and surfaces, leaving behind vacancies and vacancy clusters that subsequently form voids. A reduction in interstitial cluster mobility will limit their migration to sinks and thus enhance recombination, thereby reducing void swelling. Furthermore, Cr only weakly interacts with vacancies [52], so their population would not be affected as strongly by Cr content.

Relating this to our observations, the balance of interstitial to vacancy defects will be strongly correlated with the mobility of interstitial defects. A reduction in the mobility of interstitial clusters will increase the ratio of interstitials to vacancies in the material, leading to a greater, positive lattice strain. The range of Cr content (5–8%) that correspond to the highest level of lattice strain in this study is consistent with the range for minimum void swelling and cluster diffusivity [167, 484], suggesting this could be an explanation for the non-monotonic dependence of lattice strain on Cr content. However, we note that trends for void swelling strongly depend on irradiation temperature [65], dose [61, 130], and sample processing history (e.g. cold-worked or annealed) [173]. Further systematic studies on void swelling could reveal more insights into the role of Cr on defect populations.

For pure Fe, a delayed onset of lattice strain saturation is observed compared to the FeCr alloys. Even at 6.0 dpa, the lattice strain does not appear to have reached a peak, unlike for the other FeCr alloys where a decrease of lattice strain occurs beyond 0.8 dpa (Figure 4.3). The NRT efficiency for all FeCr alloys is reduced between 0.8E-3 dpa to 0.8E-2 dpa (Figure 4.6 (a)). This suggests defect clustering is occurring, as it causes a reduction in strain contribution per defect, which leads to an underestimation of the defect density in the material. For pure Fe, the NRT efficiency remains constant between 0.8E-3 dpa to 0.8E-2 dpa, corresponding to a linear increase in isolated defect density. This suggests that pure Fe would exhibit defect clustering at a higher dose than FeCr. Furthermore, due to the low impurity content in the Fe material, the barrier to defect recombination is low, resulting in a low NRT efficiency and defect retention. As a result, all stages of defect evolution in Fe are shifted to higher doses compared to FeCr where defect retention is higher due to the binding of interstitial defects to Cr, as discussed earlier.

4.6 Summary and Conclusion

In this study, the effect of ion irradiation at 313 K on lattice strain and hardness in Fe and FeCr alloys was investigated. A dose range of 0.00008 dpa to 6.0 dpa was covered for pure Fe and FeCr up to 12%Cr. The key findings are as follows:

- Irradiation hardening is observed for all Fe and FeCr alloys at a dose as low as 0.00008 dpa. Non-zero lattice strain in the implanted layer was also measured at that dose for Fe5Cr, which corresponds to an equivalent Frenkel pair density of 5.9×10^{24} m^{-3}. This is well below the dose limit for any defect detection reported in the literature by electron microscopy.

- The NRT efficiency was calculated for all alloys at 0.0008 dpa. The highest values ($\sim$0.2) are found for Fe5Cr and Fe8Cr, which agree with studies in the literature at similar ion energies.

- FeCr alloys reach a maximum positive strain at a dose of 0.8 dpa. Further increase in dose cause a reduction in lattice strain due to the formation of extended interstitial defect structures. This agrees with simulation results after accounting for the effects of finite temperature and impurities.

- A delay in the onset of interstitial clustering as a function of dose is observed in Fe compared to FeCr. No maximum in lattice strain is observed in Fe even at 6.0 dpa. In the absence of Cr, there is comparatively little defect pinning in Fe, especially given the high purity in the as-received material. As a result, the NRT efficiency is low. Combined with the finite temperature effects, this means the evolution of lattice strain in Fe at room temperature is delayed to significantly higher doses than in FeCr.

- Fe5Cr and Fe8Cr exhibit the highest level of positive strain out of all FeCr samples studied at any given dose level. This falls into the range of Cr concentration where the diffusivity of self-interstitial clusters is lowest, increasing their retention.

- There is a monotonic increase in hardness with irradiation for all samples investigated. However, even by 6.0 dpa, irradiation hardening has not reached saturation for Fe or FeCr alloys. Fe, Fe3Cr and Fe5Cr exhibit very low hardening rates while Fe8Cr, Fe10Cr and Fe12Cr exhibit higher hardening rates at doses beyond 0.08 dpa.

Data Availability

All data, raw and processed, as well as the processing and plotting scripts used in this study are available online at: https://doi.org/10.5281/zenodo.10804185

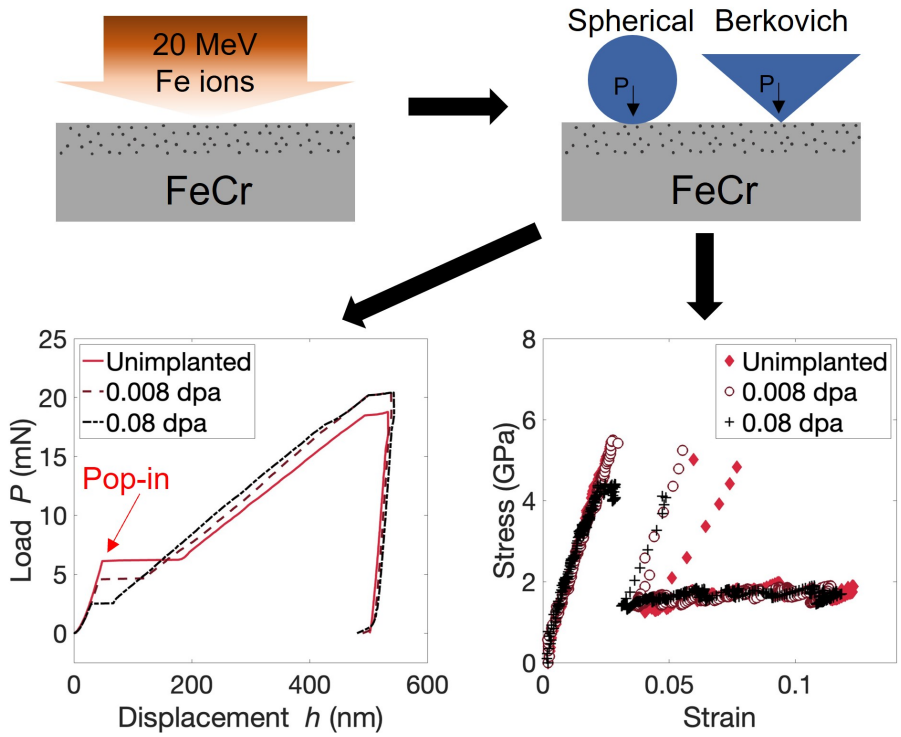
5

Deformation Behaviour of Ion-Irradiated FeCr: A Nanoindentation Study

This chapter addresses some key questions regarding the initiation of plasticity in ion-irradiated FeCr, and how irradiation dose and Cr content affects this. The study specifically examines the factors that potentially affect the nucleation and multiplication of dislocations, as well as their propagation. Spherical nanoindentation provides a convenient tool for the characterisation of stress-strain relationships in small sample volumes [404, 405, 486, 487]. This work applies the technique to ion-irradiated FeCr and makes comparisons to bulk tensile testing results from neutron-irradiated materials to determine how small-scale testing techniques can reveal insights into bulk mechanical behaviour.

The contents of this chapter have been published as: K. Song, H. Yu, P. Karamched, K. Mizohata, D. E. J. Armstrong, F. Hofmann, "Deformation Behaviour of Ion-Irradiated FeCr: A Nanoindentation Study", *Journal of Materials Research*, vol. 37, pp. 2045–2060, 2020 [469]. H. Yu polished the samples and provided assistance with HR-EBSD data collection and analysis. P. Karamched collected the ECCI data. K. Mizohata performed the ion irradiation. The rest of the work was carried out by the author with the supervision of D. E. J. Armstrong and F. Hofmann.

5.1 Abstract



Graphical Abstract

Understanding the mechanisms of plasticity in structural steels is essential for the operation of next-generation fusion reactors. This work on the deformation behaviour of FeCr, focuses on distinguishing the nucleation of dislocations to initiate plasticity, from their propagation through the material. Fe3Cr, Fe5Cr, and Fe10Cr were irradiated with 20 MeV Fe^{3+} ions at room temperature to doses of 0.008 dpa and 0.08 dpa. Nanoindentation was then carried out with Berkovich and spherical indenter tips. Our results show that the nucleation of dislocation is mainly from pre-existing sources, which are not significantly affected by the presence of irradiation defects or Cr%. Yield strength, an indicator of dislocation mobility, increases with irradiation damage and Cr content, while work hardening capacity decreases mainly due to irradiation defects. The synergistic effects of Cr and irradiation damage in FeCr appear to be more important for the propagation of dislocations than for their nucleation.

5.2 Introduction

Reduced activation ferritic/martensitic (RAFM) steels are prime candidate materials for structural components of next-generation nuclear fusion and fission reactors [16]. They are favoured over austenitic steels for their resistance to irradiation swelling and helium embrittlement, and good thermomechanical properties [12, 488]. For the safe and efficient operation of reactors, the impact of the reactor environment, mainly the effect of neutron irradiation, on the behaviour of the reactor materials must be well-understood. For the structural components of the reactor, it is particularly important to characterise the irradiation-induced evolution of mechanical properties and the onset of plasticity.

The study of FeCr binary alloy materials is useful for gaining mechanistic insight into the effects of irradiation on RAFM steels as they reduce the microstructural complexity associated with numerous minor alloying elements in industrial steels [165, 489]. In particular for comparisons with theoretical simulations, which are crucial for prediction of material properties in operation but not yet able to capture complex RAFM steels, the experimental study of pure Fe and FeCr model binary alloy provides vital information [133, 484].

Ion irradiation is a useful surrogate for simulating the damage caused by neutron irradiation [454]. It allows the accumulation of large damage doses, in a controlled environment, over a short span of time without inducing transmutation [423]. This is particularly useful for comparisons with neutron damage that produce dense defect cascades [96]. Ion irradiation eliminates transmutation-induced evolution in the chemical composition of the samples and allows for comparison to simulations [110, 490]. The drawback of ion irradiation is that the damage layer produced is only a few microns thick, which necessitates the use of specialised techniques to characterise material properties at such scales.

Nanoindentation has proved to be invaluable for providing mechanical information of ion-irradiated materials as it can extract mechanical information from the thin irradiated layers [98, 486, 491]. It has been used to investigate mechanical properties including yield strength, deformation behaviour, and elastic properties [208, 395].

Irradiated Fe and Fe-based alloys exhibit hardening and embrittlement due to the formation of point defects, dislocation loops, and clusters acting as barriers to dislocation movement [191, 492]. Changes in mechanical properties (e.g. yield strength) can be measured even at very low damage levels (10^{-4} displacements-per-atom, dpa) when defects are not yet visible with electron microscopy [129, 201]. This makes insights from mechanical characterisation very valuable. Previous nanoindentation studies on irradiated FeCr largely focused on quantifying irradiation-induced hardening behaviour [98, 208, 210, 493]. The amount of hardening has been found to increase with Cr content for doses below 1 dpa [98, 422]. There exists some experimental work on the deformation behaviour of irradiated FeCr, particularly after the onset of yield, with strain softening commonly observed [92, 211, 491]. An unanswered question from the current literature is the behaviour just before and at the onset of pop-in when the dominant effects are from dislocation nucleation and multiplication. The effect of irradiation on the mechanisms responsible for the initiation of plasticity in FeCr is also currently unclear. Both the initiation and progression of plasticity are crucial to predicting the structural integrity of steels in operation.

A second aspect missing in existing studies is the synergistic effect of Cr and irradiation damage on the initiation and progression of plasticity in FeCr. Many existing studies [54, 406, 491] have focused only on one composition of Cr% or one dose. This makes comparisons of the effect of Cr content and dose level difficult, as samples from different studies vary in processing history, irradiation condition, and data analysis protocol. From our previous study of irradiated FeCr [422], we found that enhanced defect retention from the presence of Cr caused greater changes in the hardness, thermal diffusivity, and lattice strain. The present study follows on from these previous results to focus on the synergistic effects of Cr and irradiation dose level on the deformation behaviour of irradiated FeCr.

The study of Fe and FeCr binary alloys at room temperature, as opposed to more commonly at 500–800 K is important for fundamental understanding of irradiation damage. Atomistic simulations of non-thermally activated processes, e.g. stress-driven defect evolution, are important and can only be compared to experimental

results obtained in the 'low temperature' regime when defect mobility is limited [148, 494]. This is an important step to understanding irradiation damage at reactor operation temperatures where both thermally-activated and stress-driven processes are at play. Defect microstructures in Fe and Fe-based alloys have been found to evolve on a timescale of weeks to months [184, 495] at low temperatures $T < 600$ K, and this timescale decreases exponentially with increasing temperature [496]. Therefore, irradiating and characterising at room temperature, or below, prolongs the timespan over which defect microstructures do not evolve significantly and ensures the material properties characterised after the irradiation are representative of the defects created during irradiation conditions.

We systematically examine the deformation behaviour of FeCr with nanoindentation as a function of Cr content (3, 5, and 10%), and damage level (unimplanted, 0.008, and 0.08 dpa). Irradiation and mechanical characterisation were all carried out at room temperature. Nanoindentation reveals the dose- and composition-dependent behaviour of dislocation nucleation and propagation in the irradiated regions of the materials to provide insights on the early stage deformation behaviour of irradiated FeCr. The use of indenter tips with different effective radii makes it possible to distinguish between dislocation nucleation and propagation in these measurements. Our findings are discussed in light of previous experimental and *ab initio* studies of Fe and FeCr. This information is crucial for the design and performance prediction of structural components in future reactors.

5.3 Materials and Methods

5.3.1 Materials and Ion Implantation

This investigation considers the same samples as [422], which contains full details of their preparation and history. Briefly, polycrystalline samples of FeCr with 3, 5, and 10% Cr content (here referred to as Fe3Cr, Fe5Cr, and Fe10Cr, respectively) were manufactured under the European Fusion Development Agreement (EFDA) programme by induction melting and a series of forging and recrystallisation heat treatments [66]. The samples were mechanically ground with SiC paper then polished

with diamond suspension and colloidal silica (0.04 µm). The final surface treatment performed was electropolishing with 5% perchloric acid in ethanol at 233 K using a voltage of 28 V for 3–4 minutes.

Ion implantation was performed with 20 MeV Fe^{3+} ions at room temperature using the tandem accelerator at the Helsinki Accelerator Laboratory. For each sample composition, samples were implanted to 2 nominal doses: 0.008 dpa and 0.08 dpa (by averaging over the first 2 µm of the dose profile), as calculated using the Quick K-P model in the SRIM code (20 MeV Fe ions on a Fe target with 40 eV displacement energy at normal incidence) [80]. The calculated damaged layer extends to 3.5 µm below the sample surface (Figure 5.2). Previous measurements using X-ray diffraction confirmed that the depth-dependent changes of strain in this layer match the predictions from SRIM [422]. One sample of each FeCr composition was set aside as an unimplanted reference.

5.3.2 Nanoindentation Procedures

Nanoindentation experiments were performed using an MTS Nano Indenter XP. A Berkovich tip, and two spherical tips of nominal radii 1 µm and 5 µm respectively were used. Continuous stiffness measurements (CSM) were conducted with a frequency of 45 Hz and a harmonic amplitude of 2 nm. The indenter, for all tip shapes, was loaded at a constant strain rate of 0.05 s^{-1}. Grains of near ⟨100⟩, ⟨110⟩, and ⟨111⟩ out-of-plane orientations (within ± 5°) were first identified by electron backscatter diffraction (EBSD), then chosen for indentation. At least 10 indents were performed on each sample.

5.3.3 High-Resolution Electron Backscatter Diffraction (HR-EBSD)

High-resolution electron backscatter diffraction (HR-EBSD) measurements were used to measure the geometrically necessary dislocation (GND) densities on the surface of the samples [497]. Cross-correlation analysis of high angular resolution EBSD/Kikuchi patterns was used to extract lattice rotations with respect to a reference point in an EBSD map. These rotations were then used to calculate local lattice curvatures

and then compute the surface GND densities. This technique can achieve a spatial resolution of ∼50 nanometres and a sensitivity above 10^{12} lines/m^2 [498].

HR-EBSD measurements were performed on a Zeiss Merlin SEM (20 kV, 15 nA), with a Bruker eFlash detector system. The sample was tilted by 70° with respect to the electron beam, and a working distance of 18 mm was used. The measurements used a step size of 170 nm to ensure sufficient spatial coverage over the area around an indent while maintaining reasonable measurement times. Diffraction patterns were recorded at a resolution of 800 × 600 pixels. The cross-correlation analysis was carried out using a MATLAB-based code, originally written by Britton and Wilkinson [341].

5.3.4 Electron Channelling Contrast Imaging (ECCI)

Electron channelling contrast imaging (ECCI) was also used to image and measure the dislocation densities in the material, as it can probe both GND and statistically stored dislocations (SSD). This method relies on the backscattered electron intensity signal while the electrons travel through a sample volume. The presence of lattice distortions, such as dislocations, can alter the diffraction condition and thus allow defects to be imaged under specific conditions [499].

ECCI measurements were performed on a Zeiss Crossbeam 540 SEM (30 kV, 10 nA), with a four-quadrant backscattered electron detector at nearly normal incidence to the electron beam direction.

5.4 Results

5.4.1 Initiation of Plasticity: Pop-In Analysis

All samples were indented with a Berkovich tip and two spherical tips with nominal radii of 1 µm and 5 µm. The use of different tip sizes allow distinction between different sources of dislocation nucleation, as further discussed below.

A typical load vs. displacement curve measured in this experiment is shown in Figure 5.1. The first section of the curve (Figure 5.1(a)) between points A and B is the elastic Hertzian response which can be described as the contact between a

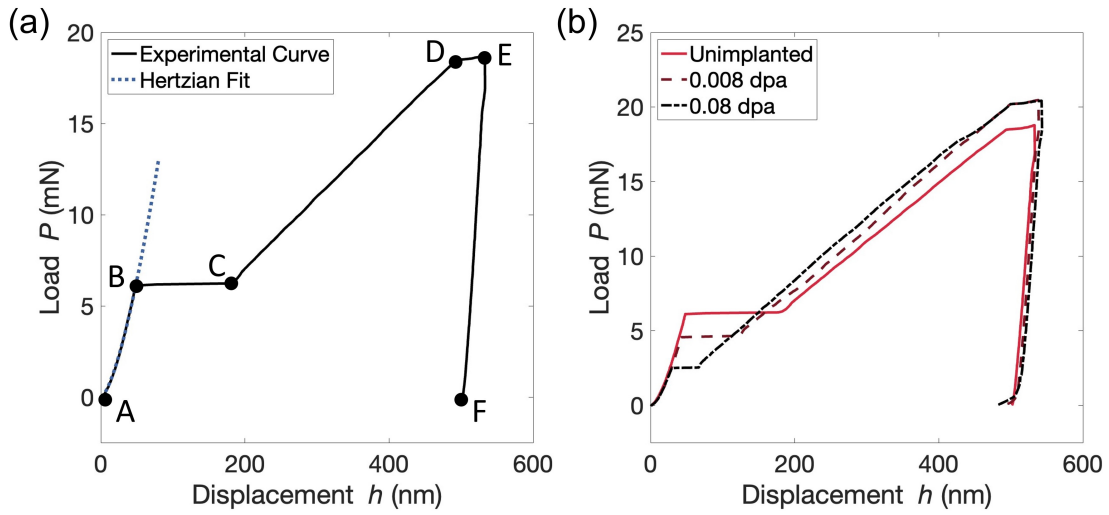


Figure 5.1: The load-displacement curves of the indentation of Fe3Cr with a nominally 5 µm radius spherical tip. (a) The indentation curve of unirradiated Fe3Cr with key segments labelled: elastic deformation described by Hertzian mechanics (A → B), pop-in (B → C), elastic-plastic deformation (C → D), creep (D → E), and unloading (E → F). (b) The effect of irradiation on increasing the pop-in loads for Fe3Cr.

sphere (the indenter tip) and an elastic half-space (the sample surface) [500]:

$$P = \frac{4}{3} E_r R^{\frac{1}{2}} {h_e}^{\frac{3}{2}} \tag{5.1}$$

where P is the applied load, R is the radius of the sphere, h_e is the elastic indentation depth. E_r is the reduced modulus given by:

$$\frac{1}{E_r} = \frac{1 - {\nu_i}^2}{E_i} + \frac{1 - {\nu_s}^2}{E_s} \tag{5.2}$$

where E is the elastic modulus and ν is the Poisson's ratio, with subscripts i and s referring to the indenter and the sample, respectively. Here we used E_i = 1140 GPa, $\nu_i = 0.07$ [389] for the diamond indenter tips and $\nu_s = 0.29$ for the FeCr alloys [501]. From our previous nanoindentation study [422], E_s was found to be 218 GPa for Fe3Cr and Fe5Cr, and 228 GPa for Fe10Cr.

The method proposed by Leitner *et al.* [502] was used to fit the radii of the tips in this study. This method fits the contact area and contact depth of the indentation, rather than the total depth. The elastic portion (between points A to B in Figure 5.1) from indentation of pure unimplanted Fe (E_s = 204 GPa) was used for the fitting. For the purposes of this work, an effective radius (R_{eff}) was calculated from the

fitting by approximating the tips as spherical. For the Berkovich tip, this assumption is only valid for small indentation depths (further discussed in text related to Figure 5.3), making use of the rounding of the tip. The R_{eff} for the Berkovich tip was found to be 120 ± 31 nm. The spherical tips were found to have effective radii of 911 ± 122 nm and 5.03 ± 0.53 µm. Note, the manufacturer reported 1.11 ± 0.04 µm and 4.83 ± 0.24 µm, respectively, for the spherical indenter tips.

A 'pop-in' occurs between points B and C (Figure 5.1(a)), and the pop-in load (at point B), P_{pop} was identified for all samples. The presence of 'pop-in's' correspond to the initiation of plasticity and can either be from nucleating new dislocations or mobilising pre-existing dislocations [503]. These two different mechanisms can be distinguished by using indenter tips with different radii. Further details are given in the text surrounding Figure 5.2.

Elastic-plastic deformation (between points C and D) occurs following a pop-in event as dislocations have been nucleated in the material. Sample creep can also be observed between points D and E when the indenter is held at the maximum load for 10 seconds.

The use of tips with different effective radii creates differently sized stress zones underneath the surface. The maximum shear stress (τ) directly ahead of the indenter tip in the sample before the occurrence of pop-ins was computed using Hertzian contact mechanics [500]:

$$\tau = \frac{1}{2}p_0 \left| (1+\nu)\left(1 - \left(\frac{z}{a}\right)\arctan\left(\frac{a}{z}\right)\right) - \frac{3}{2}\left(\frac{1}{1+z^2/a^2}\right)\right| \tag{5.3}$$

where z is the coordinate into the material normal to the surface, and a is the contact radius (see Equation 5.7). p_0 is given by [500]:

$$p_0 = \left(\frac{6P_{pop}{E_r}^2}{\pi^3 R^2}\right)^{\frac{1}{3}}. \tag{5.4}$$

The maximum shear stress under the indenter experienced by the whole sample at the onset of pop-ins, $\tau_{max-pop}$, is then given by [500]:

$$\tau_{max-pop} = 0.31p_0. \tag{5.5}$$

The load at the onset of the pop-in event (P_{pop}) was identified for all the load-displacement curves recorded. In the case of multiple pop-ins, P_{pop} was taken at the first pop-in event. The maximum shear stress as a function of depth for different indenter tip radii, was then calculated using Equations 5.3 and 5.4. Figure 5.2 shows this for the Fe10Cr sample irradiated to 0.08 dpa, but the features are representative of all the samples in this study. As the tip radius increases, the stressed zone extends deeper into the material. We consider a 'main stressed zone' as the depth range where the shear stress, τ, experienced is at least 50% of $\tau_{max-pop}$. Even for the largest tip, 5.03 µm spherical, the main stressed zone is still fully contained within the ion-irradiated layer.

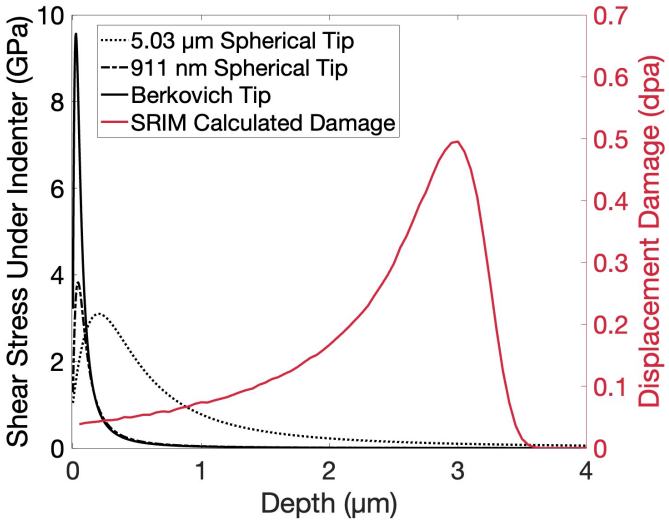


Figure 5.2: The maximum shear stress directly ahead of the indenter tip, as a function of depth, at the onset of pop-in for Fe10Cr irradiated to 0.08 dpa (black traces). The size of the highly stressed zone increases with tip size but are all still contained in the irradiated region (red trace).

From Figure 5.2, it can be seen that $\tau_{max-pop}$ (the peak height) decreases with increasing tip size. This has also been observed previously in Ni [504], W [505] and Mo [506]. This size-dependent phenomenon originates from the initiation of plasticity following either the nucleation of dislocations or the activation of existing dislocations (e.g. Frank-Read sources) in the material. The former mechanism requires shearing the crystal lattice to generate dislocations and hence generally requires a much higher applied stress than the latter mechanism, which relies on unlocking pre-existing

dislocations. Since the volume of the highly stressed zone scales with the indenter radius (Figure 5.2), the probability of encountering a pre-existing dislocation is higher in the highly stressed zone under a larger indenter, compared to applying the same load to a smaller indenter. This means for a larger indenter, plasticity most likely can be initiated once the applied stress is large enough to mobilise pre-existing defects [504]. For a smaller indenter, it is more likely that plasticity is initiated when the applied stress is greater than the ideal strength of the material so that new dislocation shear loops can be nucleated, before the highly stressed zone grows to a size large enough to encounter a pre-existing dislocation source with a lower activation barrier.

The $\tau_{max-pop}$ for loading with a Berkovich tip for the unimplanted materials is calculated using Equation 5.4 and 5.5 (Figure 5.3). In the small, relatively defect-free volume probed by the sharp Berkovich tip, $\tau_{max-pop}$ should approach the theoretical shear strength. This is because it can be assumed that for the indentation depths at which pop-in's occur for a Berkovich tip (<20 nm), the contribution of pre-existing defects is negligible due to the highly-localised stress fields. This has also been previously observed in several other material systems [504, 507]. Experimental values shown in Figure 5.3 are from indentation of grains with close to ⟨100⟩ out-of-plane orientation, and the main corresponding slip system is ⟨111⟩{110}. In our study, the experimental $\tau_{max-pop}$ is within 20% of the theoretical shear strength predicted by density functional theory (DFT) calculations [508].

The discrepancy between the experimental and theoretical results in Figure 5.3 can be attributed to two main factors. The first is that the *ab initio* calculations do not account for the triaxiality of the stress state beneath the indenter. This raises the ideal shear stress compared to the assumption made in [508] of a fully relaxed shear load. Revised *ab initio* analysis of W and Mo by Krenn *et al.* [509] show that modelling a triaxial stress state will produce a theoretical shear strength that is 6–13% higher than the fully relaxed model. Furthermore, the maximum shear stress obtained by the Hertzian contact model (Equations 5.4 and 5.5) assumes that the contact area is small compared to the size of the elastic bodies in contact [500]. This assumption does not fully stand near the yield point. From finite element analysis [509], it is reported that the maximum shear stress calculated from the Hertzian

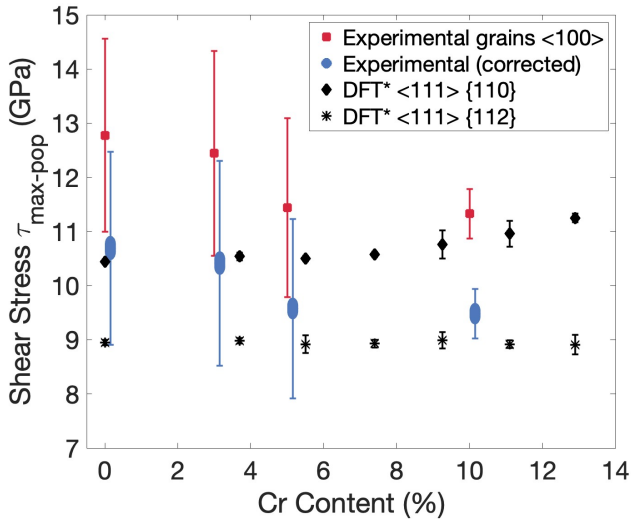


Figure 5.3: The maximum shear stress for the whole sample at the onset of pop-in ($\tau_{max-pop}$) under the Berkovich indenter tip (R_{eff} = 120 nm). The experimental values shown are for unimplanted FeCr with different levels of Cr% for grains of near ⟨100⟩ out-of-plane orientation (red circles), where the primary slip system is ⟨111⟩{110}. The error bars show one standard deviation of the measurements. Density functional theory (DFT) calculations (black diamonds and crosses) [508] are included for comparison. A range of possible corrections have been applied to correlate the experimentally measured shear stress to theoretical calculations (blue), explanations are provided in the corresponding text.

contact model overestimates the true stress by up to 20% for a large range of metals. These factors mean that the maximum shear stress obtained by nanoindentation overestimates the theoretical results by 17 to 22%. The blue bars in Figure 5.3 show the range of corrected theoretical shear strength values for each Cr content applied according to the analysis of Krenn *et al.* [509]. These corrected experimental values are in better agreement with the theoretical values.

The average $\tau_{max-pop}$ shows a weak decreasing trend with increasing Cr content. However the changes are within the experimental uncertainties of this study and further investigation would be helpful to identify underlying mechanisms. The effect of alloying elements on the theoretical strength of materials has been previously investigated in theoretical studies, for example in Ti [510] and Si [511], and depends strongly on both the matrix and solute. A previous experimental study of the shear modulus (G), which is proportional to theoretical strength, of Fe and FeCr alloys show a small increase ($\leq$5%) with Cr content between Fe and Fe10Cr [433]. However,

a further study reported a minimum value of G at Cr% = 5% [512].

For indentation with a Berkovich tip, the effect of ion irradiation on pop-in load, and thus $\tau_{max-pop}$, can be seen in Figure 5.4. The pop-in loads do not vary systematically between grains of near ⟨100⟩, ⟨110⟩ and ⟨111⟩ out-of-plane orientations, and from here on, results from all orientations are considered together.

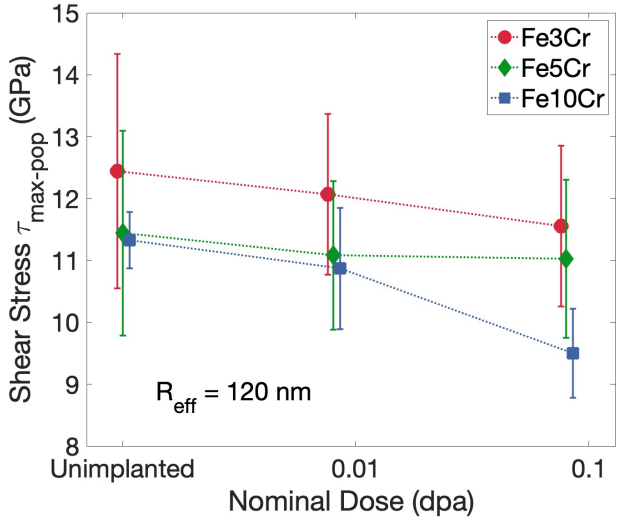


Figure 5.4: The maximum shear stress for the whole sample under the Berkovich indenter tip at the onset of pop-in ($\tau_{max-pop}$) for Fe3Cr (red circle), Fe5Cr (green diamond) and Fe10Cr (blue square) as a function of dose. The error bars show one standard deviation of the measurements.

The decrease in $\tau_{max-pop}$ with irradiation dose can be rationalised by considering irradiation-induced defects in the material as sites for heterogeneous dislocation nucleation. From TEM studies of FeCr materials produced under identical protocols, the defects caused by ion irradiation at room temperature consist of dislocation loops with Burger's vector $\frac{1}{2}a_0\langle 111\rangle$ or $a_0\langle 100\rangle$[59]. It has been shown before, in Ni-irradiated Mo, that irradiation-induced defects serve as local instabilities, which decrease the shear stress required for dislocation nucleation [513]. This differs from other pop-in studies which investigated materials damaged by mechanical straining, where the main form of heterogeneous dislocation nucleation is from Frank-Read sources with much lower activation barriers than irradiation-induced defects [514]. It also appears that the effect of Cr content on the change in $\tau_{max-pop}$ is greater than the effect of increasing irradiation dose alone (Figure 5.4). The change in $\tau_{max-pop}$ for

Fe3Cr and Fe5Cr following irradiation to 0.08 dpa is less than the change in $\tau_{max-pop}$ due to the increase in Cr% from 3% to 5%. Furthermore, Fe3Cr consistently has the largest $\tau_{max-pop}$ for all irradiation doses. Even the Fe3Cr sample irradiated to 0.08 dpa still has higher $\tau_{max-pop}$ than the unirradiated Fe5Cr and Fe10Cr samples.

The synergistic effect of Cr% and irradiation dose level can be seen in the greater decrease of $\tau_{max-pop}$ for Fe10Cr compared to Fe3Cr and Fe5Cr following irradiation. This can be attributed to greater retention of irradiation-induced defects in the presence of Cr atoms [109, 111]. The irradiation-induced change of other material properties such as hardening, decrease in thermal diffusivity and increase in irradiation strain has also been found to be greater for higher Cr% in ion-irradiated FeCr [422].

For indentation performed with larger spherical tips (R_{eff} = 911 nm and 5.03 µm), pop-ins are still noticeable in both the reference (unirradiated) and irradiated samples. $\tau_{max-pop}$ for these spherical tips are shown in Figure 5.5. Indenting with the spherical tips reveals a reduction in $\tau_{max-pop}$ with increasing dose for Fe3Cr. For Fe5Cr, this is only seen for indentation with R_{eff} = 911 nm. This is similar to the observations from the Berkovich indentation pop-ins in Figure 5.4.

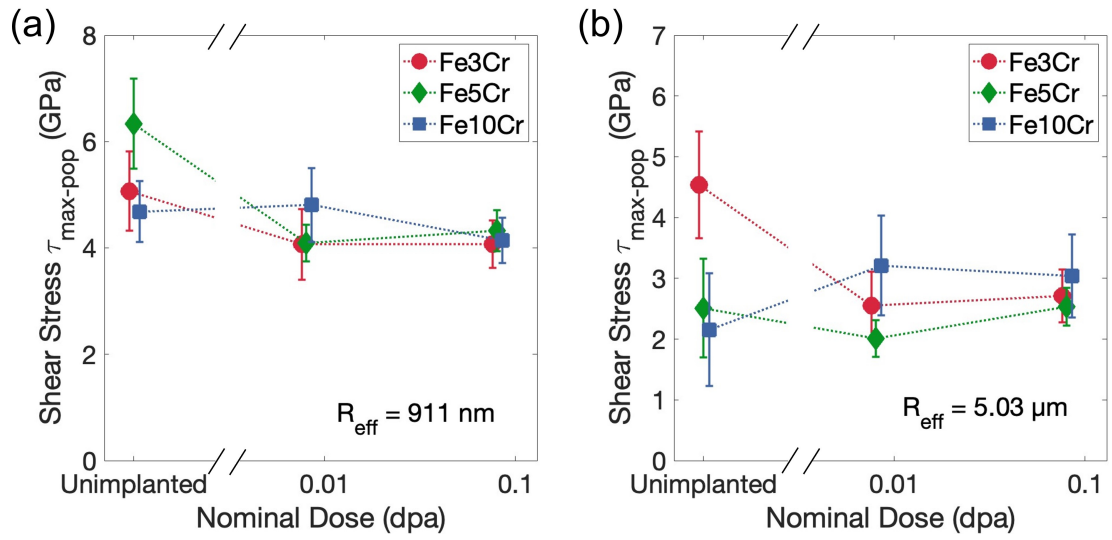


Figure 5.5: The maximum shear stress for the whole sample under the indenter tip ($\tau_{max-pop}$) at the onset of pop-in for Fe3Cr (red circle), Fe5Cr (green diamond) and Fe10Cr (blue square) as a function of dose for spherical indenters with effective radii (a) 911 nm and (b) 5.03 µm. The error bars show one standard deviation of the measurements.

For spherical tips, the $\tau_{max-pop}$ measured are all significantly lower than those

for the Berkovich tip. This drop in $\tau_{max-pop}$ for increased tip radius is much larger than the reduction in $\tau_{max-pop}$ following irradiation (Figures 5.4 and 5.5). This suggests that the dislocation nucleation sources probed during indentation with larger tips have lower activation barriers than dislocation nucleation from irradiation-induced defects. Hence the dislocation nucleation during indentation using tips with larger radii must be from sources other than irradiation-induced defects, such as other pre-existing dislocations.

The use of indenter tips with different radii makes it possible to begin to separate the contribution of Cr content and irradiation dose to the different mechanisms involved in plasticity initiation. The nucleation of dislocations by shearing the lattice is examined by exceeding the theoretical shear strength of the material using Berkovich indentation (Figures 5.3 and 5.4). The operation of pre-existing dislocation sources (e.g. Frank-Read sources) plays a much more prominent role in indentation with larger spherical tips. This is due to a larger tip being able to probe a bigger high-stress zone and initiate plasticity from pre-existing sources with lower activation energy.

Our results (Figure 5.5) show that $\tau_{max-pop}$ varies little with Cr content and irradiation dose, but rather is much more dependent on the size of the spherical tip. Due to the inherently low pre-existing dislocation population in these electropolished samples, the pop-in behaviours were difficult to study with extensive statistics. This was a particular problem for the unirradiated samples, especially Fe3Cr, where the size of the pop-ins often resulted in indents exceeding 500 nm in depth, and were not used in order to maintain experimental consistency. Thus it is likely that any apparent trends, both as a function of Cr and dose, in Figure 5.5 could be due to sampling limitations.

We note that for Fe10Cr, $\tau_{max-pop}$ increases following irradiation when probed by a spherical tip with $R_{eff} = 5.03$ µm (Figure 5.5(b)). This is different to the dependence of $\tau_{max-pop}$ on irradiation dose in all other samples, which either showed a decrease or no change in $\tau_{max-pop}$ with irradiation. It is unclear whether this is due to sampling limitations or a real effect. This may point to a more complex behaviour of dislocation nucleation following irradiation, possibly a combination of effects from irradiation-induced dislocation sources and pre-existing sources now

sampled by indenting with a larger tip. The other possible explanation is that the unimplanted Fe10Cr material possesses an unusually high level of pre-existing dislocations, which leads to a particularly low $\tau_{max-pop}$ required for the initiation of plasticity. To clarify this point, we proceed to examine the pre-existing defect concentrations in the sample with electron microscopy.

Determining Pre-Existing Dislocation Density

HR-EBSD measurements (Figure 5.6) show the GND densities in the vicinity of an indent on each of the FeCr unimplanted surfaces. The average background GND density is stated below the corresponding maps. No differences between samples of different Cr concentrations could be found after accounting for the measurement uncertainties.

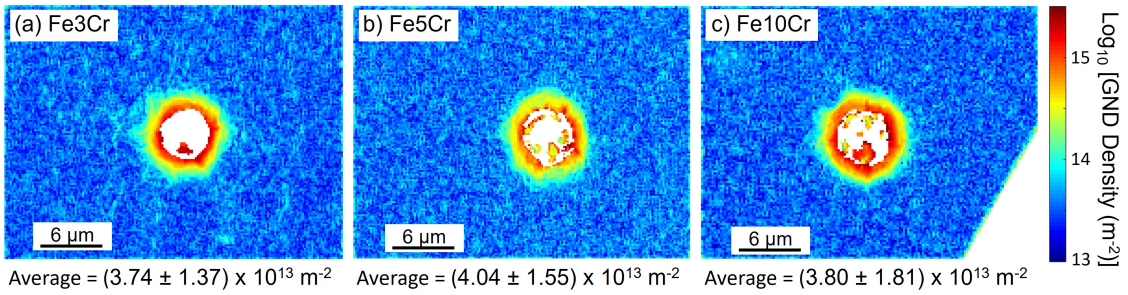


Figure 5.6: GND density distribution around spherical indents (R_{eff} = 5.03 µm) in grains of near ⟨100⟩ out-of-plane orientation on unimplanted (a) Fe3Cr, (b) Fe5Cr, and (c) Fe10Cr as measured by HR-EBSD. The average and standard deviation of the GND density are displayed below the corresponding maps.

The ECCI maps of indents made in unimplanted Fe5Cr and Fe10Cr are shown in Figure 5.7. Fe10Cr appears to exhibit slightly higher dislocation density than Fe5Cr in the region ∼1 to 2 microns away from the indent. Unfortunately, the backscatter contrast signal was not strong enough in the less deformed and undeformed regions to determine a background dislocation density. From the images, the pre-existing dislocation densities in unimplanted Fe5Cr and Fe10Cr seem to be quite low.

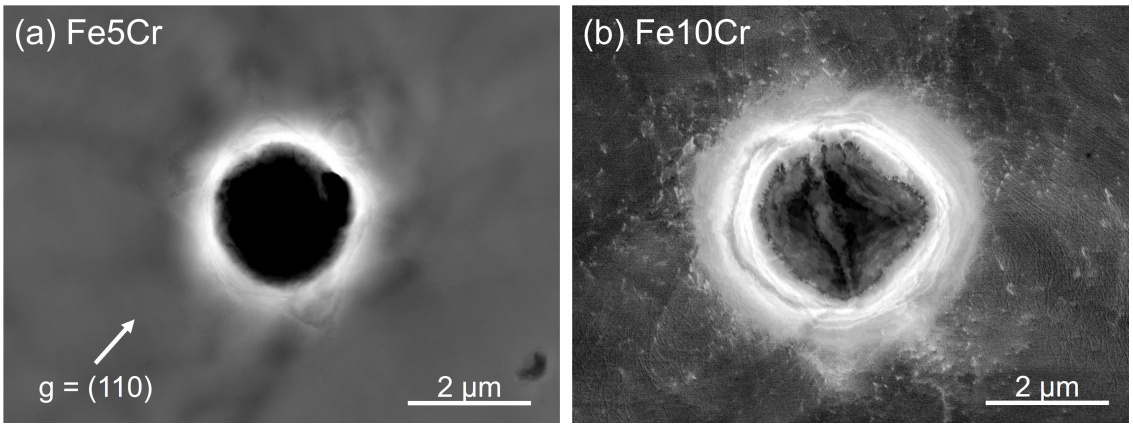


Figure 5.7: ECCI maps of regions around spherical indents (R_{eff} = 5.03 µm) in grains of near ⟨111⟩ out-of-plane orientation on unimplanted (a) Fe5Cr, and (b) Fe10Cr. Some dislocations can be observed around the indent in Fe10Cr but the contrast does not appear to be strong enough to observe dislocations in Fe5Cr.

5.4.2 Progression of Plasticity: Indentation Stress-Strain Curves

Nanoindentation measurements can also give insights into the progression of plasticity and yield in small sample volumes. The use of a spherical indenter tip can produce indentation stress-strain (ISS) curves analogous to those from bulk uniaxial tensile testing.

In our study, ISS curves were calculated using the protocols described in [404, 515]. Briefly, we start from the elastic contact described in Equation 5.1, and define contact radius $a = \sqrt{Rh_e}$. We then transform Equation 5.1 into a linear relationship during elastic contact. Indentation stress, σ_{ind}, and strain, ϵ_{ind}, in the elastic regime, are defined as [404]:

$$\sigma_{ind} = \frac{P}{\pi a^2}; \quad \epsilon_{ind} = \frac{4}{3\pi}\frac{h_e}{a} \tag{5.6}$$

For elastic-plastic indentation, h_t, the total indentation depth, is used instead of h_e, the elastic indentation depth. In this picture, it is equivalent to idealising the indentation zone as a cylindrical region, of radius a and height $\frac{3\pi}{4}a$, being compressed by h_t [404].

The contact radius a is calculated from the measured stiffness, $S = dP/dh_e$,

at each point in the loading curve:

$$a = \frac{S}{2E_r} \tag{5.7}$$

For the accurate analysis of ISS curves from spherical nanoindentation, corrections for the point of effectively zero load and displacement also have to be made according to methods described in [516]. By considering the initial elastic segment ($A \rightarrow B$, Figure 5.1(a)) in the loading curve and using Hertz's theory, the stiffness can be written as:

$$S = \frac{3P}{2h_e} = \frac{3(\tilde{P} - P^\star)}{2(\tilde{h_e} - h^\star)} \tag{5.8}$$

where $\tilde{P}$ and $\tilde{h_e}$ are the measured load and displacement signals. $P^\star$ and $h^\star$ are the values of load and displacement at the point of effective initial contact. By rearranging Equation 5.8, plotting $\tilde{P} - \frac{2}{3}S\tilde{h_e}$ against S produces a linear relationship with a slope of $-\frac{2}{3}h^\star$ and a y-intercept of $P^\star$. The values of $P^\star$ and $h^\star$ are then found by linear regression.

The ISS curves in this study were calculated using Equations 5.6 and 5.7. However, ISS analysis cannot be applied to indentation made with the Berkovich tip as the spherical approximation of the tip shape is only valid for small indentation depths (<20 nm) and beyond that depth, the self-similar geometry of the Berkovich tip means only one strain value is probed during indentation. For indents made with the 911 nm spherical tip, the pop-in stresses are so large that the analysis of the yield behaviour is difficult. At indentation depths of greater than 200 nm, the deviation of tip shape from a perfect sphere is also significant. Therefore, whilst the approximations made for the Berkovich tip and 911 nm spherical tip are appropriate for the pop-in analysis of the previous section, they cannot be used for ISS analysis. For the rest of this section, all analysis of ISS behaviour will focus solely on data obtained from indentation made with the 5.03 µm spherical tip.

The ISS curves obtained from indentation with the 5.03 µm tip are shown in Figure 5.8(a)–(c). The effects of pop-ins are clearly seen, with large elastic stresses in the ISS response before the flow portion proceeds at much lower stress levels. The trend of pop-ins, relating to the nucleation or unlocking of dislocations in the

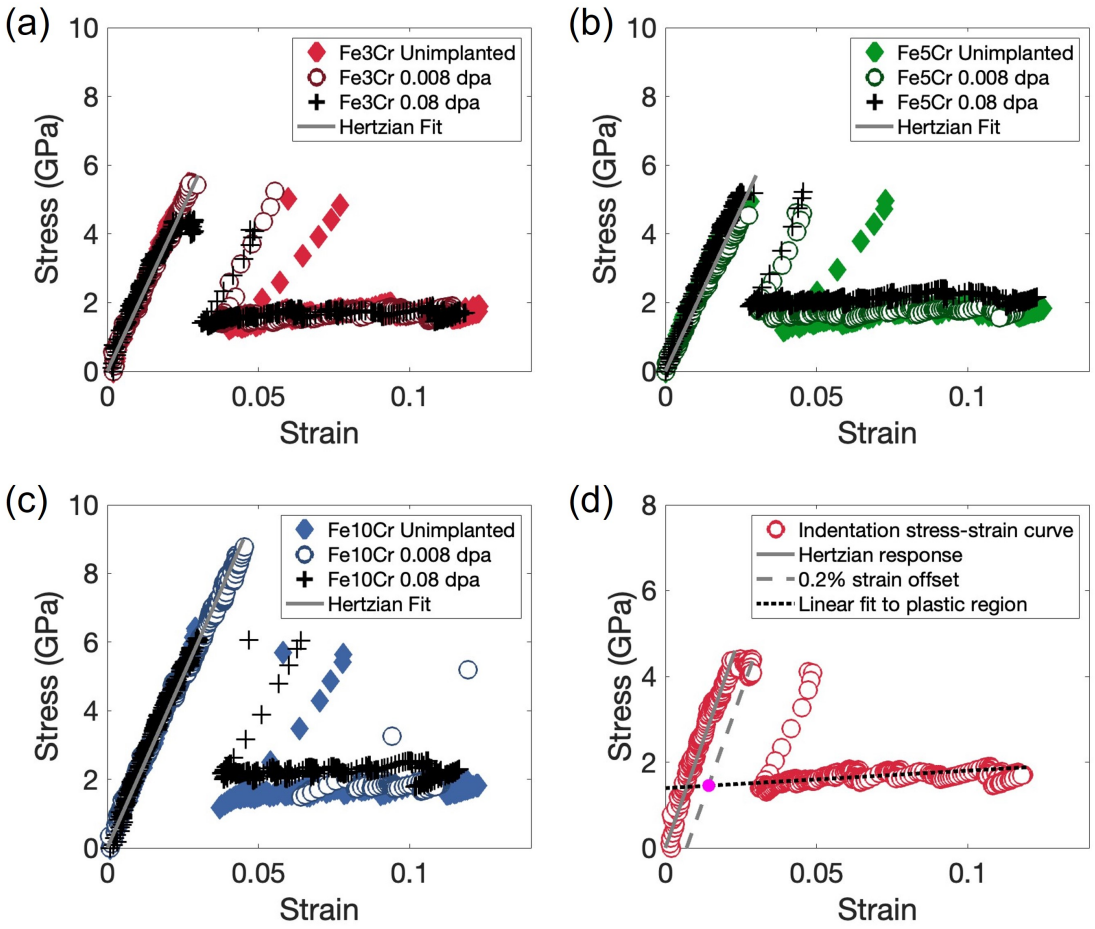


Figure 5.8: The indentation stress-strain (ISS) responses of (a) Fe3Cr, (b) Fe5Cr, and (c) Fe10Cr irradiated to different dose levels. The elastic portions of the curves are well-fitted to the prediction from Hertzian contact mechanics (Equation 5.1) with the gradient equal to the reduced modulus of each sample. (d) The back-extrapolation of the yield strength (magenta point) as the intersection of the line, which is a 0.2% strain offset from the Hertzian response (dashed grey line, offset exaggerated for clarity), and the line that is a linear fit of the plastic part of the ISS curve (black dotted line).

lattice, was extensively discussed in Section 5.4.1. The examination of ISS response for this section will focus on the flow, or plastic, portions which give insight to the propagation of dislocations in the material. Previous studies have shown that pop-ins do not affect the plastic behaviour in the ISS response as this depends on the mobility of dislocations rather than their nucleation [404, 517].

However, the presence of the pop-ins presents some difficulties in the analysis of the ISS response as they obstruct direct determination of the yield point and plastic behaviour immediately following yield. The method described in [518] is used to infer the yield point as the intersection of the elastic Hertzian response with a straight line

fitted to the flow portion of the ISS curve. The yield strength is then defined using a 0.2% strain offset (Figure 5.8(d)). This is commonly used for defining yield strength in uniaxial tensile testing but has also been used in several studies to identify yield strength in nanoindentation measurements [515, 519, 520]. This back-extrapolation technique isolates the contributions to material yield strength due to dislocation propagation and multiplication, rather than dislocation nucleation [521–523].

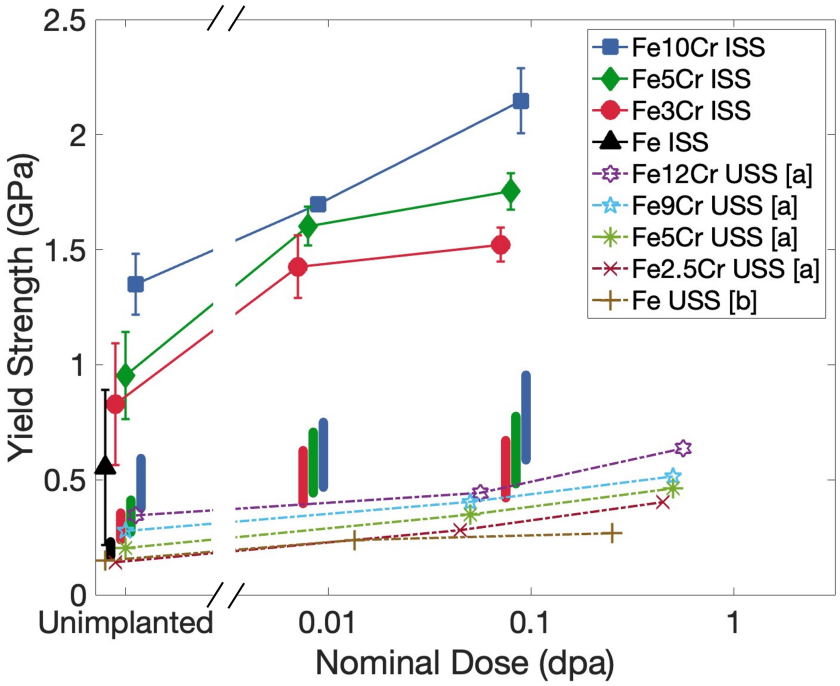


Figure 5.9: The yield strengths measured from the ISS responses of the Fe and FeCr material as a function of dose in this study, using $R_{eff} = 5.03$ µm (filled markers with solid lines). The error bars show one standard deviation of the measurements. A comparison with yield strength measured from USS responses (unfilled markers with dashed lines) is shown. The data [a] and [b] are respectively taken from [193, 524]. The elongated markers presented are the range of possible corrections to correlate the ISS and USS results based on studies in the literature [525–529]. Further discussions are given in the main text. Markers representing the same dose levels for each study have been spread laterally for visibility.

The yield strength calculated from the ISS response increases monotonically with Cr content for all irradiation doses (Figure 5.9). The origins of this, for tests all performed at the same temperature, is solid solution hardening, which is expected to increase with the square root of the solute concentration [530]. The rate of solid solution hardening in the yield strength of unirradiated FeCr is comparable to previous uniaxial tensile tests on single crystal FeCr samples [531] (detailed

comparisons in Appendix D). The yield strength also increases monotonically with irradiation dose for all FeCr materials measured, which has been previously observed in other irradiated materials [193, 486].

The rate of yield strength increase between unimplanted and 0.008 dpa is lower for Fe10Cr compared to Fe3Cr and Fe5Cr, which would be consistent with a slightly higher pre-existing dislocation density in the Fe10Cr material, as discussed above. The higher rate of yield strength increase for Fe10Cr, compared to Fe3Cr and Fe5Cr, between 0.008 dpa and 0.08 dpa, is consistent with increased retention of defects by the presence of Cr from a similar mechanism to irradiation hardening observed previously [193, 422].

These trends also agree with results from uniaxial stress-strain (USS) responses of neutron-irradiated Fe and FeCr [193, 524] (Figure 5.9). This demonstrates the usefulness of high-throughput nanoindentation techniques to reveal insights into material behaviour. The discrepancy between the absolute values of the two studies can be attributed to several factors. The material on which USS response was measured was irradiated by neutrons at around 573 K which could affect the defect evolution, compared to the materials in this study which was ion-irradiated at room temperature.

There have been numerous studies attempting to correlate indentation stress and strain values with the quantities obtained through bulk tensile testing. Huang *et al.* [532] provide a good review of the literature. Several factors lead to differences in the recorded stresses and strains, such that quantitative prediction of macroscopic stress-strain curves from nanoindentation remains challenging. An important factor is the role of lateral material constraint in indentation, which produces different stress states compared to uniaxial tests [391]. A consequence of this is the difficulty in extracting exact contact depth of the indenter due to the deformed shape of the material around the indenter [529]. Another key difference is the heterogeneity of material microstructure. In nanoindentation, the deformation is probed in, essentially, a single crystal, whereas bulk tensile testing is more indicative of polycrystalline behaviour [193, 524, 533, 534]. A consequence of this is that orientation dependence may affect results of nanoindentation testing, but not bulk tensile testing. Furthermore,

the indentation size effect, which is caused by both the presence of large plastic strain gradients and the nucleation of GNDs, is not found for bulk tensile testing [392]. For spherical indenters, this is a function of indenter size, rather than solely indentation depth as for sharp Berkovich indenters [535]. This size effect leads to a further increase of the measured yield strength in nanoindentation compared to uniaxial testing [536, 537].

Various factors have been proposed to account for these differences between ISS and macroscopic stress-strain curves. For Fe in particular, there is a range of proposed ratios, between 2.2 to 3.8, for the conversion between indentation yield stress and tensile yield stress [525–529]. Figure 5.9 shows this range of ratios applied to our data for all samples. This brings the absolute values of the yield strengths from the ISS response closer to the macroscopic values reported in [193] and [524]. Furthermore, the method of extrapolating the yield point may slightly over-estimate the yield strength as the gradient of the ISS curve near the yield point is often higher than the gradient at larger strains (Figure 5.8(d)).

The shape of the ISS curve in the flow portion gives insight into material work hardening. Past studies on irradiated Fe [524, 533, 534] have found that the work hardening response after yield is well-described by the Holloman relation:

$$\sigma = K\epsilon^n \tag{5.9}$$

where K is known as the strength coefficient and n is the work hardening exponent. The hardening exponent was calculated for the samples in this study and compared with previous studies [524, 533, 534] in Figure 5.10.

Reduced work hardening capacity is evident with increased irradiation dose for all Cr% compositions studied. After irradiation to 0.08 dpa, all samples show a similar level of reduced work hardening capacity. Considering that n decreased with Cr content for unirradiated samples, it appears the effect of irradiation dominates in the changes to work hardening capacity compared to any pre-existing effects due to different Cr content. The rate of decrease of n with irradiation dose agree with trends in literature for Fe and FeCr [524, 533, 534].

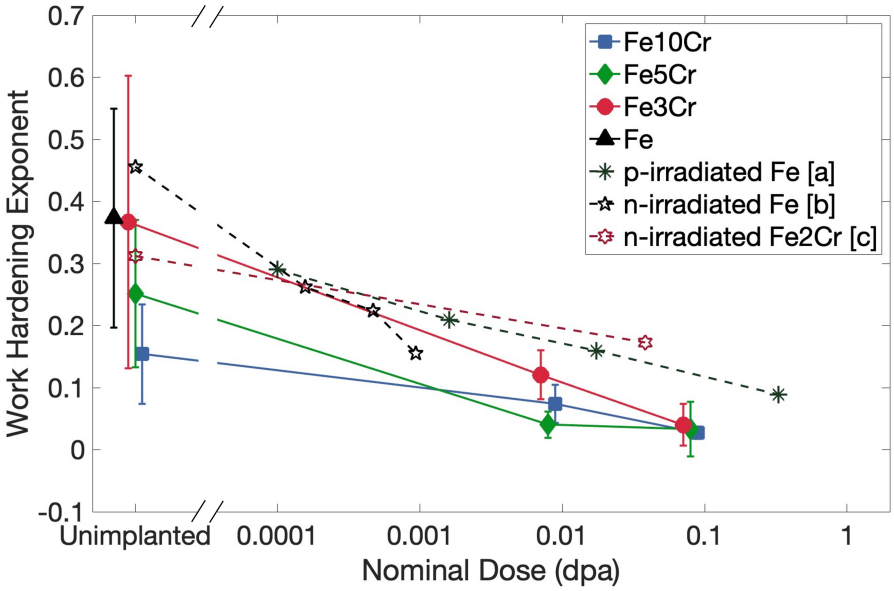


Figure 5.10: The work hardening exponent (n) fitted from the flow portion from the ISS response of FeCr materials as a function of dose level. The error bars show one standard deviation of the measurements. Experimental results from other studies of proton-irradiated Fe, neutron-irradiated Fe, and neutron-irradiated Fe2Cr are also shown for comparison. The raw data for [a–c] are from [524, 533, 534], respectively.

In a previous study, analysis of the ISS response and TEM imaging of the plastic zone under indents in ion-irradiated Fe12Cr revealed that strain softening beyond the yield point arises from the annihilation of irradiation defects by reactions with glide dislocations [406, 491]. This has also been previously observed following bulk tensile testing of irradiated Fe [524, 538]. In this study, the observed softening following deformation is also most likely due to the removal of defects by dislocation glide as slip steps in the pile-up topography visible around indents in the irradiated samples. The phenomenon of dislocation channelling leading to strain softening is also common for many irradiated material systems [129, 203, 539, 540].

5.4.3 Characterising Behaviour in the Initial Stages of Deformation

By combining the insights gathered from the nanoindentation pop-in trends and indentation stress-strain response studies, we can formulate a more coherent picture of the early stages of deformation and plasticity in irradiated FeCr.

In a volume of FeCr material free of pre-existing defects, homogeneous dislocation

nucleation occurs when the applied stress exceeds the theoretical strength of the material. When the lattice is exposed to ion irradiation, a dense population of nano-scale defects is formed [59, 109, 111]. In this study, the theoretical shear strengths of the materials are probed by studying maximum shear stress under a Berkovich indenter at the onset of plasticity (pop-ins). Our results show that even at low doses ($\leq$0.08 dpa), these act as local instabilities in the lattice, reducing the shear stress required to nucleate dislocations. Though the presence of Cr itself does not significantly affect the theoretical strength (Figure 5.3), Cr enhance the effect of irradiation defects by increasing their retention [109, 111]. This causes the larger drop in shear stress required for dislocation nucleation following irradiation for higher Cr% materials (Figure 5.4).

However, pre-existing heterogeneous dislocation sources, such as Frank-Read sources still play an important role in initiating plasticity in FeCr, as they generally require a lower stress for activation. One proposed mechanism for irradiation hardening is source hardening - whereby irradiation-induced defects cluster around pre-existing Frank-Read sources, causing the pinning or locking of dislocation lines. This increases the required stress to unlock these dislocations before they can multiply and initiate slip [84, 541]. By examining the initiation of plasticity with larger spherical tips (Figure 5.5), we are able to probe the activation of pre-existing dislocations in irradiated FeCr. Our results suggest that the source hardening contributions of irradiation defects at the dose levels examined (0.008–0.08 dpa) are quite low as the required applied stress for plasticity initiation from pre-existing sources is not significantly affected following irradiation.

Once the pre-existing sources have been activated, the ease of dislocation propagation in the material can be determined through the yield strength. This behaviour is examined through the ISS responses from spherical nanoindentation, in particular the plastic portion. The presence of Cr, even in unirradiated materials, increases the yield strength due to solid solution hardening. Following irradiation, the induced defects also act to hinder dislocation motion, further increasing the yield strength through friction hardening (also called lattice hardening) [521, 522, 542]. This finding is in line with early works on neutron-irradiated Fe and steels [543, 544]. Cr atoms

further enhance the friction hardening from irradiation defects by increasing the retention of irradiation-induced defects, causing a larger rate of increase of yield strength following irradiation for materials with high Cr content (Figure 5.9).

Irradiation also causes a reduction in work hardening capacity in FeCr due to the removal of defects by glide dislocations that form dislocation channels, similar to other works on irradiated Fe [129, 203]. This study shows that the effect of irradiation-induced defects dominates the reduction in work hardening, as samples of all Cr% compositions have similar work hardening exponent following irradiation to 0.08 dpa. This shows that the increased retention of defects due to higher Cr content between Fe3Cr and Fe10Cr does not have a significant effect on the amount of strain softening experienced by irradiated FeCr.

It appears that the presence of Cr and irradiation defects mainly affect the initial stages of plasticity in irradiated FeCr by hindering dislocation motion. The effect of irradiation dose level is enhanced by presence of Cr, due to increased retention of defects. This is significant in increasing the yield strength through friction hardening. To a lesser extent the presence of Cr and irradiation defects also hinders the nucleation of new dislocations. However, once the formation of dislocation channels occurs in the irradiated material, the effect of irradiation dose is more dominant regardless of Cr content.

5.5 Summary and Conclusion

Fe3Cr, Fe5Cr, and Fe10Cr have been irradiated with 20 MeV Fe^{3+} ions to nominal doses of 0.008 dpa and 0.08 dpa at room temperature. The effects of Cr content and irradiation dose on the initial stages of plasticity are studied using nanoindentation. We are able to separate the effects on initiation of plasticity and its early stages of progression by using indenters of different sizes and shapes. We conclude the following from our findings:

- From studying pop-in trends in Berkovich tip indentation, the theoretical shear strength - how easily the crystal lattice shears, is probed. The presence of

irradiation-induced defects reduces the theoretical shear strength of irradiated FeCr by reducing the barrier shear stress required for dislocation nucleation.

- The presence of Cr acts to increase the retention of irradiation-induced defects and causes the largest reduction in the shear stress required to initiate plasticity from the nucleation of dislocations.

- The unlocking of pre-existing dislocation sources, such as from Frank-Read sources, are still dominant for the initiation of plasticity. This is studied through pop-in trends in spherical indentation. The presence of irradiation defects and Cr content does not significantly affect the operation of these pre-existing sources.

- From the indentation stress-strain responses, the yield strength of the FeCr materials are determined, which gives insight into how easily dislocations, once nucleated or unlocked, move through the materials. The yield strength is found to increase with both Cr content and irradiation dose. The increased retention of irradiation-induced defects due to the presence of Cr further increases the yield strength. These trends agree with uniaxial stress-strain responses of neutron-irradiated FeCr material [193, 524].

- A decrease in work hardening is found following irradiation, which is quantitatively similar to previous irradiation studies [524, 533, 534]. However, the effect of Cr content is negligible after irradiation, where the irradiation-induced defect population seems to play a more dominant role in reducing work hardening capacity.

- This highlights the usefulness of nanoindentation for gaining mechanistic insights into the competing effects that control the initiation and evolution of plasticity in irradiated materials.

Data Availability

All data, raw and processed, as well as the processing and plotting scripts are available at: https://doi.org/10.5287/bodleian:Nom6Ygbbz

6

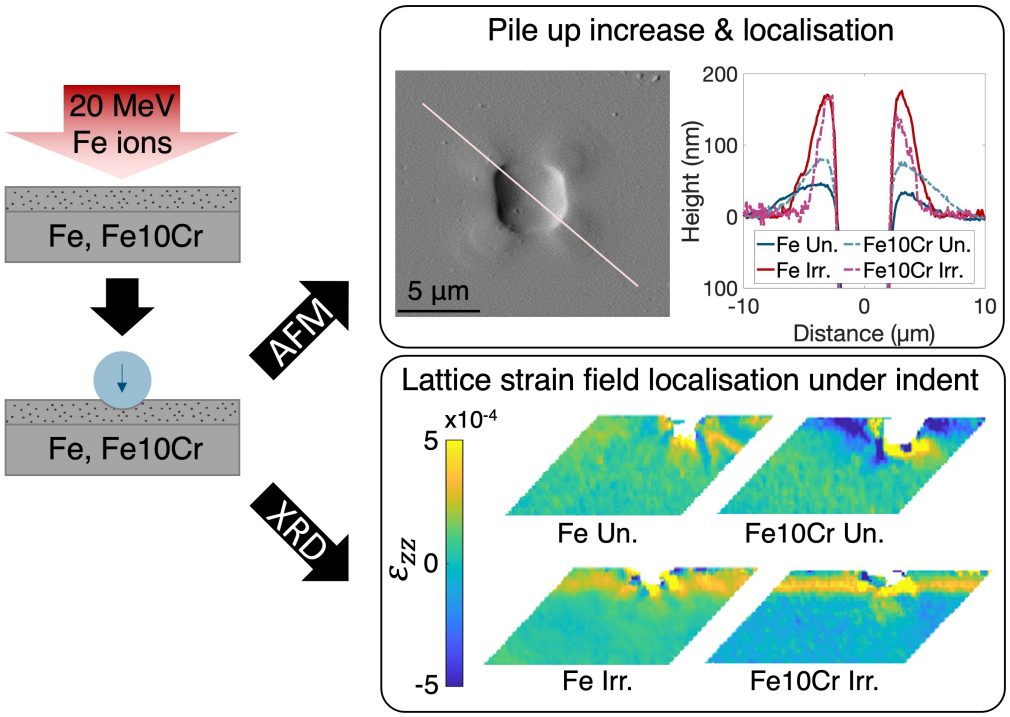
Deformation Localisation in Ion-Irradiated FeCr

Following the findings of irradiation-induced loss of strain hardening capacity in FeCr from Chapter 5, the next question is how the deformation fields associated with nanoindentation are affected by this. Even though irradiation-induced deformation localisation has been studied in other materials [15, 343, 540, 545–547], the mechanisms responsible for this remain unclear and little explored in FeCr. This study considers the effect of room-temperature ion irradiation on the deformation structures of Fe and Fe10Cr. The characterisation of the nanoindents and surrounding deformation fields with non-destructive 3D X-ray Laue diffraction and atomic force microscopy was performed to reveal the effect of irradiation and Cr content on deformation localisation in FeCr.

The contents of this chapter have been published as: K. Song, D. Sheyfer, W. Liu, J. Z. Tischler, S. Das, K. Mizohata, H. Yu, D. E. J. Armstrong, F. Hofmann "Deformation localisation in ion-irradiated Fe and Fe10Cr", *Journal of Nuclear Materials*, vol. 596, 155104, 2024 [548]. D. Sheyfer and W. Liu collected all DAXM data. J. Z. Tischler assisted with the analysis of DAXM data by providing the LaueGo software. S. Das provided the Matlab code for DAXM data analysis and visualisation. K. Mizohata assisted with the ion irradiation and helped with the design of the temperature-controlled sample holder (further detailed in Appendix A).

H. Yu assisted with sample polishing. The remainder of the work was carried out by the author with the supervision of D. E. J. Armstrong and F. Hofmann.

6.1 Abstract



Graphical Abstract

Irradiation-induced ductility loss is a major concern facing structural steels in next-generation nuclear reactors. Currently, the mechanisms for this are unclear but crucial to address for the design of reactor components. Here, the deformation characteristics around nanoindents in Fe and Fe10Cr irradiated with Fe ions to ∼1 displacement-per-atom at 313 K are non-destructively studied. Deformation localisation in the irradiated materials is evident from the increased pile-up height and slip step formation, measured by atomic force microscopy. From 3D X-ray Laue diffraction, measurements of lattice rotation and strain fields near the indent site show a large confinement, over 87%, of plasticity in the irradiated material. We find that despite causing increased irradiation hardening, Cr content has little effect on the irradiation-induced changes in pile-up topography and deformation fields. The

results demonstrate that varying Cr content in steels has limited impact on retaining strain hardening capacity and reducing irradiation-induced embrittlement.

6.2 Introduction

Understanding the mechanical behaviour of structural materials is essential for the design and operation of next-generation nuclear reactors. Reduced-activation ferritic/martensitic steels are promising candidates due to their resistance to irradiation swelling and good thermomechanical properties [16]. Nevertheless, neutron irradiation in reactor environments will still lead to increased hardening and reduced ductility of structural steels [166, 455]. Studies into the effect of microstructure and composition to mitigate these irradiation-induced changes are crucial [40, 42, 549].

A well-known phenomenon following the deformation of irradiated materials is deformation localisation [15, 343, 540, 545–547]. The accepted mechanism is that glide dislocations annihilate irradiation-induced defects [196, 197]. This creates easy glide channels with a locally reduced density of irradiation-induced defects that confine subsequent deformation [201]. The formation of these channels contributes to irradiation embrittlement and irradiation-assisted stress corrosion cracking [164].

Presently, the exact details of the mechanisms by which irradiation defects are removed still remain unclear. This is an active area for modelling and simulations [550–552]. However, there is a lack of experimental investigations to validate modelling predictions. TEM is a common way to directly observe dislocation microstructures and channels [129, 553, 554]. However, TEM is unable to provide information, especially in 3D, on the local stress and strain states, which are key to compare with simulations. A non-destructive method such as X-ray diffraction can uniquely provide information over a greater volume and in 3D [381, 555].

Here, we consider the deformation microstructure around nanoindents in Fe and Fe with 10%Cr by weight, hereafter referred to as Fe10Cr, for both the unirradiated material and following irradiation with Fe ions at 313 K. This allows the study of the effect of irradiation and Cr content. Surface topography around the indent site was examined with atomic force microscopy (AFM). 3D lattice rotation and

strain fields under the surface were probed by X-ray Laue diffraction. The samples used in this study are the same as those in previous studies of irradiation-induced lattice strain, thermal and mechanical properties [422, 469, 556]. The materials from which the samples are taken have also been investigated extensively in other irradiation studies [59–65]. This is important, as it helps to build a comprehensive understanding of the different aspects of irradiation damage whilst maintaining consistent sample processing and irradiation history [208].

6.3 Sample Preparation and Ion Implantation

The Fe and Fe10Cr materials were manufactured under the European Fusion Development Agreement (EFDA) programme (contract EFDA-06-1901) and their chemical composition is listed in Table 6.1. The materials were made by induction melting under an argon atmosphere followed by cold-forging and heat treatments [66, 67].

Alloy	Cr (wt %)	C (wppm)	S (wppm)	O (wppm)	N (wppm)	Grain Size (µm)
Fe	<0.0002	4	2	4	1	187 ± 150
Fe10Cr	10.10	4	4	4	3	98 ± 55

Table 6.1: Manufacturer-provided chemical compositions as measured by glow discharge mass spectrometry [66, 67].

The samples were mechanically ground with SiC paper, and then polished with diamond suspension and colloidal silica (0.04 µm). Finally, they were electropolished using 5% perchloric acid in ethanol with 15% ethylene glycol monobutyl ether, at 293 K for 2–3 minutes using a Struers LectroPol-5. The voltage applied was 45 V for Fe and 30 V for Fe10Cr.

Ion irradiation was performed with 20 MeV Fe^{4+} ions using the tandem accelerator at the University of Helsinki. The samples were actively held at 313 K during irradiation. The dose profile shown in Figure 6.1(a) was calculated with SRIM using the Quick K-P model [80] with 20 MeV Fe ions on a Fe target with 40 eV displacement energy [460] at normal incidence. The calculated damaged layer extends to 3.5 µm below the sample surface. The average dose in the top 580 nm, which is the maximum indentation depth (including creep), is 0.46 displacements-per-atom

(dpa). The damage profile peaks at 5 dpa at a depth of 3 µm. The average dose of the whole damage layer is 1.7 dpa.

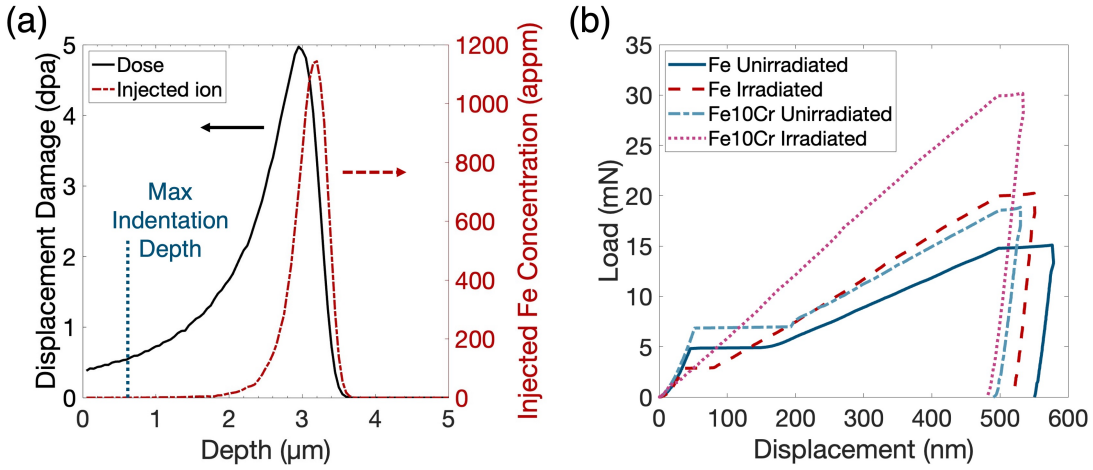


Figure 6.1: (a) The irradiation damage and injected ion profiles as calculated by SRIM [80]. (b) Representative load-displacement curves from each material.

6.4 Nanoindentation and Atomic Force Microscopy

Consistent grain orientation across different samples is important as the pile-up morphology is expected to show orientation dependence from previous studies of body-centred cubic (BCC) materials [342, 557]. Those studies also found that pile-up heights are the most sensitive to irradiation-induced changes when indenting along the ⟨001⟩ direction. In this study, electron backscatter diffraction was used to identify grains within 5° of ⟨001⟩ out-of-plane orientation on each sample for investigation with AFM and X-ray Laue diffraction. Further information about the grain orientations can be found in Appendix E.1.

Nanoindentation was performed using an MTS Nano Indenter XP with a spherical diamond tip of 5 µm nominal radius (Synton-MDP). Load-controlled indentation was performed to a nominal depth of 500 nm, with a hold segment of 10 s before unloading. The indentation depth was chosen to be less than 20% of the damaged layer thickness to ensure that a majority of the plastic zone is contained in the irradiated layer [432, 558].

The load-displacement curves (Figure 6.1(b)) for all materials show similar initial Hertzian elastic contact segments. Pop-in events occurred in all samples, and the irradiated samples show lower pop-in loads than the unirradiated samples possibly due to irradiation defects acting as extra sources of dislocation nucleation [469, 486, 513].

Analysis of the peak loads of at least 6 indents on each sample was performed to obtain an indication of the material hardness. Large pop-in loads were often observed for the unirradiated materials due to low populations of pre-existing dislocations. As a result, many indentation tests on the pre-identified grains exceed 500 nm in depth, and could not be used.

Solid solution hardening in the unirradiated materials is observed from a 20% (±6%) increase in peak load between Fe and Fe10Cr. Irradiation results in a 21% (±8%) increase in peak load for Fe and a 43% (±7%) increase for Fe10Cr. This agrees with hardness trends from previous measurements with Berkovich nanoindentation, which show a 31% (±5%) increase for Fe and a 48% (±7%) increase for Fe10Cr following irradiation [452]. The creep distance from holding the peak load is greater in Fe than Fe10Cr for both the unirradiated and irradiated materials.

Pile-up topography around the indent sites (Figure 6.2) was measured with a Veeco MultiMode 8 atomic force microscope (AFM) in ScanAsyst^{TM} mode. There is a four-fold symmetry in the pile-up pattern due to the indents being made on grains with close to ⟨001⟩ out-of-plane orientation. The pile-up lobes are oriented along the ⟨110⟩ directions, which has been previously observed in other BCC materials [342, 557, 559, 560].

For the unirradiated samples, the pile-up height increases with the addition of Cr from 37±10 nm for Fe to 74±9 nm for Fe10Cr. Pile-up has been found to increase with decreasing strain hardening exponents [396, 561, 562]. This suggests that the presence of Cr reduces strain hardening capacity. Indeed, this is consistent with our previous study of the same materials [469], which shows from nanoindentation stress-strain curves that strain hardening capacity decreases with Cr content in unirradiated FeCr.

Pile-up height increases after irradiation for Fe and Fe10Cr to 169 ± 5 nm and 154 ± 25 nm, respectively. The increase in average pile-up height is consistent with previous findings of irradiation-induced strain hardening capacity reduction

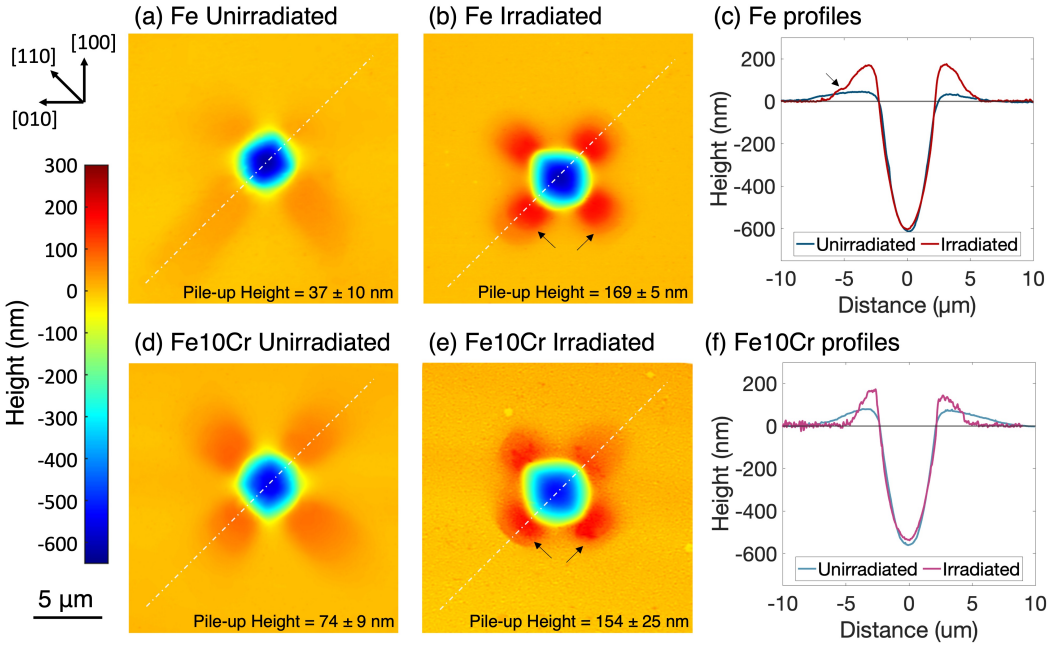


Figure 6.2: The pile-up topography surrounding the indent site for (a) unirradiated Fe and (b) irradiated Fe. The average pile-up heights were calculated from repeated measurements of the 4 pile-up lobes surrounding each indent, with the associated standard deviations shown. The white dashed line indicates the profile of pile-up height taken from the measurements and shown in (c). The same layout for Fe10Cr is shown in (d)–(f). Black arrows indicate evidence of slip steps (further details in Appendix E.2).

[405, 469, 563]. The presence of Cr has little effect on the pile-up height following irradiation. This is consistent with previous findings from stress-strain studies of the same materials, where strain hardening exponents were reduced to zero regardless of Cr content, even for a dose that is 90% lower than the current study [469]. Hardie *et al.* [211] also observed an increase in pile-up height for Fe12Cr following irradiation to 6.18 dpa. However, the orientation of the grains was not specified, which is known to significantly affect pile-up behaviour [342, 557, 564].

The pile-up topography is more localised in the irradiated samples, only extending to ± 5 µm on either side of the indent centre along the ⟨110⟩ direction (Figure 6.2(c) and (f)). In contrast, the lobes of the unirradiated materials extend up to 10 µm away from the indent. Slip steps are also observed in the pile-up of the irradiated material (black arrows in Figure 6.2(b), (c), and (e)). Hardie *et al.* [210] previously found that slip steps on the surface of ion-irradiated Fe12Cr result from shear bands beneath the surface, associated with defect-free channels in the irradiated layer. These channels

lead to irradiation-induced strain softening and localisation of deformation [538].

6.5 X-ray Measurements of Lattice Rotation and Strain

Lattice rotation and strains around the nanoindents were measured with micro-beam X-ray Laue diffraction at the 34-ID-E beamline at the Advanced Photon Source (Argonne National Laboratory, IL, USA). Differential Aperture X-ray Microscopy (DAXM) was used to obtain depth resolution into the surface of the material. The technique has been described in detail elsewhere [177, 374, 375]. Here, the sample was mounted in a 45° reflection geometry. The polychromatic incident beam ($7-30$ keV) is focused on the sample surface with a size of 170×240 nm^2. For each sample, a $30 \times 40 \times 20$ µm^3 volume was probed with $1.1 \times 1.5 \times 1$ µm^3 3D spatial resolution. Due to the sample mounting geometry, the path of the beam was at 45° to the sample surface. Hence the edges of the volume probed by X-rays is also confined by that angle (Figure 6.3 and 6.4). Further details of the set-up are included in Appendix E.3.

The orientation distribution and strain refinement calculations [379] were performed using LaueGo [565]. The calculation of lattice rotation from the orientation of each voxel, data interpolation, and visualisation of the lattice rotation and strain field were performed with code modified from [343, 381]. The reference lattice orientation was calculated from the average orientation between 18–20 µm below the sample surface.

The lattice rotations in the unirradiated Fe extend to over 20 µm away from the indentation site (Figure 6.3(a)). There is a long 'streak' present in the θ_x map, similar to previous measurements in tungsten [381]. The rotation fields of Fe10Cr (Figure 6.3(c)) are similar in spatial extent and distribution to Fe.

The rotation field induced by indentation in the irradiated samples is more localised than in the unirradiated material. This is particularly noticeable for the Fe sample (Figure 6.3(b)), where the rotation field is confined to the top 5 µm in the $\boldsymbol{z}$-direction, and ∼7 µm in the $\boldsymbol{x}$- and $\boldsymbol{y}$-directions. The distribution of lattice rotations in the irradiated Fe10Cr sample (Figure 6.3(d)) is similar to the irradiated

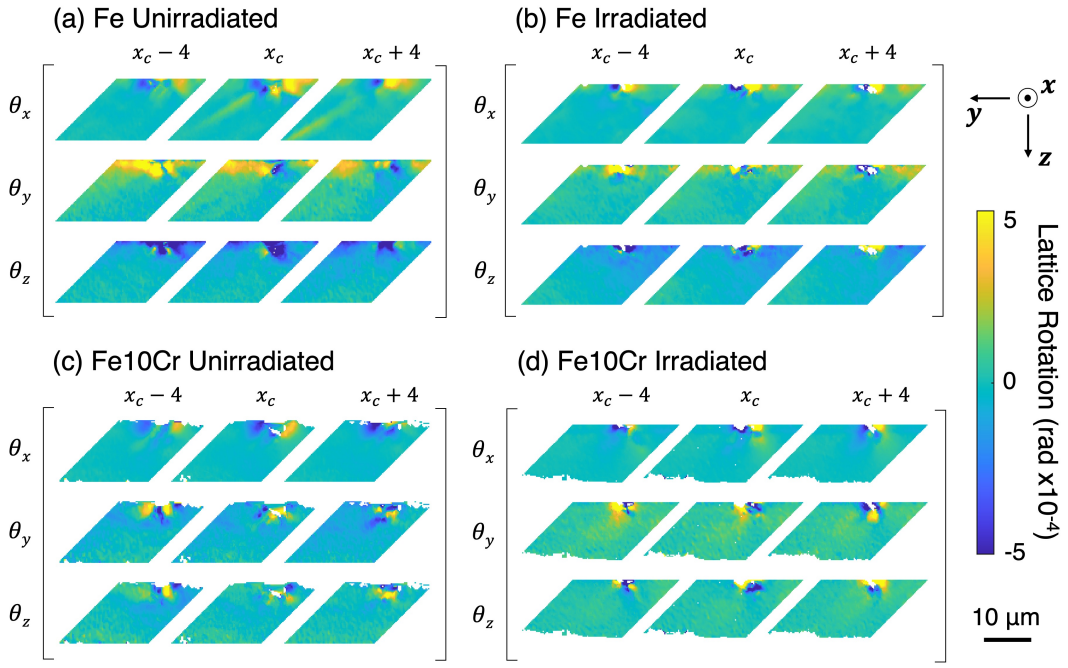


Figure 6.3: The lattice rotation under the indent for the different samples in this study. The $\boldsymbol{x} - \boldsymbol{y}$ plane is parallel to the surface of the bulk sample, while $\boldsymbol{z}$ points into the bulk material. For each sample, the lattice rotations components (θ_x, θ_y, and θ_z) are presented from 3 slices (parallel to the $\boldsymbol{y} - \boldsymbol{z}$ plane). The middle slice ($x = x_c$) is taken through the centre of the indent. The slices on either side are at a distance of 4 µm from the centre in the $\boldsymbol{x}$-direction.

Fe, with some extended regions of smaller lattice rotations ($|\theta| < 3 \times 10^{-4}$ radians) up to 10 µm from the indent centre. This represents a reduction of over 87% of the volume containing lattice rotations. This is the same ratio as determined by the lateral extent of pile-up from AFM measurements, even though the absolute radius of the deformed volume measured by X-ray diffraction is twice as large.

The spatial distribution of tensile (positive) and compressive (negative) strain is similar between the unirradiated samples of Fe and Fe10Cr (Figure 6.4). However, the spatial extent and magnitude of strain, both tensile and compressive, are greater in Fe10Cr than in Fe. This could be attributed to the greater peak load applied to Fe10Cr to reach the same indentation depth as in Fe (Figure 6.1(b)), due to greater yield strength, which in turn leads to greater residual stresses.

After irradiation, there is a large tensile strain in the $\boldsymbol{z}$ direction for Fe and Fe10Cr at a depth of ∼3 µm (Figure 6.4(b) and (d)). This is likely due to the presence of injected Fe ions from irradiation, as previously observed [422, 556].

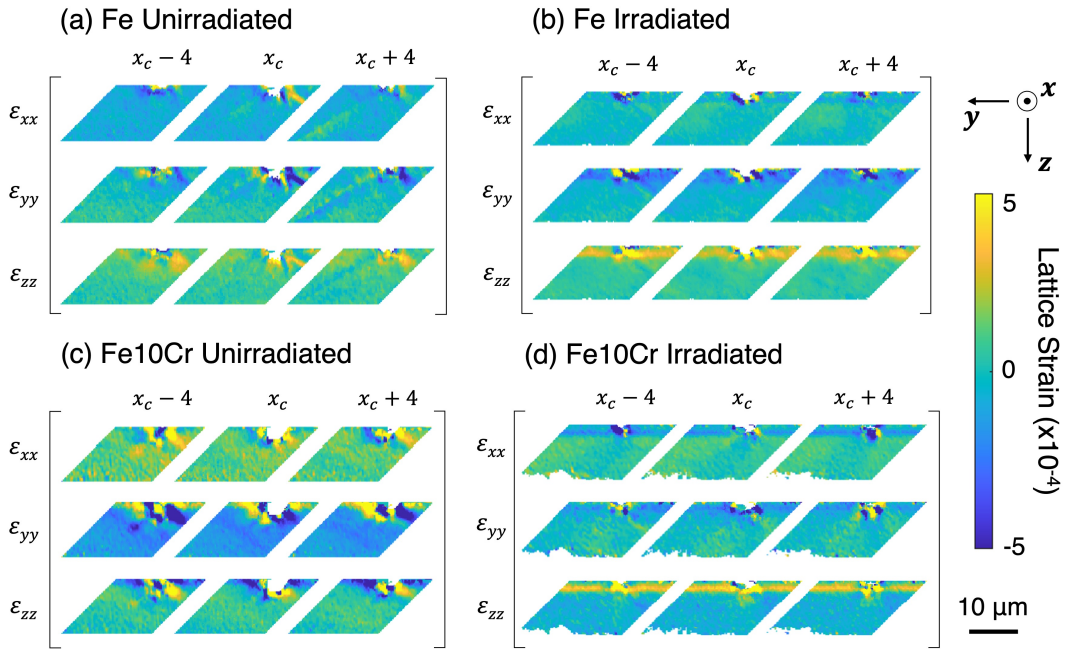


Figure 6.4: The 3 principal components of the deviatoric strain tensor, ϵ_{xx}, ϵ_{yy}, and ϵ_{zz} in the samples. The orientation of the measurements and the slicing convention are the same as described in Figure 6.3.

There is a corresponding compressive strain of lower magnitude in the $\boldsymbol{x}$- and $\boldsymbol{y}$-directions. Furthermore, the magnitudes of ϵ_{xx} and ϵ_{yy} are similar, which is consistent with irradiation-induced lattice swelling and the presence of the external boundary condition requiring geometric continuity between the irradiated layer and the unirradiated bulk [177].

For both the irradiated Fe and Fe10Cr materials, the spatial extent of the strain field beneath and surrounding the indent is mostly restricted in the $\boldsymbol{z}$-direction to the top 3–4 µm (Figure 6.4(b) and (d)). The containment of the strain field is largely within the irradiated layer, with rapidly vanishing strains at depths beyond that. Similar to lattice rotation fields, the extent of the strain fields in the $\boldsymbol{x}$- and $\boldsymbol{y}$-directions is also reduced following irradiation for both Fe and Fe10Cr. It appears that the presence of 10% Cr content does not significantly affect the strain states following irradiation and deformation. This is despite a ∼50% increase in applied load for the irradiated Fe10Cr material to achieve the same indentation depth as the irradiated Fe sample.

The localisation of lattice rotation and strain fields in the irradiated Fe and

Fe10Cr is consistent with previous observations of plastic zone confinement in irradiated Fe12Cr [210, 211]. From TEM lift-outs taken through indent cross-sections, it was observed that the spatial extent of dislocation propagation reduced by 24–31% in the irradiated material.

6.6 Discussion

Combining the nanoindentation, AFM, and DAXM measurements, we can formulate a comprehensive picture of plasticity in ion-irradiated Fe and Fe10Cr. Without irradiation, the presence of Cr causes solid solution hardening. This necessitates a greater indentation load for Fe10Cr than Fe to reach the same indentation depth. As such, the residual strains are greater. Furthermore, the presence of Cr also reduces the strain hardening capacity of the material, which leads to a greater pile-up height in Fe10Cr.

Ion irradiation introduces defects in the material that act as obstacles to glide dislocations, causing hardening. Even though the inclusion of 10%Cr causes a similar amount of net hardening as introducing irradiation defects in Fe, the respective pile-up topography and residual lattice rotation and strain fields are very different. The great increase in pile-up height due to irradiation ($\sim$450% for Fe) reflects a dramatic reduction in strain hardening capacity, as previously observed from nanoindentation stress-strain curves of the same materials [469]. In comparison, the pile-up height only increases $\sim$200% from the addition of 10%Cr to Fe in the unirradiated case, despite showing similar hardening. The mechanism of strain softening in the irradiated material can be explained by the observation of slip steps, an indication of dislocation channelling, which provides paths for subsequently-generated glide dislocations to move at a lower stress. Irradiation-induced strain softening also causes a corresponding localisation of pile-up topography, further indicating deformation localisation. We directly observed plastic zone confinement of over 87% in the irradiated materials from the localisation of lattice strain and rotation fields surrounding the indents.

The effect of Cr on the post-irradiation deformation behaviour is limited. Even though the irradiation-induced hardening is much greater in Fe10Cr than in Fe, the height and spatial extent of the pile-up topography are very similar for both irradiated materials. This supports previous observations that post-irradiation reduction in strain hardening capacity does not depend on Cr [469]. In this study, we also observed the effect of this on the lattice rotation and strain fields in both Fe and Fe10Cr, which are reduced to similar extents following irradiation. The 3D measurements in this study also provide valuable comparisons for future modelling studies, which will be crucial to understanding the mechanical properties of reactor structural materials in operation.

6.7 Conclusion

In summary, deformation localisation has been characterised in ion-irradiated Fe and Fe10Cr following nanoindentation. Following irradiation, there is an increase in pile-up height, localisation of the pile-up topography, and formation of slip steps. Lattice rotation and strain fields surrounding the indent in the irradiated material are confined to a volume less than 13% of that in the unirradiated materials. In practice, the localisation of deformation and the confinement of plastic zones means that a material is less able to absorb energy associated with deformation, leading to embrittlement. Despite significant differences in irradiation hardening, the irradiated Fe and Fe10Cr materials show very similar pile-up topography and deformation fields. Our results suggest that Cr content does not seem to mitigate the loss of strain hardening capacity. This means that strategies other than varying the composition of steels are required to retain post-irradiation ductility, a key consideration to guide the design of future reactor component materials.

Data Availability

All data, raw and processed, as well as the processing and plotting scripts used in this study are available online at: https://doi.org/10.5281/zenodo.11059510

7

Microstructural and Material Property Changes in Severely Deformed Eurofer-97

The previous studies on FeCr in this thesis has demonstrated a range of techniques to characterise the deformation and irradiation behaviour of FeCr alloys. This chapter applies these methods, along with more detailed microstructural characterisation, to Eurofer-97, a prototypical RAFM steel. To advance the development of structural steels, SPD-processing of Eurofer-97 was carried out to determine whether grain refinement can be a potential method to improve the irradiation resistance of the material.

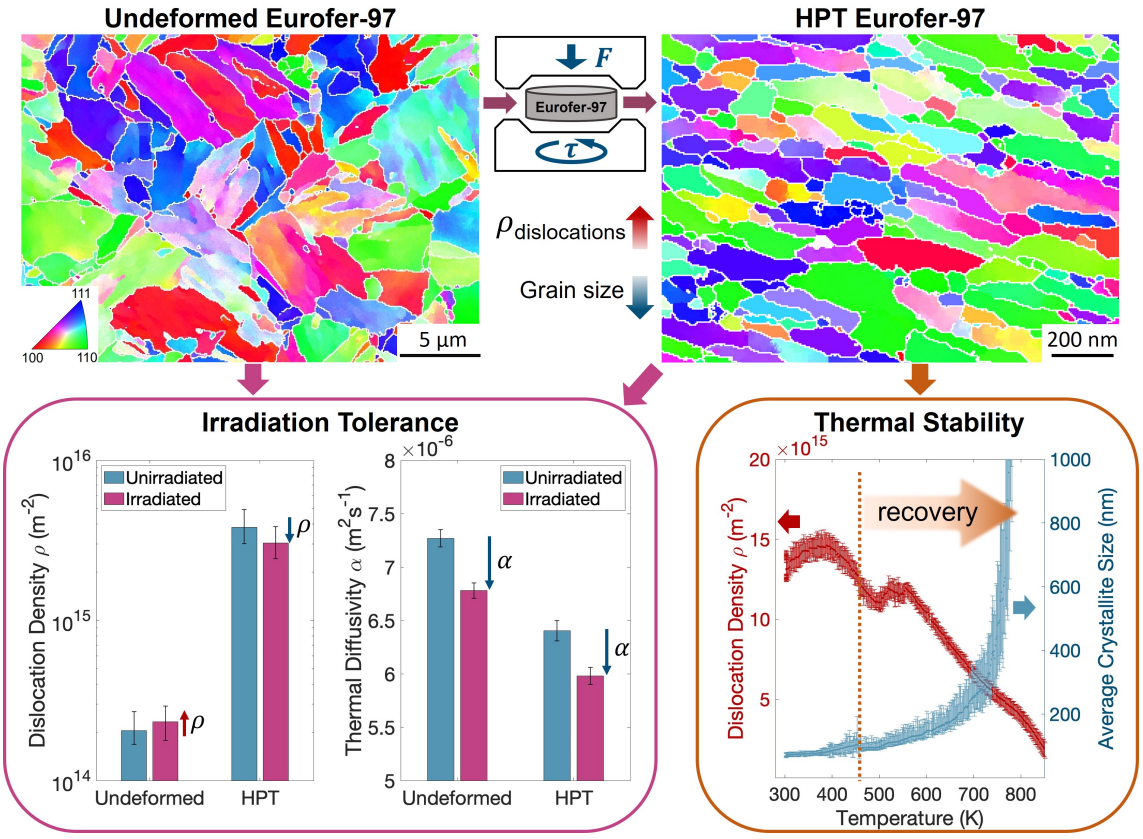
This chapter is a combination of two manuscripts. A majority of the results from this chapter has been published as: K. Song, G. He, A. Reza, T. Ungár, P. Karamched, D. Yang, I. Tolkachev, S. Thompson, E. Connolly, R. Atwood, S. Michalik, K. Mizohata, D. E. J. Armstrong, F. Hofmann, "Microstructural and material property changes in severely deformed Eurofer-97", *Materials Characterization*, vol. 215, 114144, 2024 [566]. The nanoindentation section of this chapter has been published as: G. Strangward-Pryce, K. Song, K. Mizohata, F. Hofmann, "The effect of high-pressure torsion on irradiation hardening of Eurofer-97", *Nuclear Materials and Energy*, vol. 36, 101468, 2023 [567].

The nanoindentation work [567] was carried out as a part of a summer project with G. Strangward-Pryce. The nanoindentation data collection and analysis was jointly carried out by the author and G. Strangward-Pryce. The extent to which the paper has been included in this chapter is in Section 7.4.3. The data has been

re-plotted (Figure 7.11) based on the published results. All the discussions of the nanoindentation results in this chapter have been written by the author.

G. He performed all TEM imaging and EDX analysis. G. He and P. Karamched assisted with TKD data collection and jointly performed all FIB milling. A. Reza collected and analysed all TGS data. T. Ungár assisted with data analysis using CMWP. D. Yang, I. Tolkachev, S. Thompson, E. Connolly, R. Atwood, and S. Michalik assisted with XRD data collection. K. Mizohata performed the ion irradiation. The remainder of the work was carried out by the author with the supervision of D. E. J. Armstrong and F. Hofmann.

7.1 Abstract



Graphical Abstract

Severe plastic deformation changes the microstructure and properties of steels, which may be favourable for their use in structural components of nuclear reactors. In this study, high-pressure torsion (HPT) was used to refine the grain structure of

Eurofer-97, a ferritic/martensitic steel. Electron microscopy and X-ray diffraction were used to characterise the microstructural changes. Following HPT, the average grain size reduced by a factor of ∼30, with a marked increase in high-angle grain boundaries. Dislocation density also increased by more than one order of magnitude. The thermal stability of the deformed material was investigated via in-situ annealing during synchrotron X-ray diffraction. This reveals substantial recovery between $450 - 800$ K. Irradiation with 20 MeV Fe ions to 0.08 dpa caused a 20% reduction in dislocation density compared to the as-deformed material. Prior deformation via HPT causes subsequent irradiation softening at 0.008 dpa. However, HPT deformation prior to irradiation to 0.08 dpa does not have a significant effect in mitigating the irradiation-induced reductions in hardness, thermal diffusivity and surface acoustic wave velocity of the material. These results provide a multi-faceted understanding of the changes in ferritic/martensitic steels due to severe plastic deformation, and how these changes can be used to alter material properties.

7.2 Introduction

A key challenge for next-generation nuclear power is the development and processing of highly radiation-resistant materials for structural components [19]. Reduced activation ferritic/martensitic steels, such as Eurofer-97, are leading candidates due to their favourable mechanical and thermal properties [35], as well as good resistance to void swelling [15]. While the exchange of Mo, Nb, and Ni for W and Ta in Eurofer-97 helps to achieve low activation capability [18], the material still suffers from irradiation-induced changes such as hardening and embrittlement, which affect its performance below 600 K [160].

Recently, nanostructuring and grain refinement via severe plastic deformation (SPD) has been proposed as a potential method for increasing the radiation tolerance of materials [316]. The goal for a radiation-resistant material is for its structure and properties to remain stable, or unchanged, under irradiation. It is proposed that SPD increases the density of grain boundaries in the material, which act as sinks for

irradiation-induced defects such as vacancies and interstitials, removing them from the bulk material and reducing their overall effect on the material properties [317].

The effects of SPD on the irradiation response of structural steels include reducing irradiation-induced segregation of alloyed solutes [321, 322], reducing the population of irradiation-induced defects [324], and lowering irradiation hardening [334]. Some studies have shown that grain refinement can suppress irradiation-induced void swelling by over an order of magnitude [326, 329]. However, Aydogan *et al.* [330] have found higher swelling near the surface region (top 1 µm) in the irradiated SPD material compared to the as-annealed material.

The suitability of grain refinement by SPD for increasing radiation resistance of structural steels is also unclear due to the varying compositions and crystal structures between different steels. For example, in face-centred cubic (FCC) materials, the grain refinement mechanism depends greatly on the stacking fault energy and twinning. However for body-centred cubic (BCC) materials, the results of SPD depend more on dislocation slip and the plasticity of the individual material [264, 568]. The range of conditions over which SPD can be carried out (method of deformation, temperature, pre-/post-annealing treatments) can also affect the final grain refinement and resultant material properties [230, 316]. Furthermore, the process of SPD itself also changes the properties of steels by increasing yield strength but reducing ductility, which will affect their operational performance [264, 299]. Previous studies on austenitic (FCC) stainless steels have found less irradiation hardening in SPD-processed materials compared to coarse-grain materials [332, 333]. A study in ferritic (BCC) steels found similar results [334], but the literature is limited. Therefore, more comprehensive studies of the combined effect of SPD and irradiation are warranted in light of its potential use to modify nuclear structural materials. In particular, there are comparatively fewer studies in the literature on the effect of SPD on ferritic/martensitic steels, and subsequent irradiation response, compared to austenitic steels [230, 264]. As such, the study of Eurofer-97, a prototypical ferritic/martensitic steel is particularly interesting.

High-pressure torsion (HPT) is a method which subjects materials to a compressive force and simultaneous torsional straining. It is an effective method of producing

nanocrystalline materials with grain sizes less than 100 nm [227]. HPT produces a disc with radially increasing shear strain, γ, from 0 at the centre of the disc to:

$$\gamma = \frac{2\pi N r}{h} \tag{7.1}$$

where N is the number of rotations, r is the distance from the centre of the disc, and h is the thickness of the disc [227]. As such, a range of strains can be accessed within the same sample.

Here we present a study on the effect of HPT, performed at room temperature, on the microstructure, thermal stability, and irradiation response of Eurofer-97. A range of experimental characterisation techniques including electron microscopy, X-ray diffraction, nanoindentation, and transient grating spectroscopy were carried out. The results allow us to study the evolution of grain size, dislocation density and character as a function of deformation, annealing temperature, and irradiation. Hardening due to HPT and irradiation, both individually and in combination, were measured. The thermal transport and elastic properties of the deformed and irradiated materials were also probed. Considering the combination of these results, a multi-faceted picture of the effect of HPT on the structure and properties of Eurofer-97, as well as its thermal stability and irradiation response, emerges. This in turn allows us to examine the effectiveness of SPD as a means of enhancing the radiation resistance and material properties of Eurofer-97 as a nuclear structural component.

7.3 Materials and Methods

7.3.1 Sample Preparation

The Eurofer-97 material was provided by the UK Atomic Energy Authority. The original 4 mm thick plate was produced by Böhler Bleche GMBH (Heat 993394) [37]. After hot rolling, the material was normalised at 1253 K for 10 minutes and then tempered at 1033 K for 1.5 hours. The manufacturer-provided composition is shown in Table 7.1.

Samples were cut into discs of 5 mm diameter and 1 mm thickness. HPT was performed using a Zwick Roell Z100 Materials Testing machine in a quasi-constrained

Element	Cr	W	V	Ta	C	Mn	N	Fe
wt%	9.08	1.07	0.24	0.13	0.11	0.56	0.04	Bal.

Table 7.1: The chemical composition of Eurofer-97 with all values in wt% [37].

set-up [227] with custom-made anvils made from M42 tool steel. The samples were compressed with 80 kN of force (∼4 GPa pressure), and 9 complete rotations were performed while maintaining this force. The final specimen thickness after HPT is 0.5 mm. Undeformed samples were also retained as reference specimens. Shear strains investigated for the specimens in this study range from 0 at the centre of the disc to 280 at the edge of the disc.

All samples were mechanically ground with SiC paper, then polished with diamond suspension and colloidal silica (0.04 µm). The final polishing step was electropolishing with 5% perchloric acid and 15% ethylene glycol monobutyl ether in ethanol at 293 K, with a voltage of 30 V for 2–3 minutes using a Struers LectroPol-5.

7.3.2 Ion Irradiation

Irradiation with 20 MeV Fe^{4+} ions at room temperature was performed using the tandem accelerator at the Helsinki Accelerator Laboratory. Both the HPT-processed and undeformed samples were irradiated. The dose profile was calculated using the Quick K-P model in the SRIM code [80], using 20 MeV Fe ions on a Fe target with 40 eV displacement energy at normal incidence (Figure 7.1). The calculated damaged layer extends to 3.5 µm below the sample surface. The average dose in the first 2 µm below the surface, where the injected ion concentration is small, is 0.08 displacements-per-atom (dpa). The peak dose is 0.5 dpa at a depth of 3 µm and the average dose across the whole implanted layer (from 0 to 3.5 µm depth) is 0.17 dpa.

An extra set of samples were irradiated to a total ion fluence 10% of the previously described conditions. This set was only used in the nanoindentation experiments and the dose levels will be referred to as 0.08 dpa and 0.008 dpa, respectively, to be consistent with dose naming conventions of previous studies [422,

469, 556]. All discussions in this study, with the exception of nanoindentation results, will only describe the 'irradiated sample', which corresponds to the higher dose (0.08 dpa). Both these doses fall into the transition regime before the onset of defect microstructure saturation in ferritic materials [148, 422, 556].

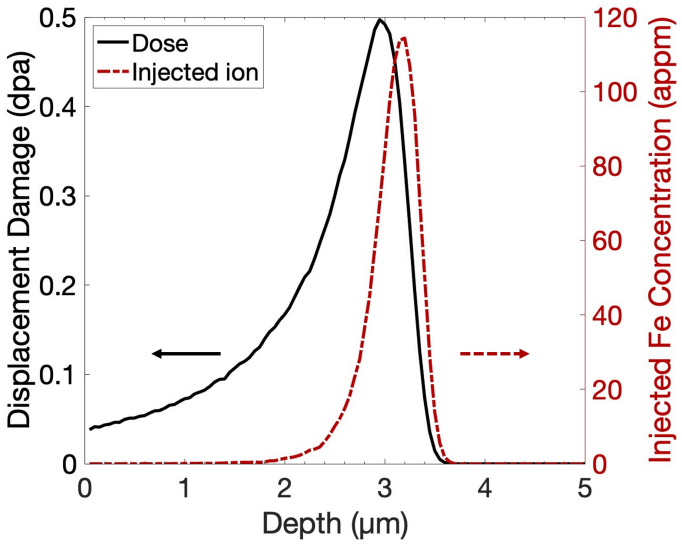


Figure 7.1: The calculated dose and injected ion profile from SRIM [80] for 20 MeV Fe ion irradiation on Fe target.

7.3.3 Electron Microscopy

SEM-based characterisation was carried out using a Zeiss Merlin FEG-SEM at the David Cockayne Centre for Electron Microscopy, University of Oxford. Backscattered electron (BSE) imaging was used for qualitative characterisation of grain morphology and carbide distribution on the sample surface. For quantitative grain size analysis of the undeformed material, electron backscatter diffraction (EBSD) was carried out at 30 kV with a beam current of 10 nA.

For the HPT-processed material, conventional EBSD did not provide sufficient spatial resolution for microstructural characterisation due to the refined grain size. Lift-out samples were made using focused ion beam (FIB) milling (Zeiss Crossbeam 540 FIB-SEM and Zeiss NVision 40 dual beam FIB-SEM, fitted with Ga ion sources). After being lifted-out, the specimen were initially thinned with 30 keV Ga ions to be transparent under 10 keV SEM views. The Ga ion current was gradually reduced

from 700 pA to 80 pA during this process. Then the specimen were thinned by 2 keV 300 pA Ga ion beam to be transparent under 5 keV SEM view. This low energy thinning step also served as the 'surface cleaning' step to remove the defects induced by high voltage Ga ions in the previous step. Lift-outs were taken at 2 different locations on each HPT sample (unirradiated and irradiated), corresponding to shear strains of $\gamma = 110$ and $\gamma = 230$.

TEM imaging was carried out with a JEOL 2100 TEM with a LaB_6 source, operating at 200 kV. EDX measurements of the TEM samples to characterise carbides in the material were carried out on a JEOL ARM-200F TEM, operating at 200 kV. On-axis transmission Kikuchi diffraction (TKD) measurements were carried out using a Zeiss Merlin FEG-SEM at 30 kV, for quantitative characterisation of grain size and dislocation density.

Grain size analysis was carried out using the Oxford Instrument HKL Channel 5 Tango software, with the grain boundary critical misorientation set to 10°. Geometrically necessary dislocation (GND) analysis was carried out in the same software, which uses the kernel average misorientation approach described in [569]. The data was first filtered with the Kuwahara method to remove some noise due to the small step sizes used for TKD [570]. The average misorientation at each point was calculated with respect to its second nearest neighbours as that was determined to be optimum for resolving the GND density distribution while not being too affected by step size-related noise.

7.3.4 Synchrotron X-ray Diffraction

Grazing-Incidence X-ray Diffraction

X-ray diffraction (XRD) measurements were made at the Diamond Light Source I11 beamline with high-resolution multi-analyser crystal (MAC) detectors. The detector set-up consists of 5 MAC arms, which hold 9 analysing Si crystals each, mounted on a 2θ-circle with 30° separation [571, 572]. Due to the narrow rocking curves of the Si crystal, a high instrument resolution can be achieved. A grazing-incidence geometry was used with a 10° incidence angle, and X-ray energy of 15 keV (λ = 0.82656 Å, $\Delta E/E = 10^{-4}$). This ensures that the majority of the diffraction signal

was dominated by contributions from the top 3–4 µm thick layer of the samples, where the implanted layer lies. The beam size was approximately 250 µm in height and 1 mm in width. Measurements were taken at positions halfway between the centre and edge of the disc samples. Accounting for the size of the beam and its footstep on the sample surface due to the incident angle, the area measured corresponds to shear strains between 65 to 160.

In-Situ Heating X-ray Diffraction

To study the thermal stability of the deformed material, in-situ heating during XRD was performed at the Diamond Light Source I12 beamline. Samples were mounted in a Linkam TS1500 heating stage for diffraction in transmission geometry. The nominal heating rate was 20 K/min, then holding for 5 minutes at the target temperature, followed by cooling to room temperature at a nominal rate of 30 K/min. The samples were held under an argon atmosphere throughout the heating cycle to prevent oxidation. The highest nominal temperature reached during the annealing cycle was 1323 K.

The X-ray beam was monochromated to an energy of 80 keV ($\lambda = 0.15498$ Å, $\Delta E/E = 10^{-4}$). The energy calibration and the instrument broadening function were measured using a CeO_2 standard sample. The beam size of 0.5 mm × 0.5 mm at the sample was defined using slits. The position at which measurements were taken on the sample corresponded to a shear strain of ∼110. Two-dimensional XRD patterns were collected on a Pilatus 2M CdTe detector positioned at a distance of 750 mm from the sample. Patterns were collected with 5 seconds of exposure for the entire duration of the heating and cooling cycle. Azimuthal integration of the 2D raw data to obtain intensity vs. 2θ (scattering angle) spectra was performed with the DAWN software package [573].

Though the Linkam heating stage provided a temperature reading for each diffraction pattern, a calibration was necessary to determine the actual temperature of the sample due to imperfections in the thermal contact between the stage and the samples. The sample temperature was estimated by fitting the lattice parameter of each diffraction pattern and using the thermal expansion coefficient of Eurofer-97

[574]. Further details are included in Appendix F.1. All temperatures discussed from this point onward refer to the calibrated sample temperature.

Convolutional Multiple Whole Pattern (CMWP) Analysis

Analysis of the intensity vs. 2θ diffraction spectra (from both I11 and I12 beamlines) was performed using the convolutional multiple whole profile (CMWP) fitting method [261, 360]. This allow the extraction of crystallite size distribution, dislocation density and dislocation character. Briefly, CMWP analysis is based on fitting the sum of a background spline function and a profile function, which is a convolution of the theoretical crystallite size and strain profiles, as well as the measured instrument profile. The crystallite size profile is modelled as a log-normal distribution. The strain profile considers the dislocation density, as well as the characteristic length scale of their strain fields, which depends on their physical ordering and arrangement [359, 362].

7.3.5 Nanoindentation

Nanoindentation was performed using an MTS Nano Indenter XP and a Berkovich tip, with the tip area function calibrated on fused silica. Continuous stiffness measurements (CSM) were made to 2 µm below the surface using a 0.05 s^{-1} strain rate, 45 Hz CSM frequency, and a 2 nm harmonic amplitude. In the HPT-deformed materials, hardness at different shear strains were measured by indents spaced 50 µm apart across the diameter of the samples. From CSM, hardness as a function of depth was measured. In order to examine contributions to hardness from the irradiated layer, while avoiding contributions from the unirradiated bulk and size effects at shallow depths [392], the average hardness over a depth range of $400 - 600$ nm was examined for each indent on all samples.

7.3.6 Transient Grating Spectroscopy

Transient grating spectroscopy (TGS) is a laser-based non-destructive technique to measure thermal diffusivity and surface acoustic wave velocity. The details of the technique are described elsewhere [413, 414, 575]. Briefly, two short pump laser pulses

(0.5 ns duration at 532 nm, with pulse energy ∼1.5 µJ and 1 kHz repetition rate) are overlapped on the sample surface at a fixed angle to form an interference pattern with wavelength Λ. Partial absorption of the light and subsequent thermal expansion occurs at positions of constructive interference, creating a spatial grating on the surface. At the same time, this rapid thermal expansion launches two monochromatic, counter-propagating surface acoustic waves (SAW). Following excitation by the pump beams, this 'transient grating' will decay due to the diffusion of thermal energy from maxima to minima and also into the material bulk. By measuring this decay via the diffraction of a set of probe laser beams (continuous wave at 559.5 nm), the thermal diffusivity and the SAW velocity of the material can be determined. The key strength of TGS applied to ion-irradiated materials is that the thickness of the probed layer is approximately equal to $\frac{\Lambda}{\pi}$, so Λ can be adjusted to ensure the signal is dominated by contributions from the irradiated layer.

This study uses $\Lambda = 5.116 \pm 0.002$ µm for most measurements. Extra measurements were made for the HPT-deformed and irradiated sample with $\Lambda = 5.116 \pm 0.002$ µm. The resultant probed layer thickness for all measurements was ∼1.6 µm, which ensures that the signal originates from the 3.5 µm thick damaged layer in the irradiated samples. The pump and probe beam sizes were respectively 140 µm and 90 µm ($\frac{1}{e^2}$ width). In order to measure properties corresponding to different shear strains, lines of measurement points spaced 150 µm apart were taken across the diameter of the HPT-processed samples.

7.4 Results

7.4.1 Electron Microscopy

EBSD of the as-received Eurofer-97, before deformation via HPT, shows lath structures characteristic of the martensitic microstructure of the material (Figure 7.2(a)). The area-weighted average grain size of the undeformed material is 5.3 ± 3.2 µm, using an angular misorientation threshold of 10°. Following electropolishing, a dispersion of particles, each between a few nm to 200 nm in size, become evident on the sample surface (Figure 7.2(b) and (c)). Particles of similar size and spatial

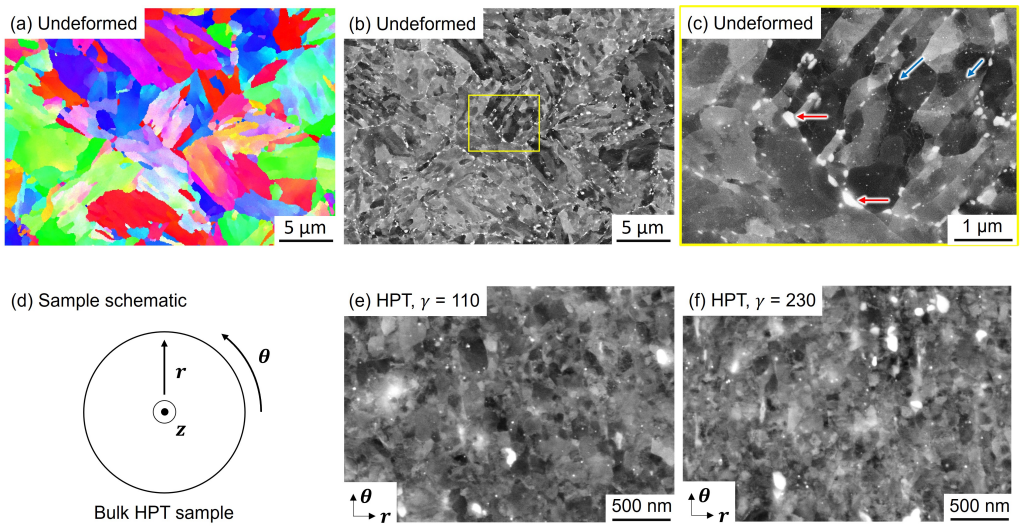


Figure 7.2: The microstructure of the same area on the as-received Eurofer-97 characterised by (a) EBSD and (b) backscattered electron (BSE) imaging. (c) A higher magnification BSE image of the as-received material (same area enclosed by the yellow rectangle in (b)). Red and blue arrows indicate the presence of large and small carbides, respectively. (d) A schematic of the sample coordinates with respect to the deformed material. The orientation shown applies to all micrographs in this figure. BSE images of Eurofer-97 after deformation at (e) $\gamma = 110$ and (f) $\gamma = 230$.

distribution have previously been observed in other studies of Eurofer-97 and similar steels, and have been identified as carbides [330, 576, 577]. The larger carbides mainly appear at the boundaries of prior austenite grains and are up to 200 nm in size (red arrows in Figure 7.2(c)). There are also smaller carbides, <10 nm in size, distributed more homogeneously across the sample (blue arrows in Figure 7.2(c)).

In this work, cylindrical coordinates are used to describe directions in the HPT-deformed material (Figure 7.2(d)). $\boldsymbol{z}$ is normal to the surface of the HPT sample (outwards positive), $\boldsymbol{r}$ is in the radial direction, and $\boldsymbol{\theta}$ is the tangential direction along which torsion is applied. Following deformation via HPT, a significant level of grain refinement is achieved (Figure 7.2(e) and (f)). Quantitative measurements of the grain size following HPT will be presented in the subsequent sections as EBSD was not able to achieve the required spatial resolution on the sample surface. From SE and BSE imaging, viewing along the $-\boldsymbol{z}$ direction (in the $\boldsymbol{r}$-$\boldsymbol{\theta}$ plane, Figure 7.2(e) and (f)), it can be seen that most of the refined grains are slightly elongated in the $\boldsymbol{\theta}$ direction. The carbides are still present following HPT but are

more homogeneously distributed. A mix of large and small carbides is present with similar size distributions as the undeformed sample.

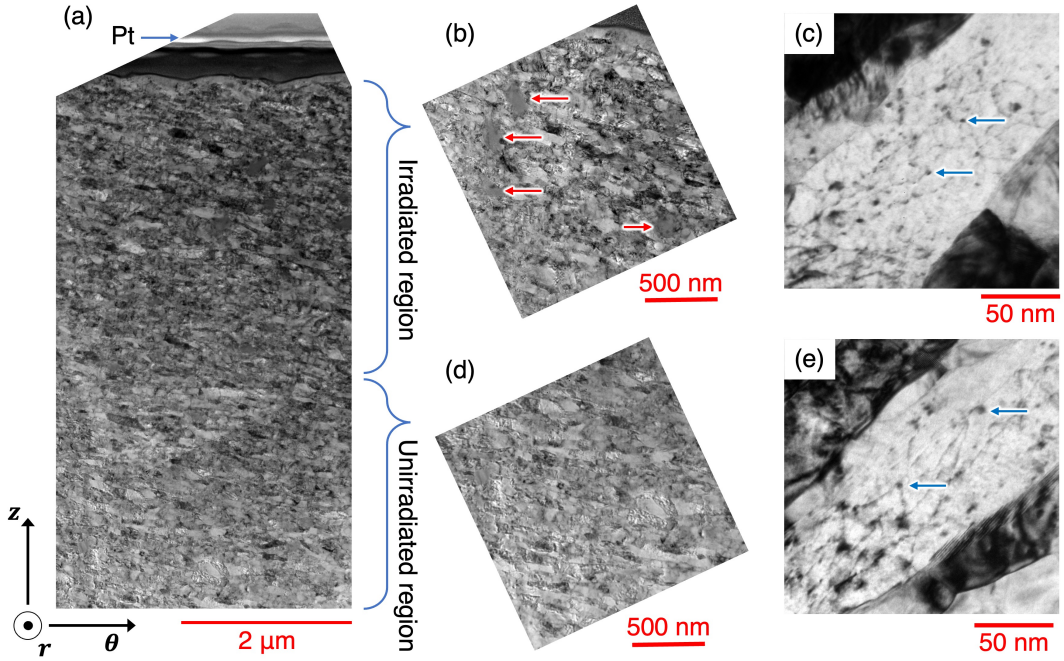


Figure 7.3: TEM images of the deformed irradiated sample with the lift-out taken from a location corresponding to $\gamma = 230$. (a) Low magnification overview of the lift-out, showing the platinum (Pt) protective layer on the bulk sample surface, with a carbon layer underneath (black). (b)&(d) Magnified micrographs showing the grain shapes and microstructure in the irradiated and unirradiated regions, respectively. The figures have been rotated to align with the $\boldsymbol{\theta}$-$\boldsymbol{z}$ plane of the bulk sample. (c)&(e) Bright-field images of individual grains within the irradiated and unirradiated regions respectively.

To further study the grain microstructures of the HPT material, FIB was used to prepare TEM lamella from different samples and radial positions. A full comparison of TEM micrographs from all samples is provided in Appendix F.2. There is no discernible difference in microstructure between $\gamma = 110$ and $\gamma = 230$, suggesting that microstructural saturation is reached before $\gamma = 110$. TEM of both the unirradiated and irradiated HPT material also shows that there is no depth dependence of the microstructure down to 10 µm below the bulk sample surface. An example is shown in Figure 7.3(a) for the top 6 µm of the deformed and irradiated sample.

When viewed along the radial direction (on the $\boldsymbol{\theta}$-$\boldsymbol{z}$ plane), the grains appear elongated (Figure 7.3(a)–(c)). The axis of elongation is not completely aligned with the direction of torsion $\boldsymbol{\theta}$ (parallel to the platinum layer on the top edge of the lift-out)

but inclined approximately 15°. This has been observed previously in other studies of HPT materials, even at shear strains beyond microstructural saturation [248–251].

The presence of large carbides is detected in the TEM images as indicated by the red arrows in Figure 7.3(b), similar to those indicated with red arrows in Figure 7.2(c). EDX was performed to confirm that these regions, which appear grey and without sharp edges, are indeed carbides enriched with Cr and W (Appendix F.3).

Bright-field images of individual grains were recorded from both the irradiated (Figure 7.3(c)) and unirradiated (Figure 7.3(e)) regions of the lift-out. Numerous dislocation lines are evident in both grains. The black spots (blue arrows), most likely carbides, also appear along the length of the dislocation lines. No evidence of irradiation-induced microstructural changes (e.g. dislocation loops) are observed at this magnification.

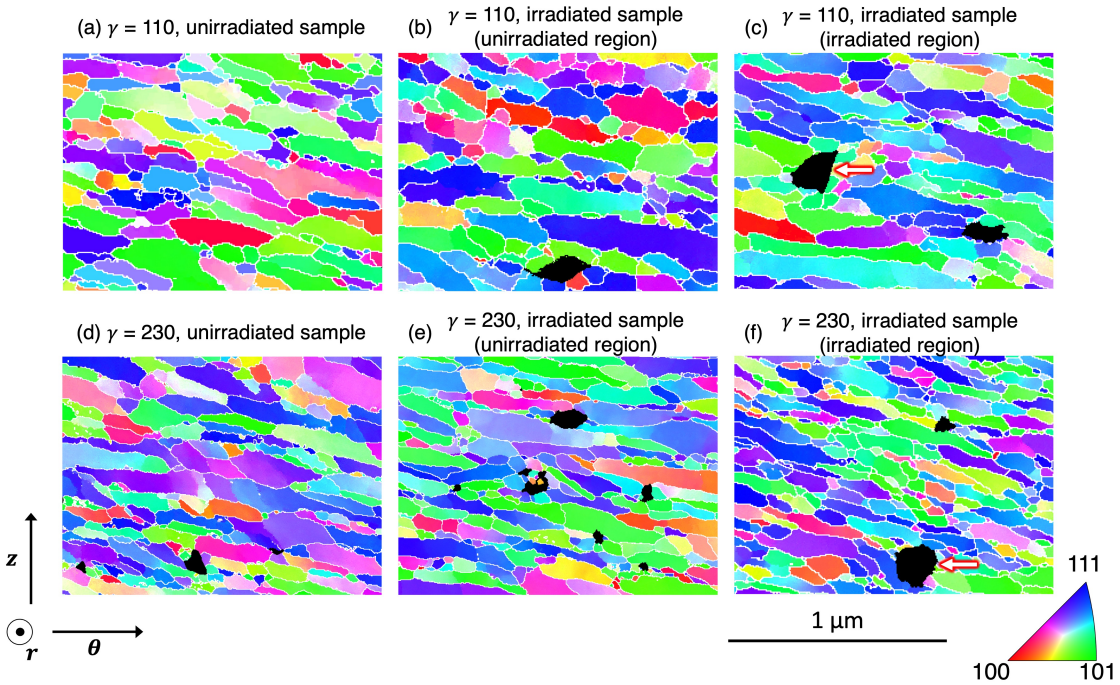


Figure 7.4: TKD maps taken from (a)&(d) the unirradiated samples and the irradiated samples in (b)&(e) the unirradiated regions, and (c)&(f) the irradiated regions, from respectively $\gamma = 110$ and $\gamma = 230$. Note that the top and bottom edges of each map are parallel to the surface of the bulk sample from which the lift-outs were taken. The grain boundaries (angular misorientation >10°) are indicated in white. Non-indexed areas are indicated in black.

Comparisons of the microstructure of different deformed samples were done with

TKD measurements (Figure 7.4). The average indexing rate was >80%. Regions of low confidence indexing occurs near the grain boundaries and around carbides (large compact black areas indicated by white arrows with red outlines in Figure 7.4(c) and (f)).

Comparing the effect of shear strain on the microstructure (top row compared with bottom row in Figure 7.4), it can be seen that the aspect ratio of the grains appears slightly larger for $\gamma = 230$ compared to $\gamma = 110$. The difference in strain level does not affect the indexing rate.

Comparing the unirradiated sample with the unirradiated regions of the irradiated sample at each strain level (Figure 7.4(a) and (c), (b) and (d)), it can be seen that the microstructure at nominally the same deformation conditions is similar across different samples. This confirms the reproducibility of the HPT method used for this study.

There appear to be no discernible irradiation-induced changes to the microstructure in the TKD maps (Figure 7.4(c) and (f)). The overall grain shapes and distribution of unindexed regions also appear to be the same for the irradiated and unirradiated regions of the sample at each strain level.

Grain Size

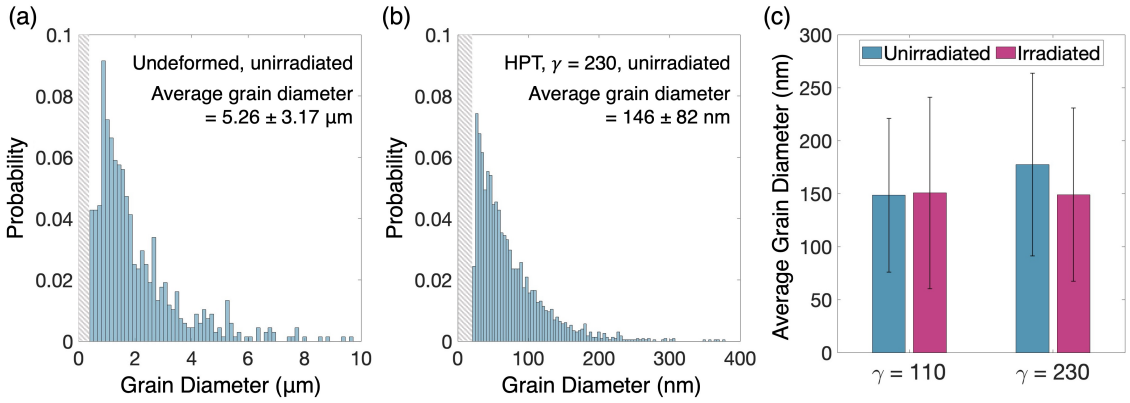


Figure 7.5: The grain diameter distribution for the (a) undeformed and (b) deformed ($\gamma = 230$) material from TKD measurements. The grey regions indicate the range of inaccessible grain sizes due to the limited measurement step size. (c) The average grain diameter for the unimplanted and implanted regions at the two strain levels where lift-outs were taken. The error bars represent ± 1 standard deviation of the grain diameter. Note that all average and standard deviation grain sizes reported are weighted by grain area.

The grain size distribution shape appears to be similar before and after deformation with HPT (Figure 7.5(a) and (b)). Due to the presence of grains much smaller than the step sizes of EBSD and TKD, it was difficult to probe the lower end of the distribution (<250 nm for EBSD and <20 nm for TKD). The average grain size following HPT, to a shear strain of $\gamma = 230$, is reduced by a factor of >35 compared to the undeformed reference. The grain sizes of the HPT-deformed samples do not change with strain level, within measurement error (Figure 7.5(c)). This confirms that the material microstructure is in the saturated regime at or before $\gamma = 110$. There is also no significant change in grain size following irradiation.

GND Density

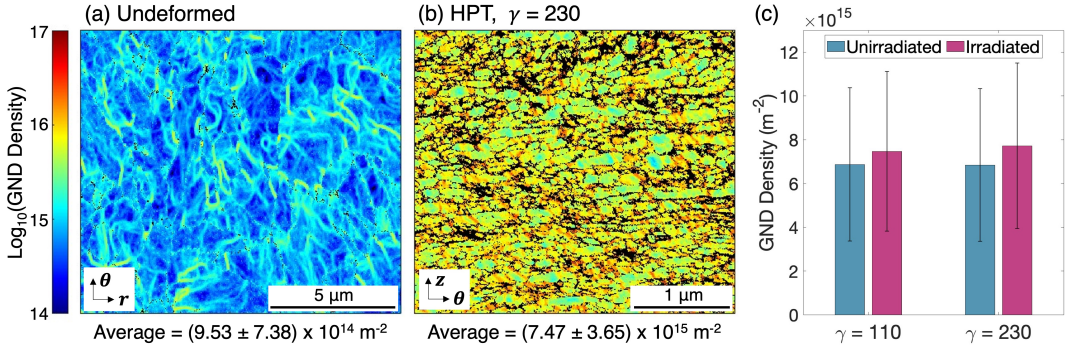


Figure 7.6: GND density map of the (a) undeformed and (b) deformed material ($\gamma = 230$). Note that the magnification and sample orientations are not the same for the two samples. (c) The average GND density for the unimplanted and implanted regions at $\gamma = 110$ and $\gamma = 230$. The error bars represent ± 1 standard deviation of the GND density.

The distribution of geometrically necessary dislocations (GND) in the undeformed material shows extended swirling structures that are distributed evenly across and within the grains (Figure 7.6(a)). The average GND density is on the order of 10^{14}–10^{15} m^{-2} as expected from other studies of Eurofer-97 and tempered martensitic steels [578, 579]. The GND density increases by an order of magnitude following HPT to 10^{15}–10^{16} m^{-2} (Figure 7.6(b)). The regions of high dislocation density are mainly near grain boundaries. Some bands of high dislocation density are oriented perpendicular to the elongated axis of the grains.

Comparing dislocation density between the different lift-out samples of the deformed materials reveals little difference in average GND density as a function

of strain between $\gamma = 110$ and $\gamma = 230$ (Figure 7.6(c)). Once again this confirms that strain saturation is achieved before $\gamma = 110$. Implantation also did not change the average GND density of the samples. This is unsurprising as at this damage level where most irradiation defects likely exist as point defects or small loops [109] and thus do not contribute to the large-scale lattice curvature from which GND density is determined.

Grain Boundaries and Texture

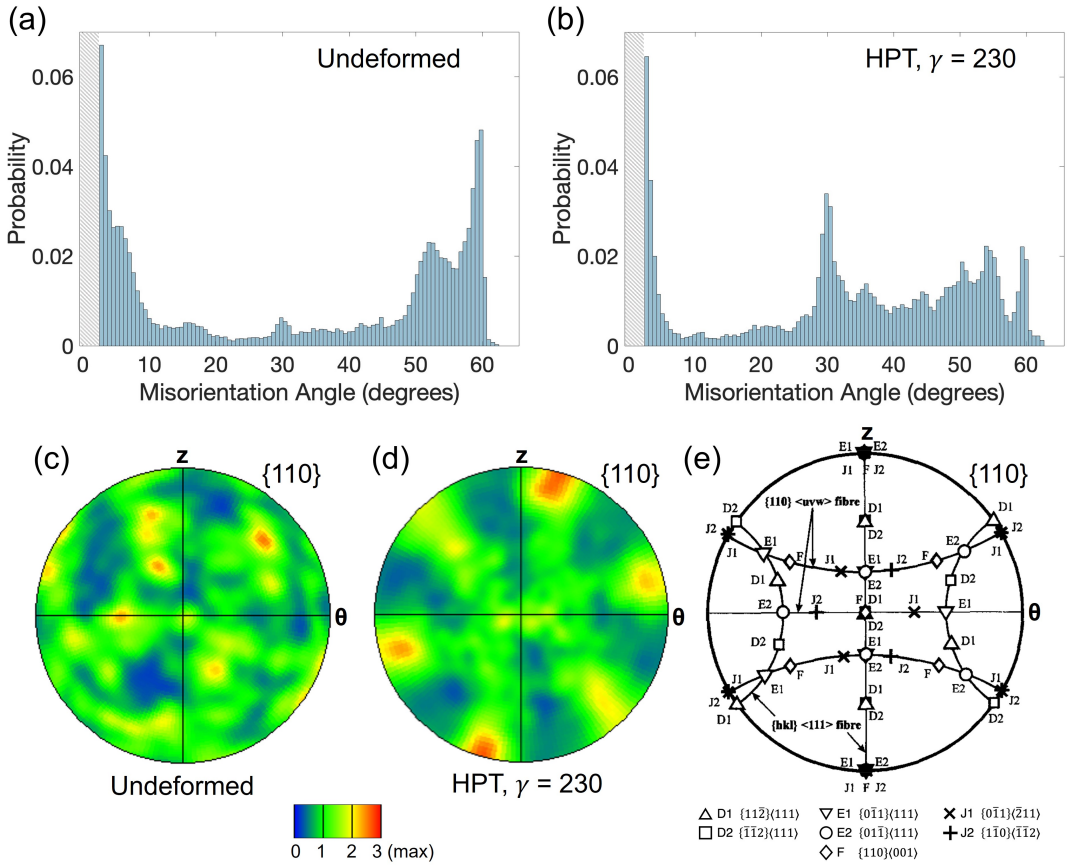


Figure 7.7: The distribution of neighbouring point misorientation angle for the (a) undeformed and (b) deformed material, along with (c)–(d) the corresponding {110} pole figures. (e) The theoretical {110} pole figure of pure iron that has been processed by torsion [580].

The undeformed Eurofer-97 material has a high proportion of neighbouring points with <10° and >50° misorientation (Figure 7.7(a)). After torsion, this distribution changes to a large proportion of grain boundaries between 30°–60° (Figure 7.7(b)). There is a significant peak around 30° which is greatly enhanced

following deformation with HPT. The true proportion of angular misorientation below 2.5° cannot be accurately determined due to experimental limitations (grey regions in Figure 7.7(a) and (b)).

The {110} pole figure for the undeformed Eurofer-97 shows little preferred orientation or texture (Figure 7.7(c)). After deformation with HPT, significant texture evolution occurs and preferred orientation is evident (Figure 7.7(d)). The experimental observations qualitatively agree with the theoretically predicted preferred orientations for torsioned iron (Figure 7.7(e)). There is a ∼15° rotation between the experimentally determined and the predicted texture. This is similar to the angular difference between the top surface of the bulk HPT sample and the axis of elongation for the grains in the $\boldsymbol{\theta}$-$\boldsymbol{z}$ plane (Figure 7.4(d)).

7.4.2 X-Ray Diffraction

Grazing-Incidence X-Ray Diffraction

Peak broadening is clearly observed in the raw diffraction patterns following HPT to $\gamma = 110$ (Figure 7.8(a)). This suggests an increase of intragranular strain and/or a decrease in grain size. The diffraction patterns shown in Figure 7.8(a) are functions of $K = 2\sin\theta/\lambda$, and the fittings from CMWP (overlaid black lines) appear to agree well with the measured data. Due to strain anisotropy, the peak broadening is not isotropic, i.e. it is not linear with K. Strain anisotropy in peak broadening can be rectified by taking into account the dislocation contrast factors, C, in the modified Williamson-Hall plot [581], where the FWHM or the integral breadth is plotted against K^2C. The contrast factor depends on the relative orientation of the diffraction vector, the Burgers vector and the line vector of dislocations, and the elastic constants of the material [359]. For polycrystalline samples, the average contrast factor of all the grains and dislocations is determined in the CMWP fitting procedure. The modified Williamson-Hall plots in Figure 7.8(b) were produced following the procedures described in [359, 581]. They demonstrate that strain anisotropy in these samples can indeed be accounted for by considering the contrast factor fitted from CMWP, as the integral peak widths are a linear function of K^2C [582].

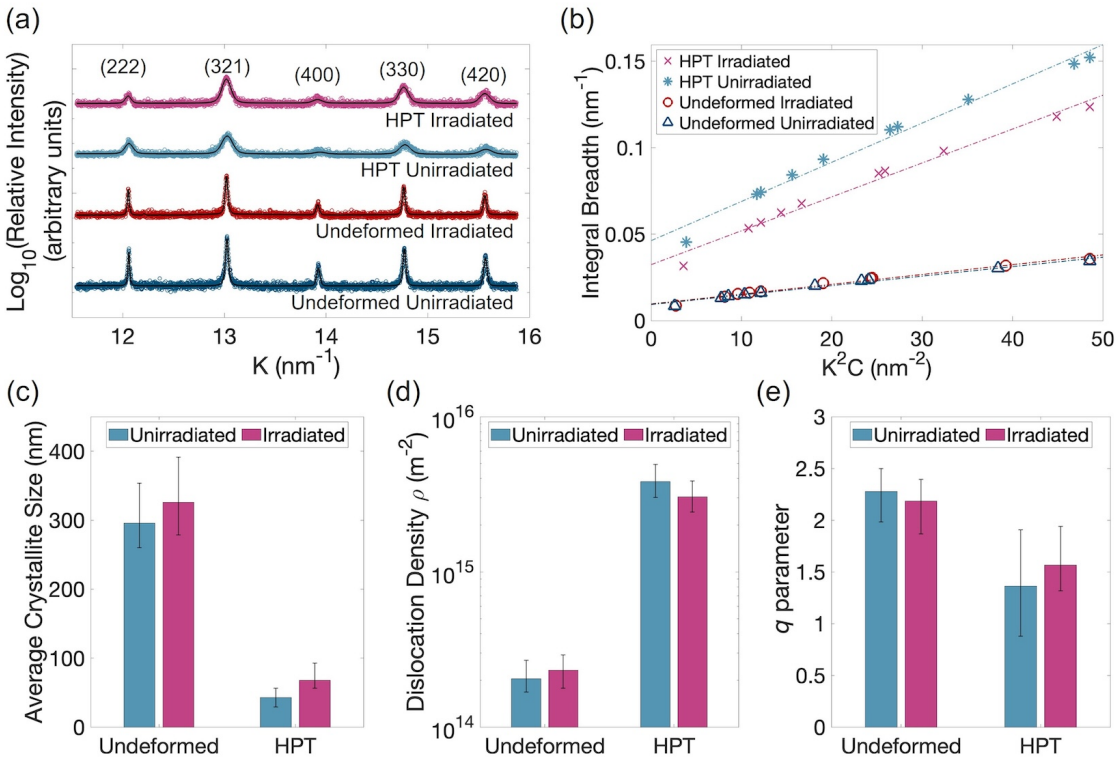


Figure 7.8: (a) A section of the diffraction patterns, plotted as a function of $K = 2\sin\theta/\lambda$, for the samples investigated. The traces have been vertically offset for clarity. The scatter points are the experimental data points and the black lines are the fitted patterns from CMWP. (b) The modified Williamson-Hall plot with C calculated from CMWP fitting. The dashed lines are included as a guide to the eye. (c) The area-weighted average crystallite size, (d) dislocation density, and (e) q parameter determined from CMWP. Further information about each parameter is given in the main text. The error bars represent the fitting errors calculated by considering the variations in the weighted-sum-of-squares residuals [261].

CMWP line-profile analysis fits the microstructural parameters including average crystallite size, dislocation density and the contrast factors, which describe the average character of the dislocations ('q parameter') [261, 359]. The results of this analysis are shown in Figure 7.8(c)–(e). A combined procedure using successive applications of a Monte Carlo (MC) statistical algorithm and Levenberg-Marquardt nonlinear least-squares algorithm was used the peaks and physical parameters of the diffraction patterns [261, 360]. The error bars presented describe the range for each parameter where the corresponding fit had a resultant weighted sum of square residuals (WSSR) that fell within p% confidence value in the MC procedure [365]. At least 2000 iterations were completed during the MC fitting, and $p = 3.5$ was used as it has been previously shown to yield a good fit, even for complicated patterns.

Further details of the fitting procedure can be found in [261, 360].

The crystallite size fitted from CMWP for the undeformed material is ∼300 nm (Figure 7.8(c)), which is much smaller than that measured by EBSD (Figure 7.2(a) and 7.5(a)). This is to be expected as X-rays are much more sensitive to smaller angular misorientations (<1°), hence effectively mapping out regions corresponding to 'subgrains' in the undeformed material [254]. For grains larger than about two microns, the size contribution to X-ray peak broadening is not possible to measure as its breadth becomes smaller than the instrument broadening contributions. Therefore, XRD is unable to accurately determine the size of 'grains' in the as-received material in this study. To measure 'grain' areas, which are usually defined with larger misorientations (typically 10–15°), SEM-based methods are more useful (Figure 7.5(a)).

After deformation via HPT to $\gamma = 110$, the area-weighted average crystallite size is 42 nm. This value is comparable to the TKD grain size measurements (∼150 nm, Figure 7.5(b)). Irradiation does not cause any significant change in crystallite size for the undeformed material. There is a slight irradiation-induced increase in crystallite size for the HPT-deformed material.

Dislocation density increases by a factor of ∼10 following HPT (Figure 7.8(d)). Subsequent irradiation of the deformed material causes a 20% reduction in dislocation density. In contrast, the undeformed reference material shows a slight increase in dislocation density following irradiation, likely due to irradiation-induced defects. The reduction in strain following irradiation of the deformed material can also be directly observed from the changes in peak broadening of the diffraction spectrum (Figure 7.8(a)) and the slope of the modified Williamson-Hall plot (Figure 7.8(b)). While the results of the deformed material shown in Figure 7.8 were measured for $\gamma \sim 110$, similar results (not shown here) were also observed for $\gamma \sim 230$. This demonstrates that self-ion irradiation removes some effects of the dislocations introduced by severe plastic deformation.

The q parameter describes the average character (screw vs. edge) of the dislocations present in the material. Its theoretical range depends on the elastic anisotropy ($A_i = 2c_{44}/(c_{11} - c_{12})$) and the ratio c_{12}/c_{44} [359]. For Eurofer-97, *ab*

initio calculations give $A_i \approx 1.5$ and $c_{12}/c_{44} \approx 1$ [583]. This leads to a corresponding q range of between 1 (pure edge dislocations) to 2.5 (pure screw dislocations). Our fitting of the q parameter suggests that the dislocations present in the undeformed material ($q \sim 2.3$) are predominantly of a screw-type character, and after HPT ($q \sim 1.4$) they are of more edge-type character (Figure 7.8(e)). Irradiation appears to have little effect on the q parameter.

In-Situ Annealing X-ray Diffraction Measurements

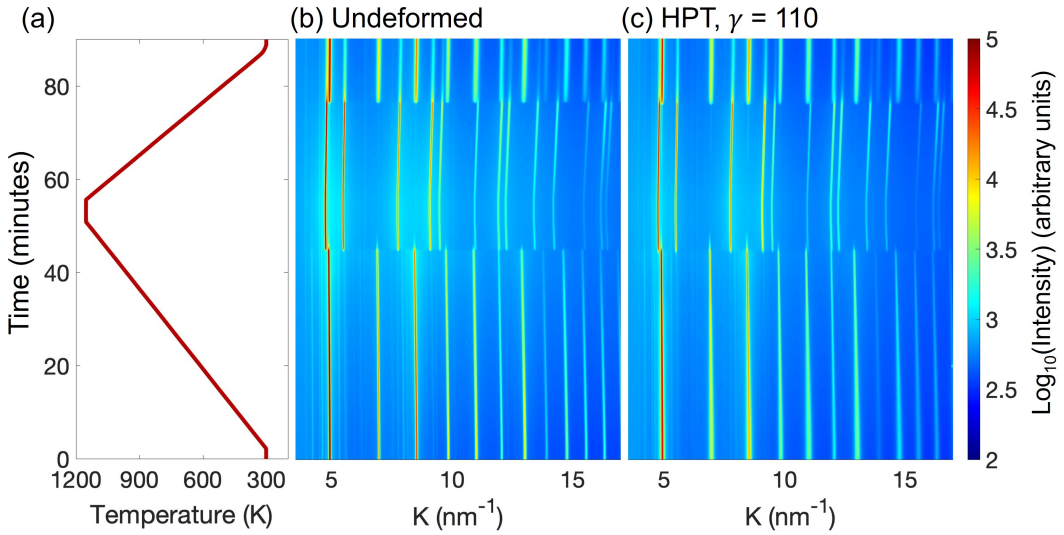


Figure 7.9: (a) The calibrated temperature profile of the annealing cycle during the in-situ XRD measurements. The diffraction intensity profiles as a function of $K = 2\sin\theta/\lambda$ and annealing cycle time are shown for (b) the reference undeformed sample, and (c) the HPT-deformed sample, respectively. The vertical axes representing time in (b) and (c) are aligned with (a), from which the annealing temperature can be read.

In the reference undeformed sample, the peak widths did not change as a function of temperature up to 1043 K, at which point a phase transition took place (Figure 7.9(b)). The temperature at which the phase transition from ferrite/martensite (body-centred cubic/tetragonal) to austenite (face-centred cubic) take place can depend on the heating rate. In other studies of Eurofer-97 in the literature, the transition begins to take place between 1025 K–1133 K [574, 584, 585]. In this study, our measurements show that all ferrite/martensite peaks disappear at 1093 K during the heating ramp. The material contains only austenite phase during holding at 1153 K, and during the cooling stage until the material cooled to 606 K. The

martensite phase returned with cooling below 606 K. This is consistent with previous findings in Eurofer-97 annealing experiments [584]. However, some austenite phase remains present in the material with broader diffraction peaks. Interestingly, the martensite peaks are also wider following the heating and cooling cycle than in the initial state. This could be due to residual strain in the martensite phase as it forms within the austenite phase upon cooling [586, 587]. There is a volume expansion associated with the formation and growth of martensite regions within the austenite grains. This will impart a hydrostatic pressure within the austenite regions, which will also in turn cause residual strains in the martensite grains [588, 589]. Appendix F.5 shows a different set of in-situ annealing XRD measurements, in which the phase transition occurs for a shorter period of time, and no austenite phase is retained following cooling. The martensite peak widths following cooling remain as narrow as right before the phase change at 973 K. This is further evidence that the post-annealing peak broadening is associated with the retained austenite phase.

During heating of the HPT-deformed material, the peak widths are initially large, then gradually reduce until around 900 K (Figure 7.9(c)). Similar to the undeformed sample, a phase transition from ferrite/martensite to austenite occurs at 1043 K, then from austenite back to martensite at 606 K during the cooling stage. Both austenite and martensite phases remain in the material even at room temperature following the heating cycle. Furthermore, the peaks after cooling, for both the martensite and austenite phases, are broader than before and during the annealing cycle, respectively.

From the CMWP fitting, the area-weighted average crystallite size is unchanged between 303 K and 367 K (∼75 nm) during the heating stage (Figure 7.10(a)). Further increase in temperature causes a corresponding increase in crystallite size until ∼725 K, where the average crystallite size is around 280 nm. After this point, the crystallite size increases dramatically with temperature, suggesting that the size-broadening contribution in the diffraction patterns is approaching zero. However, we note that recrystallisation has likely not progressed far at this temperature as the XRD patterns still showed continuous Debye-Scherrer rings up until the phase transition (see supplementary files for raw patterns).

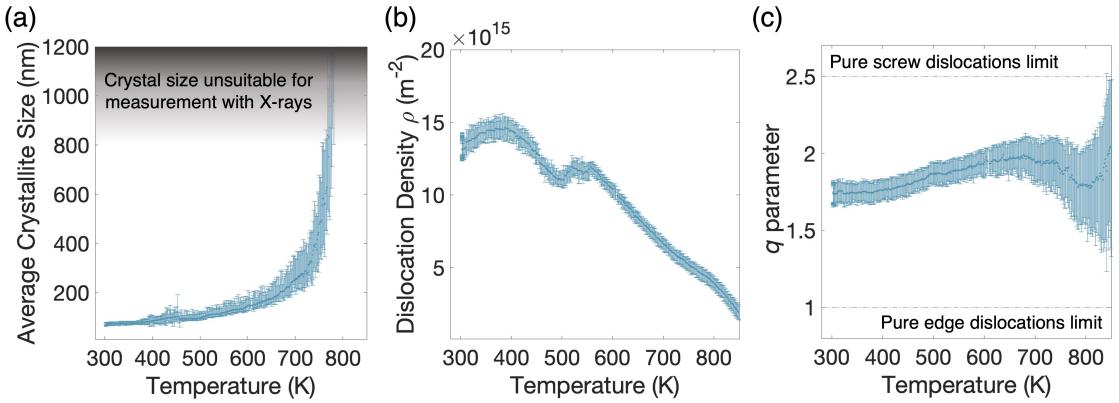


Figure 7.10: The microstructural parameters of the in-situ annealing diffraction measurements determined from CMWP analysis. An explanation of each parameter is included in the main text. The error bars are from the fitting algorithm discussed in Section 7.4.2.

There appear to be three distinct stages of evolution for dislocation density (Figure 7.10(b)). Between 303 K to 550 K, the dislocation density reduces slightly to $\sim 1.2 \times 10^{16}$ m^{-2}, which is 90% of the initial value. Between 550 K to 800 K, ρ decreases linearly to $\sim 4 \times 10^{15}$ m^{-2}. Further reduction in ρ above 800 K appears to be at a greater rate than in the previous stage, but it is also likely that the strain-induced peak broadening is too small to be quantitatively probed in this particular experiment.

The q parameter, which is indicative of the average nature of the dislocation character, also changes during annealing (Figure 7.10(c)). The q parameter slowly increases from 1.75 to 2, between temperatures of 387–680 K, after which the fitting from CMWP analysis appears to be less reliable. This suggests a general trend of the average dislocation character evolving from more edge-like to more screw-like, recovering features of the undeformed material ($q \sim 2.3$, Figure 7.8(e)).

7.4.3 Material Property Changes

The hardness of undeformed samples increases monotonically with irradiation dose due to irradiation hardening (Figure 7.11(a)). For nanoindentation, an extra set of lower dose samples (0.008 dpa) was also characterised, as detailed in Section 7.3.2. The hardness change from unimplanted to 0.008 dpa is greater than from 0.008 dpa to 0.08 dpa in undeformed samples, which is consistent with previous hardness measurements for FeCr alloys irradiated at room temperature [422, 556]. Hardness

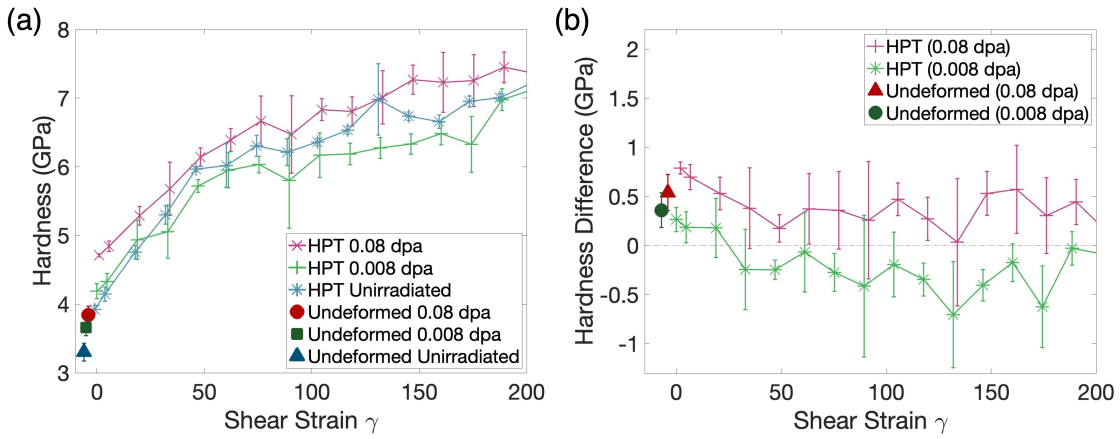


Figure 7.11: (a) Hardness of the reference (blue), irradiated (0.008 dpa - green, 0.08 dpa - red/pink), as a function of shear strain. The undeformed reference samples have been offset by a small negative strain for clarity. The error bars represent ± 1 standard deviation of the indentation hardness between 400 to 600 nm depth. The values for the deformed materials were obtained by indenting points along the diameter of the specimen to measure areas of different shear strains. (b) The difference in hardness between the irradiated samples and the corresponding unirradiated samples for the undeformed and HPT materials.

also increases with strain due to strain hardening and grain refinement, which is observed from EBSD/TKD (Figure 7.5). Furthermore, after $\gamma \sim 70$, hardening rate is reduced, which suggests that the material is approaching strain hardening saturation. This has been reported previously for other HPT-processed materials [245, 249, 278]. At nominally zero shear strain (at the centre of the HPT sample), the hardness is greater than the reference undeformed material. This difference shows that even though the centre experiences nominally only compression (∼4 GPa), which does not cause significant grain refinement, there is still a significant change in hardness. This suggests that there is an appreciable increase in dislocation density in the sample centre during the initial compression. It is also worth noting that analysing the exact centre of the sample is also experimentally challenging.

For materials processed by HPT prior to irradiation, softening of -0.21 ± 0.28 GPa is observed following irradiation to 0.008 dpa (Figure 7.11(b)). This is markedly different from the undeformed case, where irradiation to 0.008 dpa causes an increase in hardness of 0.36 ± 0.17 GPa. Softening has been observed following high-temperature irradiation (≥693 K) in ferritic/martensitic steels, including Eurofer-97, to doses on the order of 1–10 dpa [590–593]. It has been suggested that this softening

is due to irradiation-induced dislocation recovery and increase in subgrain size [591]. We suggest that this is readily occurring in the HPT-deformed material at 0.008 dpa due to the high density of dislocations from the deformation process. However, the rate of dislocation recovery is likely slow compared to irradiation-induced defect formation during room-temperature irradiation. Hence, at a higher dose of 0.08 dpa in this study, there is hardening even in the HPT-deformed sample. In comparison, in other studies at high temperatures the recovery process can occur fast enough to balance out defect formation, leading to softening at much higher doses [590].

Further irradiation to 0.08 dpa caused a net hardening compared to the unirradiated HPT-processed material (Figure 7.11(b)). However, this hardening is less than that of the undeformed material irradiated to 0.08 dpa. This could be due to the irradiation-induced defects being absorbed by the greater proportion of grain boundaries present in the HPT material [316], therefore causing less change to the hardness. There could also be competing effects between the introduction of irradiation-induced defects and the irradiation process itself causing simultaneous annealing of the pre-existing dislocations from HPT (Section 7.4.2). As these two processes act in opposition to each other, the net change to hardness after deformation and irradiation is smaller than from irradiation alone. However, we also note that the irradiation-induced difference in hardness at 0.08 dpa between the undeformed and deformed cases is small, and could be within measurement error.

Thermal diffusivity of the reference Eurofer-97 measured by TGS in this study (Figure 7.12(a)) is in agreement to within 10% of previous measurements using the laser flash technique (8.3×10^{-6} m^2s^{-1}) [594]. Following irradiation, the thermal diffusivity of the undeformed material decreases by 6.7%, which is comparable to the results of FeCr [422] and stainless steel 316 L [595] exposed to similar damage doses. It is well-known that irradiation can cause a decrease in thermal diffusivity due to the introduction of defects to the crystal that act as scattering sites for electrons. Since thermal conductivity in metals is predominately electron-mediated, an increase in electron scattering rate results in a reduction of thermal diffusivity [218]. The effect of small point defects, such as vacancies, on thermal diffusivity in other irradiated materials has been previously investigated. For most pure

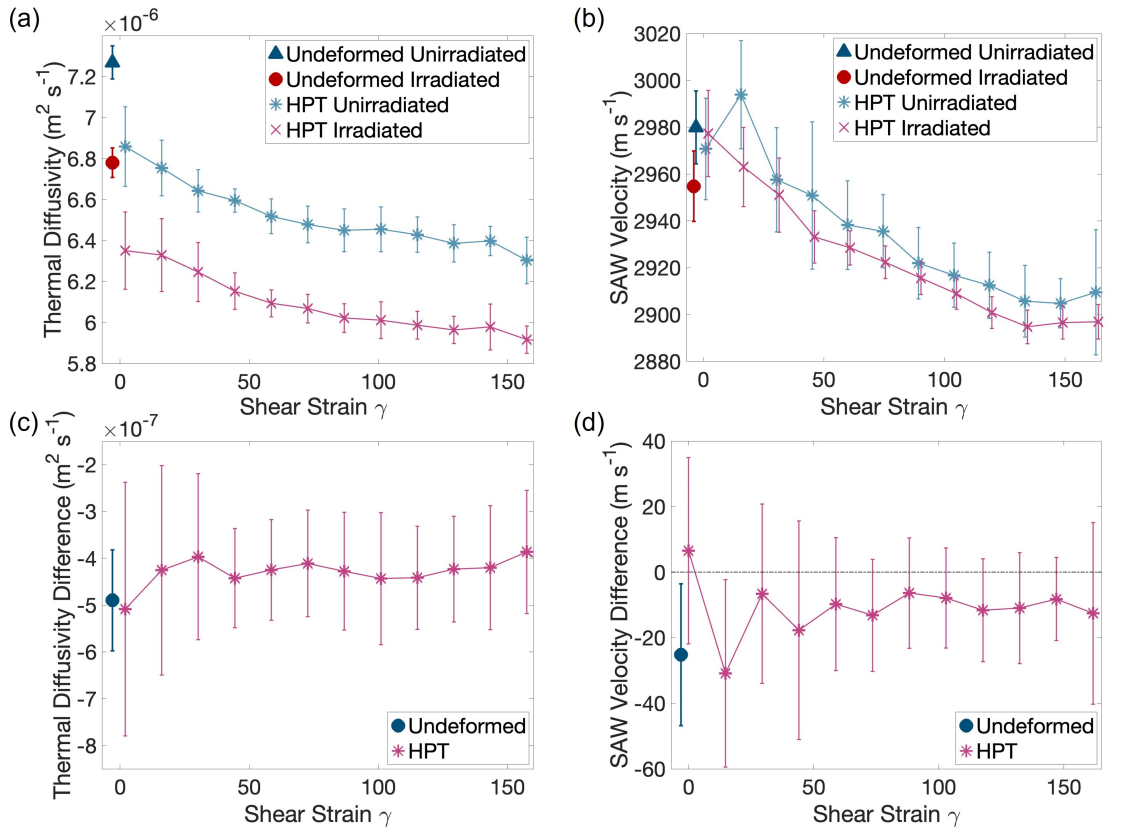


Figure 7.12: (a) Thermal diffusivity and (b) surface acoustic wave (SAW) velocity of Eurofer-97, comparing the reference (dark blue triangle), irradiated (red circle), deformed (light blue asterisk), and deformed then irradiated samples (pink cross). The difference in (c) thermal diffusivity and (d) SAW velocity following irradiation for the undeformed (blue circle) and deformed (pink asterisk) set of materials. The values for the deformed material were obtained by sampling points along the diameter of the specimen to measure areas of different shear strains.

metals, include Fe, irradiation does not cause a measurable change in thermal diffusivity [218]. Thermal diffusivity does drop significantly after irradiation for W, but saturation occurs after 0.1 dpa [337].

Plastic deformation via HPT also has the effect of reducing the thermal diffusivity of Eurofer-97 (Figure 7.12(a)). The centre of the sample, at nominally zero shear strain, still shows a significant reduction in thermal diffusivity. Similar to the hardness trends, this again shows that there is a significant increase in dislocation density from the initial compression.

Thermal diffusivity decreases with increasing shear strain (Figure 7.12(a)). At $\gamma = 160$, the maximum strain level measured on the HPT samples due to the sample geometry, there is a decrease of 12% from the reference Eurofer-97 value. HPT

deformation increases the dislocation density in the material and increases the ratio of grain boundaries to perfect crystal. Both these factors lower the mobility of charge carriers in the material and thus cause a reduction in thermal diffusivity [596, 597]. The rate of thermal diffusivity decrease appears to reduce with increasing shear strain, particularly at $\gamma > 70$.

Irradiation of the deformed material causes a further reduction in thermal diffusivity in addition to the decrease associated with the deformation. At $\gamma = 160$ in the irradiated sample, there is a total of 19% reduction in thermal diffusivity compared to the reference unirradiated Eurofer-97 sample.

Following irradiation, the material that has undergone prior HPT shows a smaller reduction in thermal diffusivity compared to the undeformed material (Figure 7.12(c)). This could be again the effect of the combination of defect absorption by grain boundaries and the irradiation-induced annealing of prior dislocations introduced by the HPT process, as discussed earlier.

Surface acoustic wave (SAW) velocity is related to the elastic constants of the material. However, since Fe and Fe-based alloys have strong elastic anisotropy, the relationship between SAW velocity and the elastic constants is dependent on the grain orientation or local texture [411]. Since our grains are many times smaller than the measurement spot even in the undeformed case, we cannot quantitatively measure the changes to the elastic constants in this study. However, changes to the SAW velocities were still measured, indicating that the material stiffness has been altered by HPT and irradiation (Figure 7.12(b)).

A 1% reduction in SAW velocity due to irradiation in the undeformed sample is observed. This could be due to the creation of point defects from irradiation. Previous studies with He ion irradiation in tungsten have shown a ∼2% reduction in SAW velocity at 0.2–0.3 dpa [176, 598]. However, studies in copper and nickel (different crystal structures to Eurofer-97) have shown an increase in SAW velocity for irradiation up to 5 dpa, which the authors attributed to the interaction of defect clusters with dislocations causing a pinning effect [599, 600].

Deformation causes a significant reduction in SAW velocity (Figure 7.12(b)). Note that due to the measurement geometry, the SAW velocities reported here

are in the radial direction $\boldsymbol{r}$ (perpendicular to the shear direction $\boldsymbol{\theta}$). At $\gamma = 160$, the SAW velocity decreased by 2.5% compared to the undeformed material. There also does not appear to be any saturation effect until $\gamma = 140$. This is a significantly greater level of strain than required for the saturation of thermal diffusivity changes (Figure 7.12(a)) and hardness [567], both of which approached saturation at $\gamma > 70$. Grain size and GND density, as observed by TKD, have both saturated by $\gamma = 110$ (Figure 7.5 and 7.6), which is also lower than the shear strain threshold for SAW velocity change saturation.

Irradiation of the deformed material causes a further reduction in SAW velocity, however this could be within measurement error. The change to SAW velocity due to irradiation is less for the materials that have undergone prior HPT deformation compared to the undeformed specimens (Figure 7.12(d)). This could again be due to a combination of the grain boundaries absorbing irradiation defects and annealing of dislocations caused by HPT during the process of irradiation.

7.5 Discussion

7.5.1 Effect of HPT

HPT causes significant grain refinement in Eurofer-97. From SEM-based analysis, the area-weighted average grain size decreases from 5.26 µm to 146 nm, which is a reduction by a factor of ∼30 (Figure 7.5). From CMWP analysis of the grazing-incidence XRD data, the area-weighted average crystallite size decreases from 295 nm to 42 nm, which is a reduction by a factor of ∼7 (Figure 7.8(c)). From CMWP analysis of the transmission XRD measurements, the grain size of the HPT-deformed sample before annealing is 75 nm (Figure 7.10(a)). Though the grain size reduction ratio from HPT is different between electron microscopy and XRD, all measurements of the grain sizes following deformation are in good agreement. This has also been observed from other studies of deformed materials that compare electron microscopy techniques with XRD [601, 602].

The discrepancies between grain size measurements of the undeformed material from EBSD and XRD can be attributed to their respective sensitivity to misorientations in the lattice (Section 7.4.2). As the XRD coherent scattering domains are small, the crystallite size measurements are more indicative of 'subgrain' size. On the other hand, for EBSD, the misorientation threshold used 10°, which allows the measurement of 'grain' size. However, the agreement between TKD and XRD measurements for the grain and crystallite size, respectively, of the HPT-deformed material shows that the distinction between 'grains' and 'subgrains' ceases to exist following grain refinement. This suggests that HPT causes the formation of high-angle grain boundaries. This is consistent with the greater distribution of grain boundaries with >30° misorientation of the HPT material compared to the undeformed (Figure 7.7(a)–(b)).

The GND density measured by EBSD/TKD for the undeformed and HPT samples are respectively 9.5×10^{14} m^{-2} and 7.5×10^{15} m^{-2} (Figure 7.6). In comparison, the total dislocation density values measured by grazing-incidence XRD is 2.5×10^{14} m^{-2} and 3.8×10^{15} m^{-2}, respectively for the undeformed and HPT-deformed samples (Figure 7.8(d)). From transmission XRD, the dislocation density of the deformed material is 1.3×10^{16} m^{-2} (Figure 7.10(b)). The factor of dislocation density increase from HPT deformation is ∼8 from EBSD/TKD, and ∼15 measured from XRD. These values are in good agreement despite the fact that EBSD/TKD only probes a thin layer near the sample surface and only GNDs. In comparison, XRD measurements average over a much larger sample volume and mainly measure statistically stored dislocations (SSDs) [345]. The comparison between TKD and XRD measurements of dislocation density in the HPT-deformed material suggests that the density of GNDs is higher than the density of SSDs. This can be rationalised by considering that in severely deformed materials, dislocations are mainly located in the vicinity of grain boundaries (also seen in Figure 7.6(b)) and in the form of GNDs [603].

For characterisation with EBSD/TKD, only the indexed points contribute to the GND density calculation, which means that sampling is skewed towards the regions further away from the grain boundaries. In contrast, XRD probes the full sample volume, including regions of strong lattice distortions close to grain boundaries, which are not indexed with EBSD/TKD. The detection of a greater increase in dislocation

density following HPT from XRD measurements compared to EBSD/TKD supports the theory that large amounts of dislocations are stored in the grain boundaries rather than the grain interiors [226, 228]. It is important to note that for EBSD/TKD, the GND density is related to the degree of misorientation between adjacent points, and hence dependent on the step size used in the measurement. A smaller step size leads to more measurement noise [498]. The step size used for the EBSD of the undeformed sample is 25 times larger than the step size used for TKD in the deformed sample, due to the measurement constraints and the vastly different grain sizes in each sample. Therefore, the GND density in the HPT-deformed samples could be slightly overestimated.

HPT processing also causes the average dislocation character to change from more screw-like to more edge-like (Figure 7.8(e)). In coarse-grained BCC metals at room temperature, the dislocation population is predominantly of screw type, which is the case for the undeformed Eurofer-97. This is due to the high Peierls barrier and low mobility of screw dislocations [604], leading to a greater retention than edge dislocations [605]. Interestingly, it has been observed in other nanocrystalline BCC metals produced by HPT including W [606], Mo [292, 607], and Ta [262], there is an increased population of dislocations with edge character compared to in the coarse-grain material. There are several proposed explanations for these observations. One of which hypothesises that the smaller grain sizes, and hence a greater proportion of grain boundaries, means that fewer dislocations are retained in the crystal as they are annihilated at the grain boundaries [608]. This reduces the significance of the difference in mobility between edge and screw dislocations, leading to more comparable populations of each type. Furthermore, HPT deformation causes a large increase in dislocation density (forest dislocations), which in turn impedes the motion of glide dislocations [609]. The mobility of glide dislocations becomes increasingly governed by the forest dislocation density. This again makes the difference in mobility between screw and edge dislocations more insignificant. The other hypothesis is that hydrostatic compression increases the mobility of screw dislocations [608, 610]. This is because higher stress reduces the activation volume for thermally-activated kink-pair formation. This in turn reduces the thermal energy

barrier for dislocation motion and assists the movement of screw dislocations at low temperatures. An increase in screw dislocation mobility would lead to a more comparable probability of retention between screw and edge dislocations. Further studies are needed to determine which mechanism, or combination of them, is at play here. The microstructure of Eurofer-97 following HPT-deformation, in terms of grain size and dislocation density, saturated by $\gamma = 110$. Furthermore, the reduction in thermal diffusivity as a function of shear strain approached saturation beyond $\gamma = 70$. Interestingly, a previous nanoindentation study of this same set of materials found that HPT-processing hardened the material significantly, also approaching saturation beyond $\gamma = 70$ [567]. On the other hand, the changes to SAW velocity only saturates beyond $\gamma = 140$.

The saturation of dislocation density and changes to material properties beyond a certain strain level is expected [227, 230]. However, it is interesting that different material properties exhibit saturation behaviour at different shear strain thresholds. In particular, after the saturation of dislocation density and grain size, the SAW velocity continues to evolve with strain. This suggests that total dislocation density and grain size are not the only factors that govern material properties. A previous study of severely deformed Cu found that the ductility of the deformed material continues to change with strain even though the dislocation density remains saturated [611]. The authors demonstrated that yield strength and ductility saturate at different deformation levels due to rearrangements of dislocations and grain boundaries.

7.5.2 Thermal Stability of HPT Eurofer-97

Considering the changes in crystallite size and dislocation density, the HPT-processed material undergoes a recovery process between 450 K to 800 K (Figure 7.10). During the start of the recovery stage (450 K to 550 K), dislocation density is not expected to change significantly. The growth in crystallite size in this temperature range can be attributed to the rearrangement of dislocations within grains, causing subgrain coarsening whilst total dislocation density does not reduce significantly [612, 613]. Further annealing causes both the growth of these subgrains as well as the annihilation of dislocations, possibly at grain boundaries [614], reducing the overall dislocation

density as crystallite sizes increase. At ∼800 K, the onset of recrystallisation causes rapid grain growth and a reduction in dislocation density. Annealing also causes the average character of dislocations in the HPT Eurofer-97 material to revert from more edge-like to more screw-like, partially recovering the features of a coarse-grain BCC material [604, 605].

Other thermal stability studies of HPT-processed steel have been reported in the literature. For stainless steel 316L with γ up to 360, the dislocation density and crystallite size prior to annealing are comparable to this study, and these quantities stayed stable up to 560 K, after which dislocation density reduced significantly [271]. It is also interesting to note, that in that study, the steel structure was initially austenitic and transformed to martensitic during the process of HPT. During annealing, it slowly transformed back to austenitic, beginning at 650 K and up to 93% transformed following annealing at 1000 K. A study with differential scanning calorimetry of a Fe-10Ni-7Mn martensitic steel processed by HPT up to $\gamma = 785$ showed that dislocation annihilation with vacancies begins around 504 K [615]. This is similar to the temperature at which dislocation density started to reduce substantially in this study.

7.5.3 Effect of Irradiation

Ion irradiation to 0.08 dpa did not cause any microstructural changes that were observable by TEM or TKD. However, clear changes were measured with XRD and TGS. The reduction in dislocation density and increase in crystallite size following irradiation in the HPT-processed samples (Figure 7.8(c)–(d)) suggest an irradiation-induced annealing type process. Similar effects have been observed following irradiation of HPT-processed austenitic stainless steel 316 [322], martensitic Fe-Cr-W steel [324], EK-181 [330], and T91 steel [331]. However, these other studies typically examined much higher doses (>1 dpa) and elevated temperatures (>673 K). Observations of crystallite growth and dislocation density reduction in our study suggest that the movement of dislocations and subgrain coarsening aided by irradiation can happen at much lower irradiation dose and temperature.

In light of the findings on the dislocation density and material properties from the present study, we can draw a combined picture of the effect of HPT and irradiation.

HPT introduces grain refinement and a large population of dislocations due to plastic deformation. Subsequent irradiation introduces point defects and dislocation loops into the material. This is supported by the fact that the dipole character parameter fitted from CMWP suggests that the dislocations are arranged in a stronger dipole formation following irradiation, a possible indication of dislocation loops (Appendix F.4). However, from grazing-incidence XRD measurements we see a reduction of total dislocation density following irradiation in the HPT material compared to the unirradiated HPT material (Figure 7.8). This indicates a relaxation or annihilation of dislocations due to irradiation from the prior plastic deformation due to the irradiation process. Due to the low irradiation dose examined in this study, the population of irradiation-induced defects is not enough to compensate for the removal of dislocations that originally resulted from plastic deformation.

HPT deformation and ion irradiation both individually cause an increase in hardness, and a decrease in SAW velocity and thermal diffusivity of Eurofer-97. The effect of HPT alone causes more changes to the material properties, and total dislocation density, than irradiation alone. The effects of HPT deformation and irradiation to 0.08 dpa on the material properties are additive, whereas for dislocation density, subsequent irradiation removed some dislocations from prior deformation. Thus, we can conclude that changes to material properties are not simply a function of the total dislocation density but on their type and length scale. The deformation-induced extended dislocations annihilated in the HPT material during irradiation at 0.08 dpa do not contribute as much change in material properties as the small defects introduced by irradiation. However, the irradiation softening at 0.008 dpa (Figure 7.11) could indicate that the initial removal of dislocations from HPT deformation can be significant for material hardening. On the other hand, while the more dispersed but smaller irradiation-induced point defects and dislocation loops contribute less to XRD peak broadening, they still have a significant effect on material properties. This is particularly noticeable for changes to thermal diffusivity. The additional reduction of thermal diffusivity following irradiation of the HPT-deformed material is comparable to the reduction from solely the HPT process. Despite the net reduction in dislocation density, the further reduction of thermal diffusivity in the HPT-deformed

material following irradiation is indicative of the sensitivity of thermal diffusivity to the presence of small defects. The effect of small point defects, such as vacancies, on thermal diffusivity in other irradiated materials has been previously investigated [337].

7.6 Summary and Conclusion

In this study, grain refinement in Eurofer-97 has been successfully achieved via HPT at room temperature. The thermal stability and irradiation response of the resultant material have been characterised. The key findings are as follows:

- Grain refinement via the creation of high-angle grain boundaries was achieved with HPT. Grains smaller than 100 nm were created and the average grain size reduced from 5.26 µm to 146 nm.

- The average dislocation density in the material increases by over an order of magnitude following HPT, up to 10^{16} m^{-2}. The majority of these dislocations are located at or near grain boundaries.

- Grain refinement from HPT increases the proportion of dislocations with edge-like character. This is consistent with observations of other nanocrystalline BCC materials in literature.

- Saturation of grain size refinement and dislocation density increase was achieved by $\gamma = 110$. Thermal diffusivity and SAW velocity changes saturated at $\gamma = 70$ and $\gamma = 140$, respectively. Hardness approaches saturation for $\gamma > 70$. The saturation of microstructure and material properties at different shear strains indicates that dislocation configurations may still evolve even when grain size and total dislocation density saturate.

- Recovery was observed during annealing between 450 K to 800 K, with subgrain coarsening from the rearrangement and subsequent annihilation of dislocations. Recrystallisation and rapid grain growth began around 800 K.

- Irradiation of the undeformed Eurofer-97 material causes an increase in dislocation density. However, for the HPT-deformed material, irradiation causes a reduction in dislocation density, suggesting an irradiation-induced annealing process.

- HPT processing prior to irradiation does not prevent additional irradiation-induced changes at 0.08 dpa in hardness, thermal diffusivity and SAW velocity, which also occurs in the undeformed case. The irradiation-induced changes are slightly smaller in magnitude in the HPT materials compared to the undeformed but the effect is not significant.

By considering the microstructure and material properties of Eurofer-97, a multi-faceted view of the effect of SPD, and its subsequent impact on thermal stability and radiation resistance for ferritic/martensitic steels, emerges.

Data Availability

All data, raw and processed, as well as the processing and plotting scripts used in this study are available online at: https://doi.org/10.5281/zenodo.12751257 and https://dx.doi.org/10.5287/ora-o12zvwdzy

8 Conclusion

The work from this thesis focuses on the characterisation of FeCr steels following room-temperature ion irradiation as a function of irradiation dose, Cr content, and processing technique. The use of specialised techniques to characterise the small ion-irradiated sample volumes reveals novel insights into irradiation defect population and their effect on material properties in FeCr. By combining the a range of characterisation techniques in systematic irradiation studies, a multi-faceted view is obtained of irradiation-induced changes in material microstructure and properties that no single technique alone can afford.

The experimental results of room-temperature ion irradiation in FeCr are crucial for obtaining fundamental understanding of irradiation damage mechanisms, and how defect evolution is affected by dose and Cr content, both individually and synergistically. The focus on micromechanical characterisation of the deformation characteristics of irradiated FeCr demonstrates that valuable insights can be obtained to inform the understanding of irradiation damage of bulk mechanical properties in steels.

Understanding of the irradiation damage mechanisms and characterisation techniques from studying FeCr model alloys is further applied to Eurofer-97, a microstructurally complex RAFM steel. The effects of grain refinement through SPD and subsequent impact on thermal stability and irradiation response is also investigated.

The key results from the thesis are outlined below to address the initial research aims from Section 2.10:

1. What are the effects of room-temperature ion irradiation on Fe and FeCr alloys, especially defect populations and their impact on material properties?

Property changes in FeCr following room-temperature ion irradiation are substantial and different to those previously studied at higher temperatures (>573 K). These changes also cannot be fully accounted for from the defects directly imaged by TEM. By comparing the trends for lattice strain, hardness and thermal diffusivity across different dose levels and FeCr compositions, unique insights into the effect of dose and Cr content are obtained in Chapters 3 and 4.

Irradiation dose has a significant non-monotonic effect on lattice strain, which increases up to 0.8 dpa, then decreases with dose. This is in agreement with predictions from atomistic simulations, confirming that defects first appear as isolated Frenkel pairs, before clustering and subsequently forming extended structures. At high doses, the material evolves back to a less defective crystal structure as a dynamic quasi-steady state. In the low and transition dose regime, lattice strain measurements provide a lower-bound estimate of the defect density in FeCr, which is an order of magnitude greater than that observed by TEM. Lattice strain has a non-monotonic dependence on Cr content, with highest lattice strain observed for 5–8%Cr. This corresponds to a Cr concentration range where the diffusivity of self-interstitial defect clusters is the lowest.

Irradiation hardening in Fe and FeCr is measured even at 0.00008 dpa, well below the dose limit for defect detection by TEM. Hardness increases with irradiation dose up to 6 dpa, the maximum investigated in this thesis, and shows no saturation behaviour, unlike the lattice strain trends. Cr content also causes a monotonic increase of hardening and hardening rate due to increased retention of defects. These results are markedly different from irradiation at 573 K and above, where non-monotonic dependence on Cr content and hardness saturation have been observed [60, 98, 210]. This is important for nuclear reactor structural steel applications, as the performance of the components will be severely affected by their operating

temperatures and the previous studies in the literature for 573 K may not be applicable to lower temperatures.

In contrast to both lattice strain and hardening, thermal diffusivity has a weak dependence on irradiation dose and depends mainly on the Cr content of the material. This is a promising finding for fusion reactor components manufactured from RAFM steels, as their thermal properties are not expected to change significantly over time with irradiation.

The trends observed in these studies are useful for informing the behaviour of irradiated FeCr steels at low temperatures. This is key for comparisons to modelling studies, particularly those concerned with athermal effects including stress-driven processes, which will still be of concern at higher and more reactor-relevant temperatures (573 K and above). From comparisons to previous FeCr studies that performed irradiation at higher temperatures, the irradiation hardening trends as a function of dose and Cr content differ from those observed in this thesis. The findings regarding specific thermal diffusivity, lattice strain, and deformation behaviour at room temperature may not be directly extrapolated to higher temperatures. The main cause for this is the dependence of defect mobility on temperature and possible further studies are outlined in the subsequent section. However, it is worth noting that due to defect recombination that occurs at higher temperatures, the absolute changes to a particular material property, such as hardness and thermal diffusivity, due to irradiation tend to decrease with temperature [26, 60]. Therefore, the trends of property evolution at room temperature could provide an upper-bound estimate for predicting changes at higher temperatures.

2. How can micromechanical studies of ion-irradiated FeCr be used to understand the mechanisms of deformation in irradiated materials, and thus gain useful insights for reactor structural steels?

The information from nanoindentation techniques and the study of post-indentation structures in small ion-irradiated sample values using electron microscopy and X-ray techniques, can inform bulk mechanical properties. Results from Chapter 5 examine the initiation of plasticity via dislocation nucleation and activation by nanoindentation pop-ins. In FeCr, even with very few initial dislocations,

the dominant source of plasticity initiation is still from pre-existing dislocation sources in the material, independent of Cr content and irradiation defect density.

Nanoindentation stress-strain relationships, as measured from spherical nanoindentation, are able to provide insight into the plastic deformation behaviour of the ion-irradiated layer in FeCr. An increase in yield strength with Cr content and irradiation dose is consistent with hardness trends from Chapters 3 and 4, and bulk tensile testing of neutron-irradiated materials [193, 524]. A decrease in work hardening capacity with irradiation dose, regardless of Cr content is also found for ion-irradiated FeCr.

Analysis of the deformation microstructure and fields surrounding indents are presented in Chapter 6. A reduction in strain hardening capacity in irradiation FeCr causes increased pile-up topography surrounding indents and slip step formation. The lattice rotation and strain field volume in the material surrounding the indents are reduced by over 87% following irradiation, compared to the unirradiated material. Notably, Cr content does not have a significant effect in mitigating the post-irradiation loss of work hardening. This result is key to informing the design of fusion reactor structural steels to prevent irradiation-induced embrittlement.

3. How can the knowledge from Fe and FeCr binary alloys be applied to improve the properties for reactor structural steels?

The techniques developed for studying ion-irradiated FeCr were applied to Eurofer-97, a prototypical RAFM steel, processed by HPT in Chapter 7. Substantial grain refinement was achieved with HPT, along with a marked increase in high-angle grain boundaries and dislocation density. This caused a substantial increase in hardness and reduction in thermal diffusivity and surface acoustic wave velocity. Thermal recovery was observed in the HPT-processed material between 450–800 K. Irradiation of the HPT-processed material causes first irradiation-induced softening at 0.008 dpa before hardening at 0.08 dpa. Thermal diffusivity and surface acoustic wave velocity continue to decrease with irradiation, even for the HPT-processed material. However, these material property changes cannot be completely explained by total dislocation

density, which is reduced following irradiation in the HPT-processed material. HPT-processing prior to ion irradiation, despite increasing grain boundary surface area, has limited effects in mitigating irradiation-induced material property changes.

8.1 Outlook

The results of this work informs some research questions that are important to follow-up to further advance our understanding of materials for nuclear fusion and beyond:

1. How can we apply the experimental methodology from this work for further materials characterisation?

A key feature of the work presented in this thesis is the combination of multiple experimental techniques for characterisation of a material system. In particular, the use of lattice strain and hardness measurements respectively give information on the ratio of defect types (interstitial vs. vacancy concentration) and total defect content in FeCr. By using multiple techniques on the same material system, a multi-faceted picture of irradiation-induced defect population and its subsequent effect on material properties can be formulated that cannot be revealed by any one individual technique. Furthermore, the combination of electron microscopy, X-ray diffraction, and material property characterisation in HPT-deformed Eurofer-97 allow insight into different effects of grain refinement and dislocation on the material. These studies demonstrate the usefulness of examining material microstructure and property evolution on the same samples, as well as comparing different material property trends to fully characterise a material system.

The first use of TGS to characterise FeCr steels adds to a growing body of work that use this technique to study irradiation damage in materials [218, 337, 599, 600, 616]. The most recent trends include using TGS with in-situ annealing [616] and in-situ irradiation [617]. This allows rapid and dynamic characterisation of irradiation-induced property evolution. Applying these in-situ methods to materials relevant for structural steels is a natural extension of this work to further understand the role of defect evolution on material properties.

X-ray Laue diffraction has been used in many different ways in the studies presented in this thesis. For the first time, it has been used in FeCr steels to study the irradiation-induced lattice strain, as well as deformation fields around indents. There is great potential to apply this technique for both irradiation and deformation characterisation of other materials. Furthermore, there are current efforts, which I am involved in with scientists at the Argonne National Laboratory, to develop in-situ nanoindentation and 3D X-ray Laue diffraction capabilities. This will allow investigation into the propagation of strain fields at different stages of deformation and further the understanding of material deformation mechanics.

2. How does irradiation affect material microstructure and properties at other temperatures relevant for nuclear fusion applications?

The results of this thesis have demonstrated that room-temperature irradiation results in different defect and property evolution compared to irradiation conducted at higher temperatures. This prompts further studies involving different irradiation temperatures. In a nuclear reactor, structural components will experience a range of different operating temperatures. For example, those in close proximity to superconducting magnets will be operating at near liquid He temperature (4 K). The irradiation-response at these temperatures remains unknown but must urgently be investigated. On the other hand, even though deformation behaviour following high-temperature (>573 K) irradiation has been studied extensively (Section 2.6.3), a majority of these mechanical tests have been performed at room temperature. Studies in Fe [618] and FeCr [193] have shown that deformation behaviour also depends on the deformation temperature. The nanoindentation techniques and characterisation of post-deformation structures covered in Chapters 5 and 6 can be applied at different deformation temperatures in future studies to better inform the operation of nuclear reactor structural materials. Furthermore, the measurement of thermal diffusivity and irradiation-induced lattice strain demonstrated for FeCr irradiated at room temperature in this thesis can, and should, be extended to materials irradiated at different temperatures.

3. How can experimental characterisation be combined with modelling studies for a more comprehensive understand of irradiation damage?

Many of the experimental results from FeCr provide valuable data for comparison with simulation and modelling studies. In particular, the results of Chapter 6 can be used to inform crystal-plasticity finite element modelling, which accounts for the crystal orientation and active slip systems. This has been done previously for numerous other materials [342, 343, 619–622]. This is the next step to further an understanding of the mechanisms behind deformation and the interaction with irradiation defects. Ultimately, this can inform finite element modelling of bulk polycrystalline material, which will be useful in predicting the performance of reactor structural steels in operation.

4. How can the issue of irradiation-induced loss of strain hardening capacity in nuclear structural materials be addressed?

The almost-total loss of strain hardening capacity due to irradiation remains one of the biggest challenges facing nuclear reactor structural steels. There should be a continued effort to better understand the mechanisms responsible and identify strategies to preserve strain hardening capacity following irradiation. The work from this study has shown that Cr content in the material has very limited abilities to achieve this, which will help inform future steel designs.

To further apply this to reactor structural materials and RAFM steels, the effect of other alloying elements and interstitial elements, such as C, N, and O, should be understood. In particular, C content has been shown to have a large effect on the yield strength and work hardening capacity of austenitic steels [623] and the post-irradiation hardness of Fe and FeCr [624]. The effect of micro-alloying and thermo-mechanical heat treatments to improve the mechanical properties of Eurofer-97 following irradiation has also shown a potentially promising path forward [42]. The approach of this thesis has demonstrated the usefulness of irradiation studies in FeCr binary alloys to identify the fundamental mechanisms of irradiation damage, and isolate the role of Cr. Thus, this approach can also be applied to isolate the effect of different interstitial elements in FeCr steels. Further understanding of how these interstitials affect different aspects of the irradiation-induced material evolution of FeCr alloys, including with techniques developed in this thesis, will advance the development of steels for nuclear reactor structural components.

Appendices

A

Design of temperature-controlled sample holder

A custom-designed sample holder for ion irradiation with active temperature-control was made for the work in this thesis, in particular Chapters 4 and 6. It was particularly important for the higher dose ($\geq$ 0.8 dpa) samples. Without active temperature-control, an ion flux on the order of 10^{11} ions·cm^{-2}·s^{-1} would have caused significant sample heating. The temperature-controlled holder made it possible to produce a range of samples at different total dose levels, as different ion fluxes are required to complete the irradiation in a practically feasible timeframe.

A schematic of the holder temperature control system is shown in Figure A.1(a) with a photograph of the actual set-up in Figure A.1(b). The idea of the system is that a temperature reading is taken close to the samples on the holder and the information fed back to a control system. The temperature will then be controlled by a combination of continuous cool by connection to a liquid nitrogen reservoir, counteracted by intermittent heating with a cartridge heater.

The sample holder is made of Al6061 and primarily composed of two halves, held in close thermal contact via a screw through the long axis (horizontal in the schematic) of the two components. The 'front' half (left half in the schematic) is for mounting the individual samples for irradiation, which will be further discussed later. A K-type thermocouple is attached to this block, within 10 mm of the samples, for accurate temperature measurements. Another thermocouple is attached to the

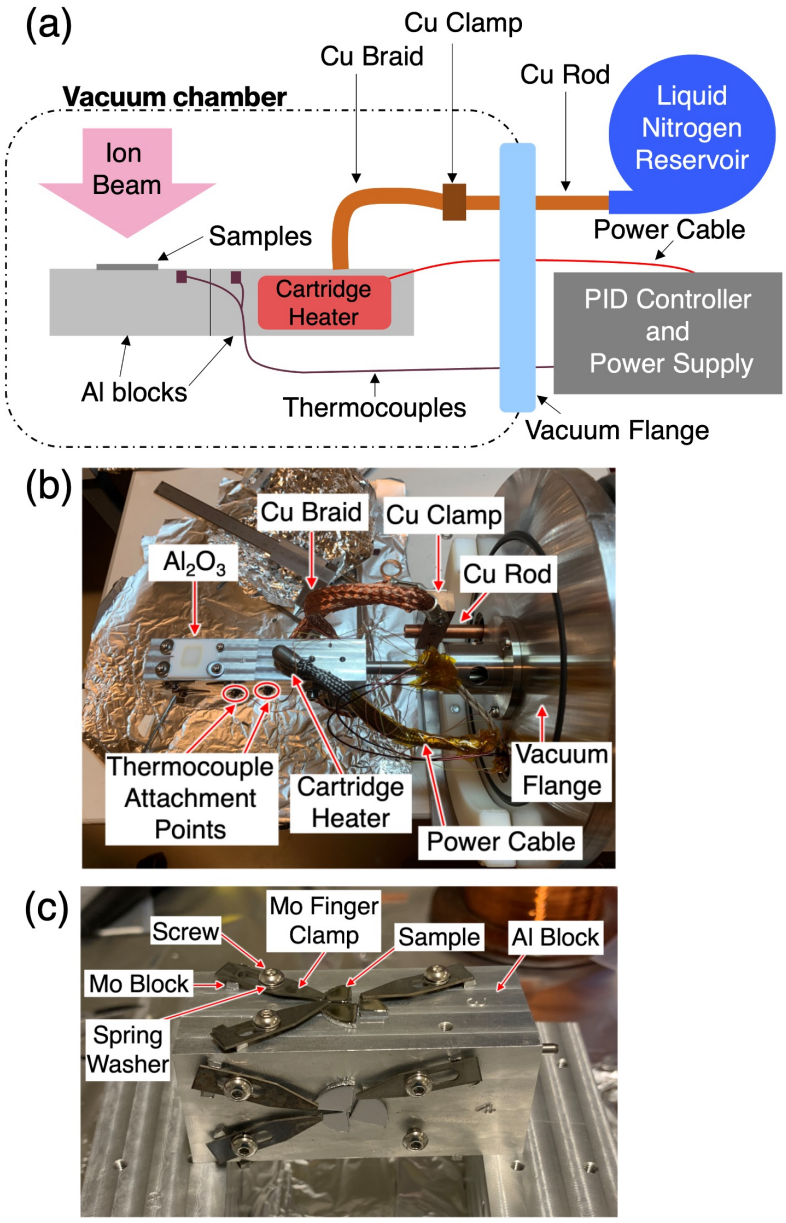


Figure A.1: (a) Schematic of temperature control system and components both inside and outside the vacuum irradiation chamber. (b) Photograph of the final assembled system to be put into the vacuum chamber for irradiation. Note that the sample mounted is a piece of Al_2O_3, which was used to calibrate the relative ion beam and sample holder positions in the chamber. (c) Close up photograph of the 'front' block where the samples are mounted with Mo finger clamps.

'back' half to monitor the thermal contact between the two blocks. This temperature difference never exceeded 2 K during irradiation. The thermocouple is attached to thermocouple connectors on the vacuum flange so that the temperature readings can be taken by the PID controller (Omron E5GC PID Temperature Controller)

external to the vacuum chamber.

The 'back' half is attached directly to a holder rod on the vacuum flange, which also allows rotation of the whole sample holder set-up, in order to irradiated different sides of the Al block. This half contains a cartridge heater, with a maximum power output of 80 W across a rod with length 15 mm and diameter 9.5 mm. Power cables are connected to electrical connections in the vacuum flange, so the power to the heater can be externally controlled by the PID controller.

Continuous active cooling is provided by a liquid nitrogen reservoir outside of the vacuum chamber. A Cu braid, crimped to Cu lugs on both ends, is attached to the Al holder block on one end and a Cu clamp on the other. The Cu clamp connects the Cu braid to the Cu rod, which runs through the vacuum flange, to be connected to the liquid nitrogen reservoir.

Figure A.1(b) shows a piece of Al_2O_3, mounted simply with washers. This material fluoresces under ion irradiation and hence was used to calibrate the irradiation area on the sample holder before mounting the FeCr samples. Figure A.1(c) shows how the actual FeCr samples are individually secured to the sample holder by finger clamps made of Mo. The use of finger clamps, of only 1 mm thickness, ensures that the clamps do not shadow the beam on any parts of the surface except directly under the clamp. Mo was chosen as the clamp material due to its low sputtering rate. The use of a screw and spring washer in the middle of the clamp, allows the samples to be held down gently but securely.

Overall, the temperature-control purpose of the set-up was successfully achieved. The samples were maintained within 313 $\pm$ 2 K during the entire duration of all the irradiation procedures for the studies in Chapters 4 and 6. Unfortunately, the one drawback of the set-up was the introduction of extra hydrocarbon contamination to the vacuum chamber, possibly from the thermocouple components. Even though the chamber was pumped for several hours prior to irradiation to ensure the vacuum level was around 10^{-7} mbar, the high dose samples (>0.8 dpa) have a visibly noticeable layer of carbon deposited on the surface. In the future, it would be helpful to ensure the thermocouples are fully vacuum compatible, but still flexible enough to accommodate the rotation of the sample holder in between irradiation stages.

B

Chapter 3 Appendix

B.1 Material Composition

Chemical analysis of the alloys in the as-delivered final metallurgical condition [66, 67].

Alloy	C (wppm)	S (wppm)	O (wppm)	N (wppm)	P (wppm)	Cr (wt%)
Fe3Cr	4	3	6	2	-	3.05
Fe5Cr	4	3	6	2	<5	5.40
Fe10Cr	4	4	4	3	<5	10.10

B.2 Elastic Modulus Data

The data shown in Figure B.1 is the average elastic from all indents taken on each sample, with the error bars representing ± one standard deviation. It can be seen that for the undamaged samples and samples with 0.08 dpa of nominal dose, the elastic modulus for Fe3Cr and Fe5Cr do not show a difference at any indentation depth. Fe10Cr exhibit slightly higher values at depths greater than 400 nm. However, these relative difference are small compared to the difference in hardness between samples of different Cr content (Figure 3.2(a)). For 0.008 dpa of nominal dose, the elastic modulus of all samples do not show any significant difference, within experimental errors.

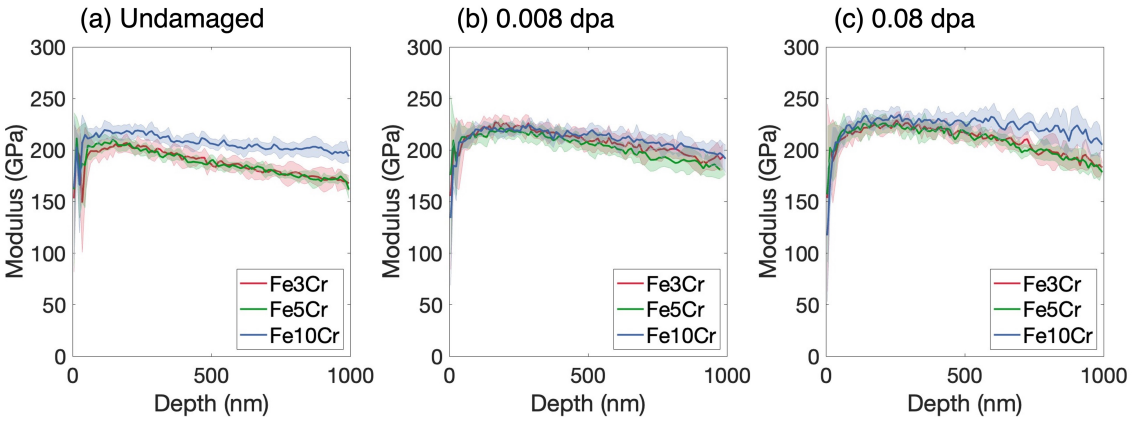


Figure B.1: Elastic modulus of the samples as a function of indented depth from CSM nanoindentation measurements. The data is grouped by dose level allowing comparison of the elastic modulus across different Cr content.

B.3 Experimental Validation of the Johnson Model

The Johnson model from Equation 3.1, modified for a Berkovich tip, is:

$$\frac{z_p}{h} = \left(\frac{2E}{3\sigma_{ys}}\right)^{1/3} \tag{B.1}$$

where z_p is the depth of the plastic zone directly beneath the indenter, h is the indentation depth, E is Young's modulus and σ_{ys} is the yield strength. The ratio $\frac{z_p}{h}$ can be obtained by looking at h_c, which is the indentation depth at which the plastic zone penetrates into the unirradiated bulk (which is known to be 3.5 µm below the surface from SRIM calculations). Therefore $\frac{z_p}{h} = \frac{3.5}{h_c}$, where h_c is in µm.

The yield strength, σ_{ys}, was obtained from a study by Matijasevic *et al.* [193] with similar Cr content (2.5%, 5% and 9%Cr). The results calculated from the 0.08 dpa samples are below:

Alloy	$\boldsymbol{h_c}$ **(nm)**	$\boldsymbol{\frac{z_p}{h}}$	$\boldsymbol{\sigma_{ys}}$ **(MPa) [193]**	$\boldsymbol{E}$ **(GPa) (between 300–600 nm)**	$\boldsymbol{\left(\frac{2E}{3\sigma_{ys}}\right)^{1/3}}$
Fe3Cr	565	4.31	409 (Fe2.5Cr)	228	7.19
Fe5Cr	525	4.71	462 (Fe5Cr)	218	6.80
Fe10Cr	745	3.03	514 (Fe9Cr)	218	6.56

We can conclude that fitting our experimental data to the Johnson model yields sensible results that agree within a factor of 2 to 3.

B.4 Parameters for Kinetic Theory Model

The parameters used to fit the kinetic theory model, in Equation 3.3, to the experimental data for thermal diffusivity.

Symbol	Quantity (of Fe)	Value	Source
C_e/T	Electronic Heat Capacity Coefficient	2.095×10^{-9} eV K^{-2} Å^{-3}	[446]
ν_f	Fermi Velocity	4.95 Å fs^{-1}	[446]
c_p	Specific Heat Capacity	25.14 J mol^{-1} K^{-1}	[625]
ρ	Density	7850 kg m^{-3}	[625]
κ_{Fe}	Thermal Conductivity	75.8 W m^{-1} K^{-1}	[436]

B.5 Calculation of Frenkel Pair Scattering Rate in Fe

In a similar form to Equation 3.3, the thermal conductivity, κ, due to scattering from Frenkel pairs in pure Fe can be written as:

$$\kappa = \frac{1}{3} C_e {\nu_f}^2 \left(\frac{c_{FP}}{\tau_{e,FP}} + \frac{1 - c_{FP}}{\tau_{e,Fe}} \right)^{-1} \tag{B.2}$$

where C_e is the electronic heat capacity, ν_f is the Fermi velocity, c_{FP} is the Frenkel pair concentration, $\tau_{e,FP}$ is the electron scattering time from the Frenkel pairs and $\tau_{e,Fe}$ is the scattering time of pure Fe.

Using the Wiedemann-Franz law, the above equation can be written as:

$$\rho_e = \frac{3LT}{C_e {\nu_f}^2} \left(\frac{c_{FP}}{\tau_{e,FP}} + \frac{1 - c_{FP}}{\tau_{e,Fe}} \right) \tag{B.3}$$

where ρ_e is the electrical resistivity, L is the Lorenz number and T is the temperature. Differentiating both sides by c_{FP}, we obtain an expression involving resistivity per Frenkel pair. This has an experimental value of 20 µΩm [626]. This allows us to solve for $\tau_{e,FP}$, which has a value of 0.052 fs.

B.6 Defect Density Calculations and Comparisons

B.6.1 Defect Density From Lattice Strain Measurements

We use the following expression for strain as a function of defect density [176]:

$$\epsilon_{zz} = \frac{1}{3}\frac{(1+\nu)}{(1-\nu)}\sum_{A} n^{(A)}\Omega_r^{(A)} \tag{B.4}$$

where ϵ_{zz} is the measured out-of-plane strain, $\nu = 0.3$ is the Poisson ratio (for pure Fe [449]), $n^{(A)}$ and $\Omega_r^{(A)}$ are respectively the number density and relative relaxation volume for each type of defect (A).

As the lattice strain values measured are all positive, this means some interstitial defects are present in our material. We then make the following assumptions in our calculations:

- There is no clustering of interstitials. This means the relaxation volume per point defect is maximised [450].
- There is no loss of interstitial defects, which are much more mobile than vacancies [44], to the surface of the materials. This means there are equal numbers of interstitial atoms (n^i) and vacancies (n^v).

By employing these assumptions, we obtain the lower bound of the equivalent Frenkel pair density (n^{FP}). If interstitials did cluster, then the relaxation volume per point defect would decrease, requiring more Frenkel pairs to be present in order to produce the same amount of positive strain that was measured (covered by assumption 1). If interstitials were lost to the surface, again more equivalent Frenkel pairs would need to be present to account for the amount of positive strain measured (covered by assumption 2).

Rearranging Equation B.4, we get:

$$n^{FP} = \frac{\epsilon_{zz}}{\Omega_r^{FP}}\left(\frac{3(1-\nu)}{(1+\nu)}\right) \tag{B.5}$$

The relative relaxation volume, per point defect, of a $\langle 111\rangle$ interstitial is $\Omega_r^{\langle 111\rangle} = 1.65$ and that of a $\langle 100\rangle$ interstitial defect is $\Omega_r^{\langle 100\rangle} = 1.86$ [179]. For a vacancy, the relative relaxation volume is $\Omega_r^v = -0.22$ [179]. In order to obtain the volumetric

number density (N^{FP}) of the equivalent Frenkel pairs, we then need to multiply by the atomic density of Fe ($\rho_{Fe} = 8.48 \times 10^{28}$ m^{-3}).

An example calculation: At 0.03 dpa of damage-at-depth, the largest strain observed is from Fe5Cr at 4.491×10^{-4} (from Figure 3.7). If all the interstitial defects are of $\langle 111 \rangle$ nature, then $\Omega_r^{FP,\langle 111 \rangle} = 1.65 - 0.22 = 1.43$. Substituting this into Equation B.5:

$$\begin{aligned} N^{FP,\langle 111 \rangle, Fe5Cr} &= \rho_{Fe} \times n^{FP,\langle 111 \rangle, Fe5Cr} \\ &= \rho_{Fe} \times \frac{\epsilon_{zz}^{Fe5Cr}}{\Omega_r^{FP,\langle 111 \rangle}} \times \left(\frac{3(1-\nu)}{(1+\nu)} \right) \\ &= (8.48 \times 10^{28}) \times \left(\frac{4.49 \times 10^{-4}}{1.43} \right) \times \left(\frac{3(1-0.3)}{(1+0.3)} \right) \\ &= 4.29 \times 10^{25} \text{ m}^{-3} \end{aligned}$$

As Fe5Cr has the highest strain, and $\langle 111 \rangle$ defects have the lowest relaxation volume per defect, this value is the upper range of our equivalent Frenkel pair density estimate at 0.04 dpa of damage-at-depth. For the lower range, this will come from the calculation using the strain value of Fe3Cr ($\epsilon_{zz}^{Fe3Cr} = 2.69 \times 10^{-4}$ from Figure 3.7) and assuming all interstitial defects are of $\langle 100 \rangle$ nature ($\Omega_r^{FP,\langle 100 \rangle} = 1.86 - 0.22 = 1.64$). Using the same calculation steps as above, we obtain $N^{FP,\langle 100 \rangle, Fe3Cr} = 2.25 \times 10^{25}$ m^{-3}.

For 0.3 dpa of damage-at-depth, we repeat the same calculations, using $\epsilon_{zz}^{Fe5Cr} = 5.69 \times 10^{-4}$ and $\epsilon_{zz}^{Fe3Cr} = 3.85 \times 10^{-4}$ (from Figure 3.7). We get the range of equivalent Frenkel pair volumetric number density $3.22 - 5.44 \times 10^{25}$ m^{-3}.

To summarise, from our lattice strain measurements, we estimate equivalent Frenkel pair volumetric number densities:

- At 0.03 dpa of damage-at-depth: $2.25 - 4.29 \times 10^{25}$ m^{-3}
- At 0.3 dpa of damage-at-depth: $3.22 - 5.44 \times 10^{25}$ m^{-3}

B.6.2 Defect Density from TEM Studies

For calculations of equivalent Frenkel pair density from TEM studies, we make the following assumption:

- All dislocation loops and defects observed are of interstitial nature.

TEM studies have found that a majority of the defects observed are interstitials rather than vacancies [59, 122]. This is generally attributed to the lower mobility of vacancies, leading to less growth of vacancy loops to sizes observable in TEM. By assuming all observable defects are of interstitial nature, we calculate the upper bound of the equivalent Frenkel pair density in the material.

From Yao *et al.* - 0.4 dpa

Yao *et al.* [109] found the following:

- Areal defect density = 1×10^{15} m^{-2} (see Figure B.2).
- Average defect diameter = 2.1 nm (see Figure B.3).
- Damage layer thickness = 19 nm.

For simplicity, only one value of damage level was compared. 0.4 dpa was chosen as it has the largest difference in damage compared to the other TEM study in reference [59].

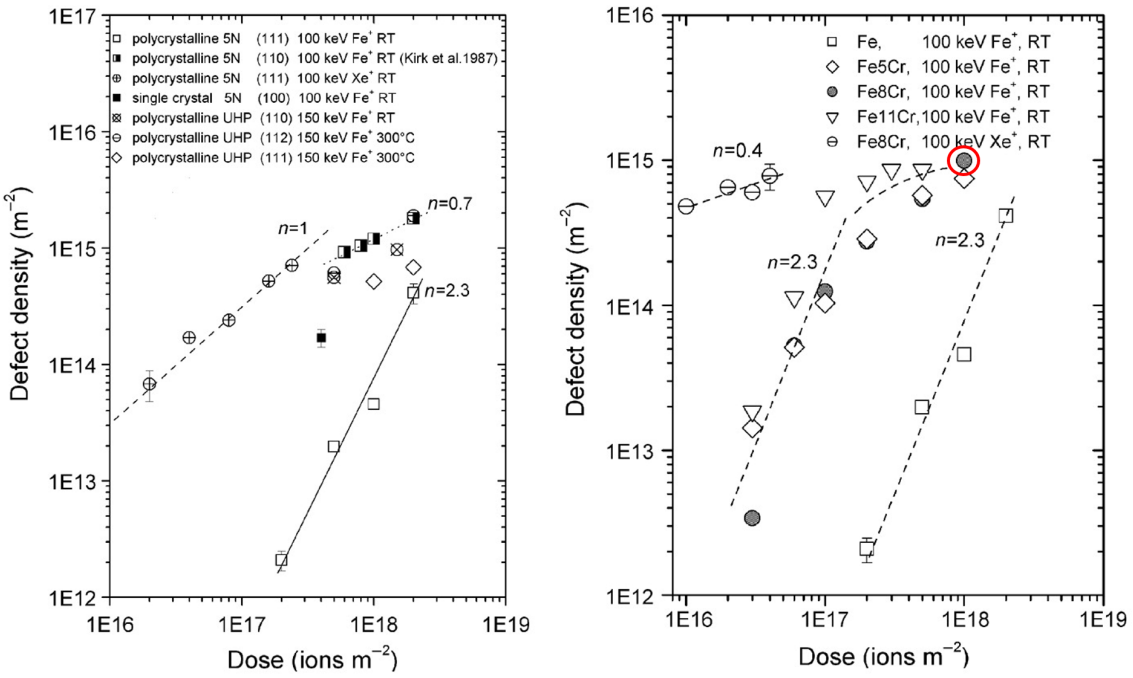


Figure B.2: Data from Figure 2 of [109]. Yao *et al.* quoted 2×10^{16} ions m^{-2} as being equivalent to 0.01 dpa. The defect density for FeCr at 8×10^{17} ions m^{-2} is then taken to be approximately 1×10^{15} m^{-2}. The red circle was added to indicate the data point from which the value was taken.

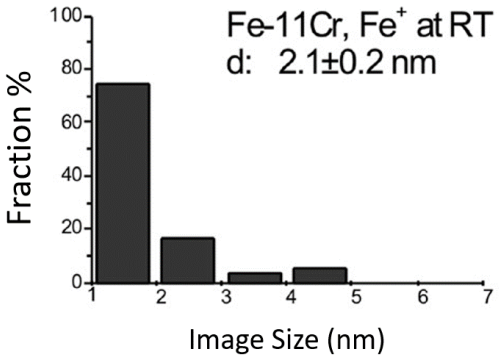


Figure B.3: Data from Figure 6 of [109]. The only reported values for defect sizes in FeCr are of Fe11Cr. The damage level is equivalent to 0.15 dpa but the authors reported similar distribution of sizes for damage levels below 0.5 dpa.

The lattice parameter of BCC Fe is $a_0 = 0.287$ nm. The planar density of the (100) plane is $\frac{1}{{a_0}^2} = 12.1$ atoms·nm^{-2}. For the (111) plane, the planar density is $\frac{1}{\sqrt{3}{a_0}^2} = 7.0$ atoms·nm^{-2}. We also need to take into account the defects that are invisible due to $\mathbf{g} \cdot \mathbf{b} = 0$. In the TEM study, $\mathbf{g} = \{110\}$, which means only $\frac{1}{2}$ of the $\langle 111 \rangle$ defects and $\frac{2}{3}$ of the $\langle 100 \rangle$ defects are actually visible.

The equivalent Frenkel pair volumetric density (N^{FP}) can be calculated by:

$$N^{FP} = \frac{\text{areal defect density} \times \text{defect area} \times \text{planar density}}{\text{damage layer thickness} \times \text{fraction of defects visible}} \tag{B.6}$$

If all interstitials were of $\langle 111 \rangle$ nature:

$$\begin{aligned} N^{FP,\langle 111 \rangle} &= \frac{(1 \times 10^{15}) \times ((1.05 \times 10^{-9})^2 \times \pi) \times (7.0 \times 10^{18})}{19 \times 10^{-9} \times \frac{1}{2}} \\ &= 2.6 \times 10^{24} \text{ m}^{-3} \end{aligned}$$

Similarly, if all interstitials were of $\langle 100 \rangle$ nature:

$$\begin{aligned} N^{FP,\langle 100 \rangle} &= \frac{(1 \times 10^{15}) \times ((1.05 \times 10^{-9})^2 \times \pi) \times (12.1 \times 10^{18})}{19 \times 10^{-9} \times \frac{2}{3}} \\ &= 3.3 \times 10^{24} \text{ m}^{-3} \end{aligned}$$

From Schäublin *et al.* - 0.05 dpa

Schäublin *et al.* [59] found the following:

- Volume defect density $= 1 \times 10^{23}$ m^{-3} (see Figure B.4, corrections for $\mathbf{g} \cdot \mathbf{b} = 0$ already made).

- Average defect diameter = 1.1 nm (see Figure B.5).

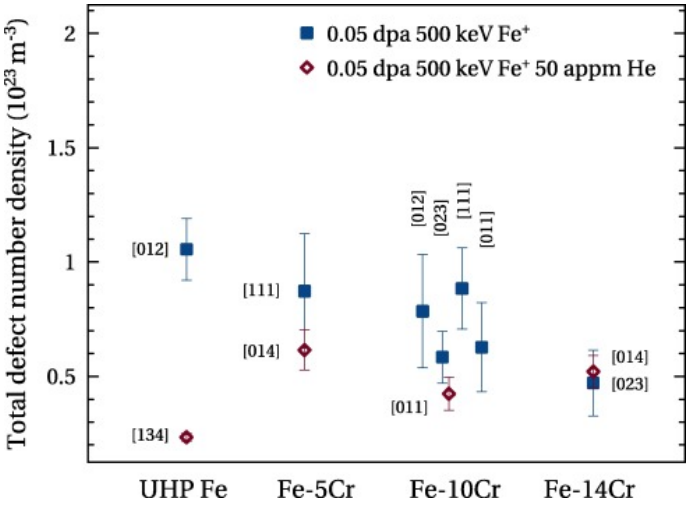


Figure B.4: Data from Figure 5 of [59]. At 0.05 dpa (Fe^+ irradiation only), the highest defect density observed in FeCr is 8×10^{23} m^{-3}.

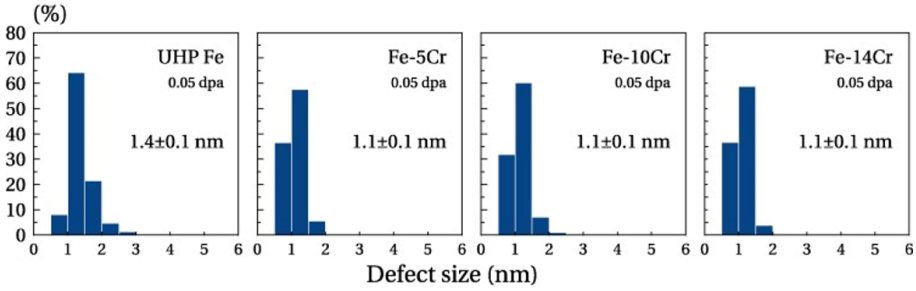


Figure B.5: Data from Figure 6 of [59]. At 0.05 dpa (Fe^+ irradiation only), the average defect size in FeCr is 1.1 nm.

The equivalent Frenkel pair volumetric density (n_d) can be calculated by:

$$N^{FP} = \text{volume defect density} \times \text{defect area} \times \text{planar density} \tag{B.7}$$

If all interstitials were of $\langle 111 \rangle$ nature:

$$\begin{aligned} N^{FP,\langle 111 \rangle} &= (1 \times 10^{23}) \times ((0.55 \times 10^{-9})^2 \times \pi) \times (7.0 \times 10^{18}) \\ &= 6.65 \times 10^{23} \text{ m}^{-3} \end{aligned}$$

Similarly, if all interstitials were of $\langle 100 \rangle$ nature:

$$\begin{aligned} N^{FP,\langle 100 \rangle} &= (1 \times 10^{23}) \times ((0.55 \times 10^{-9})^2 \times \pi) \times (12.1 \times 10^{18}) \\ &= 1.15 \times 10^{24} \text{ m}^{-3} \end{aligned}$$

B.6.3 Comparisons

The following table summarises the equivalent Frenkel pair densities from lattice strain measurements and TEM studies:

Dose (dpa)	**Lattice Strain Measurements ($\times 10^{23}$ m^{-3})**	**TEM Measurements ($\times 10^{23}$ m^{-3})**
0.03–0.05	225 - 429	6.7 - 11.5
0.3–0.4	322 - 544	26 - 33

We note that since these calculations used the average loop size instead of the full log-normal size distribution, the defect density could be underestimated. This calculation has been repeated using the approach reported by Haley *et al.* [627]. The full loop size distribution was taken into account. The number of defects per loop, with diameter d for a BCC material was calculated by [627]:

$$N(d) = \sqrt{3}\left(\frac{d}{2a_0}^2\right). \tag{B.8}$$

Furthermore, a power-law function was fitted to the density of clusters as a function of the cluster size. This allows the extrapolation of the density of cluster sizes too small to be observed by TEM [627–629]. Even with this combined approach, the estimates of Frenkel pair density from TEM observations are still 1–2 orders of magnitude below the estimates from the lattice strain measurements.

C

Chapter 4 Appendix

C.1 EBSD Maps of Samples

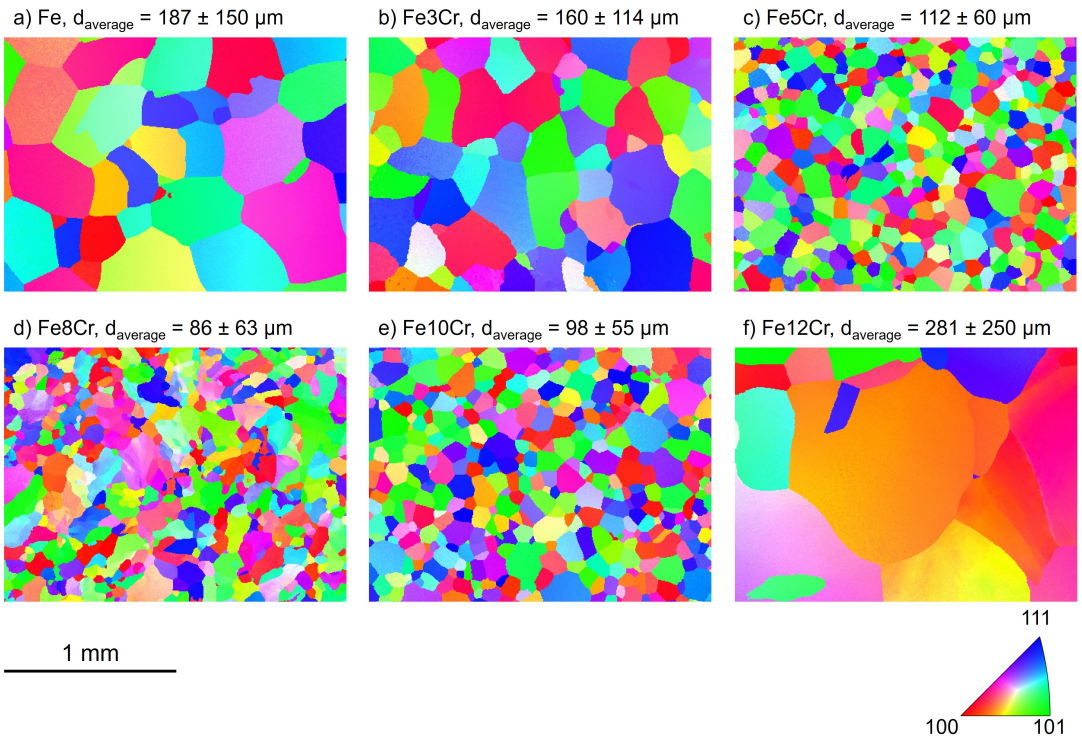


Figure C.1: Representative grain maps for each composition of FeCr in this study measured by EBSD.

Electron backscatter diffraction (EBSD) was carried on a Zeiss Merlin FEG-SEM at the David Cockayne Electron Microscopy Centre at the University of Oxford. The acceleration voltage used was 30 kV with a probe beam current of 10 nA.

Post-processing was performed using the Oxford Instruments HKL Channel 5 Tango software to remove noise and determine the grain sizes.

The representative orientation maps (Figure C.1) were used to select the appropriate areas for lattice strain measurements. The microstructure of the Fe8Cr material also exhibits signs of cold-work (intragranular misorientation). However, this did not have a significant impact on the lattice strain measurements.

C.2 Defect Density Calculations

The method used to calculate the defect density from the lattice strain measurements is similar to the method used in our previous study [422]. For further details and example calculations, readers are referred to the supplementary file of [422] (Appendix B.6). In this section, we provide an overview of the equations used and assumptions made in our defect calculations.

C.2.1 Defect Density from Lattice Strain Measurements

The out-of-plane strain, ϵ_{zz}, induced by irradiation defects can be expressed as [176]:

$$\epsilon_{zz} = \frac{1}{3}\frac{(1+\nu)}{(1-\nu)}\sum_{A} n^{(A)}\Omega_r^{(A)} \tag{C.1}$$

where $\nu = 0.3$ is the Poisson ratio (for pure Fe [449]), $n^{(A)}$ and $\Omega_r^{(A)}$ are respectively the number density and relative relaxation volume for each type of defect (A).

For low irradiation dose ($\leq$0.008 dpa), we made the following assumptions in our calculations:

- There is no clustering of interstitials or vacancies. This means the relaxation volume per point defect is maximised [450].

- There is no loss of defects, particularly interstitials, to the surface of the materials or to sinks such as grain boundaries. This means that there is an equal number of interstitial atoms (n^i) and vacancies (n^v).

Using these assumptions, we obtain a lower bound of the equivalent Frenkel pair density (n^{FP}). Clustering of interstitials would decrease the relaxation volume per point defect [179], requiring more Frenkel pairs to be present in order to produce the same amount of positive strain that was measured (covered by assumption 1). If interstitials were lost to the surface, more equivalent Frenkel pairs would need to be present to account for the amount of positive strain measured (covered by assumption 2).

Rearranging Equation C.1 and multiplying by the atomic density of Fe (ρ_{Fe} = 8.48 $\times 10^{28}$ m^{-3}) yields the volumetric number density of equivalent Frenkel pairs:

$$N^{FP} = \frac{\rho_{Fe}\epsilon_{zz}}{\Omega_r^{FP}}\left(\frac{3(1-\nu)}{(1+\nu)}\right) \tag{C.2}$$

The relative relaxation volume, per point defect, of a $\langle 111 \rangle$ interstitial is $\Omega_r^{\langle 111 \rangle}$ = 1.65 and that of a $\langle 100 \rangle$ interstitial defect is $\Omega_r^{\langle 100 \rangle}$ = 1.86 [179]. For a vacancy, the relative relaxation volume is Ω_r^{v} = -0.22 [179]. As a $\langle 100 \rangle$ interstitial has a higher positive relaxation volume, we can use $\Omega_r^{FP} = 1.86 - 0.22 = 1.64$ to get a lower bound estimate on the equivalent Frenkel pair density in the irradiated samples.

C.2.2 NRT Efficiency Calculation

The NRT efficiency describes the ratio of produced and retain defect density to the value predicted by the NRT-dpa model [72]. The calculation of the NRT-dpa was from the vacancy.txt file generated by SRIM using the Quick K-P model, following the descriptions provided in [70, 461]. The NRT efficiency can then be expressed by:

$$\begin{aligned} \text{NRT efficiency} &= \frac{n^{FP}}{dpa} \\ &= \frac{\epsilon_{zz}}{(dpa)\Omega_r^{FP}}\left(\frac{3(1-\nu)}{(1+\nu)}\right) \end{aligned} \tag{C.3}$$

From Figure 4.6, the NRT efficiency value for each sample was calculated from the average NRT-dpa in the top 2 µm of each implantation dose profile. This is consistent with the calculation of the nominal dose for each sample.

C.3 Nix-Gao Analysis

The fitted h^* parameter, representing the ISE characteristic length scale as a function of dose is shown in Figure C.2. h^* appears to decrease with increasing dose and does not show a clear dependence on Cr content. We note that the fitting for 3.6 dpa and 6 dpa samples appear to show quite large errors compared to the lower dose samples.

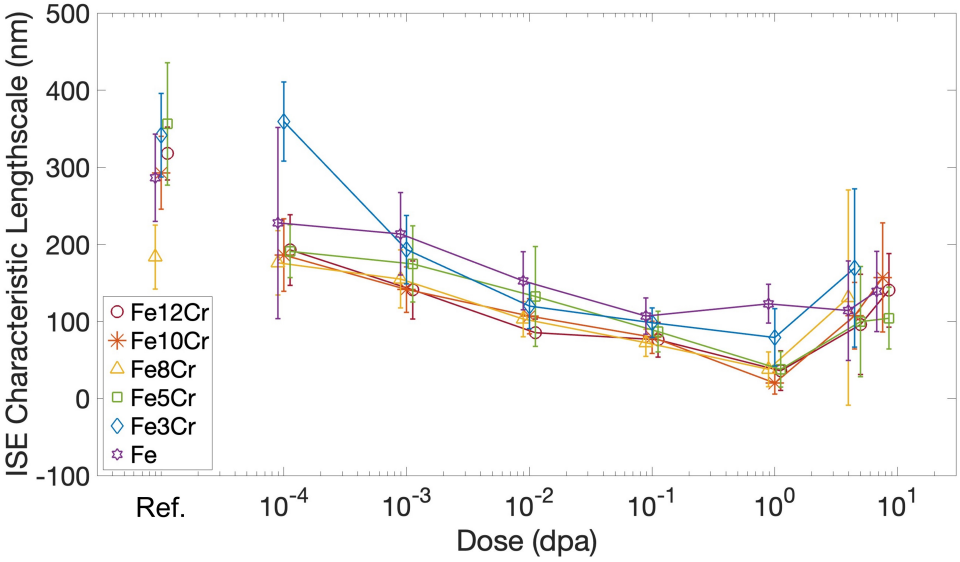


Figure C.2: h^* as a function of dose for different compositions.

C.4 Atom Probe Tomography Results

Due to concerns about possible carbon contamination during the irradiation process, atom probe tomography (APT) was performed on the Fe10Cr sample, exposed to 0.8 dpa, to quantify the concentration of carbon present in the sample. APT analysis was performed using a Leap 5000XR microscope in laser mode. The laser energy was 50 pJ with a pulse frequency of 200 kHz and detection rate of 0.5. Samples were maintained at 50 K for the analysis.

The depth profiles of a few key elements are presented in Figure C.3. Near the surface ($0 <$ depth $<$ 100 nm), there is a high concentration of C and N, possibly due to surface contamination and FIB milling process. There is a spike in C concentration at ~400 nm depth, which also correlated with a spike in O atoms and C-Cr ions (not shown in plot).

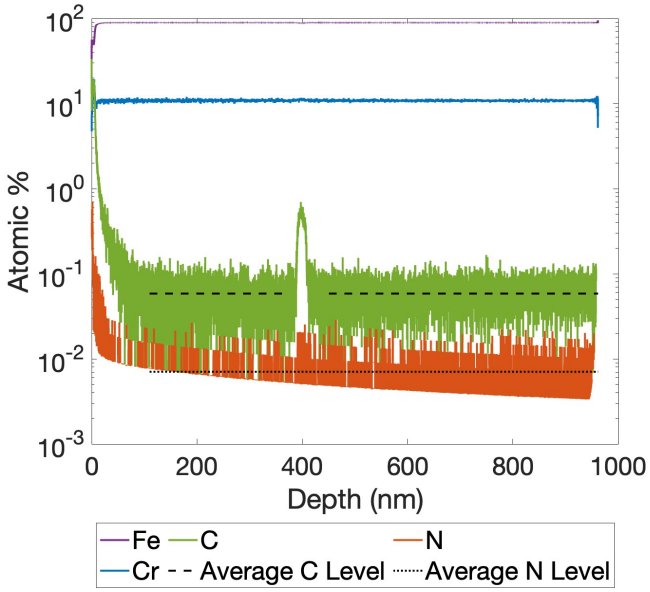


Figure C.3: Depth profile of Fe, Cr, C, and N as measured by APT from the Fe10Cr 0.8 dpa sample.

Element	Nominal content from manufacturer (appm)	Measured content from APT (appm)
C	18.5 ± 3.7	585 ± 236
N	11.9 ± 2.4	71 ± 37
O	17.3 ± 3.5	160 ± 107
P	8.9 ± 1.8	103 ± 84

Table C.1: A comparison of the concentration of different elements in the Fe10Cr alloy as reported by the manufacturer and measured by APT (averaged between 100 nm to 950 nm below the surface, excluding the C spike between depths of 380 nm to 410 nm).

APT results indicate a higher concentration of impurity elements in the Fe10Cr alloy than reported by the manufacturer (analysed by glow discharge mass spectrometry [66]). For N, O and P, the concentrations measured by APT are between 7 to 11 times higher than the manufacturer-reported values. For C, the difference is a factor of 30. It is important to consider that the APT sample preparation required FIB milling and lift-out, which itself will introduce some contamination. Similar discrepancies between the manufacturer-reported values and those measured

by APT have been reported previously for samples cut from the same raw material [60]. The true amount of C enrichment following irradiation is probably around 100–200 appm for the 0.8 dpa samples.

It is also important to note that since the C contamination originated from the irradiation process, the level of contamination scales with irradiation time and dose. This means for samples irradiated to less than 0.8 dpa, the C enrichment is not expected to play a significant role. From a visual assessment of the materials, only samples irradiated to 0.8 dpa and above show a slight to moderate browning due to carbon deposition on the surface.

D

Chapter 5 Appendix

D.1 Comparison to Uniaxial Tensile Tests

A comparison is made between the solid solution hardening from the indentation yield strength results of this study and uniaxial tensile tests performed by Horne *et al.* [531] on single crystal samples of Fe and FeCr at 300 K. The amount of hardening between Fe and Fe-11.9%Cr (in this study Fe10Cr) is similar between the two studies (Figure D.1). It is unclear why there is a reduction in CRSS in the single crystal study from Fe to Fe-2.1%Cr and Fe to Fe-4.8%Cr. The overall slope of the fitting hardening rate is similar.

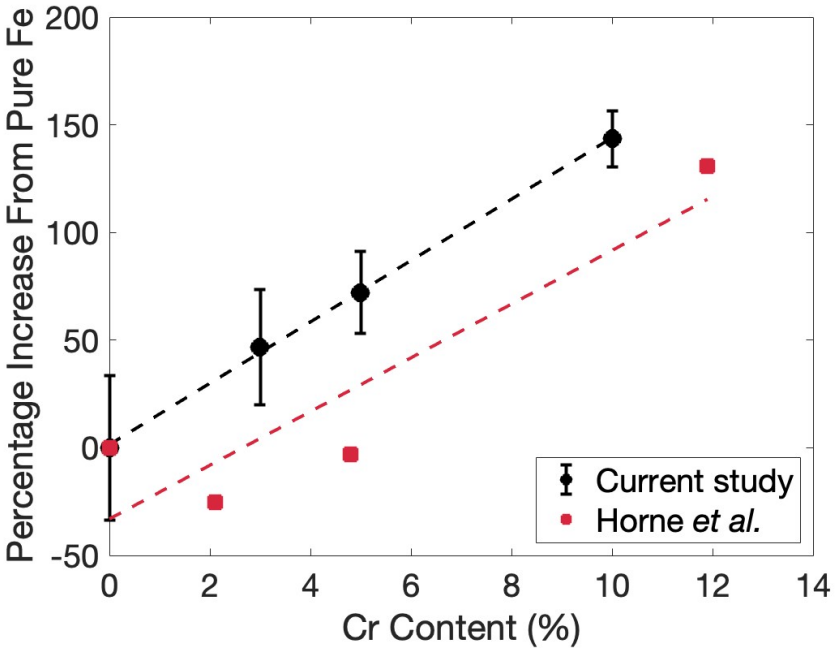


Figure D.1: The rate of yield stress increase (relative to the yield stress of pure Fe samples in the respective studies) of values obtained via uniaxial tensile testing (red squares) from Horne *et al.* [531] compared to those obtained via ISS analysis in this study (black circles).

E

Chapter 6 Appendix

E.1 Grain Orientation

The orientations of the grains analysed with AFM (Figure 2) and DAXM (Figures 3 and 4).

Sample	Euler Angles (ϕ, θ, ψ in ZXZ' convention)	Misorientation with $\langle 001 \rangle$ (degrees)
Fe Unirradiated	(207.26, 34.53, 325.12)	3.33
Fe Irradiated	(197.09, 41.09, 299.44)	3.97
Fe10Cr Unirradiated	(223.51, 9.83, 356.97)	2.44
Fe10Cr Irradiated	(212.18, 28.26, 307.19)	3.54

E.2 AFM Deflection Error

A plot of the deflection error, which is the difference between the measured deflection of the AFM probe and the set point, of the scan of a nanoindent on the irradiated Fe sample (Figure E.1). From this plot, the slip steps can be more easily identified in the pile-up lobes.

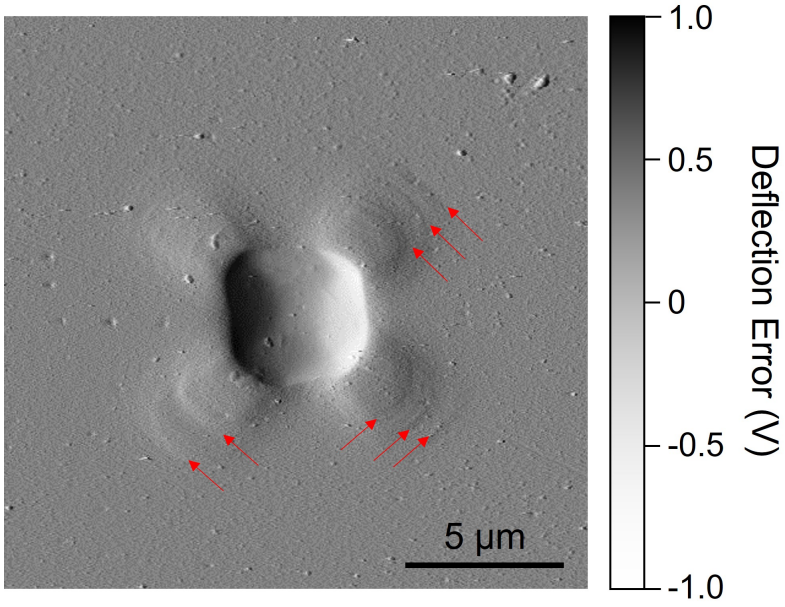


Figure E.1: The deflection error of the scan surrounding a nanoindent on the irradiated Fe sample. Red arrows point to regions where slip steps can be easily identified.

E.3 DAXM Set-Up

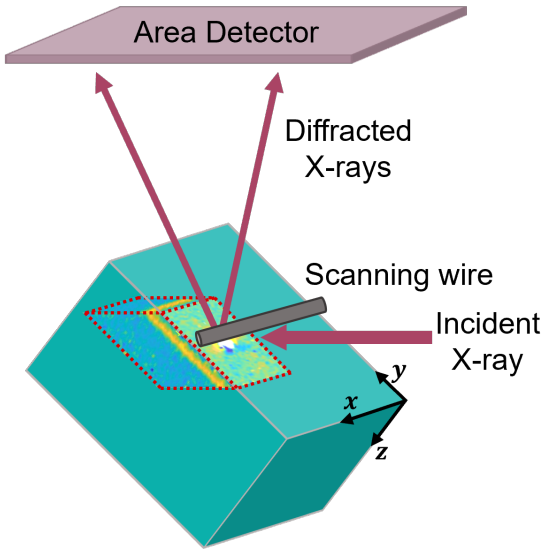


Figure E.2: A schematic of the DAXM measurements showing the coordinates used in this study, the relative position of the indent, the scanned volume (dashed red lines), the bulk sample, and the beamline set-up. The example data shown here is from the Fe10Cr irradiated sample. The relative size of the scanned volume and the bulk sample is not to scale.

The sample is mounted in a 45° reflection geometry. The diffraction patterns are

captured by a 2D area detector (Perkin-Elmer, #XRD 1621) positioned ∼511 mm above the sample. A platinum wire, of ∼100 µm in diameter, is scanned parallel to the sample surface, perpendicular to the incoming beam. As it cuts through the diffracted beams, it blocks signal from certain depths in the sample. By comparing the recorded intensity associated with different wire positions, an intensity profile as a function of depth along the beam path can be calculated for each detector pixel. Further information on the DAXM technique can be found in [177, 374, 375].

We also note that with polychromatic X-ray Laue measurements, only the deviatoric strain components are measured since the there is no information on the radial positions of the diffraction peaks in reciprocal space [379]. This is because the volumetric components of strain can only be determined if the the absolute lattice spacing is known from monochromatic X-ray Laue measurements. There are two ways to determine the full elastic strain tensor. The first is to obtain a monochromatic measurement of one diffraction peak to determine the absolute lattice plane spacing, then combine it with the deviatoric strain measurements from polychromatic X-ray Laue diffraction [176, 630]. The second method is to conduct energy scans to determine the absolute reciprocal space position of at least three non-collinear reflections [177, 379, 631].

Depth-resolved energy scans of the irradiated samples have been previously reported in [556], but only for isolated points on the sample to determine the absolute change in lattice spacing due to ion irradiation. However, these energy scans were not performed for the 3D volume around the nanoindents in this study as the energy scan measurements take a long time and the deviatoric strains are sufficient for studying the deformation characteristics.

E.4 Lattice Rotations and Strains in the $x - y$ Plane

Lattice rotations and strains have been plotted in the $x - y$ plane, which is parallel to the bulk sample surface, at a slice taken from 2.5–3 µm below the surface (Figures E.3

and E.4). The spatial symmetries on the rotation and strain fields are as expected for indentation with a spherical indenter.

Deformation localisation can be seen in both the lattice rotation and strain fields in the irradiated materials. In particular, the lattice strain field of the indent in the unirradiated Fe10Cr material has a very wide spatial distribution, up to 20 µm from the indent centre (Figure E.4). However, for the irradiated material the strain field is significantly more confined, only extending up to 10 µm away from the indent centre.

The distribution of large positive strain in the z direction for the irradiated Fe sample, even far away from the indent, is most likely due to the presence of the injected ions from the ion irradiation, as discussed in the main text and previously in [422, 556].

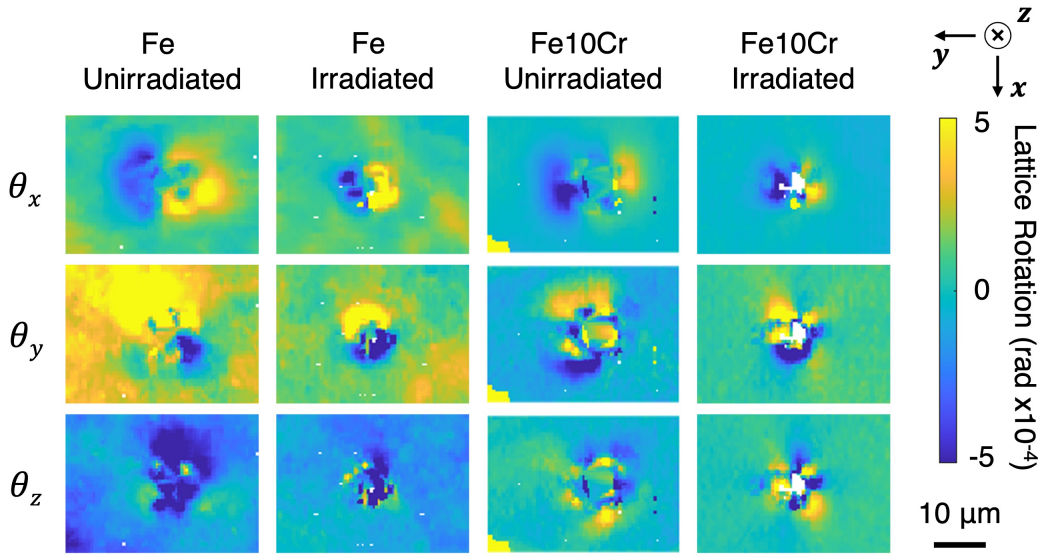


Figure E.3: Lattice rotation in the $x - y$ plane at a depth of 2.5–3 µm below the surface.

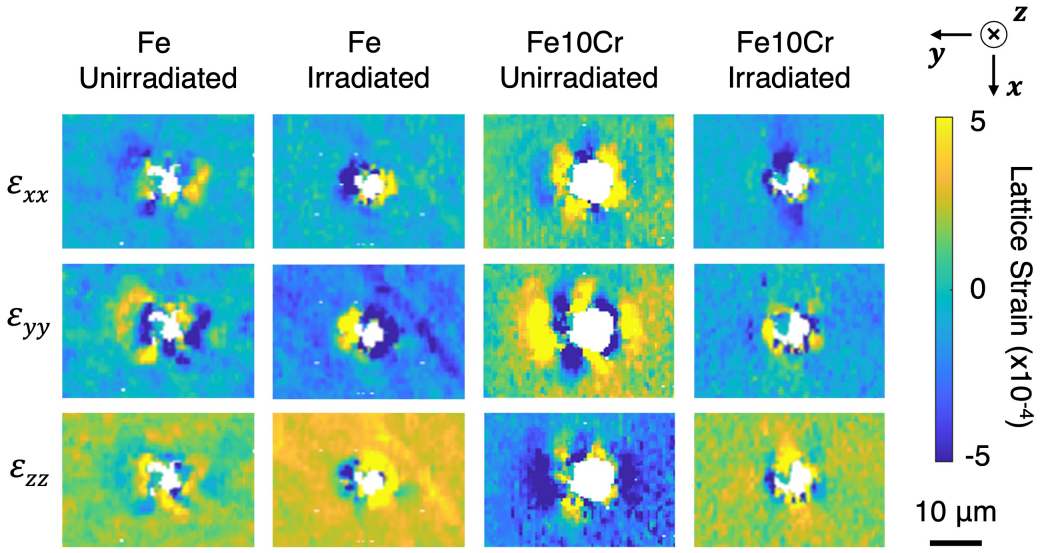


Figure E.4: Lattice strains in the $\boldsymbol{x} - \boldsymbol{y}$ plane at a depth of 2.5–3 µm below the surface.

F

Chapter 7 Appendix

F.1 Annealing Temperature Calibration

During the in-situ annealing experiment at Diamond Light Source I12 beamline, the temperature was initially recorded as the temperature read-out (T_L) from the Linkam heating stage device. However, due to imperfections in the thermal contact between the heater and the sample, this read-out value may not have been exactly the same as the actual temperature of the sample (T_s). In order to find the relationship between T_L and T_s, the lattice parameter of the sample (calculated from the measured diffraction data) and the coefficient of thermal expansion were used. For simplicity, this relationship was approximated as linear and the calculations only considered the patterns up to the point of ferrite/martensite-to-austenite phase transition.

Consider the undeformed Eurofer-97 sample as an example. Figure F.1, considering only the left-hand-side axis for now, shows the lattice constant fitted from the experimental diffraction patterns (a_s). It also shows the lattice constant predicted from the Linkam temperature read-out (a_L) as a function of time. a_L at a certain temperature T_L is given by:

$$a_{L(T=T_L)} = a_{s(T=303K)} + \alpha \times a_{s(T=303)} \times (T_L - 303)$$

where $\alpha = 12.74 \times 10^{-6}$ is the average coefficient of thermal expansion of Eurofer-97 between 293 K to 1073 K [38]. It is assumed at 303 K, the start of the experiment, that $T_L = T_s = 303$ K and thus $a_L = a_s = 2.875$ Å (fitted from experiment).

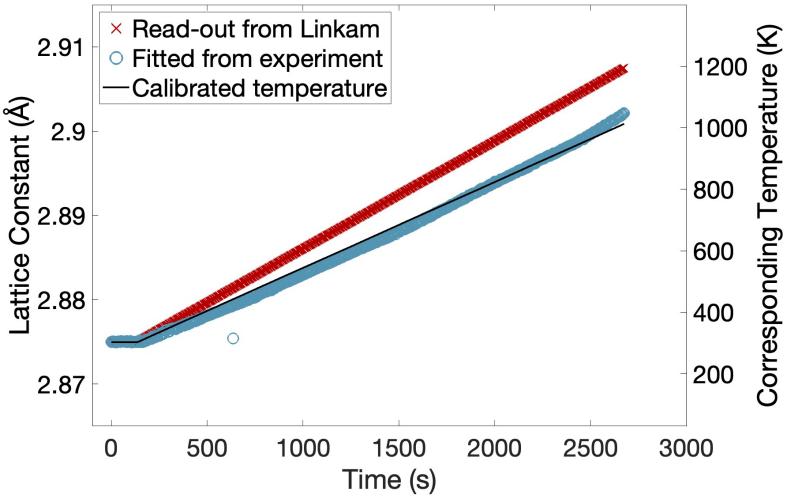


Figure F.1: The lattice constant and corresponding temperature calculated and measured from the experimental diffraction patterns, and the Linkam temperature read-out. The method for obtaining the calibrated temperature curve is explained in the accompanying text.

Since the lattice constant is linearly dependent on temperature, the value of T_s is at a given time can be calculated from the lattice constant by replacing a_L and T_L of the above equation and rearranging:

$$T_s = \frac{a_{s(T=T_s)} - a_{s(T=303K)}}{\alpha \times a_{s(T=303K)}} + 303$$

which gives the corresponding right-hand-side y-axis of Figure F.1.

A linear fit was obtained for T_s and T_L. Then a proportionality constant was also obtained, assuming the linear fits for T_s and T_L intersect at 303 K, to correlate T_s and T_L (as shown in the black line of Figure F.1).

F.2 TEM of All Samples

The full comparison of TEM micrographs taken for each lift-out examined is included in Figures F.2 and F.3. Low-magnification images have been rotated such that they are aligned with the coordinates indicated.

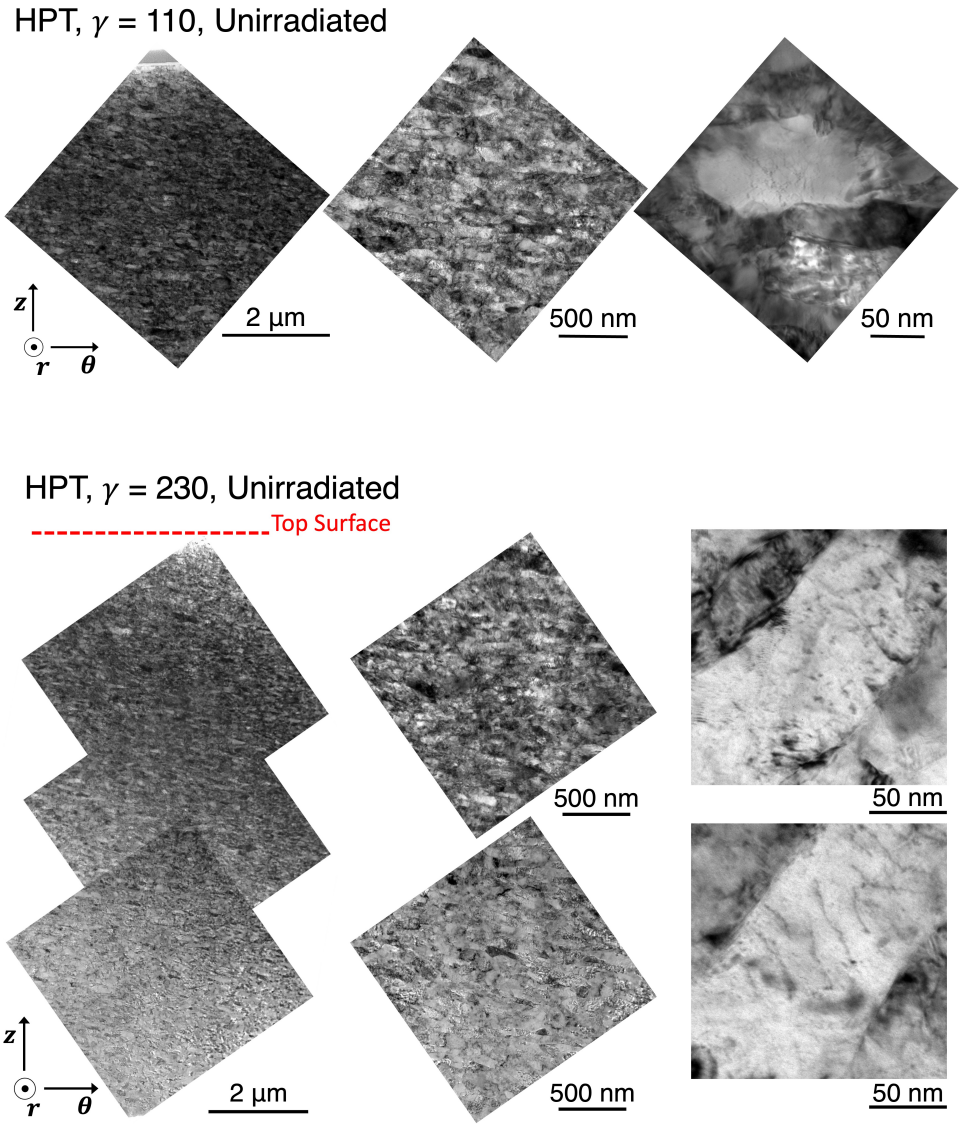


Figure F.2: TEM images of the HPT sample at $\gamma = 110$ and $\gamma = 230$ with no irradiation at different levels of magnification. Dislocation lines are evident within certain grains. There is no significant depth dependence of microstructural features.

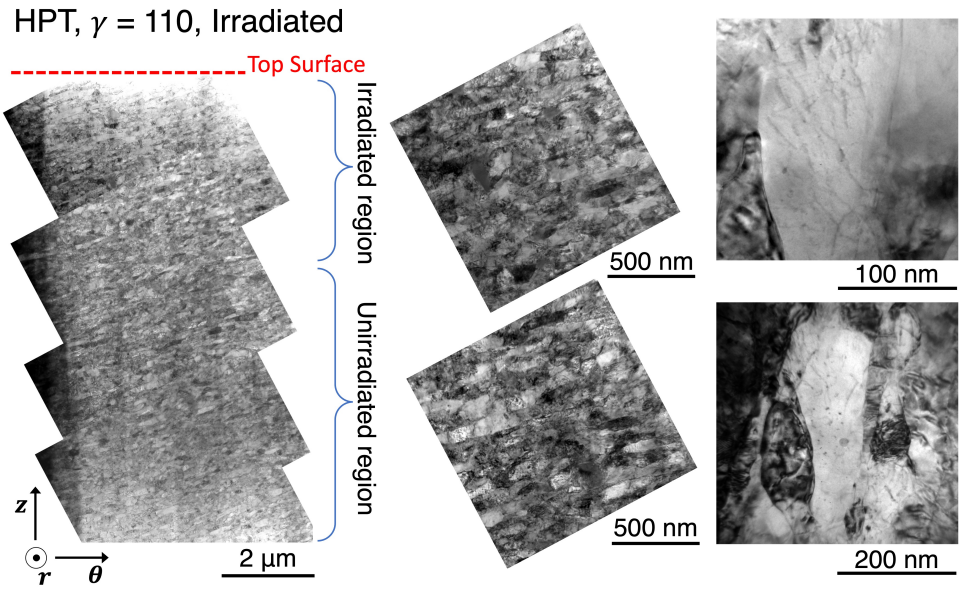


Figure F.3: TEM images of the HPT sample at $\gamma = 110$ with the irradiated region indicated, and imaged at different levels of magnification. Dislocation lines are evident within certain grains. There is no depth dependence of features and irradiation defects could not be unambiguously identified in this study due to the complexity of the microstructure.

F.3 Elemental Analysis of Second-Phase Regions

Second-phase regions were observed in TEM and TKD as discussed in the main text. Energy dispersive X-ray spectroscopy (EDX) was performed on a TEM lift-out of the deformed ($\gamma = 230$) and irradiated sample (Figure F.4). Those regions are found to be enriched with Cr (up to 30%), W (up to 10%), Mn and C. This is consistent with the carbides found in Eurofer-97 by another study [577].

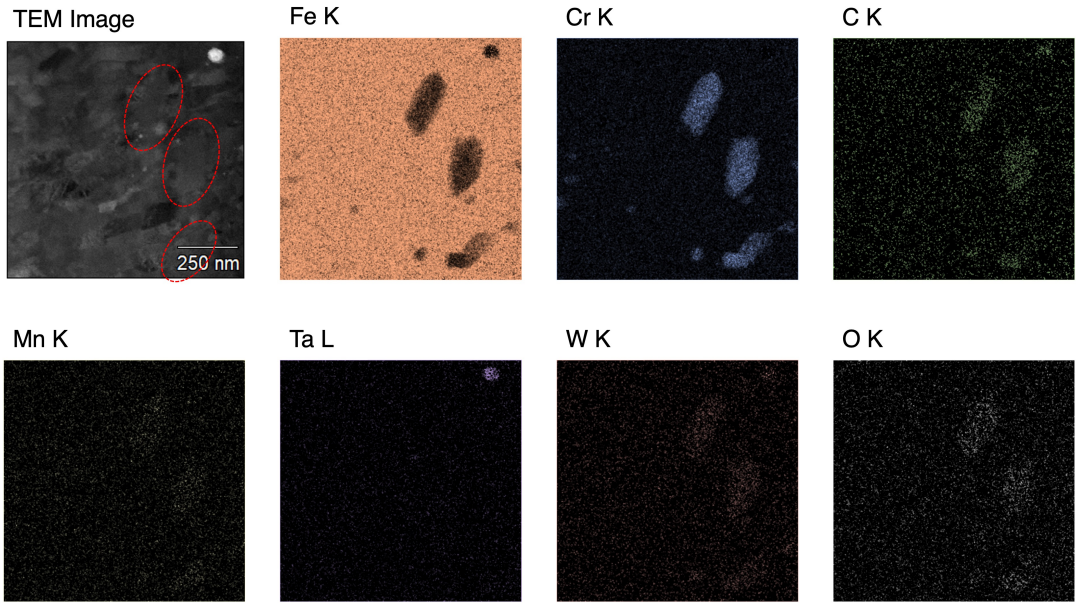


Figure F.4: EDX maps of the carbide regions (circled in red) found between individual grains after HPT.

F.4 Further X-ray Diffraction Analysis

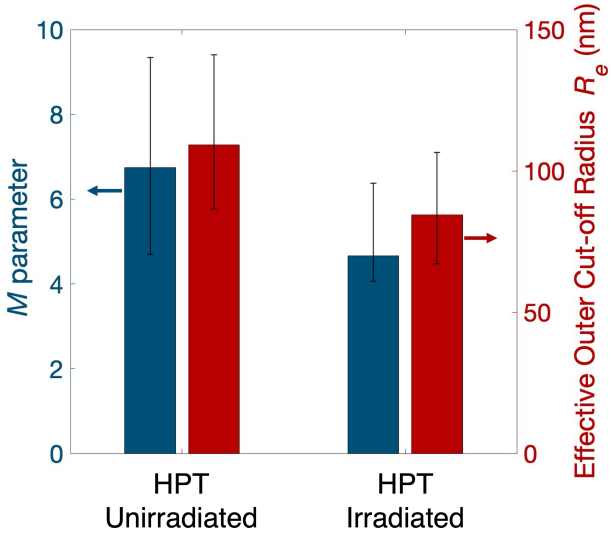


Figure F.5: The values of the M parameter (blue bars) and the effective outer cut-off radius of the dislocations (red bars, R_e) fitted from CMWP analysis.

The effective outer cut-off radius of the dislocations (R_e) gives an indication of the range of elastic strain from the dislocations. The 'randomness' of the dislocation arrangement can be described by cylinders of radius R_e that contain equal numbers of screw dislocations of positive and negative sign, and these cylinders fill the whole crystal [362]. Since R_e actually depends on the dislocation density ρ, the dimensionless parameter M is defined to give an indication of the dipole characteristic of the dislocation. It is calculated by $M = R_e\sqrt{\rho}$. When $M \gg 1$, the dislocations are distributed randomly and in an uncorrelated arrangement. Smaller M, on the other hand, indicates that dislocations of opposite sign are positioned close to each other [360].

From CMWP fitting, reductions in the M and R_e values are seen following irradiation in the HPT-deformed sample (Figure F.5). This suggests that the strain fields are becoming shorter range and possibly indicates the formation of dislocation loops [367]. To characterise the exact density of dislocation loops and line dislocations separately, the contrast factor C of each type needs to be known. This has been calculated for hexagonal materials [632] but remains to be investigated for cubic materials.

F.5 Further In-Situ Annealing X-ray Diffraction Results

The purpose of this section is to demonstrate that the peak broadening in the martensite and austenite phases post-annealing is due to the presence of the retained austenite phase. We will re-present the data from Figure 7.9 here, with more analysis, for a clearer comparison with another set of in-situ annealing XRD data.

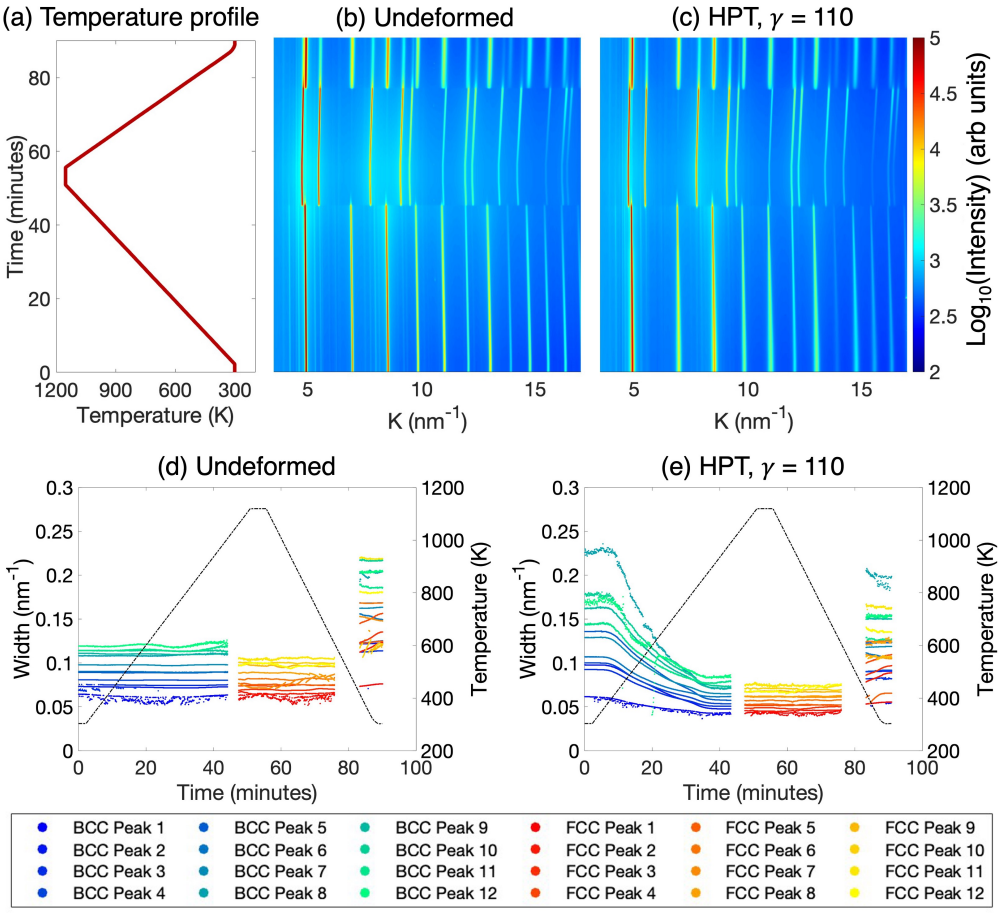


Figure F.6: (a) The temperature ramp of the annealing cycle. The raw time vs $K = 2\sin\theta/\lambda$ plots of the (b) undeformed and (c) HPT sample (as discussed in Section 7.4.2 of the main text). The peak widths (FWHM) of the (d) undeformed and (e) HPT sample as a function of time during the annealing cycle. The calibrated temperature profile is shown as the black dashed line. The ferrite/martensite phase was fitted to a BCC structure, and the austenite was fitted to a FCC structure.

The fitted peak widths as a function of time are shown alongside the raw data in Figure F.6. Key features of the raw data were discussed in Section 7.4.2 of the main text. The peak temperature reached for this set of annealed samples is

1153 K. The phase transition (ferrite/martensite to austenite) occurred from around 1025 K onwards. The peak widths of both samples just before the onset of the phase transition are similar. After the annealing and cooling cycle, some austenite phase remains in the sample as evidenced in the diffraction pattern. The peak widths of both the martensite and austenite phases show significant broadening after the martensite phase reappeared around 606 K during the subsequent cooling stage (Figure F.6(d) and (e)). The peak width of the sample after annealing is similar in both the undeformed and HPT samples.

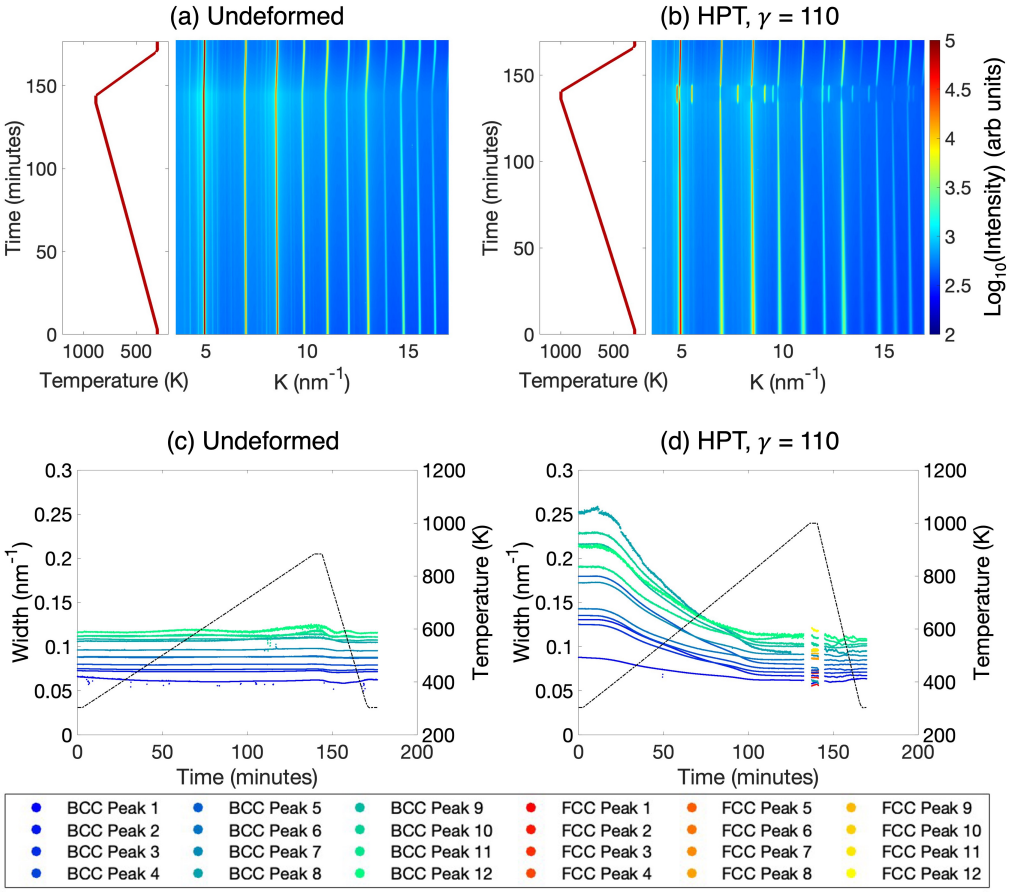


Figure F.7: The temperature ramp and time vs. $K = 2\sin\theta/\lambda$ for the (a) undeformed and (b) HPT samples annealed to a lower target temperature compared to Figure F.6. (c)–(d) Their respective peak widths (FWHM) as a function of time as well as the temperature profile (black dashed line). The ferrite/martensite phase was fitted to a BCC structure, and the austenite was fitted to a FCC structure.

Another set of samples was annealed for this study but not discussed in the main text as the temperature ramp was not well-controlled (Figure F.7). Specifically, for the annealing of the undeformed sample, the peak temperature only reached

883 K due to poor thermal contact. The peak widths of the undeformed sample did not change significantly during the whole annealing cycle and no phase transitions occurred. For the deformed sample, the peak annealing temperature was 1000 K, and it underwent a phase transformation starting at 977 K. The peak widths of the ferrite/martensite phase right before the phase transformation occurred are comparable to the peak widths of the undeformed sample. Upon cooling the austenite phase disappeared around 913 K. Due to the different heating rate of these samples compared to the samples presented in Figure F.6, it is not surprising that the phase transition occurred at a different temperature.

The key difference compared to the first set of annealed samples (Figure F.6) is that the peak widths following cooling remained small and there is no retained austenite phase (Figure F.7). The continuity of the Debye-Scherrer rings (included in the supplementary files) after cooling is reduced compared to the initial state. This suggests that some grain growth has taken place to produce crystals that are dislocation- and strain-free, as expected. This gives further evidence that the retained austenite phase, and associated residual stress, is the cause of peak broadening post-annealing in the set of annealed samples discussed in Section 7.4.2 and Figure F.6.

F.6 Supplementary Files

Four movies are included in the supplementary files which show the raw diffraction patterns from the in-situ annealing portion of the study. The samples are discussed alongside Figure 7.9 (main text) and F.6 (Appendix F.5). The 'LowTemp' files correspond to the samples discussed in Figure F.7 (Appendix F.5).

References

[1] IPCC, "Climate Change 2023: Synthesis Report. A Report of the Intergovernmental Panel on Climate Change. Contribution of Working Groups I, II and III to the Sixth Assessment Report of the Intergovernmental Panel on Climate Change," IPCC, Geneva, Switzerland, Tech. Rep., 2023.

[2] IPCC, "Global Warming of 1.5°C. An IPCC Special Report on the impacts of global warming of 1.5°C above pre-industrial levels and related global greenhouse gas emission pathways, in the context of strengthening the global response to the threat of climate change," Cambridge University Press, Cambridge, Tech. Rep., 2018.

[3] IRENA, "Renewable Power Generation Costs in 2021," International Renewable Energy Agency, Abu Dhabi, Tech. Rep., 2021.

[4] IRENA, "Electricity Storage and Renewables: Costs and Markets to 2030," International Renewable Energy Agency, Abu Dhabi, Tech. Rep., 2017.

[5] IEA, *Nuclear Power*, 2023.

[6] NRC, "Backgrounder on Radioactive Waste," US Nuclear Regulatory Commission, Washington DC, Tech. Rep., 2019.

[7] JET Team, "Fusion energy production from a deuterium-tritium plasma in the JET tokamak," *Nucl. Fusion*, vol. 32, no. 2, pp. 187–203, 1992.

[8] K. L. Jones, "How Hot Is Too Hot In Fusion?" Oak Ridge National Laboratory, Oak Ridge, Tech. Rep., 2017.

[9] W. Picot, "Magnetic Fusion Confinement with Tokamaks and Stellarators," *IAEA Bull.*, 2021.

[10] A. Costley, "On the fusion triple product and fusion power gain of tokamak pilot plants and reactors," *Nucl. Fusion*, vol. 56, no. 6, p. 066 003, 2016.

[11] Y Shimomura, R Aymar, V Chuyanov, M Huguet, R Parker, and I. J. C. Team, "ITER overview," *Nucl. Fusion*, vol. 39, no. 9Y, pp. 1295–1308, 1999.

[12] K. Ehrlich, "Materials research towards a fusion reactor," *Fusion Eng. Des.*, vol. 56-57, pp. 71–82, 2001.

[13] S. Zinkle, J. Blanchard, R. Callis, C. Kessel, R. Kurtz, P. Lee, K. McCarthy, N. Morley, F. Najmabadi, R. Nygren, G. Tynan, D. Whyte, R. Willms, and B. Wirth, "Fusion materials science and technology research opportunities now and during the ITER era," *Fusion Eng. Des.*, vol. 89, no. 7-8, pp. 1579–1585, 2014.

[14] D. J. Ward and S. L. Dudarev, "Economically competitive fusion," *Mater. Today*, vol. 11, no. 12, pp. 46–53, 2008.

[15] S. Zinkle, "Radiation-Induced Effects on Microstructure," in *Compr. Nucl. Mater.* Vol. 1, Elsevier, 2012, pp. 65–98.

[16] N Baluc, R Schäublin, P Spätig, and M Victoria, "On the potentiality of using ferritic/martensitic steels as structural materials for fusion reactors," *Nucl. Fusion*, vol. 44, no. 1, pp. 56–61, 2004.

[17] H. Tanigawa, E. Gaganidze, T. Hirose, M. Ando, S. Zinkle, R. Lindau, and E. Diegele, "Development of benchmark reduced activation ferritic/martensitic steels for fusion energy applications," *Nucl. Fusion*, vol. 57, no. 9, p. 092 004, 2017.

[18] K. Ehrlich, "The development of structural materials for fusion reactors," *Philos. Trans. R. Soc. London. Ser. A Math. Phys. Eng. Sci.*, vol. 357, no. 1752, C. Windsor, M. Keilhacker, J. D. Lawson, G. J. Pert, and D. C. Robinson, Eds., pp. 595–623, 1999.

[19] A. Möslang, E. Diegele, M. Klimiankou, R. Lässer, R. Lindau, E. Lucon, E. Materna-Morris, C. Petersen, R. Pippan, J. W. Rensman, M. Rieth, B. Van Der Schaaf, H. C. Schneider, and F. Tavassoli, "Towards reduced activation structural materials data for fusion DEMO reactors," *Nucl. Fusion*, vol. 45, no. 7, p. 649, 2005.

[20] A. Bhattacharya, S. J. Zinkle, J. Henry, S. M. Levine, P. D. Edmondson, M. R. Gilbert, H. Tanigawa, and C. E. Kessel, "Irradiation damage concurrent challenges with RAFM and ODS steels for fusion reactor first-wall/blanket: a review," *J. Phys. Energy*, vol. 4, no. 3, p. 034 003, 2022.

[21] E. Bloom, R. Conn, J. Davis, R. Gold, R. Little, K. Schultz, D. Smith, and F. Wiffen, "Low activation materials for fusion applications," *J. Nucl. Mater.*, vol. 122, no. 1-3, pp. 17–26, 1984.

[22] H. Tanigawa, K. Shiba, A. Möslang, R. Stoller, R. Lindau, M. Sokolov, G. Odette, R. Kurtz, and S. Jitsukawa, "Status and key issues of reduced activation ferritic/martensitic steels as the structural material for a DEMO blanket," *J. Nucl. Mater.*, vol. 417, no. 1-3, pp. 9–15, 2011.

[23] L. Tan, Y. Katoh, A. A. Tavassoli, J. Henry, M. Rieth, H. Sakasegawa, H. Tanigawa, and Q. Huang, "Recent status and improvement of reduced-activation ferritic-martensitic steels for high-temperature service," *J. Nucl. Mater.*, vol. 479, pp. 515–523, 2016.

[24] R. L. Klueh and D. R. Harries, *High-Chromium Ferritic and Martensitic Steels for Nuclear Applications*, R. Klueh and D. Harries, Eds. West Conshohocken, PA 19428-2959: ASTM International, 2001.

[25] E Lucon and W Vandermeulen, "Overview and Critical Assessment of the Tensile Properties of unirradiated and irradiated EUROFER97," Tech. Rep., 2007.

[26] S. J. Zinkle and N. M. Ghoniem, "Operating temperature windows for fusion reactor structural materials," *Fusion Eng. Des.*, vol. 51-52, pp. 55–71, 2000.

[27] M. Gilbert and J.-C. Sublet, "Scoping of material response under DEMO neutron irradiation: Comparison with fission and influence of nuclear library selection," *Fusion Eng. Des.*, vol. 125, pp. 299–306, 2017.

[28] H. Kayano, A. Kimura, M. Narui, Y. Sasaki, Y. Suzuki, and S. Ohta, "Irradiation embrittlement of neutron-irradiated low activation ferritic steels," *J. Nucl. Mater.*, vol. 155-157, no. PART 2, pp. 978–981, 1988.

[29] A. Kohyama, A. Hishinuma, D. Gelles, R. Klueh, W. Dietz, and K. Ehrlich, "Low-activation ferritic and martensitic steels for fusion application," *J. Nucl. Mater.*, vol. 233-237, no. PART 1, pp. 138–147, 1996.

[30] R. Klueh, K. Ehrlich, and F. Abe, "Ferritic/martensitic steels: promises and problems," *J. Nucl. Mater.*, vol. 191-194, pp. 116–124, 1992.

[31] M. Victoria, N. Baluc, and P. Spätig, "Structural materials for fusion reactors," *Nucl. Fusion*, vol. 41, no. 8, pp. 1047–1053, 2001.

[32] B. van der Schaaf, C. Petersen, Y. De Carlan, J. Rensman, E. Gaganidze, and X. Averty, "High dose, up to 80 dpa, mechanical properties of Eurofer 97," *J. Nucl. Mater.*, vol. 386-388, pp. 236–240, 2009.

[33] R. Klueh and D. Alexander, "Impact behavior of reduced-activation steels irradiated to 24 dpa," *J. Nucl. Mater.*, vol. 233-237, pp. 336–341, 1996.

[34] A. Kohyama, Y. Kohno, K. Asakura, and H. Kayano, "R & D of low activation ferritic steels for fusion in japanese universities," *J. Nucl. Mater.*, vol. 212-215, pp. 684–689, 1994.

[35] R. Lindau, A. Möslang, M. Rieth, M. Klimiankou, E. Materna-Morris, A. Alamo, A.-A. F. Tavassoli, C. Cayron, A.-M. Lancha, P. Fernandez, N. Baluc, R. Schäublin, E. Diegele, G. Filacchioni, J. Rensman, B. Schaaf, E. Lucon, and W. Dietz, "Present development status of EUROFER and ODS-EUROFER for application in blanket concepts," *Fusion Eng. Des.*, vol. 75-79, no. SUPPL. Pp. 989–996, 2005.

[36] E. Gaganidze, F. Gillemot, I. Szenthe, M. Gorley, M. Rieth, and E. Diegele, "Development of EUROFER97 database and material property handbook," *Fusion Eng. Des.*, vol. 135, pp. 9–14, 2018.

[37] Böhler Bleche, "Certificate No. 201308 Datasheet," Völklingen, Germany, Tech. Rep., 2003.

[38] M Rieth, M Schirra, A Falkenstein, P Graf, S Heger, H Kempe, R Lindau, and H Zimmermann, "EUROFER 97. Tensile, charpy, creep and structural tests," Forschungszentrum Karlsruhe GmbH Technik und Umwelt, Karlsruhe, Tech. Rep., 2003.

[39] E. Gaganidze and J. Aktaa, "Assessment of neutron irradiation effects on RAFM steels," *Fusion Eng. Des.*, vol. 88, no. 3, pp. 118–128, 2013.

[40] A. Bhattacharya, X. Chen, T. Graening, J. W. Geringer, J. Reed, J. Henry, L. Pilloni, D. Terentyev, A. Puype, T. S. Byun, Y. Katoh, M. Rieth, and S. J. Zinkle, "Irradiation hardening and ductility loss of Eurofer97 steel variants after neutron irradiation to ITER-TBM relevant conditions," *Fusion Eng. Des.*, vol. 173, p. 112 935, 2021.

[41] M. Roldán, P. Fernández, J. Rams, D. Jiménez-Rey, E. Materna-Morris, and M. Klimenkov, "Comparative study of helium effects on EU-ODS EUROFER and EUROFER97 by nanoindentation and TEM," *J. Nucl. Mater.*, vol. 460, pp. 226–234, 2015.

[42] M. Rieth, E. Simondon, G. Pintsuk, G. Aiello, J. Henry, D. Terentyev, A. Puype, C. Cristalli, L. Pilloni, O. Tassa, M. Klimenkov, H.-C. Schneider, P. Fernandez, T. Gräning, X. Chen, A. Bhattacharya, J. Reed, J. Geringer, M. Sokolov, Y. Katoh, and L. Snead, "Technological aspects in blanket design: Effects of micro-alloying and thermo-mechanical treatments of EUROFER97 type steels after neutron irradiation," *Fusion Eng. Des.*, vol. 168, p. 112 645, 2021.

[43] K. Nordlund, "Historical review of computer simulation of radiation effects in materials," *J. Nucl. Mater.*, vol. 520, pp. 273–295, 2019.

[44] N. Soneda and T. Diaz De La Rubia, "Defect production, annealing kinetics and damage evolution in α-Fe: An atomic-scale computer simulation," *Philos. Mag. A Phys. Condens. Matter, Struct. Defects Mech. Prop.*, vol. 78, no. 5, pp. 995–1019, 1998.

[45] J. Knaster, A. Moeslang, and T. Muroga, "Materials research for fusion," *Nat. Phys.*, vol. 12, no. 5, pp. 424–434, 2016.

[46] A. F. Calder and D. J. Bacon, "A molecular dynamics study of displacement cascades in α-iron," *J. Nucl. Mater.*, vol. 207, no. C, pp. 25–45, 1993.

[47] K. Nordlund, J. Wallenius, and L. Malerba, "Molecular dynamics simulations of threshold displacement energies in Fe," *Nucl. Instruments Methods Phys. Res. Sect. B Beam Interact. with Mater. Atoms*, vol. 246, no. 2, pp. 322–332, 2006.

[48] D. A. Terentyev, L. Malerba, R. Chakarova, K. Nordlund, P. Olsson, M. Rieth, and J. Wallenius, "Displacement cascades in Fe-Cr: A molecular dynamics study," *J. Nucl. Mater.*, vol. 349, no. 1-2, pp. 119–132, 2006.

[49] L. Malerba, "Molecular dynamics simulation of displacement cascades in α-Fe: A critical review," *J. Nucl. Mater.*, vol. 351, no. 1-3, pp. 28–38, 2006.

[50] L. Malerba, A. Caro, and J. Wallenius, "Multiscale modelling of radiation damage and phase transformations: The challenge of FeCr alloys," *J. Nucl. Mater.*, vol. 382, no. 2-3, pp. 112–125, 2008.

[51] S. Dudarev, "Density Functional Theory Models for Radiation Damage," *Annu. Rev. Mater. Res.*, vol. 43, no. 1, pp. 35–61, 2013.

[52] P. Olsson, C. Domain, and J. Wallenius, "Ab initio study of Cr interactions with point defects in bcc Fe," *Phys. Rev. B - Condens. Matter Mater. Phys.*, vol. 75, no. 1, p. 014 110, 2007.

[53] C. K. Dolph, D. J. da Silva, M. J. Swenson, and J. P. Wharry, "Plastic zone size for nanoindentation of irradiated Fe–9%Cr ODS," *J. Nucl. Mater.*, vol. 481, pp. 33–45, 2016.

[54] D. Armstrong, C. Hardie, J. Gibson, A. Bushby, P. Edmondson, and S. Roberts, "Small-scale characterisation of irradiated nuclear materials: Part II nanoindentation and micro-cantilever testing of ion irradiated nuclear materials," *J. Nucl. Mater.*, vol. 462, pp. 374–381, 2015.

[55] C. Shin, H.-h. Jin, and M.-W. Kim, "Evaluation of the depth-dependent yield strength of a nanoindented ion-irradiated Fe–Cr model alloy by using a finite element modeling," *J. Nucl. Mater.*, vol. 392, no. 3, pp. 476–481, 2009.

[56] M. R. Gilbert, K. Arakawa, Z. Bergstrom, M. J. Caturla, S. L. Dudarev, F. Gao, A. M. Goryaeva, S. Y. Hu, X. Hu, R. J. Kurtz, A. Litnovsky, J. Marian, M. C. Marinica, E. Martinez, E. A. Marquis, D. R. Mason, B. N. Nguyen, P. Olsson, Y. Osetskiy, D. Senor, W. Setyawan, M. P. Short, T. Suzudo, J. R. Trelewicz, T. Tsuru, G. S. Was, B. D. Wirth, L. Yang, Y. Zhang, and S. J. Zinkle, "Perspectives on multiscale modelling and experiments to accelerate materials development for fusion," *J. Nucl. Mater.*, vol. 554, p. 153 113, 2021.

[57] M. Samaras and M. Victoria, "Modelling in nuclear energy environments," *Mater. Today*, vol. 11, no. 12, pp. 54–62, 2008.

[58] C. Fazio, A. Alamo, A. Almazouzi, S. De Grandis, D. Gomez-Briceno, J. Henry, L. Malerba, and M. Rieth, "European cross-cutting research on structural materials for Generation IV and transmutation systems," *J. Nucl. Mater.*, vol. 392, no. 2, pp. 316–323, 2009.

[59] R. Schäublin, B. Décamps, A. Prokhodtseva, and J. F. Löffler, "On the origin of the primary ½ a0 <111> and a0 <100> loops in irradiated Fe(Cr) alloys," *Acta Mater.*, vol. 133, pp. 427–439, 2017.

[60] C. D. Hardie, C. A. Williams, S. Xu, and S. G. Roberts, "Effects of irradiation temperature and dose rate on the mechanical properties of self-ion implanted Fe and Fe–Cr alloys," *J. Nucl. Mater.*, vol. 439, no. 1-3, pp. 33–40, 2013.

[61] A. Bhattacharya, E. Meslin, J. Henry, A. Barbu, S. Poissonnet, and B. Décamps, "Effect of chromium on void swelling in ion irradiated high purity Fe–Cr alloys," *Acta Mater.*, vol. 108, pp. 241–251, 2016.

[62] D. Brimbal, B. Décamps, J. Henry, E. Meslin, and A. Barbu, "Single- and dual-beam in situ irradiations of high-purity iron in a transmission electron microscope: Effects of heavy ion irradiation and helium injection," *Acta Mater.*, vol. 64, pp. 391–401, 2014.

[63] D. Brimbal, E. Meslin, J. Henry, B. Décamps, and A. Barbu, "He and Cr effects on radiation damage formation in ion-irradiated pure iron and Fe–5.40 wt. % Cr: A transmission electron microscopy study," *Acta Mater.*, vol. 61, no. 13, pp. 4757–4764, 2013.

[64] M. Roldán, P. Fernández, R. Vila, A. Gómez-Herrero, and F. Sánchez, "The effect of triple ion beam irradiation on cavity formation on pure EFDA iron," *J. Nucl. Mater.*, vol. 479, pp. 100–111, 2016.

[65] Y.-R. Lin, A. Bhattacharya, D. Chen, J.-J. Kai, J. Henry, and S. J. Zinkle, "Temperature-dependent cavity swelling in dual-ion irradiated Fe and Fe-Cr ferritic alloys," *Acta Mater.*, vol. 207, p. 116 660, 2021.

[66] J. L. Coze, "Procurement of pure Fe metal and Fe-based alloys with controlled chemical alloying element contents and microstructure," ARMINES Ecole Nationale Superieure des Mines, Tech. Rep., 2007.

[67] A Fraczkiewicz, "Material Delivery Report BC4000483543/P5B51," Ecole des Mines, France, Tech. Rep., 2011.

[68] S. Ishino, "Effect of Cascade as Fundamental Research on Radiation Damage of Core Component Materials," *J. Nucl. Sci. Technol.*, vol. 26, no. 1, pp. 137–142, 1989.

[69] G. S. Was, *Fundamentals of radiation materials science: Metals and alloys, second edition*. Springer New York, 2016, pp. 1–1002.

[70] R. E. Stoller, M. B. Toloczko, G. S. Was, A. G. Certain, S. Dwaraknath, and F. A. Garner, "On the use of SRIM for computing radiation damage exposure," *Nucl. Instruments Methods Phys. Res. Sect. B Beam Interact. with Mater. Atoms*, vol. 310, pp. 75–80, 2013.

[71] J. A. Brinkman, "Production of Atomic Displacements by High-Energy Particles," *Am. J. Phys.*, vol. 24, no. 4, pp. 246–267, 1956.

[72] K. Nordlund, S. J. Zinkle, A. E. Sand, F. Granberg, R. S. Averback, R. E. Stoller, T. Suzudo, L. Malerba, F. Banhart, W. J. Weber, F. Willaime, S. L. Dudarev, and D. Simeone, "Primary radiation damage: A review of current understanding and models," *J. Nucl. Mater.*, vol. 512, pp. 450–479, 2018.

[73] K. Vörtler, C. Björkas, D. Terentyev, L. Malerba, and K. Nordlund, "The effect of Cr concentration on radiation damage in Fe-Cr alloys," *J. Nucl. Mater.*, vol. 382, no. 1, pp. 24–30, 2008.

[74] C. Björkas, K. Nordlund, L. Malerba, D. Terentyev, and P. Olsson, "Simulation of displacement cascades in Fe90Cr10 using a two band model potential," *J. Nucl. Mater.*, vol. 372, no. 2-3, pp. 312–317, 2008.

[75] L. Malerba, D. Terentyev, P. Olsson, R. Chakarova, and J. Wallenius, "Molecular dynamics simulation of displacement cascades in Fe-Cr alloys," in *J. Nucl. Mater.*, vol. 329-333, North-Holland, 2004, pp. 1156–1160.

[76] M. J. Norgett, M. T. Robinson, and I. M. Torrens, "A proposed method of calculating displacement dose rates," *Nucl. Eng. Des.*, vol. 33, no. 1, pp. 50–54, 1975.

[77] K. Nordlund, A. E. Sand, F. Granberg, S. Zinkle, R. Stoller, R. S. Averback, T. Suzudo, L. Malerba, F. Banhart, W. J. Weber, F. Willaime, S. Dudarev, and D. Simeone, "Primary Radiation Damage in Materials - Review of Current Understanding and Proposed New Standard Displacement Damage Model to Incorporate in Cascade Defect Production Efficiency and Mixing Effects," OECD Nuclear Energy Agency, Paris, Tech. Rep., 2015.

[78] M. T. Robinson and I. M. Torrens, "Computer simulation of atomic-displacement cascades in solids in the binary-collision approximation," *Phys. Rev. B*, 1974.

[79] R. Averback, T. De La Rubia, and R. Benedek, "Dynamics and structure of energetic displacement cascades," *Nucl. Instruments Methods Phys. Res. Sect. B Beam Interact. with Mater. Atoms*, vol. 33, no. 1-4, pp. 693–700, 1988.

[80] J. F. Ziegler, M. D. Ziegler, and J. P. Biersack, "SRIM - The stopping and range of ions in matter (2010)," *Nucl. Instruments Methods Phys. Res. Sect. B Beam Interact. with Mater. Atoms*, vol. 268, no. 11-12, pp. 1818–1823, 2010.

[81] P. Garin, E. Diegele, R. Heidinger, A. Ibarra, S. Jitsukawa, H. Kimura, A. Möslang, T. Muroga, T. Nishitani, Y. Poitevin, M. Sugimoto, and M. Zmitko, "IFMIF specifications from the users point of view," *Fusion Eng. Des.*, vol. 86, no. 6-8, pp. 611–614, 2011.

[82] M. R. Gilbert, S. L. Dudarev, S Zheng, L. W. Packer, and J. C. Sublet, "An integrated model for materials in a fusion power plant: Transmutation, gas production, and helium embrittlement under neutron irradiation," *Nucl. Fusion*, vol. 52, no. 8, p. 083 019, 2012.

[83] S. González de Vicente, J.-L. Boutard, S. Zinkle, and H. Tanigawa, "Materials testing facilities and programmes for fission and ion implantation damage," *Nucl. Fusion*, vol. 57, no. 9, p. 092 011, 2017.

[84] G. Was, "Irradiation Hardening and Deformation," in *Fundam. Radiat. Mater. Sci.* Springer, Berlin, Heidelberg, 2007, pp. 581–642.

[85] G. Was and T. Allen, "Radiation-induced segregation in multicomponent alloys: Effect of particle type," *Mater. Charact.*, vol. 32, no. 4, pp. 239–255, 1994.

[86] R. E. Stoller, "Role of cascade energy and temperature in primary defect formation in iron," *J. Nucl. Mater.*, vol. 276, no. 1, pp. 22–32, 2000.

[87] F. A. Garner, H. L. Heinisch, R. L. Simons, and F. M. Mann, "Implications of neutron spectrum and flux differences on fission-fusion correlations at high neutron fluence," *Radiat. Eff. Defects Solids*, vol. 113, no. 1-3, pp. 229–255, 1990.

[88] C. Abromeit, "Aspects of simulation of neutron damage by ion irradiation," *J. Nucl. Mater.*, vol. 216, no. C, pp. 78–96, 1994.

[89] L. Mansur, "Correlation of neutron and heavy-ion damage," *J. Nucl. Mater.*, vol. 78, no. 1, pp. 156–160, 1978.

[90] L. Mansur, "Theory of transitions in dose dependence of radiation effects in structural alloys," *J. Nucl. Mater.*, vol. 206, no. 2-3, pp. 306–323, 1993.

[91] M. Hernández-Mayoral, C. Heintze, and E. Oñorbe, "Transmission electron microscopy investigation of the microstructure of Fe–Cr alloys induced by neutron and ion irradiation at 300 °C," *J. Nucl. Mater.*, vol. 474, pp. 88–98, 2016.

[92] C. D. Hardie, G. R. Odette, Y. Wu, S. Akhmadaliev, and S. G. Roberts, "Mechanical properties and plasticity size effect of Fe-6%Cr irradiated by Fe ions and by neutrons," *J. Nucl. Mater.*, vol. 482, pp. 236–247, 2016.

[93] J. Haley, S. de Moraes Shubeita, P. Wady, A. London, G. Odette, S. Lozano-Perez, and S. Roberts, "Microstructural examination of neutron, proton and self-ion irradiation damage in a model Fe9Cr alloy," *J. Nucl. Mater.*, vol. 533, p. 152 130, 2020.

[94] M. Swenson and J. Wharry, "TEM characterization of irradiated microstructure of Fe-9%Cr ODS and ferritic-martensitic alloys," *J. Nucl. Mater.*, vol. 502, pp. 30–41, 2018.

[95] E. R. Reese, N. Almirall, T. Yamamoto, S. Tumey, G. Robert Odette, and E. A. Marquis, "Dose rate dependence of Cr precipitation in an ion-irradiated Fe 18Cr alloy," *Scr. Mater.*, vol. 146, pp. 213–217, 2018.

[96] G. S. Was and R. S. Averback, "Radiation Damage Using Ion Beams," *Compr. Nucl. Mater.*, vol. 1, pp. 195–221, 2012.

[97] C. Gasparrini, A. Xu, K. Short, T. Wei, J. Davis, T. Palmer, D. Bhattacharyya, L. Edwards, and M. R. Wenman, "Micromechanical testing of unirradiated and helium ion irradiated SA508 reactor pressure vessel steels: Nanoindentation vs in-situ microtensile testing," *Mater. Sci. Eng. A*, vol. 796, p. 139 942, 2020.

[98] C. Heintze, F. Bergner, and M. Hernández-Mayoral, "Ion-irradiation-induced damage in Fe–Cr alloys characterized by nanoindentation," *J. Nucl. Mater.*, vol. 417, no. 1-3, pp. 980–983, 2011.

[99] O. Tissot, C. Pareige, E. Meslin, B. Décamps, and J. Henry, "Influence of injected interstitials on α' precipitation in Fe–Cr alloys under self-ion irradiation," *Mater. Res. Lett.*, vol. 5, no. 2, pp. 117–123, 2017.

[100] L. Shao, C.-C. Wei, J. Gigax, A. Aitkaliyeva, D. Chen, B. Sencer, and F. Garner, "Effect of defect imbalance on void swelling distributions produced in pure iron irradiated with 3.5 MeV self-ions," *J. Nucl. Mater.*, vol. 453, no. 1-3, pp. 176–181, 2014.

[101] E. Lee, L. Mansur, and M. Yoo, "Spatial variation in void volume during charged particle bombardment — the effects of injected interstitials," *J. Nucl. Mater.*, vol. 85-86, pp. 577–581, 1979.

[102] T Tanaka, K Oka, S Ohnuki, S Yamashita, T Suda, S Watanabe, and E Wakai, "Synergistic effect of helium and hydrogen for defect evolution under multi-ion irradiation of Fe–Cr ferritic alloys," *J. Nucl. Mater.*, vol. 329-333, pp. 294–298, 2004.

[103] D. Brimbal, B. Décamps, A. Barbu, E. Meslin, and J. Henry, "Dual-beam irradiation of α-iron: Heterogeneous bubble formation on dislocation loops," *J. Nucl. Mater.*, vol. 418, no. 1-3, pp. 313–315, 2011.

[104] X. Y. Liu, Y. P. Li, G. Ran, Q. Han, and P. H. Chen, "In situ transmission electron microscopy studies of 30 keV H2+ and He+ dual-beam irradiated Pd: defect generation and microstructural evolution under varied temperatures and foil thicknesses," *Mater. Today Energy*, vol. 21, p. 100 731, 2021.

[105] D. E. Armstrong, X. Yi, E. A. Marquis, and S. G. Roberts, "Hardening of self ion implanted tungsten and tungsten 5-wt% rhenium," *J. Nucl. Mater.*, vol. 432, no. 1-3, pp. 428–436, 2013.

[106] Y. Li, F. Ma, F. Yue, Q. Ren, H. Zhou, and G. Lu, "Radiation-induced precipitation of transmutation elements rhenium/osmium and their effects on hydrogen behavior in tungsten," *Prog. Nat. Sci. Mater. Int.*, vol. 29, no. 3, pp. 285–294, 2019.

[107] X. Hu, C. M. Parish, K. Wang, T. Koyanagi, B. P. Eftink, and Y. Katoh, "Transmutation-induced precipitation in tungsten irradiated with a mixed energy neutron spectrum," *Acta Mater.*, vol. 165, pp. 51–61, 2019.

[108] F. Garner, N. Sekimura, M. Grossbeck, A. Ermi, J. Newkirk, H. Watanabe, and M. Kiritani, "Influence of details of reactor history on microstructural development during neutron irradiation," *J. Nucl. Mater.*, vol. 205, pp. 206–218, 1993.

[109] Z Yao, M Hernández-Mayoral, M. L. Jenkins, and M. A. Kirk, "Heavy-ion irradiations of Fe and Fe–Cr model alloys Part 1: Damage evolution in thin-foils at lower doses," *Philos. Mag.*, vol. 88, no. 21, pp. 2851–2880, 2008.

[110] X. Yi, A. E. Sand, D. R. Mason, M. A. Kirk, S. G. Roberts, K. Nordlund, and S. L. Dudarev, "Direct observation of size scaling and elastic interaction between nano-scale defects in collision cascades," *Europhys. Lett.*, vol. 110, no. 3, p. 36 001, 2015.

[111] M. Hernandez-Mayoral, Z. Yao, M. L. Jenkins, and M. A. Kirk, "Heavy-ion irradiations of Fe and Fe-Cr model alloys Part 2: Damage evolution in thin-foils at higher doses," *Philos. Mag.*, vol. 88, no. 21, pp. 2881–2897, 2008.

[112] M. Jenkins, Z. Yao, M. Hernández-Mayoral, and M. Kirk, "Dynamic observations of heavy-ion damage in Fe and Fe–Cr alloys," *J. Nucl. Mater.*, vol. 389, no. 2, pp. 197–202, 2009.

[113] A. Prokhodtseva, B. Décamps, A. Ramar, and R. Schäublin, "Impact of He and Cr on defect accumulation in ion-irradiated ultrahigh-purity Fe(Cr) alloys," *Acta Mater.*, vol. 61, no. 18, pp. 6958–6971, 2013.

[114] I. M. Robertson, M. A. Kirk, and W. E. King, "Formation of dislocation loops in iron by self-ion irradiations at 40K," *Scr. Metall.*, vol. 18, no. 4, pp. 317–320, 1984.

[115] S. Dudarev, J.-L. Boutard, R. Lässer, M. Caturla, P. Derlet, M. Fivel, C.-C. Fu, M. Lavrentiev, L. Malerba, M. Mrovec, D. Nguyen-Manh, K. Nordlund, M. Perlado, R. Schäublin, H. Van Swygenhoven, D. Terentyev, J. Wallenius, D. Weygand, and F. Willaime, "The EU programme for modelling radiation effects in fusion reactor materials: An overview of recent advances and future goals," *J. Nucl. Mater.*, vol. 386-388, pp. 1–7, 2009.

[116] C. C. Fu and F. Willaime, "First principles calculations in iron: structure and mobility of defect clusters and defect complexes for kinetic modelling," *Comptes Rendus Phys.*, vol. 9, no. 3-4, pp. 335–342, 2008.

[117] M. R. Gilbert, Z. Yao, M. A. Kirk, M. L. Jenkins, and S. L. Dudarev, "Vacancy defects in Fe: Comparison between simulation and experiment," *J. Nucl. Mater.*, vol. 386-388, no. C, pp. 36–40, 2009.

[118] D. Bacon, A. Calder, F. Gao, V. Kapinos, and S. Wooding, "Computer simulation of defect production by displacement cascades in metals," *Nucl. Instruments Methods Phys. Res. Sect. B Beam Interact. with Mater. Atoms*, vol. 102, no. 1-4, pp. 37–46, 1995.

[119] W. J. Phythian, R. E. Stoller, A. J. Foreman, A. F. Calder, and D. J. Bacon, "A comparison of displacement cascades in copper and iron by molecular dynamics and its application to microstructural evolution," *J. Nucl. Mater.*, vol. 223, no. 3, pp. 245–261, 1995.

[120] R. E. Stoller, "Point defect survival and clustering fractions obtained from molecular dynamics simulations of high energy cascades," *J. Nucl. Mater.*, vol. 233-237, no. PART II, pp. 999–1003, 1996.

[121] E. A. Little and B. L. Eyre, "The geometry of dislocation loops generated in α-iron by 1 MeV electron irradiation at 550°C," *J. Microsc.*, vol. 97, no. 1-2, pp. 107–111, 1973.

[122] S. Xu, Z. Yao, and M. Jenkins, "TEM characterisation of heavy-ion irradiation damage in FeCr alloys," *J. Nucl. Mater.*, vol. 386-388, no. C, pp. 161–164, 2009.

[123] B. L. Eyre and R. Bullough, "On the formation of interstitial loops in b.c.c. metals," *Philos. Mag.*, vol. 12, no. 115, pp. 31–39, 1965.

[124] C. A. English and M. L. Jenkins, "Heavy-Ion Damage in Solids," in *Treatise Heavy-Ion Sci.* Boston, MA: Springer US, 1985, pp. 323–359.

[125] N. Soneda, S. Ishino, and T. D. de la Rubia, "Vacancy loop formation by 'cascade collapse' in a-Fe: A molecular dynamics study of 50keV cascades," *Philos. Mag. Lett.*, vol. 81, no. 9, pp. 649–659, 2001.

[126] M. L. Jenkins and M. A. Kirk, *Characterization of radiation damage by transmission electron microscopy*. 2000.

[127] M. Eldrup, B. N. Singh, S. J. Zinkle, T. S. Byun, and K. Farrell, "Dose dependence of defect accumulation in neutron irradiated copper and iron," *J. Nucl. Mater.*, vol. 307-311, no. 2 SUPPL. Pp. 912–917, 2002.

[128] M. Eldrup and B. N. Singh, "Accumulation of point defects and their complexes in irradiated metals as studied by the use of positron annihilation spectroscopy - A brief review," in *J. Nucl. Mater.*, vol. 323, North-Holland, 2003, pp. 346–353.

[129] S. Zinkle and B. Singh, "Microstructure of neutron-irradiated iron before and after tensile deformation," *J. Nucl. Mater.*, vol. 351, no. 1-3, pp. 269–284, 2006.

[130] D. Gelles, "Microstructural examination of neutron-irradiated simple ferritic alloys," *J. Nucl. Mater.*, vol. 108-109, no. C, pp. 515–526, 1982.

[131] A. E. Ward and S. B. Fisher, "Dislocation loop growth in pure iron under electron irradiation," *J. Nucl. Mater.*, vol. 166, no. 3, pp. 227–234, 1989.

[132] H. H. Jin, C. Shin, D. H. Kim, K. H. Oh, and J. H. Kwon, "Irradiation induced dislocation loop and its influence on the hardening behavior of Fe-Cr alloys by an Fe ion irradiation," *Nucl. Instruments Methods Phys. Res. Sect. B Beam Interact. with Mater. Atoms*, vol. 266, no. 21, pp. 4845–4848, 2008.

[133] F. Granberg, J. Byggmästar, and K. Nordlund, "Defect accumulation and evolution during prolonged irradiation of Fe and FeCr alloys," *J. Nucl. Mater.*, vol. 528, p. 151 843, 2020.

[134] F. Gao, D. J. Bacon, A. F. Calder, P. E. Flewitt, and T. A. Lewis, "Computer simulation study of cascade overlap effects in α-iron," *J. Nucl. Mater.*, vol. 230, no. 1, pp. 47–56, 1996.

[135] A. E. Sand, J. Byggmästar, A. Zitting, and K. Nordlund, "Defect structures and statistics in overlapping cascade damage in fusion-relevant bcc metals," *J. Nucl. Mater.*, vol. 511, pp. 64–74, 2018.

[136] M. L. Jenkins, M. A. Kirk, and W. J. Phythian, "Experimental studies of cascade phenomena in metals," *J. Nucl. Mater.*, vol. 205, no. C, pp. 16–30, 1993.

[137] M. A. Kirk, I. M. Robertson, M. L. Jenkins, C. A. English, T. J. Black, and J. S. Vetrano, "The collapse of defect cascades to dislocation loops," *J. Nucl. Mater.*, vol. 149, no. 1, pp. 21–28, 1987.

[138] M. L. Jenkins, C. A. English, and B. L. Eyre, "Heavy-ion irradiation of α-iron," *Philos. Mag. A Phys. Condens. Matter, Struct. Defects Mech. Prop.*, vol. 38, no. 1, pp. 97–114, 1978.

[139] R. Alexander, M.-C. Marinica, L. Proville, F. Willaime, K. Arakawa, M. R. Gilbert, and S. L. Dudarev, "Ab initio scaling laws for the formation energy of nanosized interstitial defect clusters in iron, tungsten, and vanadium," *Phys. Rev. B*, vol. 94, no. 2, p. 024 103, 2016.

[140] Y. Zhang, X. M. Bai, M. R. Tonks, and S. B. Biner, "Formation of prismatic loops from C15 Laves phase interstitial clusters in body-centered cubic iron," *Scr. Mater.*, vol. 98, pp. 5–8, 2015.

[141] J. Byggmästar and F. Granberg, "Dynamical stability of radiation-induced C15 clusters in iron," *J. Nucl. Mater.*, vol. 528, p. 151 893, 2020.

[142] C. English and M. Jenkins, "Insight into Cascade Processes Arising from Studies of Cascade Collapse," *Mater. Sci. Forum*, vol. 15-18, pp. 1003–1022, 1987.

[143] B. C. Masters, "Dislocation loops in irradiated iron," *Philos. Mag.*, vol. 11, no. 113, pp. 881–893, 1965.

[144] J. Marian, B. D. Wirth, and J. M. Perlado, "Mechanism of Formation and Growth of <100> Interstitial Loops in Ferritic Materials," *Phys. Rev. Lett.*, vol. 88, no. 25, p. 255 507, 2002.

[145] H. Xu, R. E. Stoller, Y. N. Osetsky, and D. Terentyev, "Solving the Puzzle of <100> Interstitial Loop Formation in bcc Iron," *Phys. Rev. Lett.*, vol. 110, no. 26, p. 265 503, 2013.

[146] L. K. Béland, Y. N. Osetsky, R. E. Stoller, and H. Xu, "Interstitial loop transformations in FeCr," *J. Alloys Compd.*, vol. 640, pp. 219–225, 2015.

[147] C. Dethloff, E. Gaganidze, and J. Aktaa, "Microstructural defects in EUROFER 97 after different neutron irradiation conditions," *Nucl. Mater. Energy*, vol. 9, pp. 471–475, 2016.

[148] P. M. Derlet and S. L. Dudarev, "Microscopic structure of a heavily irradiated material," *Phys. Rev. Mater.*, vol. 4, no. 2, p. 023 605, 2020.

[149] W.-Y. Chen, Y. Miao, J. Gan, M. A. Okuniewski, S. A. Maloy, and J. F. Stubbins, "Neutron irradiation effects in Fe and Fe-Cr at 300 °C," *Acta Mater.*, vol. 111, pp. 407–416, 2016.

[150] S. Porollo, A. Dvoriashin, A. Vorobyev, and Y. Konobeev, "The microstructure and tensile properties of Fe–Cr alloys after neutron irradiation at 400°C to 5.5–7.1 dpa," *J. Nucl. Mater.*, vol. 256, no. 2-3, pp. 247–253, 1998.

[151] A. Okada, H. Maeda, K. Hamada, and I. Ishida, "Defect structure development in a pure iron and dilute iron alloys irradiated with neutrons and electrons," *J. Nucl. Mater.*, vol. 271-272, pp. 133–138, 1999.

[152] A. Prokhodtseva, B. Décamps, and R. Schäublin, "Comparison between bulk and thin foil ion irradiation of ultra high purity Fe," *J. Nucl. Mater.*, vol. 442, no. 1-3, S786–S789, 2013.

[153] J. Chen, F. Duval, P. Jung, R. Schäublin, N. Gao, and M. F. Barthe, "Dislocation loops in ultra-high purity Fe(Cr) alloys after 7.2 MeV proton irradiation," *J. Nucl. Mater.*, vol. 503, pp. 81–90, 2018.

[154] D. Terentyev, M. Klimenkov, and L. Malerba, "Confinement of motion of interstitial clusters and dislocation loops in BCC Fe–Cr alloys," *J. Nucl. Mater.*, vol. 393, no. 1, pp. 30–35, 2009.

[155] Z. Yao, M. L. Jenkins, M. Hernández-Mayoral, and M. A. Kirk, "The temperature dependence of heavy-ion damage in iron: A microstructural transition at elevated temperatures," *Philos. Mag.*, vol. 90, no. 35-36, pp. 4623–4634, 2010.

[156] S. Xu, "A study of irradiation damage in iron and Fe-Cr alloys," Ph.D. dissertation, University of Oxford, 2013.

[157] Y. N. Osetsky, D. J. Bacon, A. Serra, B. N. Singh, and S. I. Golubov, "Stability and mobility of defect clusters and dislocation loops in metals," *J. Nucl. Mater.*, vol. 276, no. 1, pp. 65–77, 2000.

[158] S. L. Dudarev, R. Bullough, and P. M. Derlet, "Effect of the α-γ Phase Transition on the Stability of Dislocation Loops in bcc Iron," *Phys. Rev. Lett.*, vol. 100, no. 13, p. 135 503, 2008.

[159] M. Klimenkov, U. Jäntsch, M. Rieth, and A. Möslang, "Correlation of microstructural and mechanical properties of neutron irradiated EUROFER97 steel," *J. Nucl. Mater.*, vol. 538, p. 152 231, 2020.

[160] M. Klimenkov, E. Materna-Morris, and A. Möslang, "Characterization of radiation induced defects in EUROFER 97 after neutron irradiation," *J. Nucl. Mater.*, vol. 417, no. 1-3, pp. 124–126, 2011.

[161] A Hishinuma and L. Mansur, "Critical radius for bias-driven swelling — a further analysis and its application to bimodal cavity size distributions," *J. Nucl. Mater.*, vol. 118, no. 1, pp. 91–99, 1983.

[162] A. Brailsford and R. Bullough, "The rate theory of swelling due to void growth in irradiated metals," *J. Nucl. Mater.*, vol. 44, no. 2, pp. 121–135, 1972.

[163] C. Cawthorne and E. J. Fulton, "Voids in Irradiated Stainless Steel," *Nature*, vol. 216, no. 5115, pp. 575–576, 1967.

[164] S. Zinkle and G. Was, "Materials challenges in nuclear energy," *Acta Mater.*, vol. 61, no. 3, pp. 735–758, 2013.

[165] F. A. Garner, M. B. Toloczko, and B. H. Sencer, "Comparison of swelling and irradiation creep behavior of fcc-austenitic and bcc-ferritic/martensitic alloys at high neutron exposure," *J. Nucl. Mater.*, vol. 276, no. 1, pp. 123–142, 2000.

[166] R. J. Kurtz and G. R. Odette, "Overview of Reactor Systems and Operational Environments for Structural Materials in Fusion Reactors," in *Struct. Alloy. Nucl. Energy Appl.* Elsevier, 2019, pp. 51–102.

[167] E. A. Little and D. A. Stow, "Void-swelling in irons and ferritic steels. II. An experimental survey of materials irradiated in a fast reactor," *J. Nucl. Mater.*, vol. 87, no. 1, pp. 25–39, 1979.

[168] B. Singh and S. Zinkle, "Influence of irradiation parameters on damage accumulation in metals and alloys," *J. Nucl. Mater.*, vol. 217, no. 1-2, pp. 161–171, 1994.

[169] D. Gelles, "Void swelling in binary FeCr alloys at 200 dpa," *J. Nucl. Mater.*, vol. 225, pp. 163–174, 1995.

[170] Y. Katoh, A. Kohyama, and D. S. Gelles, "Swelling and dislocation evolution in simple ferritic alloys irradiated to high fluence in FFTF/MOTA," *J. Nucl. Mater.*, vol. 225, pp. 154–162, 1995.

[171] L. Horton, J. Bentley, and W. Jesser, "The microstructure of "triple-beam" ion irradiated Fe and Fe-Cr alloys," *J. Nucl. Mater.*, vol. 104, pp. 1085–1089, 1981.

[172] W. Johnston, T Lauritzen, J. Rosolowski, and A. Turkalo, "Void Swelling of Ferritic Alloys Bombarded with Nickel Ions," in *Eff. Radiat. Mater. Proc. 11th Int. Symp.*, ASTM International, 1982, pp. 809–823.

[173] B. H. Sencer and F. A. Garner, "Compositional and temperature dependence of void swelling in model Fe–Cr base alloys irradiated in the EBR-II fast reactor," *J. Nucl. Mater.*, vol. 283-287, no. PART I, pp. 164–168, 2000.

[174] S. J. Zinkle, W. G. Wolfer, G. L. Kulcinski, and L. E. Seitzman, "II. Effect of oxygen and helium on void formation in metals," *Philos. Mag. A*, vol. 55, no. 1, pp. 127–140, 1987.

[175] S. L. Dudarev, D. R. Mason, E. Tarleton, P.-W. Ma, and A. E. Sand, "A multi-scale model for stresses, strains and swelling of reactor components under irradiation," *Nucl. Fusion*, vol. 58, no. 12, p. 126 002, 2018.

[176] F. Hofmann, D. Nguyen-Manh, M. Gilbert, C. Beck, J. Eliason, A. Maznev, W. Liu, D. Armstrong, K. Nelson, and S. Dudarev, "Lattice swelling and modulus change in a helium-implanted tungsten alloy: X-ray micro-diffraction, surface acoustic wave measurements, and multiscale modelling," *Acta Mater.*, vol. 89, pp. 352–363, 2015.

[177] S. Das, W. Liu, R. Xu, and F. Hofmann, "Helium-implantation-induced lattice strains and defects in tungsten probed by X-ray micro-diffraction," *Mater. Des.*, vol. 160, pp. 1226–1237, 2018.

[178] S. L. Dudarev and P.-W. Ma, "Elastic fields, dipole tensors, and interaction between self-interstitial atom defects in bcc transition metals," *Phys. Rev. Mater.*, vol. 2, no. 3, p. 033 602, 2018.

[179] P.-W. Ma and S. L. Dudarev, "Universality of point defect structure in body-centered cubic metals," *Phys. Rev. Mater.*, vol. 3, no. 1, p. 013 605, 2019.

[180] A. Richard, H. Palancher, E. Castelier, J. S. Micha, M. Gamaleri, G. Carlot, H. Rouquette, P. Goudeau, G. Martin, F. Rieutord, J. P. Piron, and P. Garcia, "Strains in light-ion-implanted polycrystals: Influence of grain orientation," *J. Appl. Crystallogr.*, vol. 45, no. 4, pp. 826–833, 2012.

[181] A. Debelle, J.-P. Crocombette, A. Boulle, A. Chartier, T. Jourdan, S. Pellegrino, D. Bachiller-Perea, D. Carpentier, J. Channagiri, T.-H. Nguyen, F. Garrido, and L. Thomé, "Lattice strain in irradiated materials unveils a prevalent defect evolution mechanism," *Phys. Rev. Mater.*, vol. 2, p. 13 604, 2018.

[182] D. Yun, Y. Miao, R. Xu, Z. Mei, K. Mo, W. Mohamed, B. Ye, M. J. Pellin, and A. M. Yacout, "Characterization of high energy Xe ion irradiation effects in single crystal molybdenum with depth-resolved synchrotron microbeam diffraction," *J. Nucl. Mater.*, vol. 471, pp. 272–279, 2016.

[183] D. R. Mason, S. Das, P. M. Derlet, S. L. Dudarev, A. J. London, H. Yu, N. W. Phillips, D. Yang, K. Mizohata, R. Xu, and F. Hofmann, "Observation of Transient and Asymptotic Driven Structural States of Tungsten Exposed to Radiation," *Phys. Rev. Lett.*, vol. 125, no. 22, p. 225 503, 2020.

[184] K. Papamihail, K. Mergia, F. Ott, Y. Serruys, T. Speliotis, G. Apostolopoulos, and S. Messoloras, "Magnetic effects induced by self-ion irradiation of Fe films," *Phys. Rev. B*, vol. 93, no. 10, p. 100 404, 2016.

[185] K. Papamihail, K. Mergia, F. Ott, Y. Serruys, T. Speliotis, G. Apostolopoulos, and S. Messoloras, "Fe + ion irradiation induced changes in structural and magnetic properties of iron films," *Nucl. Mater. Energy*, vol. 9, pp. 459–464, 2016.

[186] M. W. Ullah, Y. Zhang, N. Sellami, A. Debelle, H. Bei, and W. J. Weber, "Evolution of irradiation-induced strain in an equiatomic NiFe alloy," *Scr. Mater.*, vol. 140, pp. 35–39, 2017.

[187] E. Jossou, T. A. Assefa, A. F. Suzana, L. Wu, C. Campbell, R. Harder, W. Cha, K. Kisslinger, C. Sun, J. Gan, L. Ecker, I. K. Robinson, and S. K. Gill, "Three-dimensional strain imaging of irradiated chromium using multi-reflection Bragg coherent diffraction," *npj Mater. Degrad.*, vol. 6, no. 1, p. 99, 2022.

[188] N. Phillips, H. Yu, S. Das, D. Yang, K. Mizohata, W. Liu, R. Xu, R. Harder, and F. Hofmann, "Nanoscale Lattice Strains in Self-ion-implanted Tungsten," *Acta Mater.*, 2020.

[189] Z. Zhou, M. L. Jenkins, S. L. Dudarev, A. P. Sutton, and M. A. Kirk, "Simulations of weak-beam diffraction contrast images of dislocation loops by the many-beam Howie–Basinski equations," *Philos. Mag.*, vol. 86, no. 29-31, pp. 4851–4881, 2006.

[190] T. Byun and K Farrell, "Irradiation hardening behavior of polycrystalline metals after low temperature irradiation," *J. Nucl. Mater.*, vol. 326, no. 2-3, pp. 86–96, 2004.

[191] M. Victoria, N. Baluc, C. Bailat, Y. Dai, M. I. Luppo, R. Schäublin, and B. N. Singh, "The microstructure and associated tensile properties of irradiated fcc and bcc metals," *J. Nucl. Mater.*, vol. 276, no. 1-3, pp. 114–122, 2000.

[192] A. K. Seeger, "On the theory of radiation damage and radiation hardening," Max-Planck-Inst. fur Metallforschung, Stuttgart, Tech. Rep., 1958.

[193] M. Matijasevic and A. Almazouzi, "Effect of Cr on the mechanical properties and microstructure of Fe-Cr model alloys after n-irradiation," *J. Nucl. Mater.*, vol. 377, no. 1, pp. 147–154, 2008.

[194] N. Luzginova, J.-W. Rensman, M. Jong, P. ten Pierick, T. Bakker, and H. Nolles, "Overview of 10 years of irradiation projects on Eurofer97 steel at High Flux Reactor in Petten," *J. Nucl. Mater.*, vol. 455, no. 1-3, pp. 21–25, 2014.

[195] B. L. Eyre, "Direct observations of neutron irradiation damage in α-iron," *Philos. Mag.*, vol. 7, no. 84, pp. 2107–2113, 1962.

[196] G Saada and J Washburn, "Interaction between prismatic and glissile dislocations," Lawrence Livermore National Laboratory (LLNL), Livermore, CA (United States), Tech. Rep., 1962.

[197] A. J. E. Foreman and J. V. Sharp, "A mechanism for the sweeping-up of loops by glide dislocations during deformation," *Philos. Mag.*, vol. 19, no. 161, pp. 931–937, 1969.

[198] X. Xiao, "Fundamental Mechanisms for Irradiation-Hardening and Embrittlement: A Review," *Metals (Basel).*, vol. 9, no. 10, p. 1132, 2019.

[199] W. Liu, L. Chen, L. Yu, J. Fu, and H. Duan, "Continuum modeling of dislocation channels in irradiated metals based on stochastic crystal plasticity," *Int. J. Plast.*, vol. 151, p. 103 211, 2022.

[200] P. J. Doyle, K. M. Benensky, and S. J. Zinkle, "Modeling of dislocation channel width evolution in irradiated metals," *J. Nucl. Mater.*, vol. 499, pp. 47–64, 2018.

[201] E. A. Little, "Neutron-irradiation hardening in irons and ferritic steels," *Int. Met. Rev.*, vol. 21, no. 1, pp. 25–60, 1976.

[202] A. Okada, T. Yasujima, T. Yoshiie, I. Ishida, and M. Kiritani, "Mechanical property changes and microstructures of iron irradiated with fission and fusion neutrons," *J. Nucl. Mater.*, vol. 179-181, pp. 1083–1087, 1991.

[203] S. M. Ohr, "Work hardening characteristics of neutron irradiated iron," *Scr. Metall.*, vol. 2, no. 4, pp. 213–216, 1968.

[204] B. L. Eyre and A. F. Bartlett, "An electron microscope study of neutron irradiation damage in alpha-iron," *Philos. Mag.*, vol. 12, no. 116, pp. 261–272, 1965.

[205] P. A. Smidt and B. Mastel, "Some observations of dislocation channelling in irradiated iron," *Philos. Mag.*, vol. 20, no. 165, pp. 651–656, 1969.

[206] ASTM E1035-18, "Standard Practice for Determining Neutron Exposures for Nuclear Reactor Vessel Support Structures," in *Annu. B. ASTM Stand.* Vol. 12.02, 2023, p. 3.

[207] P. Hosemann, C. Vieh, R. Greco, S. Kabra, J. Valdez, M. Cappiello, and S. Maloy, "Nanoindentation on ion irradiated steels," *J. Nucl. Mater.*, vol. 389, no. 2, pp. 239–247, 2009.

[208] X. Xiao and L. Yu, "Nano-indentation of ion-irradiated nuclear structural materials: A review," *Nucl. Mater. Energy*, vol. 22, p. 100 721, 2020.

[209] F. Halliday, D. E. Armstrong, J. D. Murphy, and S. G. Roberts, "Nanoindentation and Micromechanical Testing of Iron-Chromium Alloys Implanted with Iron Ions," in *Adv. Mater. Res.* Vol. 59, 2008, pp. 304–307.

[210] C. D. Hardie and S. G. Roberts, "Nanoindentation of model Fe–Cr alloys with self-ion irradiation," *J. Nucl. Mater.*, vol. 433, no. 1-3, pp. 174–179, 2013.

[211] C. D. Hardie, S. G. Roberts, and A. J. Bushby, "Understanding the effects of ion irradiation using nanoindentation techniques," *J. Nucl. Mater.*, vol. 462, pp. 391–401, 2015.

[212] C. Heintze, F. Bergner, M. Hernández-Mayoral, R. Kögler, G. Müller, and A. Ulbricht, "Irradiation hardening of Fe–9Cr-based alloys and ODS Eurofer: Effect of helium implantation and iron-ion irradiation at 300 °C including sequence effects," *J. Nucl. Mater.*, vol. 470, pp. 258–267, 2016.

[213] J. Ziman, *Electrons and Phonons. The theory of transport phenomena in solids.* Oxford: Oxford University Press, 1961.

[214] W. G. Wolfer, "Fundamental properties of defects in metals," in *Compr. Nucl. Mater.* Vol. 1, Elsevier Ltd, 2012, pp. 1–45.

[215] S. A. Fabritsiev, A. S. Pokrovsky, S. J. Zinkle, A. F. Rowcliffe, D. J. Edwards, F. A. Garner, V. A. Sandakov, B. N. Singh, and V. R. Barabash, "The effect of neutron spectrum on the mechanical and physical properties of pure copper and copper alloys," *J. Nucl. Mater.*, vol. 233-237, no. PART 1, pp. 526–533, 1996.

[216] H. M. Frost and J. C. Kennedy, "Porosity swelling and transmutation contributions to conductivity changes in some neutron-irradiated copper alloys," *J. Nucl. Mater.*, vol. 141-143, no. PART 1, pp. 169–173, 1986.

[217] S. E. Ferry, C. A. Dennett, K. B. Woller, and M. P. Short, "Inferring radiation-induced microstructural evolution in single-crystal niobium through changes in thermal transport," *J. Nucl. Mater.*, vol. 523, pp. 378–382, 2019.

[218] A. P. C. Wylie, K. B. Woller, S. A. A. Al Dajani, B. R. Dacus, E. J. Pickering, M. Preuss, and M. P. Short, "Thermal diffusivity in ion-irradiated single-crystal iron, chromium, vanadium, and tungsten measured using transient grating spectroscopy," *J. Appl. Phys.*, vol. 132, no. 4, p. 045 102, 2022.

[219] A. James and M. Lord, *Macmillan's chemical and physical data*. London: Macmillan, 1992.

[220] R. K. Williams, D. W. Yarbrough, J. W. Masey, T. K. Holder, and R. S. Graves, "Experimental determination of the phonon and electron components of the thermal conductivity of bcc iron," *J. Appl. Phys.*, vol. 52, p. 5167, 1981.

[221] A. J. Hillel and P. L. Rossiter, "Resistivity mechanisms during clustering in alloys," *Philos. Mag. B Phys. Condens. Matter; Stat. Mech. Electron. Opt. Magn. Prop.*, vol. 44, no. 3, pp. 383–388, 1981.

[222] R. K. Williams, R. K. Nanstad, R. S. Graves, and R. G. Berggren, "Irradiation effects on thermal conductivity of a light-water reactor pressure vessel steel," *J. Nucl. Mater.*, vol. 115, no. 2-3, pp. 211–215, 1983.

[223] H. Gleiter, "Nanostructured materials: basic concepts and microstructure," *Acta Mater.*, vol. 48, no. 1, pp. 1–29, 2000.

[224] H. Gleiter, "Nanocrystalline materials," *Prog. Mater. Sci.*, vol. 33, no. 4, pp. 223–315, 1989.

[225] C. Suryanarayana, *Non-equilibrium Processing of Materials*. Elsevier, 1999, pp. 225–288.

[226] R. Valiev, A. Korznikov, and R. Mulyukov, "Structure and properties of ultrafine-grained materials produced by severe plastic deformation," *Mater. Sci. Eng. A*, vol. 168, no. 2, pp. 141–148, 1993.

[227] A. P. Zhilyaev and T. G. Langdon, "Using high-pressure torsion for metal processing: Fundamentals and applications," *Prog. Mater. Sci.*, vol. 53, no. 6, pp. 893–979, 2008.

[228] R. Valiev, R. Islamgaliev, and I. Alexandrov, "Bulk nanostructured materials from severe plastic deformation," *Prog. Mater. Sci.*, vol. 45, no. 2, pp. 103–189, 2000.

[229] R. Z. Valiev, Y. Estrin, Z. Horita, T. G. Langdon, M. J. Zechetbauer, and Y. T. Zhu, "Producing bulk ultrafine-grained materials by severe plastic deformation," *JOM*, vol. 58, no. 4, pp. 33–39, 2006.

[230] K. Edalati, A. Bachmaier, V. A. Beloshenko, Y. Beygelzimer, V. D. Blank, W. J. Botta, K. Bryła, J. Čížek, S. Divinski, N. A. Enikeev, Y. Estrin, G. Faraji, R. B. Figueiredo, M. Fuji, T. Furuta, T. Grosdidier, J. Gubicza, A. Hohenwarter, Z. Horita, J. Huot, Y. Ikoma, M. Janeček, M. Kawasaki, P. Král, S. Kuramoto, T. G. Langdon, D. R. Leiva, V. I. Levitas, A. Mazilkin, M. Mito, H. Miyamoto, T. Nishizaki, R. Pippan, V. V. Popov, E. N. Popova, G. Purcek, O. Renk, Á. Révész, X. Sauvage, V. Sklenicka, W. Skrotzki, B. B. Straumal, S. Suwas, L. S. Toth, N. Tsuji, R. Z. Valiev, G. Wilde, M. J. Zehetbauer, and X. Zhu, "Nanomaterials by severe plastic deformation: review of historical developments and recent advances," *Mater. Res. Lett.*, vol. 10, no. 4, pp. 163–256, 2022.

[231] V. Stolyarov, Y. Zhu, T. Lowe, R. Islamgaliev, and R. Valiev, "A two step SPD processing of ultrafine-grained titanium," *Nanostructured Mater.*, vol. 11, no. 7, pp. 947–954, 1999.

[232] A. Zhilyaev, B.-K. Kim, J. Szpunar, M. Baró, and T. Langdon, "The microstructural characteristics of ultrafine-grained nickel," *Mater. Sci. Eng. A*, vol. 391, no. 1-2, pp. 377–389, 2005.

[233] A. Zhilyaev, B.-K. Kim, G. Nurislamova, M. Baró, J. Szpunar, and T. Langdon, "Orientation imaging microscopy of ultrafine-grained nickel," *Scr. Mater.*, vol. 46, no. 8, pp. 575–580, 2002.

[234] G. Sakai, K. Nakamura, Z. Horita, and T. G. Langdon, "Developing high-pressure torsion for use with bulk samples," *Mater. Sci. Eng. A*, vol. 406, no. 1-2, pp. 268–273, 2005.

[235] Z. Horita, Y. Tang, T. Masuda, and Y. Takizawa, "Severe Plastic Deformation under High Pressure: Upsizing Sample Dimensions," *Mater. Trans.*, vol. 61, no. 7, pp. 1177–1190, 2020.

[236] Y. Ivanisenko, R. Kulagin, V. Fedorov, A. Mazilkin, T. Scherer, B. Baretzky, and H. Hahn, "High Pressure Torsion Extrusion as a new severe plastic deformation process," *Mater. Sci. Eng. A*, vol. 664, pp. 247–256, 2016.

[237] A. Hohenwarter, "Incremental high pressure torsion as a novel severe plastic deformation process: Processing features and application to copper," *Mater. Sci. Eng. A*, vol. 626, pp. 80–85, 2015.

[238] Y. Iwahashi, Z. Horita, M. Nemoto, and T. Langdon, "An investigation of microstructural evolution during equal-channel angular pressing," *Acta Mater.*, vol. 45, no. 11, pp. 4733–4741, 1997.

[239] W. Skrotzki, "Deformation Heterogeneities in Equal Channel Angular Pressing," *Mater. Trans.*, vol. 60, no. 7, pp. 1331–1343, 2019.

[240] R. Z. Valiev and T. G. Langdon, "Principles of equal-channel angular pressing as a processing tool for grain refinement," *Prog. Mater. Sci.*, vol. 51, no. 7, pp. 881–981, 2006.

[241] S. Frint, M. Hockauf, P. Frint, and M. F.-X. Wagner, "Scaling up Segal's principle of Equal-Channel Angular Pressing," *Mater. Des.*, vol. 97, pp. 502–511, 2016.

[242] N. Hansen, R. F. Mehl, and A. Medalist, "New discoveries in deformed metals," *Metall. Mater. Trans. A*, vol. 32, no. 12, pp. 2917–2935, 2001.

[243] N. Tsuji, R. Gholizadeh, R. Ueji, N. Kamikawa, L. Zhao, Y. Tian, Y. Bai, and A. Shibata, "Formation Mechanism of Ultrafine Grained Microstructures: Various Possibilities for Fabricating Bulk Nanostructured Metals and Alloys," *Mater. Trans.*, vol. 60, no. 8, pp. 1518–1532, 2019.

[244] R. Islamgaliev, F. Chmelik, and R. Kuzel, "Thermal structure changes in copper and nickel processed by severe plastic deformation," *Mater. Sci. Eng. A*, vol. 234-236, pp. 335–338, 1997.

[245] R. Valiev, Y. Ivanisenko, E. Rauch, and B. Baudelet, "Structure and deformaton behaviour of Armco iron subjected to severe plastic deformation," *Acta Mater.*, vol. 44, no. 12, pp. 4705–4712, 1996.

[246] A. Popov, I. Pyshmintsev, S. Demakov, A. Illarionov, T. Lowe, A. Sergeyeva, and R. Valiev, "Structural and mechanical properties of nanocrystalleve titanium processed by severe plastic deformation," *Scr. Mater.*, vol. 37, no. 7, pp. 1089–1094, 1997.

[247] R. Valiev, E. Kozlov, Y. Ivanov, J. Lian, A. Nazarov, and B. Baudelet, "Deformation behaviour of ultra-fine-grained copper," *Acta Metall. Mater.*, vol. 42, no. 7, pp. 2467–2475, 1994.

[248] M. Hafok and R. Pippan, "High-pressure torsion applied to nickel single crystals," *Philos. Mag.*, vol. 88, no. 12, pp. 1857–1877, 2008.

[249] R. Pippan, S. Scheriau, A. Taylor, M. Hafok, A. Hohenwarter, and A. Bachmaier, "Saturation of Fragmentation During Severe Plastic Deformation," *Annu. Rev. Mater. Res.*, vol. 40, no. 1, pp. 319–343, 2010.

[250] G. B. Rathmayr, A. Hohenwarter, and R. Pippan, "Influence of grain shape and orientation on the mechanical properties of high pressure torsion deformed nickel," *Mater. Sci. Eng. A*, vol. 560, pp. 224–231, 2013.

[251] S. Naghdy, H. Pirgazi, P. Verleysen, R. Petrov, and L. Kestens, "Morphological and crystallographic anisotropy of severely deformed commercially pure aluminium by three-dimensional electron backscatter diffraction," *J. Appl. Crystallogr.*, vol. 50, no. 5, pp. 1512–1523, 2017.

[252] R. Islamgaliev, F. Chmelik, and R. Kuzel, "Thermal stability of submicron grained copper and nickel," *Mater. Sci. Eng. A*, vol. 237, no. 1, pp. 43–51, 1997.

[253] P Scardi and M Leoni, "Acta Crystallographica Section A Foundations of Crystallography Whole powder pattern modelling," *Acta Cryst. A*, pp. 190–200, 2002.

[254] T. Ungár, G. Tichy, J. Gubicza, and R. J. Hellmig, "Correlation between subgrains and coherently scattering domains," *Powder Diffr.*, vol. 20, no. 4, pp. 366–375, 2005.

[255] K. Edalati, D. Akama, A. Nishio, S. Lee, Y. Yonenaga, J. M. Cubero-Sesin, and Z. Horita, "Influence of dislocation–solute atom interactions and stacking fault energy on grain size of single-phase alloys after severe plastic deformation using high-pressure torsion," *Acta Mater.*, vol. 69, pp. 68–77, 2014.

[256] A. Sergueeva, C Song, R. Valiev, and A. Mukherjee, "Structure and properties of amorphous and nanocrystalline NiTi prepared by severe plastic deformation and annealing," *Mater. Sci. Eng. A*, vol. 339, no. 1-2, pp. 159–165, 2003.

[257] H. Jiang, Y. Zhu, D. P. Butt, I. V. Alexandrov, and T. C. Lowe, "Microstructural evolution, microhardness and thermal stability of HPT-processed Cu," *Mater. Sci. Eng. A*, vol. 290, no. 1-2, pp. 128–138, 2000.

[258] R. Z. Valiev, V. Y. Gertsman, O. A. Kaibyshev, and S. K. Khannanov, "Non-Equilibrium State and Recovery of Grain Boundary Structure," *Phys. Status Solidi*, vol. 77, no. 1, pp. 97–105, 1983.

[259] R. Z. Valiev, V. Y. Gertsman, and O. A. Kaibyshev, "Non-equilibrium state and recovery of grain boundary structure. II. Energetic Analysis," *Phys. Status Solidi*, vol. 78, no. 1, pp. 177–186, 1983.

[260] R. Z. Valiev, V. Y. Gertsman, and O. A. Kaibyshev, "Grain boundary structure and properties under external influences," *Phys. status solidi*, vol. 97, no. 1, pp. 11–56, 1986.

[261] G. Ribárik, B. Jóni, and T. Ungár, "Global optimum of microstructure parameters in the CMWP line-profile-analysis method by combining Marquardt-Levenberg and Monte-Carlo procedures," *J. Mater. Sci. Technol.*, vol. 35, no. 7, pp. 1508–1514, 2019.

[262] Q. Wei, Z. Pan, X. Wu, B. Schuster, L. Kecskes, and R. Valiev, "Microstructure and mechanical properties at different length scales and strain rates of nanocrystalline tantalum produced by high-pressure torsion," *Acta Mater.*, vol. 59, no. 6, pp. 2423–2436, 2011.

[263] J. Gubicza, "Defect Structure in Bulk Nanomaterials Processed by Severe Plastic Deformation," in *Defect Struct. Prop. Nanomater.* Elsevier, 2017, pp. 59–93.

[264] Y. Cao, S. Ni, X. Liao, M. Song, and Y. Zhu, "Structural evolutions of metallic materials processed by severe plastic deformation," *Mater. Sci. Eng. R Reports*, vol. 133, pp. 1–59, 2018.

[265] J. Gubicza, N. Q. Chinh, J. L. Lábár, Z. Hegedűs, and T. G. Langdon, "Principles of self-annealing in silver processed by equal-channel angular pressing: The significance of a very low stacking fault energy," *Mater. Sci. Eng. A*, vol. 527, no. 3, pp. 752–760, 2010.

[266] L. Balogh, T. Ungár, Y. Zhao, Y. Zhu, Z. Horita, C. Xu, and T. G. Langdon, "Influence of stacking-fault energy on microstructural characteristics of ultrafine-grain copper and copper–zinc alloys," *Acta Mater.*, vol. 56, no. 4, pp. 809–820, 2008.

[267] J. Gubicza, "Lattice Defects and Their Influence on the Mechanical Properties of Bulk Materials Processed by Severe Plastic Deformation," *Mater. Trans.*, vol. 60, no. 7, pp. 1230–1242, 2019.

[268] D. Setman, E. Schafler, E. Korznikova, and M. J. Zehetbauer, "The presence and nature of vacancy type defects in nanometals detained by severe plastic deformation," *Mater. Sci. Eng. A*, vol. 493, no. 1-2, pp. 116–122, 2008.

[269] J. Čížek, M. Janeček, O. Srba, R. Kužel, Z. Barnovská, I. Procházka, and S. Dobatkin, "Evolution of defects in copper deformed by high-pressure torsion," *Acta Mater.*, vol. 59, no. 6, pp. 2322–2329, 2011.

[270] J. Čížek, M. Janeček, T. Krajňák, J. Stráská, P. Hruška, J. Gubicza, and H. Kim, "Structural characterization of ultrafine-grained interstitial-free steel prepared by severe plastic deformation," *Acta Mater.*, vol. 105, pp. 258–272, 2016.

[271] M. El-Tahawy, Y. Huang, H. Choi, H. Choe, J. L. Lábár, T. G. Langdon, and J. Gubicza, "High temperature thermal stability of nanocrystalline 316L stainless steel processed by high-pressure torsion," *Mater. Sci. Eng. A*, vol. 682, pp. 323–331, 2017.

[272] L. S. Tóth, R. Arruffat Massion, L. Germain, S. C. Baik, and S. Suwas, "Analysis of texture evolution in equal channel angular extrusion of copper using a new flow field," *Acta Mater.*, vol. 52, no. 7, pp. 1885–1898, 2004.

[273] W Skrotzki, A Pukenas, B Joni, E Odor, T Ungar, A Hohenwarter, R Pippan, and E. P. George, "Microstructure and texture evolution during severe plastic deformation of CrMnFeCoNi high-entropy alloy," *IOP Conf. Ser. Mater. Sci. Eng.*, vol. 194, p. 012 028, 2017.

[274] N. Nadammal, S. V. Kailas, J. Szpunar, and S. Suwas, "Microstructure and Crystallographic Texture Evolution During the Friction-Stir Processing of a Precipitation-Hardenable Aluminum Alloy," *JOM*, vol. 67, no. 5, pp. 1014–1021, 2015.

[275] Y. Tian, S. Gao, L. Zhao, S. Lu, R. Pippan, Z. Zhang, and N. Tsuji, "Remarkable transitions of yield behavior and Lüders deformation in pure Cu by changing grain sizes," *Scr. Mater.*, vol. 142, pp. 88–91, 2018.

[276] E. N. Popova and I. L. Deryagina, "Evolution of Structure of Cu–Nb Composite under High-Pressure Torsion and Subsequent Annealing," *Phys. Met. Metallogr.*, vol. 121, no. 12, pp. 1182–1187, 2020.

[277] D. Terada, M. Inoue, H. Kitahara, and N. Tsuji, "Change in Mechanical Properties and Microstructure of ARB Processed Ti during Annealing," *Mater. Trans.*, vol. 49, no. 1, pp. 41–46, 2008.

[278] O. Renk and R. Pippan, "Saturation of Grain Refinement during Severe Plastic Deformation of Single Phase Materials: Reconsiderations, Current Status and Open Questions," *Mater. Trans.*, vol. 60, no. 7, pp. 1270–1282, 2019.

[279] O. Renk and R. Pippan, "Transition from thermally assisted to mechanically driven boundary migration and related apparent activation energies," *Scr. Mater.*, vol. 154, pp. 212–215, 2018.

[280] A. Vorhauer and R. Pippan, "On the Onset of a Steady State in Body-Centered Cubic Iron during Severe Plastic Deformation at Low Homologous Temperatures," *Metall. Mater. Trans. A*, vol. 39, no. 2, pp. 417–429, 2008.

[281] O. Renk, P. Ghosh, and R. Pippan, "Generation of extreme grain aspect ratios in severely deformed tantalum at elevated temperatures," *Scr. Mater.*, vol. 137, pp. 60–63, 2017.

[282] E. O. Hall, "The Deformation and Ageing of Mild Steel: III Discussion of Results," *Proc. Phys. Soc. Sect. B*, vol. 64, no. 9, pp. 747–753, 1951.

[283] N. J. Petch, "The Cleavage Strength of Polycrystals," *J. Iron Steel Inst.*, vol. 173, no. 5, pp. 25–28, 1953.

[284] M. Furukawa, Z. Horita, M. Nemoto, R. Z. Valiev, and T. G. Langdon, "Factors influencing the flow and hardness of materials with ultrafine grain sizes," *Philos. Mag. A*, vol. 78, no. 1, pp. 203–216, 1998.

[285] K. Oh-ishi, Z. Horita, D. J. Smith, R. Z. Valiev, M. Nemoto, and T. G. Langdon, "Fabrication and thermal stability of a nanocrystalline Ni–Al–Cr alloy: Comparison with pure Cu and Ni," *J. Mater. Res.*, vol. 14, no. 11, pp. 4200–4207, 1999.

[286] A. Zhilyaev, A. Gimazov, E. Soshnikova, Á. Révész, and T. Langdon, "Microstructural characteristics of nickel processed to ultrahigh strains by high-pressure torsion," *Mater. Sci. Eng. A*, vol. 489, no. 1-2, pp. 207–212, 2008.

[287] A. Sergueeva, V. Stolyarov, R. Valiev, and A. Mukherjee, "Advanced mechanical properties of pure titanium with ultrafine grained structure," *Scr. Mater.*, vol. 45, no. 7, pp. 747–752, 2001.

[288] Y. Cao, Y. Wang, X. An, X. Liao, M. Kawasaki, S. Ringer, T. Langdon, and Y. Zhu, "Concurrent microstructural evolution of ferrite and austenite in a duplex stainless steel processed by high-pressure torsion," *Acta Mater.*, vol. 63, pp. 16–29, 2014.

[289] K. Edalati and Z. Horita, "Significance of homologous temperature in softening behavior and grain size of pure metals processed by high-pressure torsion," *Mater. Sci. Eng. A*, vol. 528, no. 25-26, pp. 7514–7523, 2011.

[290] M. Kawasaki, "Different models of hardness evolution in ultrafine-grained materials processed by high-pressure torsion," *J. Mater. Sci.*, vol. 49, no. 1, pp. 18–34, 2014.

[291] J. Gubicza, M. El-Tahawy, Y. Huang, H. Choi, H. Choe, J. L. Lábár, and T. G. Langdon, "Microstructure, phase composition and hardness evolution in 316L stainless steel processed by high-pressure torsion," *Mater. Sci. Eng. A*, vol. 657, pp. 215–223, 2016.

[292] G. Cheng, W. Jian, W. Xu, H. Yuan, P. Millett, and Y. Zhu, "Grain Size Effect on Deformation Mechanisms of Nanocrystalline bcc Metals," *Mater. Res. Lett.*, vol. 1, no. 1, pp. 26–31, 2013.

[293] Q Wei, S Cheng, K. Ramesh, and E Ma, "Effect of nanocrystalline and ultrafine grain sizes on the strain rate sensitivity and activation volume: fcc versus bcc metals," *Mater. Sci. Eng. A*, vol. 381, no. 1-2, pp. 71–79, 2004.

[294] W. Blum, "Role of Dislocation Annihilation during Steady-State Deformation," *Phys. Status Solidi*, vol. 45, no. 2, pp. 561–571, 1971.

[295] I. Ovid'ko, R. Valiev, and Y. Zhu, "Review on superior strength and enhanced ductility of metallic nanomaterials," *Prog. Mater. Sci.*, vol. 94, pp. 462–540, 2018.

[296] Y. Wang and E. Ma, "Three strategies to achieve uniform tensile deformation in a nanostructured metal," *Acta Mater.*, vol. 52, no. 6, pp. 1699–1709, 2004.

[297] Y. Wang, M. Chen, F. Zhou, and E. Ma, "High tensile ductility in a nanostructured metal," *Nature*, vol. 419, no. 6910, pp. 912–915, 2002.

[298] Z. Horita, K. Ohashi, T. Fujita, K. Kaneko, and T. G. Langdon, "Achieving High Strength and High Ductility in Precipitation-Hardened Alloys," *Adv. Mater.*, vol. 17, no. 13, pp. 1599–1602, 2005.

[299] R. Z. Valiev, I. V. Alexandrov, Y. T. Zhu, and T. C. Lowe, "Paradox of Strength and Ductility in Metals Processed Bysevere Plastic Deformation," *J. Mater. Res.*, vol. 17, no. 1, pp. 5–8, 2002.

[300] N. Akhmadeev, N. Kobelev, R. Mulyukov, Y. Soifer, and R. Valiev, "The effect of heat treatment on the elastic and dissipative properties of copper with the submicrocrystalline structure," *Acta Metall. Mater.*, vol. 41, no. 4, pp. 1041–1046, 1993.

[301] A. Lebedev, S. Pulnev, V. Kopylov, Y. Burenkov, V. Vetrov, and O. Vylegzhanin, "Thermal stability of submicrocrystalline copper and Cu: ZrO2 composite," *Scr. Mater.*, vol. 35, no. 9, pp. 1077–1081, 1996.

[302] A. B. Lebedev, Y. A. Burenkov, S. A. Pulnev, V. V. Vetrov, and V. I. Kopylov, "Recovery of Young's Modulus During Annealing of Submicrocrystalline Cu and Cu : ZrO2 Composite," *Le J. Phys. IV*, vol. 06, no. C8, pp. C8–365–C8–368, 1996.

[303] R. Mulyukov, M. Weller, R. Valiev, T. Gessmann, and H.-E. Schaefer, "Internal friction and shear modulus in submicrograined Cu," *Nanostructured Mater.*, vol. 6, no. 5-8, pp. 577–580, 1995.

[304] K. Y. Xie, Y. Wang, Y. Zhao, L. Chang, G. Wang, Z. Chen, Y. Cao, X. Liao, E. J. Lavernia, R. Z. Valiev, B. Sarrafpour, H. Zoellner, and S. P. Ringer, "Nanocrystalline β-Ti alloy with high hardness, low Young's modulus and excellent in vitro biocompatibility for biomedical applications," *Mater. Sci. Eng. C*, vol. 33, no. 6, pp. 3530–3536, 2013.

[305] R Valiev, "Structural Modeling and Physical Properties of SPD-Processed Materials," in *Bulk Nanostructured Mater.* Hoboken, NJ: John Wiley & Sons, Inc, 2013, pp. 291–330.

[306] A. Lebedev, Y. Burenkov, A. Romanov, V. Kopylov, V. Filonenko, and V. Gryaznov, "Softening of the elastic modulus in submicrocrystalline copper," *Mater. Sci. Eng. A*, vol. 203, no. 1-2, pp. 165–170, 1995.

[307] J. Skiba, M. Kulczyk, W. Pachla, T. S. Wisniewski, J. Smalc-Koziorowska, M. Kubis, M. Wroblewska, and M. Przybysz, "Effect of Severe Plastic Deformation Realized by Hydrostatic Extrusion on Heat Transfer in CP Ti Grade 2 and 316L Austenitic Stainless Steel," *J. Nanomedicine Nanotechnol.*, vol. 09, no. 04, 2018.

[308] G. Rogl, S. Ghosh, L. Wang, J. Bursik, A. Grytsiv, M. Kerber, E. Bauer, R. C. Mallik, X.-Q. Chen, M. Zehetbauer, and P. Rogl, "Half-Heusler alloys: Enhancement of ZT after severe plastic deformation (ultra-low thermal conductivity)," *Acta Mater.*, vol. 183, pp. 285–300, 2020.

[309] S. Harish, M. Tabara, Y. Ikoma, Z. Horita, Y. Takata, D. G. Cahill, and M. Kohno, "Thermal conductivity reduction of crystalline silicon by high-pressure torsion," *Nanoscale Res. Lett.*, vol. 9, no. 1, p. 326, 2014.

[310] R. Lapovok, M. Dubrovsky, A. Kosinova, and G. Raab, "Effect of Severe Plastic Deformation on the Conductivity and Strength of Copper-Clad Aluminium Conductors," *Metals (Basel).*, vol. 9, no. 9, p. 960, 2019.

[311] Y.-T. Kao, "Effect of Severe Plastic Deformation and Subsequent Heat Treatment on Hardness and Electrical Conductivity of Oxygen-Free High Conductivity (OFHC) Copper, Commercial Pure Copper, and Copper Chromium Alloy," Masters, Texas A&M University, 2014.

[312] P. T. Hung, M. Kawasaki, J.-K. Han, Á. Szabó, J. L. Lábár, Z. Hegedűs, and J. Gubicza, "Thermal stability of nanocrystalline CoCrFeNi multi-principal element alloy: Effect of the degree of severe plastic deformation," *Intermetallics*, vol. 142, p. 107 445, 2022.

[313] J. Gubicza, S. Dobatkin, E. Khosravi, A. Kuznetsov, and J. Lábár, "Microstructural stability of Cu processed by different routes of severe plastic deformation," *Mater. Sci. Eng. A*, vol. 528, no. 3, pp. 1828–1832, 2011.

[314] Y. Huang, S. Sabbaghianrad, A. I. Almazrouee, K. J. Al-Fadhalah, S. N. Alhajeri, and T. G. Langdon, "The significance of self-annealing at room temperature in high purity copper processed by high-pressure torsion," *Mater. Sci. Eng. A*, vol. 656, pp. 55–66, 2016.

[315] V. V. Popov, E. N. Popova, D. D. Kuznetsov, A. V. Stolbovskii, and V. P. Pilyugin, "Thermal stability of nickel structure obtained by high-pressure torsion in liquid nitrogen," *Phys. Met. Metallogr.*, vol. 115, no. 7, pp. 682–691, 2014.

[316] N. A. Enikeev, V. K. Shamardin, and B. Radiguet, "Radiation Tolerance of Ultrafine-Grained Materials Fabricated by Severe Plastic Deformation," *Mater. Trans.*, vol. 60, no. 9, pp. 1723–1731, 2019.

[317] X. Zhang, K. Hattar, Y. Chen, L. Shao, J. Li, C. Sun, K. Yu, N. Li, M. L. Taheri, H. Wang, J. Wang, and M. Nastasi, "Radiation damage in nanostructured materials," *Prog. Mater. Sci.*, vol. 96, pp. 217–321, 2018.

[318] X.-M. Bai, A. F. Voter, R. G. Hoagland, M. Nastasi, and B. P. Uberuaga, "Efficient Annealing of Radiation Damage Near Grain Boundaries via Interstitial Emission," *Science (80-.).*, vol. 327, no. 5973, pp. 1631–1634, 2010.

[319] M. Rose, A. Balogh, and H. Hahn, "Instability of irradiation induced defects in nanostructured materials," *Nucl. Instruments Methods Phys. Res. Sect. B Beam Interact. with Mater. Atoms*, vol. 127-128, pp. 119–122, 1997.

[320] Y. Chimi, A. Iwase, N. Ishikawa, M. Kobiyama, T. Inami, and S. Okuda, "Accumulation and recovery of defects in ion-irradiated nanocrystalline gold," *J. Nucl. Mater.*, vol. 297, no. 3, pp. 355–357, 2001.

[321] A. Etienne, B. Radiguet, N. J. Cunningham, G. R. Odette, R. Valiev, and P. Pareige, "Comparison of radiation-induced segregation in ultrafine-grained and conventional 316 austenitic stainless steels," *Ultramicroscopy*, vol. 111, no. 6, pp. 659–663, 2011.

[322] B. Radiguet, A. Etienne, P. Pareige, X. Sauvage, and R. Valiev, "Irradiation behavior of nanostructured 316 austenitic stainless steel," *J. Mater. Sci.*, vol. 43, no. 23-24, pp. 7338–7343, 2008.

[323] P. B. R. Rajan, I Monnet, E Hug, A Etienne, N Enikeev, C Keller, X Sauvage, R Valiev, and B Radiguet, "Irradiation resistance of a nanostructured 316 austenitic stainless steel," *IOP Conf. Ser. Mater. Sci. Eng.*, vol. 63, p. 012 121, 2014.

[324] A. Mazilkin, Y. Ivanisenko, X. Sauvage, A. Etienne, B. Radiguet, R. Valiev, M. Abramova, and N. Enikeev, "Nanostructured Fe–Cr–W Steel Exhibits Enhanced Resistance to Self-Ion Irradiation," *Adv. Eng. Mater.*, vol. 22, no. 10, p. 1 901 333, 2020.

[325] N. Nita, R. Schaeublin, and M. Victoria, "Impact of irradiation on the microstructure of nanocrystalline materials," *J. Nucl. Mater.*, vol. 329-333, no. 1-3 PART B, pp. 953–957, 2004.

[326] M. Song, Y. Wu, D. Chen, X. Wang, C. Sun, K. Yu, Y. Chen, L. Shao, Y. Yang, K. Hartwig, and X. Zhang, "Response of equal channel angular extrusion processed ultrafine-grained T91 steel subjected to high temperature heavy ion irradiation," *Acta Mater.*, vol. 74, pp. 285–295, 2014.

[327] O. El-Atwani, M. Efe, B. Heim, and J. P. Allain, "Surface damage in ultrafine and multimodal grained tungsten materials induced by low energy helium irradiation," *J. Nucl. Mater.*, vol. 434, no. 1-3, pp. 170–177, 2013.

[328] O. El-Atwani, J. A. Hinks, G. Greaves, S. Gonderman, T. Qiu, M. Efe, and J. P. Allain, "In-situ TEM observation of the response of ultrafine- and nanocrystalline-grained tungsten to extreme irradiation environments," *Sci. Rep.*, vol. 4, no. 1, p. 4716, 2014.

[329] C. Sun, S. Zheng, C. C. Wei, Y. Wu, L. Shao, Y. Yang, K. T. Hartwig, S. A. Maloy, S. J. Zinkle, T. R. Allen, H. Wang, and X. Zhang, "Superior radiation-resistant nanoengineered austenitic 304L stainless steel for applications in extreme radiation environments," *Sci. Rep.*, vol. 5, no. 1, p. 7801, 2015.

[330] E. Aydogan, T. Chen, J. Gigax, D. Chen, X. Wang, P. Dzhumaev, O. Emelyanova, M. Ganchenkova, B. Kalin, M. Leontiva-Smirnova, R. Valiev, N. Enikeev, M. Abramova, Y. Wu, W. Lo, Y. Yang, M. Short, S. Maloy, F. Garner, and L. Shao, "Effect of self-ion irradiation on the microstructural changes of alloy EK-181 in annealed and severely deformed conditions," *J. Nucl. Mater.*, vol. 487, pp. 96–104, 2017.

[331] J. G. Gigax, H. Kim, T. Chen, F. Garner, and L. Shao, "Radiation instability of equal channel angular extruded T91 at ultra-high damage levels," *Acta Mater.*, vol. 132, pp. 395–404, 2017.

[332] E. Hug, R. Prasath Babu, I. Monnet, A. Etienne, F. Moisy, V. Pralong, N. Enikeev, M. Abramova, X. Sauvage, and B. Radiguet, "Impact of the nanostructuration on the corrosion resistance and hardness of irradiated 316 austenitic stainless steels," *Appl. Surf. Sci.*, vol. 392, pp. 1026–1035, 2017.

[333] V. Shamardin, M. Abramova, T. Bulanova, A. Karsakov, A. Fedoseev, A. Obukhov, R. Valiev, I. Alexandrov, G. Raab, and N. Enikeev, "Stability of the structure and properties of an ultrafine-grained Cr-Ni steel irradiated with neutrons in nuclear reactor core conditions," *Mater. Sci. Eng. A*, vol. 712, pp. 365–372, 2018.

[334] A. Alsabbagh, A. Sarkar, B. Miller, J. Burns, L. Squires, D. Porter, J. I. Cole, and K. Murty, "Microstructure and mechanical behavior of neutron irradiated ultrafine grained ferritic steel," *Mater. Sci. Eng. A*, vol. 615, pp. 128–138, 2014.

[335] V. K. Shamardin, T. M. Bulanova, A. E. Fedoseev, A. A. Karsakov, R. Z. Valiev, M. M. Abramova, I. V. Smirnov, and N. A. Enikeev, "The effect of neutron irradiation on the impact toughness of austenitic stainless steel in ultrafine-grained state," *J. Nucl. Mater.*, vol. 544, p. 152 680, 2021.

[336] A. Aitkaliyeva, J. W. Madden, B. D. Miller, J. I. Cole, and J. Gan, "Comparison of preparation techniques for nuclear materials for transmission electron microscopy (TEM)," *J. Nucl. Mater.*, vol. 459, pp. 241–246, 2015.

[337] A. Reza, H. Yu, K. Mizohata, and F. Hofmann, "Thermal diffusivity degradation and point defect density in self-ion implanted tungsten," *Acta Mater.*, vol. 193, pp. 270–279, 2020.

[338] R. A. Schwarzer, D. P. Field, B. L. Adams, M. Kumar, and A. J. Schwartz, "Present State of Electron Backscatter Diffraction and Prospective Developments," in *Electron Backscatter Diffr. Mater. Sci.* Boston, MA: Springer US, 2009, pp. 1–20.

[339] A. J. Wilkinson, G. Meaden, and D. J. Dingley, "High resolution mapping of strains and rotations using electron backscatter diffraction," *Mater. Sci. Technol.*, vol. 22, no. 11, pp. 1271–1278, 2006.

[340] A. J. Wilkinson, G. Meaden, and D. J. Dingley, "High resolution mapping of strains and rotations using electron backscatter diffraction," *Mater. Sci. Technol.*, vol. 22, no. 11, pp. 1271–1278, 2006.

[341] T. B. Britton and A. J. Wilkinson, "High resolution electron backscatter diffraction measurements of elastic strain variations in the presence of larger lattice rotations," *Ultramicroscopy*, vol. 114, pp. 82–95, 2012.

[342] S. Das, H. Yu, K. Mizohata, E. Tarleton, and F. Hofmann, "Modified deformation behaviour of self-ion irradiated tungsten: A combined nano-indentation, HR-EBSD and crystal plasticity study," *Int. J. Plast.*, vol. 135, p. 102 817, 2020.

[343] S. Das, H. Yu, E. Tarleton, and F. Hofmann, "Hardening and Strain Localisation in Helium-Ion-Implanted Tungsten," *Sci. Rep.*, vol. 9, no. 1, p. 18 354, 2019.

[344] A. J. Leide, R. I. Todd, and D. E. J. Armstrong, "Effect of Ion Irradiation on Nanoindentation Fracture and Deformation in Silicon Carbide," *JOM*, vol. 73, no. 6, pp. 1617–1628, 2021.

[345] J. Gallet, M. Perez, R. Guillou, C. Ernould, C. Le Bourlot, C. Langlois, B. Beausir, E. Bouzy, T. Chaise, and S. Cazottes, "Experimental measurement of dislocation density in metallic materials: A quantitative comparison between measurements techniques (XRD, R-ECCI, HR-EBSD, TEM)," *Mater. Charact.*, vol. 199, p. 112 842, 2023.

[346] H. Yu, P. Karamched, S. Das, J. Liu, K. Mizohata, and F. Hofmann, "New perspectives on collision cascade damage in self-ion irradiated tungsten from HR-EBSD and ECCI," *J. Nucl. Mater.*, vol. 554, p. 153 074, 2021.

[347] R. Keller and R. Geiss, "Transmission EBSD from 10 nm domains in a scanning electron microscope," *J. Microsc.*, vol. 245, no. 3, pp. 245–251, 2012.

[348] J. Fundenberger, E. Bouzy, D. Goran, J. Guyon, H. Yuan, and A. Morawiec, "Orientation mapping by transmission-SEM with an on-axis detector," *Ultramicroscopy*, vol. 161, pp. 17–22, 2016.

[349] P. W. Trimby, "Orientation mapping of nanostructured materials using transmission Kikuchi diffraction in the scanning electron microscope," *Ultramicroscopy*, vol. 120, pp. 16–24, 2012.

[350] H. Yu, J. Liu, P. Karamched, A. J. Wilkinson, and F. Hofmann, "Mapping the full lattice strain tensor of a single dislocation by high angular resolution transmission Kikuchi diffraction (HR-TKD)," *Scr. Mater.*, vol. 164, pp. 36–41, 2019.

[351] G. He, H. Yu, P. Karamched, J. Liu, and F. Hofmann, "Elastic strain associated with irradiation-induced defects in self-ion irradiated tungsten," *Scr. Mater.*, vol. 237, p. 115 687, 2023.

[352] W. Bragg, "The structure of some crystals as indicated by their diffraction of X-rays," *Proc. R. Soc. London. Ser. A, Contain. Pap. a Math. Phys. Character*, vol. 89, no. 610, pp. 248–277, 1913.

[353] W. Bragg and W. Bragg, "The reflection of X-rays by crystals," *Proc. R. Soc. London. Ser. A, Contain. Pap. a Math. Phys. Character*, vol. 88, no. 605, pp. 428–438, 1913.

[354] G. Williamson and W. Hall, "X-ray line broadening from filed aluminium and wolfram," *Acta Metall.*, vol. 1, no. 1, pp. 22–31, 1953.

[355] B. E. Warren and B. L. Averbach, "The Effect of Cold-Work Distortion on X-Ray Patterns," *J. Appl. Phys.*, vol. 21, no. 6, pp. 595–599, 1950.

[356] T. Simm, "Peak Broadening Anisotropy and the Contrast Factor in Metal Alloys," *Crystals*, vol. 8, no. 5, p. 212, 2018.

[357] T. Ungár, J. Gubicza, G. Ribárik, and A. Borbély, "Crystallite size distribution and dislocation structure determined by diffraction profile analysis: principles and practical application to cubic and hexagonal crystals," *J. Appl. Crystallogr.*, vol. 34, no. 3, pp. 298–310, 2001.

[358] T. Ungár, "Dislocation model of strain anisotropy," *Powder Diffr.*, vol. 23, no. 2, pp. 125–132, 2008.

[359] T. Ungár and G. Tichy, "The effect of dislocation contrast on X-ray line profiles in untextured polycrystals," *Phys. Status Solidi Appl. Res.*, vol. 171, no. 2, pp. 425–434, 1999.

[360] G. Ribárik, B. Jóni, and T. Ungár, "The Convolutional Multiple Whole Profile (CMWP) Fitting Method, a Global Optimization Procedure for Microstructure Determination," *Crystals*, vol. 10, no. 7, p. 623, 2020.

[361] M. Krivoglaz and K. Ryaboshapka, "Theory of X-ray Scattering by Crystals Containing Dislocations, Randomly Distributed Dislocation Loops," *Phys. Met. Met.*, vol. 16, pp. 1–13, 1963.

[362] M. Wilkens, "The determination of density and distribution of dislocations in deformed single crystals from broadened X-ray diffraction profiles," *Phys. Status Solidi*, vol. 2, no. 2, pp. 359–370, 1970.

[363] K. A. Levenberg, "Method for the Solution of Certain Non-Linear Problems in Least Squares," *Quart. Appl. Mathcs.*, vol. 2, pp. 164–168, 1944.

[364] D. Marquardt, "An Algorithm for Least-Squares Estimation of Nonlinear Parameters," *SIAM Rev. Soc. Ind. Appl. Mathcs.*, vol. 2, pp. 431–441, 1963.

[365] H. Tyralis, D. Koutsoyiannis, and S. Kozanis, "An algorithm to construct Monte Carlo confidence intervals for an arbitrary function of probability distribution parameters," *Comput. Stat.*, vol. 28, no. 4, pp. 1501–1527, 2013.

[366] A. R. Warwick, R. Thomas, M. Boleininger, Ö. Koç, G. Zilahi, G. Ribárik, Z. Hegedues, U. Lienert, T. Ungar, C. Race, M. Preuss, P. Frankel, and S. Dudarev, "Dislocation density transients and saturation in irradiated zirconium," *Int. J. Plast.*, vol. 164, p. 103 590, 2023.

[367] T. Ungár, G. Ribárik, M. Topping, R. M. A. Jones, X. Dan Xu, R. Hulse, A. Harte, G. Tichy, C. P. Race, P. Frankel, and M. Preuss, "Characterizing dislocation loops in irradiated polycrystalline Zr alloys by X-ray line profile analysis of powder diffraction patterns with satellites," *J. Appl. Crystallogr.*, vol. 54, no. 3, pp. 803–821, 2021.

[368] T. Ungár, P. Frankel, G. Ribárik, C. P. Race, and M. Preuss, "Size-distribution of irradiation-induced dislocation-loops in materials used in the nuclear industry," *J. Nucl. Mater.*, vol. 550, p. 152 945, 2021.

[369] G. Ribárik, J. Gubicza, and T. Ungár, "Correlation between strength and microstructure of ball-milled Al–Mg alloys determined by X-ray diffraction," *Mater. Sci. Eng. A*, vol. 387-389, pp. 343–347, 2004.

[370] W. Skrotzki, A. Pukenas, E. Odor, B. Joni, T. Ungar, B. Völker, A. Hohenwarter, R. Pippan, and E. P. George, "Microstructure, Texture, and Strength Development during High-Pressure Torsion of CrMnFeCoNi High-Entropy Alloy," *Crystals*, vol. 10, no. 4, p. 336, 2020.

[371] Z. Fan, B. Jóni, G. Ribárik, É. Ódor, Z. Fogarassy, and T. Ungár, "The Microstructure and strength of a V–5Cr–5Ti alloy processed by high pressure torsion," *Mater. Sci. Eng. A*, vol. 758, pp. 139–146, 2019.

[372] X. Li, S. Holdsworth, S. Kalácska, L. Balogh, J.-S. Park, A. Sologubenko, X. Maeder, S. Kabra, E. Mazza, and E. Hosseini, "Primary creep regeneration in 10In-situ and ex-situ microstructure studies," *Mater. Des.*, vol. 199, p. 109 405, 2021.

[373] H. Dannoshita, H. Hasegawa, S. Higuchi, H. Matsuda, W. Gong, T. Kawasaki, S. Harjo, and O. Umezawa, "Evolution of dislocation structure determined by neutron diffraction line profile analysis during tensile deformation in quenched and tempered martensitic steels," *Mater. Sci. Eng. A*, vol. 854, p. 143 795, 2022.

[374] B. C. Larson, W. Yang, G. E. Ice, J. D. Budai, and J. Z. Tischler, "Three-dimensional X-ray structural microscopy with submicrometre resolution," *Nature*, vol. 415, no. 6874, pp. 887–890, 2002.

[375] W. Liu, G. E. Ice, B. C. Larson, W. Yang, J. Z. Tischler, and J. D. Budai, "The three-dimensional X-ray crystal microscope: A new tool for materials characterization," *Metall. Mater. Trans. A Phys. Metall. Mater. Sci.*, vol. 35 A, no. 7, pp. 1963–1967, 2004.

[376] W. Yang, B. C. Larson, J. Z. Tischler, G. E. Ice, J. D. Budai, and W. Liu, "Differential-aperture X-ray structural microscopy: A submicron-resolution three-dimensional probe of local microstructure and strain," in *Micron*, vol. 35, Pergamon, 2004, pp. 431–439.

[377] W. Liu, P. Zschack, J. Tischler, G. Ice, and B. Larson, "X-ray laue diffraction microscopy in 3D at the advanced photon source," in *AIP Conf. Proc.*, vol. 1365, American Institute of PhysicsAIP, 2010, pp. 108–111.

[378] J. Z. Tischler, *LaueGo*, Argonne National Laboratory, 2020.

[379] J. S. Chung and G. E. Ice, "Automated indexing for texture and strain measurement with broad-bandpass x-ray microbeams," *J. Appl. Phys.*, vol. 86, no. 9, pp. 5249–5255, 1999.

[380] F. Hofmann, D. R. Mason, J. K. Eliason, A. A. Maznev, K. A. Nelson, and S. L. Dudarev, "Non-Contact Measurement of Thermal Diffusivity in Ion-Implanted Nuclear Materials," *Sci. Rep.*, vol. 5, no. 1, p. 16 042, 2015.

[381] S. Das, D. Armstrong, Y. Zayachuk, W. Liu, R. Xu, and F. Hofmann, "The effect of helium implantation on the deformation behaviour of tungsten: X-ray micro-diffraction and nanoindentation," *Scr. Mater.*, vol. 146, pp. 335–339, 2018.

[382] P. Sudharshan Phani and W. Oliver, "Ultra High Strain Rate Nanoindentation Testing," *Materials (Basel).*, vol. 10, no. 6, p. 663, 2017.

[383] W. C. Oliver and G. M. Pharr, "Measurement of hardness and elastic modulus by instrumented indentation: Advances in understanding and refinements to methodology," Tech. Rep., 2004.

[384] X. Li and B. Bhushan, "A review of nanoindentation continuous stiffness measurement technique and its applications," *Mater. Charact.*, vol. 48, no. 1, pp. 11–36, 2002.

[385] W. Oliver and G. Pharr, "An improved technique for determining hardness and elastic modulus using load and displacement sensing indentation experiments," *J. Mater. Res.*, vol. 7, no. 6, pp. 1564–1583, 1992.

[386] I. N. Sneddon, "The relation between load and penetration in the axisymmetric boussinesq problem for a punch of arbitrary profile," *Int. J. Eng. Sci.*, vol. 3, no. 1, pp. 47–57, 1965.

[387] R. King, "Elastic analysis of some punch problems for a layered medium," *Int. J. Solids Struct.*, vol. 23, no. 12, pp. 1657–1664, 1987.

[388] G. Pharr, W. Oliver, and F. Brotzen, "On the generality of the relationship among contact stiffness, contact area, and elastic modulus during indentation," *J. Mater. Res.*, vol. 7, no. 3, pp. 613–617, 1992.

[389] A. C. Fischer-Cripps, *Nanoindentation*, 3rd. New York, NY: Springer, 2011, pp. 21–37.

[390] J. B. Pethica and W. C. Oliver, "Mechanical Properties of Nanometre Volumes of Material: use of the Elastic Response of Small Area Indentations," *MRS Proc.*, vol. 130, p. 13, 1988.

[391] K. L. Johnson, "The correlation of indentation experiments," *J. Mech. Phys. Solids*, vol. 18, no. 2, pp. 115–126, 1970.

[392] W. D. Nix and H. Gao, "Indentation size effects in crystalline materials: A law for strain gradient plasticity," *J. Mech. Phys. Solids*, vol. 46, no. 3, pp. 411–425, 1998.

[393] D. Kramer, H. Huang, M. Kriese, J. Robach, J. Nelson, A. Wright, D. Bahr, and W. W. Gerberich, "Yield strength predictions from the plastic zone around nanocontacts," *Acta Mater.*, vol. 47, no. 1, pp. 333–343, 1998.

[394] P. Hosemann, D. Kiener, Y. Wang, and S. A. Maloy, "Issues to consider using nano indentation on shallow ion beam irradiated materials," *J. Nucl. Mater.*, vol. 425, no. 1-3, pp. 136–139, 2012.

[395] D. Kiener, A. M. Minor, O. Anderoglu, Y. Wang, S. A. Maloy, and P. Hosemann, "Application of small-scale testing for investigation of ion-beam-irradiated materials," *J. Mater. Res.*, vol. 27, no. 21, pp. 2724–2736, 2012.

[396] B. Taljat and G. Pharr, "Development of pile-up during spherical indentation of elastic–plastic solids," *Int. J. Solids Struct.*, vol. 41, no. 14, pp. 3891–3904, 2004.

[397] L. N. Zhu, B. S. Xu, H. D. Wang, C. B. Wang, and D. X. Yang, "Measurement of mechanical properties of 1045 steel with significant pile-up by sharp indentation," *J. Mater. Sci.*, vol. 46, no. 4, pp. 1083–1086, 2011.

[398] E. Hasenhuetl, R. Kasada, Z. Zhang, K. Yabuuchi, Y. J. Huang, and A. Kimura, "Evaluation of ion-irradiation hardening of tungsten single crystals by nanoindentation technique considering material pile-up effect," *Mater. Trans.*, vol. 58, no. 5, pp. 749–756, 2017.

[399] C. E. Beck, F. Hofmann, J. K. Eliason, A. A. Maznev, K. A. Nelson, and D. E. Armstrong, "Correcting for contact area changes in nanoindentation using surface acoustic waves," *Scr. Mater.*, vol. 128, pp. 83–86, 2017.

[400] H. Gao and Y. Huang, "Geometrically necessary dislocation and size-dependent plasticity," *Scr. Mater.*, vol. 48, no. 2, pp. 113–118, 2003.

[401] G. M. Pharr, E. G. Herbert, and Y. Gao, "The Indentation Size Effect: A Critical Examination of Experimental Observations and Mechanistic Interpretations," *Annu. Rev. Mater. Res.*, vol. 40, no. 1, pp. 271–292, 2010.

[402] S. Pathak, J. Michler, K. Wasmer, and S. R. Kalidindi, "Studying grain boundary regions in polycrystalline materials using spherical nano-indentation and orientation imaging microscopy," *J. Mater. Sci.*, vol. 47, no. 2, pp. 815–823, 2012.

[403] F. Pöhl, "Pop-in behavior and elastic-to-plastic transition of polycrystalline pure iron during sharp nanoindentation," *Sci. Rep.*, vol. 9, no. 1, pp. 1–12, 2019.

[404] S. Pathak and S. R. Kalidindi, "Spherical nanoindentation stress–strain curves," *Mater. Sci. Eng. R Reports*, vol. 91, pp. 1–36, 2015.

[405] X. Xiao, D. Terentyev, and L. Yu, "Model for the spherical indentation stress-strain relationships of ion-irradiated materials," *J. Mech. Phys. Solids*, vol. 132, p. 103 694, 2019.

[406] C. D. Hardie, S. G. Roberts, and A. J. Bushby, "Mechanical Behavior of Ion-Irradiated Fe-Cr alloys Investigated by Spherical Indentation," *MRS Proc.*, vol. 1424, mrsf11–1424–ss02–01, 2012.

[407] I.-C. Choi and J.-i. Jang, "A Survey of Nanoindentation Studies on HPT-Processed Materials," *Adv. Eng. Mater.*, vol. 22, no. 1, p. 1 900 648, 2020.

[408] I.-C. Choi, D.-H. Lee, B. Ahn, K. Durst, M. Kawasaki, T. G. Langdon, and J.-i. Jang, "Enhancement of strain-rate sensitivity and shear yield strength of a magnesium alloy processed by high-pressure torsion," *Scr. Mater.*, vol. 94, pp. 44–47, 2015.

[409] A. A. Maznev, A. Mazurenko, L. Zhuoyun, and M. Gostein, "Laser-based surface acoustic wave spectrometer for industrial applications," *Rev. Sci. Instrum.*, vol. 74, no. 1, pp. 667–669, 2003.

[410] O. Cometto, C. A. Dennett, S. H. Tsang, M. P. Short, and E. H. Teo, "A thermal study of amorphous and textured carbon and carbon nitride thin films via transient grating spectroscopy," *Carbon N. Y.*, vol. 130, pp. 355–361, 2018.

[411] F. Hofmann, M. P. Short, and C. A. Dennett, "Transient grating spectroscopy: An ultrarapid, nondestructive materials evaluation technique," *MRS Bull.*, vol. 44, no. 5, pp. 392–402, 2019.

[412] J. A. Johnson, A. A. Maznev, M. T. Bulsara, E. A. Fitzgerald, T. C. Harman, S. Calawa, C. J. Vinels, G. Turner, and K. A. Nelson, "Phase-controlled, heterodyne laser-induced transient grating measurements of thermal transport properties in opaque material," *J. Appl. Phys.*, vol. 111, no. 2, p. 023 503, 2012.

[413] O. W. Kading, H. Skurk, A. A. Maznev, and E. Matthias, "Transient thermal gratings at surfaces for thermal characterization of bulk materials and thin films," *Appl. Phys. A Mater. Sci. Process.*, vol. 61, no. 3, pp. 253–261, 1995.

[414] C. A. Dennett and M. P. Short, "Time-resolved, dual heterodyne phase collection transient grating spectroscopy," *Appl. Phys. Lett.*, vol. 110, no. 21, p. 211 106, 2017.

[415] A. G. Every, A. A. Maznev, W. Grill, M. Pluta, J. D. Comins, O. B. Wright, O. Matsuda, W. Sachse, and J. P. Wolfe, "Bulk and surface acoustic wave phenomena in crystals: Observation and interpretation," *Wave Motion*, vol. 50, no. 8, pp. 1197–1217, 2013.

[416] C. A. Dennett and M. P. Short, "Thermal diffusivity determination using heterodyne phase insensitive transient grating spectroscopy," *J. Appl. Phys.*, vol. 123, no. 21, p. 215 109, 2018.

[417] S. V. Garnov, V. I. Konov, A. S. Silenok, O. G. Tsarkova, V. N. Tokarev, and F. Dausinger, "Experimental study of temperature dependence of reflectivity and heat capacity of steels and alloys at continuous wave Nd:YAG laser heating," V. I. Konov and M. N. Libenson, Eds., 1997, pp. 160–175.

[418] P. G. Malischewsky, "Comparison of approximated solutions for the phase velocity of Rayleigh waves (Comment on 'Characterization of surface damage via surface acoustic waves')," *Nanotechnology*, vol. 16, no. 6, pp. 995–996, 2005.

[419] X. Du and J.-C. Zhao, "Facile measurement of single-crystal elastic constants from polycrystalline samples," *npj Comput. Mater.*, vol. 3, no. 1, p. 17, 2017.

[420] S. Cui, R. P. Doerner, M. J. Simmonds, C. Xu, Y. Wang, E. Dechaumphai, E. Fu, G. R. Tynan, and R. Chen, "Thermal conductivity degradation and recovery in ion beam damaged tungsten at different temperature," *J. Nucl. Mater.*, vol. 511, pp. 141–147, 2018.

[421] A. Wylie, A. Reza, G. Harrison, M. Taylor, B. Dacus, F. Hofmann, M. Short, S. Kirk, M. Preuss, and E. Pickering, "Thermal diffusivity, microstructure and nanohardness of laser-welded proton-irradiated Eurofer97," *J. Nucl. Mater.*, vol. 586, p. 154 661, 2023.

[422] K. Song, S. Das, A. Reza, N. W. Phillips, R. Xu, H. Yu, K. Mizohata, D. E. Armstrong, and F. Hofmann, "Characterising Ion-Irradiated FeCr: Hardness, Thermal Diffusivity and Lattice Strain," *Acta Mater.*, vol. 201, pp. 535–546, 2020.

[423] G. S. Was, Z. Jiao, E. Getto, K. Sun, A. M. Monterrosa, S. A. Maloy, O. Anderoglu, B. H. Sencer, and M. Hackett, "Emulation of reactor irradiation damage using ion beams," *Scr. Mater.*, vol. 88, pp. 33–36, 2014.

[424] R. W. Harrison, "On the use of ion beams to emulate the neutron irradiation behaviour of tungsten," *Vacuum*, vol. 160, pp. 355–370, 2019.

[425] S. Das, "Recent advances in characterising irradiation damage in tungsten for fusion power," *SN Appl. Sci.*, vol. 1, no. 12, pp. 1–20, 2019.

[426] P. Olsson, C. S. Becquart, and C. Domain, "Ab initio threshold displacement energies in iron," *Mater. Res. Lett.*, vol. 4, no. 4, pp. 219–225, 2016.

[427] N. Juslin, K. Nordlund, J. Wallenius, and L. Malerba, "Simulation of threshold displacement energies in FeCr," *Nucl. Instruments Methods Phys. Res. Sect. B Beam Interact. with Mater. Atoms*, vol. 255, no. 1 SPEC. ISS. Pp. 75–77, 2007.

[428] H. E. Bennett, A. J. Glass, A. H. Guenther, and B. E. Newnam, "Laser Induced Damage In Optical Materials: 1980," ASTM International, West Conshohocken, Tech. Rep., 1981, pp. 174–179.

[429] W. W. Coblentz, "The Reflecting Power of Various Metals," *Bull. Bur. Stand.*, vol. 7, no. 2, pp. 197–225, 1910.

[430] F. Hofmann, B. Abbey, W. Liu, R. Xu, B. F. Usher, E. Balaur, and Y. Liu, "X-ray micro-beam characterization of lattice rotations and distortions due to an individual dislocation," *Nat. Commun.*, vol. 4, no. 1, pp. 1–8, 2013.

[431] X. Xiao and L. Yu, "Comparison of linear and square superposition hardening models for the surface nanoindentation of ion-irradiated materials," *J. Nucl. Mater.*, vol. 503, pp. 110–115, 2018.

[432] M. Mata, O. Casals, and J. Alcalá, "The plastic zone size in indentation experiments: The analogy with the expansion of a spherical cavity," *Int. J. Solids Struct.*, vol. 43, no. 20, pp. 5994–6013, 2006.

[433] G. R. Speich, A. J. Schwoeble, and W. C. Leslie, "Elastic constants of binary iron-base alloys," *Metall. Trans.*, vol. 3, no. 8, pp. 2031–2037, 1972.

[434] H. Masumoto, S. Sawaya, and M. Kikuchi, "Thermal Expansion and Temperature Dependence of Young's Modulus in Fe-Cr Alloys," *Trans. Japan Inst. Met.*, vol. 12, no. 2, pp. 86–89, 1971.

[435] R. Kasada, Y. Takayama, K. Yabuuchi, and A. Kimura, "A new approach to evaluate irradiation hardening of ion-irradiated ferritic alloys by nano-indentation techniques," *Fusion Engineering and Design*, vol. 86, pp. 2658–2661, 9-11 2011.

[436] W Fulkerson, J. P. Moore, and D. L. McElroy, *Comparison of the thermal conductivity, electrical resistivity, and seebeck coefficient of a high-purity iron and an armco iron to 1000°C*, 1966.

[437] D. Yarbrough and R. Williams, "Method for estimating the lattice thermal conductivity of metallic alloys," Oak Ridge National Laboratory (ORNL), Oak Ridge, TN (United States), Tech. Rep., 1978.

[438] S. Shelton, "Thermal conductivity of some irons and steels over the temperature range 100 to 500 C," *Bur. Stand. J. Res.*, vol. 12, no. 4, p. 441, 1934.

[439] ASM Handbook Committee, *ASM Handbook, Vol 1: Properties and Selection: Irons, Steels, and High-Performance Alloys*. ASM International, 1990, vol. 1, pp. 910–927.

[440] B. Pujilaksono, T. Jonsson, H. Heidari, M. Halvarsson, J. E. Svensson, and L. G. Johansson, "Oxidation of binary FeCr alloys (Fe-2.25Cr, Fe-10Cr, Fe-18Cr and Fe-25Cr) in O 2 and in O 2 + H 2O environment at 600 °c," *Oxid. Met.*, vol. 75, no. 3-4, pp. 183–207, 2011.

[441] C. J. Smithells, *Metals Reference Book*, 2nd. London: Butterworths Scientific Publications, 1955, p. 647.

[442] M Alam, R Imhof, B Zhang, and R. E. Imhof, "Transient surface grating technique for thermal diffusivity measurement," *Physique*, vol. 111, 1994.

[443] X. D. Xu, D. Ma, S. Y. Zhang, A. H. Luo, and W. Kiyotaka, "Thermal diffusivity of film/substrate structures characterized by transient thermal grating method," *Chinese Phys. Lett.*, vol. 25, no. 1, pp. 176–179, 2008.

[444] G. Wang and Y. Li, "Effects of alloying elements and temperature on thermal conductivity of ferrite," *J. Appl. Phys.*, vol. 126, no. 12, p. 125 118, 2019.

[445] H. Wiesmann, M. Gurvitch, H. Lutz, A. Ghosh, B. Schwarz, M. Strongin, P. B. Allen, and J. W. Halley, "Simple model for characterizing the electrical resistivity in A-15 superconductors," *Phys. Rev. Lett.*, vol. 38, no. 14, pp. 782–785, 1977.

[446] D. Mason, "Incorporating non-adiabatic effects in embedded atom potentials for radiation damage cascade simulations," *J. Phys. Condens. Matter*, vol. 27, no. 14, p. 145 401, 2015.

[447] N. W. Ashcroft and N. D. Mermin, *Solid State Physics*. Holt, Rinehart and Winston, 1976.

[448] V. Kuksenko, C. Pareige, and P. Pareige, "Cr precipitation in neutron irradiated industrial purity Fe-Cr model alloys," *J. Nucl. Mater.*, vol. 432, no. 1-3, pp. 160–165, 2013.

[449] F. Cardarelli, "Ferrous Metals and Their Alloys," in *Mater. Handb.* Springer International Publishing, 2018, pp. 101–248.

[450] D. R. Mason, D. Nguyen-Manh, M.-C. Marinica, R. Alexander, A. E. Sand, and S. L. Dudarev, "Relaxation volumes of microscopic and mesoscopic irradiation-induced defects in tungsten," *J. Appl. Phys.*, vol. 126, no. 7, p. 75 112, 2019.

[451] M. C. Marinica, F. Willaime, and J. P. Crocombette, "Irradiation-induced formation of nanocrystallites with C15 laves phase structure in bcc iron," *Phys. Rev. Lett.*, vol. 108, no. 2, p. 025 501, 2012.

[452] K. Song, D. Sheyfer, K. Mizohata, M. Zhang, W. Liu, D. Gürsoy, D. Yang, I. Tolkachev, H. Yu, D. E. Armstrong, and F. Hofmann, "Dose and compositional dependence of irradiation-induced property change in fecr," *Journal of Nuclear Materials*, vol. 594, p. 154 998, 2024.

[453] S. J. Zinkle and J. T. Busby, "Structural materials for fission & fusion energy," *Mater. Today*, vol. 12, no. 11, pp. 12–19, 2009.

[454] G. S. Was, "Challenges to the use of ion irradiation for emulating reactor irradiation," *J. Mater. Res.*, vol. 30, no. 9, pp. 1158–1182, 2015.

[455] S. J. Zinkle, "Fusion materials science: Overview of challenges and recent progress," *Phys. Plasmas*, vol. 12, no. 5, p. 058 101, 2005.

[456] K. Arakawa, M. Hatanaka, H. Mori, and K. Ono, "Effects of chromium on the one-dimensional motion of interstitial-type dislocation loops in iron," *J. Nucl. Mater.*, vol. 329-333, no. 1-3 PART B, pp. 1194–1198, 2004.

[457] L. L. Horton, J. Bentley, and K. Farrell, "A TEM study of neutron-irradiated iron," *J. Nucl. Mater.*, vol. 108-109, no. C, pp. 222–233, 1982.

[458] H. Vaghela, V. J. Lakhera, and B. Sarkar, "Forced flow cryogenic cooling in fusion devices: A review," *Heliyon*, vol. 7, no. 1, e06053, 2021.

[459] P. Spätig, J. C. Chen, and G. Robert Odette, "Ferritic and Tempered Martensitic Steels," *Struct. Alloy. Nucl. Energy Appl.*, pp. 485–527, 2019.

[460] ASTM E521, "Standard Practice for Investigating the Effects of Neutron Radiation Damage Using Charged-Particle Irradiation," in *Annu. B. ASTM Stand.* Vol. 12.02, West Conshohocken, PA: ASTM International, 2016.

[461] S. Agarwal, Y. Lin, C. Li, R. Stoller, and S. Zinkle, "On the use of SRIM for calculating vacancy production: Quick calculation and full-cascade options," *Nucl. Instruments Methods Phys. Res. Sect. B Beam Interact. with Mater. Atoms*, vol. 503, pp. 11–29, 2021.

[462] D. Gürsoy, D. Sheyfer, M. Wojcik, W. Liu, and J. Z. Tischler, "Depth-resolved Laue microdiffraction with coded apertures," *J. Appl. Crystallogr.*, vol. 55, no. 5, pp. 1104–1110, 2022.

[463] D. Gürsoy, D. Sheyfer, M. Wojcik, W. Liu, and J. Z. Tischler, "Digital autofocusing of a coded-aperture Laue diffraction microscope," *Rev. Sci. Instrum.*, vol. 94, no. 1, p. 013 702, 2023.

[464] P. Zhu, Y. Zhao, Y.-R. Lin, J. Henry, and S. J. Zinkle, "Defect-specific strength factors and superposition model for predicting strengthening of ion irradiated fe18cr alloy," *Journal of Nuclear Materials*, vol. 588, p. 154 823, 2024.

[465] Y. Yang, C. Zhang, J. Gou, and J. Li, "The impact of dose rate on defect clustering and irradiation hardening in reactor pressure vessel steel under fe ion irradiation," *Journal of Materials Science*, vol. 59, pp. 1056–1067, 3 2024.

[466] A. Das, E. Altstadt, C. Kaden, G. Kapoor, S. Akhmadaliev, and F. Bergner, "Nanoindentation response of ion-irradiated fe, fe-cr alloys and ferritic-martensitic steel eurofer 97: The effect of ion energy," *Frontiers in Materials*, vol. 8, 2022.

[467] H. Liu, W. Ge, and Y. Wang, "Re-evaluating ion and neutron irradiation data with calculated applicable arc-dpa," *Radiat. Eff. Defects Solids*, vol. 176, no. 5-6, pp. 441–452, 2021.

[468] F. H. Hammad, M. K. Matta, and K. E. Mohammed, "Effect of fast-neutron irradiation on mechanical properties of iron and some iron binary solid solutions," *J. Nucl. Mater.*, vol. 108-109, no. C, pp. 428–435, 1982.

[469] K. Song, H. Yu, P. Karamched, K. Mizohata, D. E. J. Armstrong, and F. Hofmann, "Deformation behaviour of ion-irradiated FeCr: A nanoindentation study," *J. Mater. Res.*, vol. 37, no. 12, pp. 2045–2060, 2022.

[470] Q. U. A. Sahi and Y. S. Kim, "Primary radiation damage characterization of α-iron under irradiation temperature for various PKA energies," *Mater. Res. Express*, vol. 5, no. 4, p. 046 518, 2018.

[471] N. Castin, A. Dubinko, G. Bonny, A. Bakaev, J. Likonen, A. De Backer, A. E. Sand, K. Heinola, and D. Terentyev, "The influence of carbon impurities on the formation of loops in tungsten irradiated with self-ions," *J. Nucl. Mater.*, vol. 527, p. 151 808, 2019.

[472] W. Spitzig and A. Keh, "The effect of orientation and temperature on the plastic flow properties of iron single crystals," *Acta Metall.*, vol. 18, no. 6, pp. 611–622, 1970.

[473] S. Takaki, J. Fuss, H. Kugler, U. Dedek, and H. Schultz, "The resistivity recovery of high purity and carbon doped iron following low temperature electron irradiation," *Radiat. Eff.*, vol. 79, no. 1-4, pp. 87–122, 1983.

[474] C. Domain and C. S. Becquart, "Ab initio calculations of defects in Fe and dilute Fe-Cu alloys," *Phys. Rev. B*, vol. 65, no. 2, p. 024 103, 2001.

[475] R. A. Johnson, "Interstitials and Vacancies in α-Iron," *Phys. Rev.*, vol. 134, no. 5A, A1329–A1336, 1964.

[476] T. Amino, K. Arakawa, and H. Mori, "Detection of one-dimensional migration of single self-interstitial atoms in tungsten using high-voltage electron microscopy," *Sci. Rep.*, vol. 6, no. 1, pp. 1–9, 2016.

[477] D. Nguyen-Manh, A. P. Horsfield, and S. L. Dudarev, "Self-interstitial atom defects in bcc transition metals: Group-specific trends," *Phys. Rev. B - Condens. Matter Mater. Phys.*, vol. 73, no. 2, p. 020 101, 2006.

[478] D. Terentyev, N. Anento, A. Serra, V. Jansson, H. Khater, and G. Bonny, "Interaction of carbon with vacancy and self-interstitial atom clusters in α-iron studied using metallic–covalent interatomic potential," *J. Nucl. Mater.*, vol. 408, no. 3, pp. 272–284, 2011.

[479] Y.-Z. Niu, Y.-H. Li, Q.-Y. Ren, Z.-Z. Li, D. Terentyev, H.-Z. Ma, H.-B. Zhou, and G.-H. Lu, "Influence of carbon on the evolution of irradiation defects in tungsten," *J. Nucl. Mater.*, vol. 579, p. 154 393, 2023.

[480] N. Hashimoto, S. Sakuraya, J. Tanimoto, and S. Ohnuki, "Effect of impurities on vacancy migration energy in Fe-based alloys," *J. Nucl. Mater.*, vol. 445, no. 1-3, pp. 224–226, 2014.

[481] S. A. Karpov and G. D. Tolstolutskaya, "Irradiation-induced hardening of structural materials after low temperature irradiation," in *13th Int. Conf. "Interaction Radiat. with Solids"*, Minsk, Belarus, 2019, pp. 103–106.

[482] Y. Chang, J. Zhang, X. Li, Q. Guo, F. Wan, and Y. Long, "Microstructure and nanoindentation of the CLAM steel with nanocrystalline grains under Xe irradiation," *J. Nucl. Mater.*, vol. 455, no. 1, pp. 624–629, 2014.

[483] J. Wang, M. B. Toloczko, K. Kruska, D. K. Schreiber, D. J. Edwards, Z. Zhu, and J. Zhang, "Carbon Contamination during Ion Irradiation-Accurate Detection and Characterization of its Effect on Microstructure of Ferritic/Martensitic Steels," *Sci. Rep.*, vol. 7, no. 1, pp. 1–12, 2017.

[484] L. Malerba, G. Bonny, D. Terentyev, E. E. Zhurkin, M. Hou, K. Vörtler, and K. Nordlund, "Microchemical effects in irradiated Fe–Cr alloys as revealed by atomistic simulation," *J. Nucl. Mater.*, vol. 442, no. 1-3, pp. 486–498, 2013.

[485] D. Terentyev, L. Malerba, and A. V. Barashev, "On the correlation between self-interstitial cluster diffusivity and irradiation-induced swelling in Fe–Cr alloys," *Philos. Mag. Lett.*, vol. 85, no. 11, pp. 587–594, 2005.

[486] S. Pathak, S. R. Kalidindi, J. S. Weaver, Y. Wang, R. P. Doerner, and N. A. Mara, "Probing nanoscale damage gradients in ion-irradiated metals using spherical nanoindentation," *Sci. Rep.*, vol. 7, no. 1, pp. 1–12, 2017.

[487] J. S. Weaver, C. Sun, Y. Wang, S. R. Kalidindi, R. P. Doerner, N. A. Mara, and S. Pathak, "Quantifying the mechanical effects of He, W and He + W ion irradiation on tungsten with spherical nanoindentation," *J. Mater. Sci.*, vol. 53, no. 7, pp. 5296–5316, 2018.

[488] A. A. Tavassoli, "Present limits and improvements of structural materials for fusion reactors - A review," *J. Nucl. Mater.*, vol. 302, no. 2-3, pp. 73–88, 2002.

[489] M. Lambrecht and L. Malerba, "Positron annihilation spectroscopy on binary Fe-Cr alloys and ferritic/martensitic steels after neutron irradiation," *Acta Mater.*, vol. 59, no. 17, pp. 6547–6555, 2011.

[490] D. R. Mason, A. E. Sand, X. Yi, and S. L. Dudarev, "Direct observation of the spatial distribution of primary cascade damage in tungsten," *Acta Mater.*, vol. 144, pp. 905–917, 2018.

[491] A. J. Bushby, S. G. Roberts, and C. D. Hardie, "Nanoindentation investigation of ion-irradiated Fe–Cr alloys using spherical indenters," *J. Mater. Res.*, vol. 27, no. 1, pp. 85–90, 2012.

[492] K. Suganuma and H. Kayano, "Irradiation hardening of Fe-Cr alloys," *J. Nucl. Mater.*, vol. 118, no. 2-3, pp. 234–241, 1983.

[493] S. Li, Y. Wang, X. Dai, F. Liu, J. Li, and X. Wang, "Evaluation of hardening behaviors in ion-irradiated Fe–9Cr and Fe–20Cr alloys by nanoindentation technique," *J. Nucl. Mater.*, vol. 478, pp. 50–55, 2016.

[494] X. Hu, D. Xu, T. S. Byun, and B. D. Wirth, "Modeling of irradiation hardening of iron after low-dose and low-temperature neutron irradiation," *Model. Simul. Mater. Sci. Eng.*, vol. 22, no. 6, p. 065 002, 2014.

[495] B. A. Gurovich, E. A. Kuleshova, D. A. Mal'tsev, Y. M. Semchenkov, A. S. Frolov, Y. I. Shtrombakh, and A. V. Shutikov, "Mechanism of Change In VVER-440, -1000 Vessel Material Properties in Irradiation–Recovery Annealing–Irradiation Cycle," *At. Energy*, vol. 125, no. 2, pp. 95–102, 2018.

[496] A. R. Allnatt and A. B. Lidiard, *Atomic Transport in Solids*. Cambridge University Press, 1993.

[497] D. Wallis, L. N. Hansen, T. Ben Britton, and A. J. Wilkinson, "Geometrically necessary dislocation densities in olivine obtained using high-angular resolution electron backscatter diffraction," *Ultramicroscopy*, vol. 168, pp. 34–45, 2016.

[498] J. Jiang, T. B. Britton, and A. J. Wilkinson, "Measurement of geometrically necessary dislocation density with high resolution electron backscatter diffraction: Effects of detector binning and step size," *Ultramicroscopy*, vol. 125, pp. 1–9, 2013.

[499] S. Zaefferer and N. N. Elhami, "Theory and application of electron channelling contrast imaging under controlled diffraction conditions," *Acta Mater.*, vol. 75, pp. 20–50, 2014.

[500] K. Johnson, *Contact mechanics*. Cambridge University Press, 1987.

[501] H. M. Ledbetter and R. P. Reed, "Elastic Properties of Metals and Alloys, I. Iron, Nickel, and Iron-Nickel Alloys," *J. Phys. Chem. Ref. Data*, vol. 2, no. 3, pp. 531–618, 1973.

[502] A. Leitner, V. Maier-Kiener, and D. Kiener, "Essential refinements of spherical nanoindentation protocols for the reliable determination of mechanical flow curves," *Mater. Des.*, vol. 146, pp. 69–80, 2018.

[503] X. Xiao and L. Yu, "A unified statistical model for indentation pop-in: Effects of indenter radius and microstructure density on the transition from homogeneous nucleation to heterogeneous nucleation to bulk plasticity," *Int. J. Plast.*, vol. 141, p. 102 980, 2021.

[504] S. Shim, H. Bei, E. P. George, and G. M. Pharr, "A different type of indentation size effect," *Scr. Mater.*, vol. 59, no. 10, pp. 1095–1098, 2008.

[505] B. D. Beake and S. Goel, "Incipient plasticity in tungsten during nanoindentation: Dependence on surface roughness, probe radius and crystal orientation," *Int. J. Refract. Met. Hard Mater.*, vol. 75, pp. 63–69, 2018.

[506] J. R. Morris, H. Bei, G. M. Pharr, and E. P. George, "Size effects and stochastic behavior of nanoindentation pop in," *Phys. Rev. Lett.*, vol. 106, no. 16, p. 165 502, 2011.

[507] T.-H. Ahn, C.-S. Oh, K. Lee, E. P. George, and H. N. Han, "Relationship between yield point phenomena and the nanoindentation pop-in behavior of steel," *J. Mater. Res.*, vol. 27, no. 1, pp. 39–44, 2012.

[508] L. Casillas-Trujillo, L. Xu, and H. Xu, "Compositional effects on ideal shear strength in Fe-Cr alloys," *J. Alloys Compd.*, vol. 720, pp. 466–472, 2017.

[509] C. R. Krenn, D. Roundy, M. L. Cohen, D. C. Chrzan, and J. W. Morris, "Connecting atomistic and experimental estimates of ideal strength," *Phys. Rev. B - Condens. Matter Mater. Phys.*, vol. 65, no. 13, pp. 1–4, 2002.

[510] Y. Song, D. Xu, R. Yang, D. Li, W. Wu, and Z. Guo, "Theoretical study of the effects of alloying elements on the strength and modulus of β-type bio-titanium alloys," *Mater. Sci. Eng. A*, vol. 260, no. 1-2, pp. 269–274, 1999.

[511] Y. M. Huang, J. C. Spence, and O. F. Sankey, "The effect of impurities on the ideal tensile strength of silicon," *Philos. Mag. A Phys. Condens. Matter, Struct. Defects Mech. Prop.*, vol. 70, no. 1, pp. 53–62, 1994.

[512] C Heintze, F Bergner, and A Ulbricht, *Characterization of Fe-Cr alloys using SANS, nanoindentation and ultrasound*, 2009.

[513] K. Jin, Y. Xia, M. Crespillo, H. Xue, Y. Zhang, Y. F. Gao, and H. Bei, "Quantifying early stage irradiation damage from nanoindentation pop-in tests," *Scr. Mater.*, vol. 157, pp. 49–53, 2018.

[514] H. Bei, Y. Z. Xia, R. I. Barabash, and Y. F. Gao, "A tale of two mechanisms: Strain-softening versus strain-hardening in single crystals under small stressed volumes," *Scr. Mater.*, vol. 110, pp. 48–52, 2016.

[515] D. K. Patel and S. R. Kalidindi, "Correlation of spherical nanoindentation stress-strain curves to simple compression stress-strain curves for elastic-plastic isotropic materials using finite element models," *Acta Mater.*, vol. 112, pp. 295–302, 2016.

[516] S. R. Kalidindi and S. Pathak, "Determination of the effective zero-point and the extraction of spherical nanoindentation stress-strain curves," *Acta Mater.*, vol. 56, no. 14, pp. 3523–3532, 2008.

[517] S. Pathak, D. Stojakovic, R. Doherty, and S. R. Kalidindi, "Importance of surface preparation on the nano-indentation stress-strain curves measured in metals," *J. Mater. Res.*, vol. 24, no. 3, pp. 1142–1155, 2009.

[518] T Zhu, A Bushby, and D Dunstan, "Size effect in the initiation of plasticity for ceramics in nanoindentation," *J. Mech. Phys. Solids*, vol. 56, no. 4, pp. 1170–1185, 2008.

[519] J. S. Weaver, A. Khosravani, A. Castillo, and S. R. Kalidindi, "High throughput exploration of process-property linkages in Al-6061 using instrumented spherical microindentation and microstructurally graded samples," *Integr. Mater. Manuf. Innov.*, vol. 5, no. 1, pp. 192–211, 2016.

[520] J. S. Weaver, M. W. Priddy, D. L. McDowell, and S. R. Kalidindi, "On capturing the grain-scale elastic and plastic anisotropy of α-Ti with spherical nanoindentation and electron back-scattered diffraction," *Acta Mater.*, vol. 117, pp. 23–34, 2016.

[521] M. J. Makin and F. J. Minter, "Irradiation hardening in copper and nickel," *Acta Metall.*, vol. 8, no. 10, pp. 691–699, 1960.

[522] K. Linga Murty and D. J. Oh, "Friction and source hardening in irradiated mild steel," *Scr. Metall.*, vol. 17, no. 3, pp. 317–320, 1983.

[523] S. B. Kass and K Linga Murty, "Effect of Neutron Irradiation on Mechanical Properties of Ferritic Steels," in *Proc. TMS-symposium Microstruct. Mech. Prop. Aging Mater. II*, P. K. Liaw, Ed., Las Vegas, 1995, pp. 27–35.

[524] M. Luppo, C Bailat, R Schäublin, and M Victoria, "Tensile properties and microstructure of 590 MeV proton-irradiated pure Fe and a Fe–Cr alloy," *J. Nucl. Mater.*, vol. 283-287, no. PART I, pp. 483–487, 2000.

[525] D Tabor, "A simple theory of static and dynamic hardness," *Proc. R. Soc. London. Ser. A. Math. Phys. Sci.*, vol. 192, no. 1029, pp. 247–274, 1948.

[526] E. G. Herbert, E. G. Herbert, G. M. Pharr, W. C. Oliver, J. L. Hay, and B. N. Lucas, "On the measurement of stress-strain curves by spherical indentation," *Thin Solid Films*, vol. 398, no. 399, pp. 331–335, 2001.

[527] S. Basu, A. Moseson, and M. W. Barsoum, "On the determination of spherical nanoindentation stress-strain curves," *J. Mater. Res.*, vol. 21, no. 10, pp. 2628–2637, 2006.

[528] B. R. Donohue, A. Ambrus, and S. R. Kalidindi, "Critical evaluation of the indentation data analyses methods for the extraction of isotropic uniaxial mechanical properties using finite element models," *Acta Mater.*, vol. 60, no. 9, pp. 3943–3952, 2012.

[529] B. Xu and X. Chen, "Determining engineering stress-strain curve directly from the load-depth curve of spherical indentation test," *J. Mater. Res.*, vol. 25, no. 12, pp. 2297–2307, 2010.

[530] G. Dieter, *Mechanical Metallurgy*. McGraw-Hill Book Company Inc., 1961.

[531] G. Horne, R. Roy, and H. Paxton, "Tensile properties of single crystals of iron-chromium alloys," *J. iron steel Inst.*, vol. 201, pp. 161–167, 1963.

[532] F. Y. Huang, Y. W. Liu, and J. C. Kuo, "Uncertainties in the representative indentation stress and strain using spherical nanoindentation," *Appl. Nanosci.*, vol. 11, no. 3, pp. 895–909, 2021.

[533] I. L. Mogford and D. Hull, "Effect of temperature and neutron irradiation on yield and work hardening in iron," *J. Iron Steel Inst.*, vol. 201, pp. 55–60, 1963.

[534] A. Okada, N. Kawaguchi, M. Hamilton, K. Hamada, T. Yoshiie, I. Ishida, and E. Hirota, "Mechanical property change in neutron irradiated Fe-Cr and Fe-Mn alloys, and their defect structures," *J. Nucl. Mater.*, vol. 212-215, no. PART 1, pp. 382–387, 1994.

[535] J. G. Swadener, E. P. George, and G. M. Pharr, "The correlation of indentation size effect experiments with pyramidal and spherical indenters," *Mater. Res. Soc. Symp. - Proc.*, vol. 695, pp. 451–456, 2002.

[536] J. G. Swadener, E. P. George, and G. M. Pharr, "The correlation of the indentation size effect measured with indenters of various shapes," *J. Mech. Phys. Solids*, vol. 50, no. 4, pp. 681–694, 2002.

[537] Y. V. Milman, A. A. Golubenko, and S. N. Dub, "Indentation size effect in nanohardness," *Acta Mater.*, vol. 59, no. 20, pp. 7480–7487, 2011.

[538] B. N. Singh, A. Horsewell, and P. Toft, "Effects of neutron irradiation on microstructure and mechanical properties of pure iron," *J. Nucl. Mater.*, vol. 271-272, pp. 97–101, 1999.

[539] T. S. Byun, N. Hashimoto, K. Farrell, and E. H. Lee, "Characteristics of microscopic strain localization in irradiated 316 stainless steels and pure vanadium," *J. Nucl. Mater.*, vol. 349, no. 3, pp. 251–264, 2006.

[540] N. Hashimoto, T. S. Byun, K. Farrell, and S. J. Zinkle, "Deformation microstructure of neutron-irradiated pure polycrystalline metals," *J. Nucl. Mater.*, vol. 329-333, no. 1-3 PART B, pp. 947–952, 2004.

[541] F. Bergner, M. Hernández-Mayoral, C. Heintze, M. J. Konstantinović, L. Malerba, and C. Pareige, "TEM Observation of Loops Decorating Dislocations and Resulting Source Hardening of Neutron-Irradiated Fe-Cr Alloys," *Metals (Basel).*, vol. 10, no. 1, p. 147, 2020.

[542] K. Linga Murty, "Role and significance of source hardening in radiation embrittlement of iron and ferritic steels," *J. Nucl. Mater.*, vol. 270, no. 1-2, pp. 115–128, 1999.

[543] D. Hull and I. L. Mogford, "Ductile-brittle transition in steels irradiated with neutrons," *Philos. Mag.*, vol. 3, no. 35, pp. 1213–1222, 1958.

[544] J. G. Y. Chow and S. B. Mcrickard, "Effects on neutron irradiation on the yield strength and grain size relationship in iron and iron-carbon alloys," *Philos. Mag.*, vol. 8, no. 96, pp. 2097–2099, 1963.

[545] T. S. Byun and N. Hashimoto, "Strain Localization in Irradiated Materials," *Nucl. Eng. Des.*, vol. 38, no. 7, pp. 619–638, 2006.

[546] J. V. Sharp, "Deformation of neutron-irradiated copper single crystals," *Philos. Mag.*, vol. 16, no. 139, pp. 77–96, 1967.

[547] K. Farrell, T. Byun, and N. Hashimoto, "Deformation mode maps for tensile deformation of neutron-irradiated structural alloys," *J. Nucl. Mater.*, vol. 335, no. 3, pp. 471–486, 2004.

[548] K. Song, D. Sheyfer, W. Liu, J. Z. Tischler, S. Das, K. Mizohata, H. Yu, D. E. Armstrong, and F. Hofmann, "Deformation localisation in ion-irradiated fe and fe10cr," *Journal of Nuclear Materials*, vol. 596, p. 155 104, 2024.

[549] S. Oh, J. Lee, C. Jang, and A. Kimura, "Irradiation hardening and embrittlement in high-Cr oxide dispersion strengthened steels," *J. Nucl. Mater.*, vol. 386-388, pp. 503–506, 2009.

[550] A. Patra and D. L. McDowell, "Continuum modeling of localized deformation in irradiated bcc materials," *J. Nucl. Mater.*, vol. 432, no. 1-3, pp. 414–427, 2013.

[551] A. Patra and D. L. McDowell, "Crystal plasticity investigation of the microstructural factors influencing dislocation channeling in a model irradiated bcc material," *Acta Mater.*, vol. 110, pp. 364–376, 2016.

[552] Y. Cui, N. Ghoniem, and G. Po, "Plasticity of irradiated materials at the nano and micro-scales," *J. Nucl. Mater.*, vol. 546, p. 152 746, 2021.

[553] M. N. Gussev, K. G. Field, and J. T. Busby, "Deformation localization and dislocation channel dynamics in neutron-irradiated austenitic stainless steels," *J. Nucl. Mater.*, vol. 460, pp. 139–152, 2015.

[554] Y Dai, X Jia, J. Chen, W. Sommer, M Victoria, and G. Bauer, "Microstructure of both as-irradiated and deformed 304L stainless steel irradiated with 800 MeV protons," *J. Nucl. Mater.*, vol. 296, no. 1-3, pp. 174–182, 2001.

[555] G. Altinkurt, M. Fèvre, G. Geandier, M. Dehmas, O. Robach, and J.-S. Micha, "Local strain redistribution in a coarse-grained nickel-based superalloy subjected to shot-peening, fatigue or thermal exposure investigated using synchrotron X-ray Laue microdiffraction," *J. Mater. Sci.*, vol. 53, no. 11, pp. 8567–8589, 2018.

[556] K. Song, D. Sheyfer, K. Mizohata, M. Zhang, W. Liu, D. Gürsoy, D. Yang, I. Tolkachev, H. Yu, D. E. J. Armstrong, and F. Hofmann, "Dose and compositional dependence of irradiation-induced property change in FeCr," *arXiv Repos.*, 2023. arXiv: 2308.00771.

[557] S. Das, H. Yu, E. Tarleton, and F. Hofmann, "Orientation-dependent indentation response of helium-implanted tungsten," *Appl. Phys. Lett.*, vol. 114, no. 22, p. 221 905, 2019.

[558] J. Chen and S. Bull, "On the relationship between plastic zone radius and maximum depth during nanoindentation," *Surf. Coatings Technol.*, vol. 201, no. 7, pp. 4289–4293, 2006.

[559] H. Yu, S. Das, H. Yu, P. Karamched, E. Tarleton, and F. Hofmann, "Orientation dependence of the nano-indentation behaviour of pure Tungsten," *Scr. Mater.*, vol. 189, pp. 135–139, 2020.

[560] R. Smith, D. Christopher, S. D. Kenny, A. Richter, and B. Wolf, "Defect generation and pileup of atoms during nanoindentation of Fe single crystals," *Phys. Rev. B*, vol. 67, no. 24, p. 245 405, 2003.

[561] R Hill, B Storakers, and A. B Zdunek, "A theoretical study of the Brinell hardness test," *Proc. R. Soc. London. A. Math. Phys. Sci.*, vol. 423, no. 1865, pp. 301–330, 1989.

[562] S Biwa, "An analysis of fully plastic Brinell indentation," *J. Mech. Phys. Solids*, vol. 43, no. 8, pp. 1303–1333, 1995.

[563] H. J. Qu, K. H. Yano, P. V. Patki, M. J. Swenson, and J. P. Wharry, "Understanding plasticity in irradiated alloys through TEM in situ compression pillar tests," *J. Mater. Res.*, vol. 35, no. 8, pp. 1037–1050, 2020.

[564] Y. Zayachuk, D. Armstrong, K. Bystrov, S. Van Boxel, T. Morgan, and S. Roberts, "Nanoindentation study of the combined effects of crystallography, heat treatment and exposure to high-flux deuterium plasma in tungsten," *J. Nucl. Mater.*, vol. 486, pp. 183–190, 2017.

[565] J. Z. Tischler, *LaueGo*, Argonne National Laboratory, 2020.

[566] K. Song, G. He, A. Reza, T. Ungár, P. Karamched, D. Yang, I. Tolkachev, K. Mizohata, S. P. Thompson, E. T. Connolly, R. C. Atwood, S. Michalik, D. E. Armstrong, and F. Hofmann, "Microstructural and material property changes in severely deformed eurofer-97," *Materials Characterization*, vol. 215, p. 114 144, 2024.

[567] G. Strangward-Pryce, K. Song, K. Mizohata, and F. Hofmann, "The Effect of High-Pressure Torsion on Irradiation Hardening of Eurofer-97," *Nucl. Mater. Energy*, p. 101 468, 2023.

[568] P. Edalati, A. Mohammadi, M. Ketabchi, and K. Edalati, "Microstructure and microhardness of dual-phase high-entropy alloy by high-pressure torsion: Twins and stacking faults in FCC and dislocations in BCC," *J. Alloys Compd.*, vol. 894, p. 162 413, 2022.

[569] M. Calcagnotto, D. Ponge, E. Demir, and D. Raabe, "Orientation gradients and geometrically necessary dislocations in ultrafine grained dual-phase steels studied by 2D and 3D EBSD," *Mater. Sci. Eng. A*, vol. 527, no. 10-11, pp. 2738–2746, 2010.

[570] S. I. Wright, D. P. Field, and M. M. Nowell, "Post processing effects on GND calculations from EBSD-based orientation measurements," *IOP Conf. Ser. Mater. Sci. Eng.*, vol. 89, no. 1, p. 012 049, 2015.

[571] S. P. Thompson, J. E. Parker, J. Potter, T. P. Hill, A. Birt, T. M. Cobb, F. Yuan, and C. C. Tang, "Beamline I11 at Diamond: A new instrument for high resolution powder diffraction," *Rev. Sci. Instrum.*, vol. 80, no. 7, 2009.

[572] N. Tartoni, S. P. Thompson, C. C. Tang, B. L. Willis, G. E. Derbyshire, A. G. Wright, S. C. Jaye, J. M. Homer, J. D. Pizzey, and A. M. T. Bell, "High-performance X-ray detectors for the new powder diffraction beamline I11 at Diamond," *J. Synchrotron Radiat.*, vol. 15, no. 1, pp. 43–49, 2008.

[573] J Filik, A. W. Ashton, P. C. Y. Chang, P. A. Chater, S. J. Day, M Drakopoulos, M. W. Gerring, M. L. Hart, O. V. Magdysyuk, S Michalik, A Smith, C. C. Tang, N. J. Terrill, M. T. Wharmby, and H Wilhelm, "Processing two-dimensional X-ray diffraction and small-angle scattering data in DAWN 2," *J. Appl. Cryst*, vol. 50, pp. 959–966, 2017.

[574] A. Paúl, A. Beirante, N. Franco, E. Alves, and J. A. Odriozola, "Phase Transformation and Structural Studies of EUROFER RAFM Alloy," *Mater. Sci. Forum*, vol. 514-516, pp. 500–504, 2006.

[575] A. Reza, C. A. Dennett, M. P. Short, J. Waite, Y. Zayachuk, C. M. Magazzeni, S. Hills, and F. Hofmann, "Non-contact, non-destructive mapping of thermal diffusivity and surface acoustic wave speed using transient grating spectroscopy," *Rev. Sci. Instrum.*, vol. 91, no. 5, 2020.

[576] A. Ganeev, M. Nikitina, V. Sitdikov, R. Islamgaliev, A. Hoffman, and H. Wen, "Effects of the Tempering and High-Pressure Torsion Temperatures on Microstructure of Ferritic/Martensitic Steel Grade 91," *Materials (Basel).*, vol. 11, no. 4, p. 627, 2018.

[577] R. Arredondo, M. Balden, A. Mutzke, U. von Toussaint, S. Elgeti, T. Höschen, K. Schlueter, M. Mayer, M. Oberkofler, and W. Jacob, "Impact of surface enrichment and morphology on sputtering of EUROFER by deuterium," *Nucl. Mater. Energy*, vol. 23, p. 100 749, 2020.

[578] G. Stornelli, A. Di Schino, S. Mancini, R. Montanari, C. Testani, and A. Varone, "Grain Refinement and Improved Mechanical Properties of EUROFER97 by Thermo-Mechanical Treatments," *Appl. Sci.*, vol. 11, no. 22, p. 10 598, 2021.

[579] S. Yoshida, Y. Arai, T. Hara, and M. Kato, "Effect of Block Size on the Reduction Rate of Dislocation Density during Tempering Treatment of Lath Martensite in Low Alloy Steel," *ISIJ Int.*, vol. 62, no. 2, ISIJINT–2021–469, 2022.

[580] J. Baczynski and J. Jonas, "Texture development during the torsion testing of α-iron and two IF steels," *Acta Mater.*, vol. 44, no. 11, pp. 4273–4288, 1996.

[581] T. Ungár and A. Borbély, "The effect of dislocation contrast on x-ray line broadening: A new approach to line profile analysis," *Appl. Phys. Lett.*, vol. 69, no. 21, pp. 3173–3175, 1996.

[582] A. Borbély, "The modified Williamson-Hall plot and dislocation density evaluation from diffraction peaks," *Scr. Mater.*, vol. 217, p. 114 768, 2022.

[583] X. Li, X. Li, S. Schönecker, R. Li, J. Zhao, and L. Vitos, "Understanding the mechanical properties of reduced activation steels," *Mater. Des.*, vol. 146, pp. 260–272, 2018.

[584] A. Danón and A. Alamo, "Behavior of Eurofer97 reduced activation martensitic steel upon heating and continuous cooling," *J. Nucl. Mater.*, vol. 307-311, no. 1 SUPPL. Pp. 479–483, 2002.

[585] D. Kumar, J. Hargreaves, A. Bharj, A. Scorror, L. M. Harding, H. Dominguez-Andrade, R. Holmes, R. Burrows, H. Dawson, A. D. Warren, P. E. Flewitt, and T. L. Martin, "The effects of fusion reactor thermal transients on the microstructure of Eurofer-97 steel," *J. Nucl. Mater.*, vol. 554, p. 153 084, 2021.

[586] J. Hidalgo, K. Findley, and M. Santofimia, "Thermal and mechanical stability of retained austenite surrounded by martensite with different degrees of tempering," *Mater. Sci. Eng. A*, vol. 690, pp. 337–347, 2017.

[587] G. K. Tirumalasetty, M. A. Van Huis, C. Kwakernaak, J. Sietsma, W. G. Sloof, and H. W. Zandbergen, "Deformation-induced austenite grain rotation and transformation in TRIP-assisted steel," *Acta Mater.*, vol. 60, no. 3, pp. 1311–1321, 2012.

[588] N. Nakada, Y. Ishibashi, T. Tsuchiyama, and S. Takaki, "Self-stabilization of untransformed austenite by hydrostatic pressure via martensitic transformation," *Acta Mater.*, vol. 110, pp. 95–102, 2016.

[589] M. Villa, F. B. Grumsen, K. Pantleon, and M. A. Somers, "Martensitic transformation and stress partitioning in a high-carbon steel," *Scr. Mater.*, vol. 67, no. 6, pp. 621–624, 2012.

[590] R. Klueh and J. Vitek, "Elevated-temperature tensile properties of irradiated Cr-1 Mo steel," *J. Nucl. Mater.*, vol. 126, no. 1, pp. 9–17, 1984.

[591] E. A. Little and L. P. Stoter, "Microstructural Stability of Fast Reactor Irradiated 10-12%Cr Ferritic-Martensitic Stainless Steels," in *ASTM Spec. Tech. Publ. 782*, H. Brager and J. Perrin, Eds., Philadelphia: ASTM International, 1982, pp. 207–233.

[592] Q. Li, Y. Shen, X. Huang, Z. Xu, and J. Zhu, "Irradiation-induced hardening and softening of CLAM steel under Fe ion irradiation," *Met. Mater. Int.*, vol. 23, no. 6, pp. 1106–1111, 2017.

[593] E. Materna-Morris, A. Möslang, and H.-C. Schneider, "Tensile and low cycle fatigue properties of EUROFER97-steel after 16.3dpa neutron irradiation at 523, 623 and 723K," *J. Nucl. Mater.*, vol. 442, no. 1-3, S62–S66, 2013.

[594] K. Mergia and N. Boukos, "Structural, thermal, electrical and magnetic properties of Eurofer 97 steel," *J. Nucl. Mater.*, vol. 373, no. 1-3, pp. 1–8, 2008.

[595] M. W. Graham, J. C. King, T. R. Pavlov, C. A. Adkins, S. C. Middlemas, and D. P. Guillen, "Impact of neutron irradiation on the thermophysical properties of additively manufactured stainless steel and inconel," *J. Nucl. Mater.*, vol. 549, p. 152 861, 2021.

[596] F. Badry and K. Ahmed, "A new model for the effective thermal conductivity of polycrystalline solids," *AIP Adv.*, vol. 10, no. 10, p. 105 021, 2020.

[597] H. Dong, B. Wen, and R. Melnik, "Relative importance of grain boundaries and size effects in thermal conductivity of nanocrystalline materials," *Sci. Rep.*, vol. 4, no. 1, p. 7037, 2014.

[598] R. A. Duncan, F. Hofmann, A. Vega-Flick, J. K. Eliason, A. A. Maznev, A. G. Every, and K. A. Nelson, "Increase in elastic anisotropy of single crystal tungsten upon He-ion implantation measured with laser-generated surface acoustic waves," *Appl. Phys. Lett.*, vol. 109, no. 15, p. 151 906, 2016.

[599] C. Dennett, K. So, A. Kushima, D. Buller, K. Hattar, and M. Short, "Detecting self-ion irradiation-induced void swelling in pure copper using transient grating spectroscopy," *Acta Mater.*, vol. 145, pp. 496–503, 2018.

[600] C. A. Dennett, D. L. Buller, K. Hattar, and M. P. Short, "Real-time thermomechanical property monitoring during ion beam irradiation using in situ transient grating spectroscopy," *Nucl. Instruments Methods Phys. Res. Sect. B Beam Interact. with Mater. Atoms*, vol. 440, pp. 126–138, 2019.

[601] A. P. Zhilyaev, J. Gubicza, G. Nurislamova, Á. Révész, S. Suriñach, M. D. Baró, and T. Ungár, "Microstructural characterization of ultrafine-grained nickel," *Phys. status solidi*, vol. 198, no. 2, pp. 263–271, 2003.

[602] J. Gubicza, N. Chinh, Z. Horita, and T. Langdon, "Effect of Mg addition on microstructure and mechanical properties of aluminum," *Mater. Sci. Eng. A*, vol. 387-389, pp. 55–59, 2004.

[603] Z. Zhang, É. Ódor, D. Farkas, B. Jóni, G. Ribárik, G. Tichy, S. H. Nandam, J. Ivanisenko, M. Preuss, and T. Ungár, "Dislocations in Grain Boundary Regions: The Origin of Heterogeneous Microstrains in Nanocrystalline Materials," *Metall. Mater. Trans. A Phys. Metall. Mater. Sci.*, vol. 51, no. 1, pp. 513–530, 2020.

[604] V. Vitek, "Atomic level computer modelling of crystal defects with emphasis on dislocations: Past, present and future," *Prog. Mater. Sci.*, vol. 56, no. 6, pp. 577–585, 2011.

[605] M. Duesbery and W. Xu, "The motion of edge dislocations in body-centered cubic metals," *Scr. Mater.*, vol. 39, no. 3, pp. 283–287, 1998.

[606] Q Wei, H Zhang, B Schuster, K Ramesh, R Valiev, L Kesckes, R Ddowding, L Magness, and K Cho, "Microstructure and mechanical properties of super-strong nanocrystalline tungsten processed by high-pressure torsion," *Acta Mater.*, vol. 54, no. 15, pp. 4079–4089, 2006.

[607] G. Cheng, W. Xu, W. Jian, H. Yuan, M. Tsai, Y. Zhu, Y. Zhang, and P. Millett, "Dislocations with edge components in nanocrystalline bcc Mo," *J. Mater. Res.*, vol. 28, no. 13, pp. 1820–1826, 2013.

[608] Y. Cui, G. Po, and N. Ghoniem, "Temperature insensitivity of the flow stress in body-centered cubic micropillar crystals," *Acta Mater.*, vol. 108, pp. 128–137, 2016.

[609] D. Hull and D. Bacon, "Jogs and the Intersection of Dislocations," in *Introd. to Dislocations*, Elsevier, 2011, pp. 137–155.

[610] L. Huang, Q.-J. Li, Z.-W. Shan, J. Li, J. Sun, and E. Ma, "A new regime for mechanical annealing and strong sample-size strengthening in body centred cubic molybdenum," *Nat. Commun.*, vol. 2, no. 1, p. 547, 2011.

[611] J. Gubicza, N. Chinh, J. Lábár, S. Dobatkin, Z. Hegedűs, and T. Langdon, "Correlation between microstructure and mechanical properties of severely deformed metals," *J. Alloys Compd.*, vol. 483, no. 1-2, pp. 271–274, 2009.

[612] D. Raabe, "Recovery and Recrystallization: Phenomena, Physics, Models, Simulation," in *Phys. Metall.* Elsevier, 2014, pp. 2291–2397.

[613] F. J. Humphreys and H. M. Chan, "Discontinuous and continuous annealing phenomena in aluminium–nickel alloy," *Mater. Sci. Technol.*, vol. 12, no. 2, pp. 143–148, 1996.

[614] T. Hao, Z. Q. Fan, S. X. Zhao, G. N. Luo, C. S. Liu, and Q. F. Fang, "Strengthening mechanism and thermal stability of severely deformed ferritic/martensitic steel," *Mater. Sci. Eng. A*, vol. 596, pp. 244–249, 2014.

[615] F. Javadzadeh Kalahroudi, H. Koohdar, H. R. Jafarian, Y. Haung, T. G. Langdon, and M. Nili-Ahmadabadi, "On the microstructure and mechanical properties of an Fe-10Ni-7Mn martensitic steel processed by high-pressure torsion," *Mater. Sci. Eng. A*, vol. 749, pp. 27–34, 2019.

[616] A. Reza, G. He, C. A. Dennett, H. Yu, K. Mizohata, and F. Hofmann, "Thermal diffusivity recovery and defect annealing kinetics of self-ion implanted tungsten probed by insitu transient grating spectroscopy," *Acta Mater.*, vol. 232, p. 117 926, 2022.

[617] C. A. Dennett, B. R. Dacus, C. M. Barr, T. Clark, H. Bei, Y. Zhang, M. P. Short, and K. Hattar, "The dynamic evolution of swelling in nickel concentrated solid solution alloys through in situ property monitoring," *Appl. Mater. Today*, vol. 25, p. 101 187, 2021.

[618] T. Khvan, L. Noels, D. Terentyev, F. Dencker, D. Stauffer, U. Hangen, W. Van Renterghem, C. Chang, and A. Zinovev, "High temperature nanoindentation of iron: Experimental and computational study," *J. Nucl. Mater.*, vol. 567, p. 153 815, 2022.

[619] H. Petryk, S. Stupkiewicz, and S. Kucharski, "On direct estimation of hardening exponent in crystal plasticity from the spherical indentation test," *Int. J. Solids Struct.*, vol. 112, pp. 209–221, 2017.

[620] S. Ha, J.-H. Jang, and K. Kim, "Finite element implementation of dislocation-density-based crystal plasticity model and its application to pure aluminum crystalline materials," *Int. J. Mech. Sci.*, vol. 120, pp. 249–262, 2017.

[621] Y. Liu, B. Wang, M. Yoshino, S. Roy, H. Lu, and R. Komanduri, "Combined numerical simulation and nanoindentation for determining mechanical properties of single crystal copper at mesoscale," *J. Mech. Phys. Solids*, vol. 53, no. 12, pp. 2718–2741, 2005.

[622] L. Li, L. Shen, G. Proust, C. K. Moy, and G. Ranzi, "Three-dimensional crystal plasticity finite element simulation of nanoindentation on aluminium alloy 2024," *Mater. Sci. Eng. A*, vol. 579, pp. 41–49, 2013.

[623] I. Baker, "Interstitial strengthening in f.c.c. metals and alloys," *Adv. Powder Mater.*, vol. 1, no. 4, p. 100 034, 2022.

[624] L. Hewitt, "Heavy ion irradiation as a proxy to neutron irradiation in impure Fe and Fe-Cr alloys," Ph.D. dissertation, University of Oxford, 2018.

[625] M. W. Chase, "NIST-JANAF Themochemical Tables, Fourth Edition," *J. Phys. Chem. Ref. Data*, vol. Monograph, pp. 1–1951, 1998.

[626] O. Dimitrov and C. Dimitrov, "A set of mutually consistent values of frenkel-pair resistivities," *Radiat. Eff.*, vol. 84, no. 1-2, pp. 117–129, 1984.

[627] J. C. Haley, F. Liu, E. Tarleton, A. C. Cocks, G. R. Odette, S. Lozano-Perez, and S. G. Roberts, "Helical dislocations: Observation of vacancy defect bias of screw dislocations in neutron irradiated Fe–9Cr," *Acta Mater.*, vol. 181, pp. 173–184, 2019.

[628] X. Yi, M. L. Jenkins, M. A. Kirk, Z. Zhou, and S. G. Roberts, "In-situ TEM studies of 150 keV W+ ion irradiated W and W-alloys: Damage production and microstructural evolution," *Acta Mater.*, vol. 112, pp. 105–120, 2016.

[629] A. E. Sand, M. J. Aliaga, M. J. Caturla, and K. Nordlund, "Surface effects and statistical laws of defects in primary radiation damage: Tungsten vs. iron," *EPL (Europhysics Lett.*, vol. 115, no. 3, p. 36 001, 2016.

[630] O. Robach, J. S. Micha, O. Ulrich, and P. Gergaud, "Full local elastic strain tensor from Laue microdiffraction: Simultaneous Laue pattern and spot energy measurement," *J. Appl. Crystallogr.*, vol. 44, no. 4, pp. 688–696, 2011.

[631] L. E. Levine, C. Okoro, and R. Xu, "Full elastic strain and stress tensor measurements from individual dislocation cells in copper through-Si vias," *IUCrJ*, vol. 2, no. 6, pp. 635–642, 2015.

[632] L. Balogh, F. Long, and M. R. Daymond, "Contrast factors of irradiation-induced dislocation loops in hexagonal materials," *J. Appl. Crystallogr.*, vol. 49, no. 6, pp. 2184–2200, 2016.